Dark Matter Models: The Neutrino and Flavor Portals

Dissertation
zur Erlangung des akademischen Grades

Dr. rer. nat.
im Fach Physik

Vorgelegt von
Mathias Becker[1]

Fakultät für Physik, Technische Universität Dortmund,
44221 Dortmund, Germany

Dortmund, August 2020

[1] *mathias.becker@tu-dortmund.de*

Gutachter dieser Arbeit: Prof. Dr. Heinrich Päs und Prof. Dr. Gudrun Hiller
Vorsitzender des Promotionsauschusses: Prof. Dr. Wolfgang Rhode

Datum der mündlichen Promotionsprüfung: 1. Oktober 2020

This thesis contains the following work previously published by the author:

- M.Becker and H.Päs. *Leptonic Flavor Structure in the Extra Dimensional Seesaw Mechanism*, Eur. Phys. J. **C78**, 273 (2018) [1]
- M.Becker. *Dark Matter from Freeze-In via the Neutrino Portal*, Eur. Phys. J. **C79**, 611 (2019) [2]
- M.Becker and W-C. Huang. *Two-Component Asymmetric Dark Matter via Bound States and Freeze-In Decay.* Unpublished manuscript, arXiv:1911.06788 [3]

Additionally this thesis contains content from the following ongoing projects:

- M.Becker and C. Hormigos-Feliu. *Vacuum Stability of the Neutrino Portal to Dark Matter.* To be published. [4]
- M.Becker, D.Döring, S.Karmakar, and H.Päs. *A Systematic Analysis of one-loop Solutions to R_K in the Light of Dark Matter.* To be published. [5]

Please note that parts of the first publication [1] were already part of my Master Thesis and the material is partially reused in Chapter 3.

Abstract

In this thesis, we analyze several standard model extensions involving one or multiple dark matter candidates and link the dark matter problem to different other standard model shortcomings such as neutrino mass generation and flavor anomalies. First we discuss the leptonic flavor structure of an extra dimensional seesaw mechanism, which does not include a dark matter candidate. However, the mechanism suppresses couplings to the new right-handed neutrino state. This serves as a motivation to investigate a feebly coupled neutrino portal to dark matter model where the right-handed neutrino both generates the observed neutrino masses and mediates between the standard model and the dark sector. We classify the dark matter production regimes of the model and point out its phenomenological implications. Furthermore, we apply consistency conditions to strongly coupled versions of the neutrino portal to dark matter. We find that the consistency conditions induce an upper limit on the dark matter mass in such a scenario. We continue by discussing the effects of a bound state that can form in a heavy dark sector. We find that the bound state can facilitate particle number transfer from the dark sector to other sectors even if they are only feebly coupled. We also explore a class of models in this thesis that is dedicated to one-loop solutions to the R_K anomaly in the light of dark matter searches. We find that current dark matter direct detection experiments can test the one-loop solutions to the R_K anomaly.

Zusammenfassung

In dieser Arbeit werden Erweiterung des Standard Modells thematisiert, die einen oder mehrere dunkle Materie Kandidaten beinhalten. Des Weiteren wird die Suche nach einem dunklen Materie Kandidaten mit der Modellbildung im Bereich der Neutrinomassengeneration und Flavoranomalien verknüpft. Zunächst wird ein extra dimensionaler Seesaw Mechanismus diskutiert, der keinen dunklen Materie Kandidaten beinhaltet, aber zu einer Unterdrückung der Yukawa Kopplungen des rechtshändigen Neutrinos führt. Diese kleinen Kopplungen sind eine Motivation für die Untersuchung des schwach gekoppelten Bereich des Neutrino Portals zu dunkler Materie. Es werden unterschiedliche dunkle Materie Produktionsbereiche klassifiziert und die phänomenologischen Implikationen des Modells untersucht. Zusätzlich wird geprüft, ob stark gekoppelte Versionen des Neutrino Portals zu dunkler Materie theoretischen Konsistenzbedingungen genügen. Diese Konsistenzbedingungen führen zu einer oberen Massenschranke für den dunklen Materie Kandidaten des Modells. Das nächste Modell beschäftigt sich mit gebundenen Zuständen, die sich in einem schweren dunklen Sektor bilden. Es stellt sich heraus, dass die Bindunzustände zu einem effizientem Teilchentransfer vom schweren dunklen Sektor zu einem anderen Sektor führen können. Das ist sogar der Fall, wenn die beiden Sektoren nur sehr schwach miteinander gekoppelt sind. Das letzte Modell dieser Arbeit analysiert ein-schleifen Lösungen der

R_K Anomalie im Hinblick auf dunkle Materie. Es zeigt sich, dass direkte Suchen nach dunkler Materie das betrachtete Modell stark einschränken können.

Acknowlegments

This thesis ends my four year period at the chairs T3 and T4. The work in physics is challenging and exciting but can be frustrating as well. However, it has been a very fun time due to the very supporting, interactive and vivid group.
I would like to thank all the people who contributed to this environment and took part (or forced me to participate) in the frequent and endless coffee breaks, more or less regular climbing sessions, Thursday's movie night and numerous other social events. Even in the recent times of the Corona pandemic the group immediately reacted and set up an office Discord to allow for a regular distraction from physics. It might even occur that I will miss the group meetings since, after all, I enjoy talking (about physics) too much.
Unfortunately, the PhD is not only about climbing, breaks and movies but also involves a working aspect. I would like to thank my supervisor, Heinrich Päs, for the uncomplicated work and communication in shared projects, the support and advice even in projects he was not directly involved in and for the valuable insights and the support during the phase of my applications for a Post-Doc position. Additionally, I am grateful for Wei-Chih Huang's advice during the first years of my PhD.
I would like to thank the climbing team (Peter, Tim, Dennis and Andrey to name the most stubborn ones) who forced me to climb up to two or three times a week. This in return allowed me to eat much more sweets and cake which were regularly provided in the coffee breaks.
It was a great honor to be allowed to witness the regular meetings of the movie council in person of Peter, Dennis, Clara and Philipp who introduced me to the concept of movies and made sure that I watch proper movies for instance in non-standard aspect ratios and avoid offending Hollywood productions.
I was happy to share my office with Sinan and Kevin over the last four years, as they were never shy of long and sometimes even non-annoying physics discussions.
I am certain I wont forget the time I spent with Dominik in India including a one week stay in a prison-like cell in Calcutta, numerous visits at Alladins and a trip to a monastery in the Himalaya guided by the stoned Mountain Boy.
I am happy that Clara endured my attempts to master the spanish language and taught me how to distinguish a good from a bad Hansa. Our numerous attempts to work together were more fun than productive but who cares about the latter part.
Also I would like to thank Siddhartha Karmakar for making sure that Dominik and myself survive the time in India and the lectures about drug milk.
Finally, I would like to thank my non-physics friends Marvin and Pascal and my mother and siblings for company and distraction outside of the physics world.

Contents

Acronyms

SM	standard model of particle physics
DM	dark matter
QFT	quantum field theory
vev	vacuum expectation value
PMNS	Pontecorvo–Maki–Nakagawa–Sakata
CKM	Cabibbo-Kobayashi-Maskawa
CMB	cosmic microwave background
BBN	big bang nucleosynthesis
BSM	beyond standard model
EWSB	electroweak symmetry breaking
NH	normal hierarchy
IH	inverted hierarchy
CP	charge parity conjugation symmetry
GUT	grand unified theory
LNV	lepton number violation
LHC	Large Hadron Collider
SI	spin independent
SD	spin dependent
WIMP	weakly interacting massive particle
LFV	lepton flavor violating
NPDM	neutrino portal to dark matter
BSF	bound state formation
BSD	bound state dissociation
RGE	renormalization group equations

1. Introduction

Both the observation of neutrino masses and the existence of dark matter (DM), are long-standing evidences for the existence of beyond standard model (BSM) physics. This thesis addresses various models including one or multiple DM candidates and its connection to neutrino physics. A typical approach to allow for the production of DM is to couple a DM candidate via the weak interaction, or a new gauge interaction of roughly the same interactions strength, to the SM. However, DM production can proceed via a wide range of coupling strengths and masses. During this thesis, we outline several production mechanisms and their phenomenological consequences. On the other hand, the existence of neutrino masses requires the introduction of new field content to the SM. Already the simplest extension involves a new fermionic electrically neutral singlet state and therefore a DM candidate. As both the DM and the neutrino mass problem require additional particle content, it is appealing to link both ideas which constitutes the main part of this thesis in form of the discussion of the neutrino portal to DM.
In this chapter, we introduce the standard model of particle physics (SM) as well as the standard model of cosmology and motivate the existence of BSM physics. In Chapter 2, we discuss several neutrino mass generation mechanisms. Afterwards, we give a detailed overview over DM production in models using a portal interaction to connect DM and the SM. Chapter 3 presents an extradimensional neutrino mass model and its phenomenological consequences. The small couplings arising in the extra dimensional model serve as a motivation to investigate the neutrino portal to DM in its feebly coupled regime in Chapter 4. Furthermore, this chapter discusses consistency conditions such as the stability of the scalar vacuum in strongly coupled version of the neutrino portal to DM. In Chapter 5, we examine the effects of a Yukawa bound state that can form in a heavy dark sector. In Chapter 6, we present an analysis of the DM phenomenology of a model which was constructed to provide a solution to a flavor anomaly in the b-sector at one-loop level. Finally, in Chapter 7, we summarize our results.

1.1. The Standard Model of Particle Physics

The SM of particle physics describes the elementary particles and their interactions within the framework of a quantum field theory (QFT). A QFT combines aspects of a classical field theory and quantum mechanics. The fundamental forces, namely the electromagnetic, the weak and the strong force, are embedded in the form of gauge symmetries rendering the theory invariant under transformations of the $SU(3)_C \otimes SU(2)_L \otimes U(1)_Y$ symmetry group.
Since the first works in the early 60's by Glashow and Weinberg [6, 7], the SM was tested with great success, eventually resulting in the discovery of the Higgs boson in 2012 by the ATLAS and CMS collaborations [8, 9]. In this section, the particle content is summarized and the electroweak theory, including electroweak symmetry breaking via the Higgs mechanism are reviewed briefly.

Requiring gauge invariance implies that the Lagrangian of the theory must be invariant under gauge transformations of all fields according to their charge assignment. Within the electroweak theory, gauge transformations of any field ϕ_j are of the form

$$\phi_j \to \exp\left(i\sum_{a=1}^{3}\alpha_a(x)\,t_j^a\right)\exp\left(iY_j\frac{\beta(x)}{2}\right)\phi_j\,, \tag{1.1.1}$$

with t_j^a the generators of the $SU(2)_L$ given in the representation of particle j, Y_j is the hypercharge and $\alpha_a(x)$ and $\beta(x)$ are the local parameters of the $SU(2)_L$ and $U(1)_Y$ gauge transformations respectively. In addition, the derivatives of all fields must be promoted to so called covariant derivatives depending on their representation under the respective gauge transformation

$$D_\mu = \partial_\mu - ig\sum_{a=1}^{3}A_\mu^a t_j^a - i\frac{g'}{2}Y_j B_\mu\,, \tag{1.1.2}$$

where A_μ^a and B_μ are the gauge fields of the $SU(2)_L$ and $U(1)_Y$, while g and g' are their coupling constants.

The particles of the SM can be classified within three categories: Fermions, gauge bosons and scalars. Fermions are further divided into quarks and leptons. While quarks carry a color charge, i.e. they transform non-trivial under the $SU(3)_C$, leptons are color-neutral and therefore are $SU(3)_C$ singlets. In total, there are six quarks. Three up-type quarks (u,c,t) with an electrical charge of $Q = \frac{2}{3}$, and three down type quarks (d,s,b) with $Q = -\frac{1}{3}$. Similarly, the leptons are divided into three charged leptons (e, μ, τ) with $Q = -1$, and three neutrinos (ν_e,ν_μ,ν_τ) with $Q = 0$.

Since gauge transformations are local transformations, each gauge symmetry introduces a given number of gauge bosons. The $SU(3)_C$ has eight massless gauge bosons called gluons g. The electroweak force $SU(2)_L \otimes U(1)_Y$ introduces a total of four gauge bosons: The $W^\pm$, Z^0 and the photon γ. All of those particles but the photon receive a mass after the electroweak symmetry breaking (EWSB), which requires the existence of a scalar field charged under the gauge groups of the electroweak symmetry, the Higgs field.

Another crucial feature of the electroweak symmetry in the SM is that the $SU(2)_L$ distinguishes between particles of different chirality.[1] The left-handed up- and down-type quarks are arranged into three $SU(2)_L$ doublets, defining three generations of fermions in the SM. Likewise, the left-handed charged leptons and neutrinos form three additional $SU(2)_L$ doublets. On the contrary, all right-handed SM fermions are singlets under $SU(2)_L$. The particle content with the respective charges under the SM gauge groups is summarized in table 1.1.

Explicit mass terms of both, fermions and gauge bosons, break the electroweak gauge symmetry. The introduction of the Higgs scalar field, transforming as a doublet under $SU(2)_L$ with a hypercharge of $Y = +1$, allows for breaking the electroweak symmetry via a non-zero vacuum expectation value (vev) without breaking the symmetry explicitly in the Lagrangian. With a Higgs vev of

$$\langle\phi\rangle = \frac{1}{\sqrt{2}}\begin{pmatrix}0\\ v\end{pmatrix}\,, \tag{1.1.3}$$

[1] In extensions of the SM this is not necessarily the case.

Fields	$SU(3)_C$	$SU(2)_L$	Y	Q
$\begin{pmatrix} u \\ d \end{pmatrix}_L, \begin{pmatrix} c \\ s \end{pmatrix}_L, \begin{pmatrix} t \\ b \end{pmatrix}_L$	**3**	**2**	$\frac{1}{3}$	$2/3$ $-1/3$
$\begin{pmatrix} \nu_e \\ e \end{pmatrix}_L, \begin{pmatrix} \nu_\mu \\ \mu \end{pmatrix}_L, \begin{pmatrix} \nu_\tau \\ \tau \end{pmatrix}_L$	**1**	**2**	-1	0 -1
u_R, c_R, t_R	**3**	**1**	$\frac{4}{3}$	$2/3$
d_R, s_R, b_R	**3**	**1**	$-\frac{2}{3}$	$-1/3$
e_R, μ_R, τ_R	**1**	**1**	-2	-1

Table 1.1.: Charge Assignment of the fermions in the SM. The second and third column denote the representation under $SU(3)_C$ and $SU(2)_L$, respectively. Y is the hypercharge and Q the electrical charge. In this convention, the electric charge is related to the hypercharge via $Q = T_3 + \frac{Y}{2}$.

the masses of the vector bosons arise from the kinetic term of the Higgs

$$\mathcal{L} \supset \frac{1}{2}\frac{v^2}{4}\left[2g^2 \underbrace{\frac{1}{\sqrt{2}}\left(A^1_\mu + iA^2_\mu\right)}_{=W^+_\mu}\underbrace{\frac{1}{\sqrt{2}}\left(A^1_\mu - iA^2_\mu\right)}_{=W^-_\mu} + \left(g^2+g'^2\right)\left(\underbrace{\frac{g'B_\mu - gA^3_\mu}{\sqrt{g^2+g'^2}}}_{=Z^0_\mu}\right)^2\right] . \quad (1.1.4)$$

Thus we find

$$m_W = g\frac{v}{2}, \quad m_Z = \sqrt{g^2+g'^2}\frac{v}{2}. \quad (1.1.5)$$

The remaining gauge boson is the photon

$$A_\mu = \frac{1}{\sqrt{g^2+g'^2}}\left(g'A^3_\mu - gB_\mu\right) , \quad (1.1.6)$$

which remains massless. Thus EWSB corresponds to $SU(2)_L \times U(1)_Y \to U(1)_{\text{em}}$.
The fermion masses emanate from Yukawa couplings of the SM fermions with the Higgs field:

$$\mathcal{L} \supset -\left(Y_u\right)_{ij}\left(\bar{Q}_L\right)_i \tilde{\phi}\left(u_R\right)_j - \left(Y_d\right)_{ij}\left(\bar{Q}_L\right)_i \phi\left(d_R\right)_j - \left(Y_l\right)_{ij}\left(\bar{L}_L\right)_i \tilde{\phi}\left(e_R\right)_j , \quad (1.1.7)$$

where $\tilde{\phi} = i\sigma_2\phi^*$ is the hypercharge conjugate of the Higgs doublet, $(Q_L)_i$ and $(L_L)_i$ correspond to the left-handed quark and lepton doublets of the i-th generation and $(u_R)_i$, $(d_R)_i$ and $(e_R)_i$ are the right handed up- and down quarks and the right-handed leptons of the i-th generation respectively. In Eq. (1.1.7), we sum over the generation indices i and j. After EWSB the mass matrices of the up- and down quarks as well as the masses of the charged leptons read

$$\left(M_{u/d/l}\right)_{ij} = \frac{v}{\sqrt{2}}\left(Y_{u/d/l}\right)_{ij} . \quad (1.1.8)$$

These mass matrices are not necessarily diagonal. Actually, $(M_u)_{ij}$ and $(M_d)_{ij}$ cannot be diagonalized simultaneously. This mismatch generates a mixing between different

generations mediated by the $W^{\pm}$ boson, that is parametrized by the Cabibbo-Kobayashi-Maskawa (CKM) matrix. If V_u and V_d are the unitary matrices transforming u_L and d_L into their mass eigenstates u'_L and d'_L, the CKM matrix is given by

$$V_{CKM} = V_u V_d^{\dagger} \,, \tag{1.1.9}$$

and the interaction of the quark mass eigenstates mediated by the W can be written as

$$\mathcal{L} \supset (V_{CKM})_{ij} \left(\bar{u'}_L\right)_i \gamma^{\mu} W_{\mu}^{+} \left(d'_L\right)_j + h.c. \,. \tag{1.1.10}$$

Similarly, the Pontecorvo–Maki–Nakagawa–Sakata (PMNS) matrix arises in the lepton sector and is discussed in chapter 1.3.1

1.2. The Standard Model of Cosmology

The standard model of cosmology relies on the hypothesis that the universe is homogeneous and isotropic on large scales, the so called *cosmological principle* which is supported by the cosmic microwave background (CMB). This assumption induces the Friedmann-Lemaître-Robertson-Walker metric

$$\mathrm{d}s^2 = \mathrm{d}t^2 - a\left(t\right)^2 \left(\frac{\mathrm{d}r^2}{1-kr^2} - r^2 \mathrm{d}\theta^2 - r^2 \sin^2\left(\theta\right) \mathrm{d}\phi^2 \right) , \tag{1.2.1}$$

where $a\left(t\right)$ is the scale factor that parametrizes the relative expansion of the universe and k is a constant describing the curvature. Due to the isotropy, it can only take three values representing different geometries

$$k = \begin{cases} -1, & \text{hyperbolic} \\ 0, & \text{flat} \\ 1, & \text{spherical} \end{cases} . \tag{1.2.2}$$

Combined with the Einstein equations and assuming the stress-energy tensor $T_{\mu\nu}$ to resemble the stress-energy tensor of a perfect fluid, the Friedmann-Lemaître-Robertson-Walker metric results in the time evolution of the scale factor, known as the Friedmann equations. The Friedman equations are related to the conservation of the stress-energy tensor $D_\mu T^{\mu\nu} = 0$ via the Bianchi identity. Together, they yield two independent equations

$$\mathrm{d}\left(\rho a^3\right) = -p\mathrm{d}\left(a^3\right) , \tag{1.2.3}$$

$$H^2 + \frac{k}{a^2} = \frac{8\pi G}{3} . \tag{1.2.4}$$

Eq. (1.2.3) resembles the first law of thermodynamics and the second one is typically referred to as *the Friedmann equation*. Here $H = \frac{\dot{a}}{a}$ is the Hubble parameter. By introducing the *critical density* $\rho_C = \frac{3H^2}{8\pi G}$ the Friedmann equation results in

$$\frac{k}{H^2 a^2} = \Omega - 1 , \tag{1.2.5}$$

where we defined $\Omega \equiv \frac{\rho}{\rho_C}$. Thus, the sign of $\Omega - 1$ is in direct correspondence with the curvature k. Measurements of Ω via the CMB are strongly favoring $k = 0$, hence a (close to) flat universe [10].
Equation (1.2.3) allows to find the dependence of the different energy contents (radiation, non-relativistic matter, vacuum energy) on the scale factor

$$\rho_i\left(a\right) \sim \begin{cases} a^{-4}, & \text{for radiation} \\ a^{-3}, & \text{for non-relativistic matter} \\ a^{0}, & \text{for vacuum energy} \end{cases} . \tag{1.2.6}$$

Then, the Friedmann equation can be conveniently expressed in terms of the density parameters of the various energy contents measured today $\Omega_i = \frac{\rho_{i,0}}{\rho_{C,0}}$ with

$$H^2 = H_0^2 \left[\Omega_R \left(\frac{a_0}{a}\right)^4 + \Omega_M \left(\frac{a_0}{a}\right)^3 + \Omega_k \left(\frac{a_0}{a}\right)^2 + \Omega_\Lambda \right] . \tag{1.2.7}$$

Here, the index 0 indicates the evaluation of the quantity today and we have $i \in \{M, R, \Lambda\}$ corresponding to non-relativistic matter, radiation and vacuum energy[2], respectively. The definition of Ω_k differs, as $\Omega_k = -\frac{k}{a_0^2 H_0^2}$.
The Planck collaboration determined, amongst other parameters, the density parameters Ω_i and the Hubble parameter H_0, using the measurements of the CMB by the Planck satellite [10]. They approximately find $\Omega_\Lambda \approx 0.69$, $\Omega_M \approx 0.31$ and $\Omega_R \approx 10^{-5}$ indicating $\Omega_k = 0.001 \pm 0.002$. Thus, the universe today is dominated by vacuum energy.
Employing Eq. (1.2.7), we can conclude that at earlier times, that is $a < a_0$, all contributions but the vacuum energy were larger. As we have $\Omega_R \sim a^{-4}$ and $\Omega_M \sim a^{-3}$, the universe was radiation dominated at very early times and after a period of matter domination entered the vacuum energy dominated phase we observe today. However, while not confirmed experimentally yet, it is widely assumed and accepted that the universe experienced a phase of exponential growth at very early times, known as *inflation*. Inspecting Eq. (1.2.7) again, we find that H must be independent of the scale factor $a(t)$ to provide exponential growth, thus requiring a dominant contribution from vacuum energy.
Typically, inflation is modeled introducing a scalar field ϕ, the inflaton, with a specific potential $V(\phi)$. The potential must provide a sizable vev for a sufficiently long period of time to guarantee a successful inflation. The period of inflation is introduced to solve the so called *horizon problem*: We observe areas in the sky to be extremely homogeneous even within separations that could not have been in causal contact without inflation. It appears highly unlikely that those areas look similar if they were not correlated at some point. If inflation provides a sufficiently large expansion at early times it can address this problem.
The era of inflation ends, when the inflaton decays into relativistic (SM) particles and the universe enters a radiation dominated era. The process of the inflaton-decay is usually referred to as *reheating*, as the temperature of the plasma increases with the energy that is injected into it by the inflaton decays. Afterwards the temperature decreases and the universe undergoes phase transition(s), e.g. the electroweak phase transition.
When the photon temperature drops below $T_\gamma \sim 0.1\,\mathrm{MeV}$, the photons are not able to break up nucleons anymore and light elements, such as deuterium, are formed. This procedure is called big bang nucleosynthesis (BBN).
For a photon temperature of $T_\gamma \lesssim 0.1\,\mathrm{eV}$, atoms like the hydrogen atom are not efficiently ionized by photons and therefore their number increases significantly, a period referred to as *recombination*. Since after recombination most of the electrons are bound in neutral atoms, photons can propagate freely afterwards. These photons are the ones that constitute the CMB, which therefore provides information about the time of recombination. Roughly at the time of recombination the universe enters its matter dominated phase in which the gravitational induced evolution of matter perturbations leads to the formation of structures we observe today, before it finally evolves into the era of vacuum energy domination.

[2]The abbreviation Λ instead of V for vacuum energy became common as a vacuum energy contribution to the stress-energy tensor can be absorbed into the cosmological constant.

1.3. Evidence for Physics Beyond the Standard Model

While the SM has provided extremely successful predictions and consistent result over the past decades, a few shortcoming serve as motivation for BSM physics. This work is mainly motivated by the pressing evidence for particle DM, reviewed in Section 1.3.3, and the fact that neutrinos have a non-zero but small mass presented in Section 1.3.1. Beside that, we mention in Section 1.3.2 the flavor problem in the SM, describing the hierarchic structures in the couplings and masses arising in the flavor sector and the tensions within experimental data, hinting at lepton flavor non-universality.

1.3.1. Neutrino Oscillations

Neutrino oscillations were first proposed by Pontecorvo in 1957 [11] and eventually discovered in 2001 by the Sudbury Neutrino Observatory [12] and by the Super-Kamiokande experiment [13]. The phenomenon of neutrino oscillations describes the oscillatory transition of a certain neutrino flavor to another, for instance $\nu_e \to \nu_\mu$. For the sake of simplicity, we assume neutrino mass generation via the Higgs mechanism. More evolved neutrino mass generation mechanisms are the subject of Section 2.1. In the case of mass generation via the Higgs mechanism, the mass terms in the lepton sector after EWSB are given by

$$\mathcal{L} \supset -\left(M_\nu\right)_{ij} \left(\bar{\nu}_L\right)_i \left(\nu_R\right)_j - \left(M_l\right)_{ij} \left(\bar{l}_L\right)_i \left(l_R\right)_j + h.c.\,. \tag{1.3.1}$$

The mass matrices M_ν and M_l are in general not diagonal. In direct analogy to the quark sector they can be diagonalized via transformations of the fields $\nu_{L/R}$ and $l_{L/R}$, $\nu'_{L/R} = U_\nu / V_\nu \, \nu_{L/R}$ and $l'_{L/R} = U_l / V_l \, l_{L/R}$ with the unitary matrices $U_{\nu/l}$ and $V_{\nu/l}$, such that the resulting mass matrices

$$\tilde{M}_{\nu/l} = U_{\nu/l} M_{\nu/l} V^\dagger_{\nu/l}\,, \tag{1.3.2}$$

are diagonal. This affects the interaction of charged leptons and neutrinos via the $W^\pm$

$$\mathcal{L} \supset \left(U_{\text{PMNS}}\right)_{ij} \left(\bar{\nu'}_L\right)_i W^+_\mu \left(l'_L\right)_j\,, \tag{1.3.3}$$

with $U_{\text{PMNS}} = U_\nu U_l^\dagger$. Typically, one chooses $U_l = \mathbb{1}$ and thus has $U_{\text{PMNS}} = U_\nu$. An essential quantity for neutrino oscillations is the probability for a neutrino of a certain flavor to oscillate into a neutrino of a different flavor, given by $P_{\nu_\alpha \to \nu_\beta}$. Already a calculation on the level of basic quantum mechanics, which we sketch in the following, yields the oscillation probability. Note, however, that considerations employing quantum field theoretical methods obtain the same result [14]. We find

$$P_{\nu_\alpha \to \nu_\beta} = \left| \left\langle \nu_\beta \left(t\right) \middle| \nu_\alpha \right\rangle \right|^2 \tag{1.3.4}$$

The states $|\nu_\alpha\rangle$ are given as superpositions of mass eigenstates $|\nu_i\rangle$ in terms of the PMNS matrix U, $|\nu_i\rangle = \sum\limits_\alpha \left(U^\dagger\right)_{i\alpha} |\nu_\alpha\rangle$ and the time evolution of the mass eigenstates satisfies

$$\left|\nu_i\left(t\right)\right\rangle = \exp\left(E_i t - \vec{p}_i \vec{x}\right) \left|\nu_i\left(t=0\right)\right\rangle \tag{1.3.5}$$

$$\overset{p_i \gg m_i}{\approx} \exp\left(-\mathrm{i}\frac{m_i^2 L}{2E}\right) \left|\nu_i\left(t=0\right)\right\rangle\,, \tag{1.3.6}$$

where the second line assumes the ultra-relativistic limit and therefore $L \approx t$. This assumption is justified as the neutrino mass, though non-zero, is very small compared to the energy scales of the experiments. The oscillation probability results in

$$P_{\nu_\alpha \to \nu_\beta} = \delta_{\alpha\beta} - 4 \sum_{k>j} \mathrm{Re}\left[(U)_{k\alpha} (U)^*_{k\beta} (U)^*_{j\alpha} (U)_{j\beta} \right] \sin\left(\frac{m_k^2 - m_j^2}{4E} L \right)^2 + 2 \sum_{k>j} \mathrm{Im}\left[(U)_{k\alpha} (U)^*_{k\beta} (U)^*_{j\alpha} (U)_{j\beta} \right] \sin\left(\frac{m_k^2 - m_j^2}{4E} L \right)^2 . \quad (1.3.7)$$

Remarkably, there are no flavor transitions if there are no mass differences between the different neutrino mass eigenstates. Hence, the observation of neutrino oscillations implies a non-vanishing neutrino mass for at least two neutrino mass eigenstates since the oscillation probability only depends on the mass differences and not on the absolute neutrino mass scale.
In fact, neutrino oscillations measure two mass squared differences $\Delta m^2_{21} = m_2^2 - m_1^2$ and $\Delta m^2_{31} = m_3^2 - m_1^2$. However, the sign of Δm^2_{31} is unknown allowing for two types of orderings along the neutrino mass eigenstates, the normal hierarchy (NH) and inverted hierarchy (IH) with

$$\mathrm{NH}: \; m_3 \gg m_2 > m_1 \,, \quad \mathrm{IH}: \; m_2 > m_1 \gg m_3 \,. \quad (1.3.8)$$

A democratic mixing with $\sum_i m_i \gg \sqrt{\Delta m^2_{31}}$ can be excluded by means of measurements of the sum of the neutrino masses that place upper bounds on this quantity. While direct detection experiments such as KATRIN can only place a limit of $\sum m_i < 1.1\,\mathrm{eV}$ [15], results from the Planck satellite find $\sum m_i < 0.12\,\mathrm{eV}$ [10]. An improvement on this upper bound can potentially rule out the IH in the near future, as $\sum_i m_i \gtrsim 0.1\,\mathrm{eV}$ in the IH.
The neutrino oscillation experiments further constrain the elements of the PMNS matrix, which is typically parametrized as

$$U_{\mathrm{PMNS}} = \begin{pmatrix} c_{12}c_{13} & s_{12}c_{13} & s_{13}\mathrm{e}^{-\mathrm{i}\delta_{CP}} \\ -s_{12}c_{23} - c_{12}s_{23}s_{13}\mathrm{e}^{-\mathrm{i}\delta_{CP}} & c_{12}c_{23} - s_{12}s_{23}s_{13}\mathrm{e}^{-\mathrm{i}\delta_{CP}} & s_{23}c_{13} \\ s_{12}s_{23} - c_{12}c_{23}s_{13}\mathrm{e}^{-\mathrm{i}\delta_{CP}} & -c_{12}s_{23} - s_{12}c_{23}s_{13}\mathrm{e}^{-\mathrm{i}\delta_{CP}} & c_{23}c_{13} \end{pmatrix} , \quad (1.3.9)$$

with $s_{ij} = \sin\theta_{ij}$ and $c_{ij} = \cos\theta_{ij}$. If $\delta_{CP} \neq 0$ neutrino oscillations violate charge parity conjugation symmetry (CP). In case that neutrinos are Majorana particles the PMNS matrix obtains to additional phases resulting in $U_{\mathrm{PMNS}} = U_\nu U_l^\dagger \mathrm{diag}\left(1, \mathrm{e}^{\mathrm{i}\alpha}, \mathrm{e}^{\mathrm{i}\beta}\right)$. Neutrino oscillations, however, are insensitive to these Majorana phases α and β. The Majorana nature of neutrinos is probed e.g. in experiments trying to observe the neutrinoless double-beta decay.

1.3.2. Flavor Physics

The SM contains six flavors of quarks and leptons, which are categorized within three generation, only distinguished by their mass. This mass, however, varies over several orders of magnitude. For instance, the ratio of the electron and top Yukawa coupling

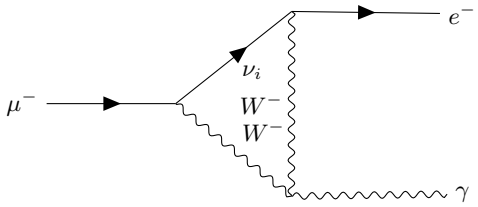

Figure 1.1.: One-loop contribution to the rare decay $\mu \to e\gamma$ mediated by the W. The ν_i refer to the different neutrino mass eigenstates.

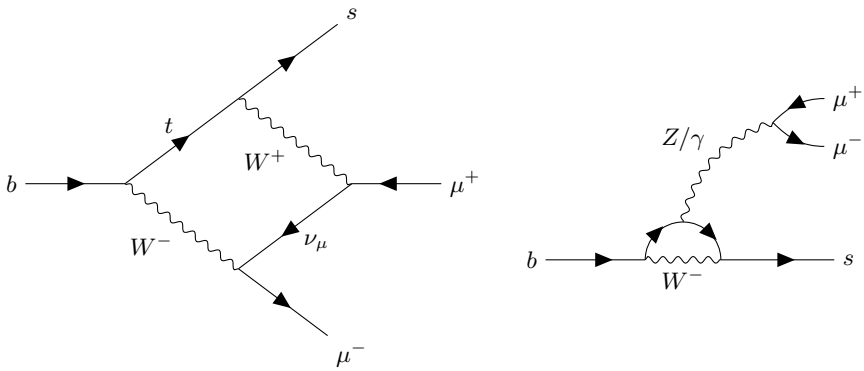

Figure 1.2.: One-loop diagrams contributing to the rare decay $b \to sll$.

is roughly $\frac{y_e}{y_t} \sim 10^{-6}$. The discrepancy between the Yukawa couplings becomes even more pronounced if neutrino masses are purely Dirac and generated via Yukawa couplings y_ν to right-handed neutrinos, resulting in $\frac{y_\nu}{y_t} \sim 10^{-13}$. These hierarchies, are the foundation of a vast number of neutrino mass models and motivate the introduction of flavor symmetries such as S_N and A_N [16, 17]. This approach not only allows for an explanation of the large mass hierarchies but also gives rise to certain patterns in the CKM and PMNS matrix.

Moreover, already the electroweak interaction allows for flavor transitions such as quark decays resulting in meson or hadron decays or neutrino oscillations. Often, however, these decays are forbidden on tree-level or come with a large number of electroweak vertices, resulting in a large suppression. This, in return, is a great opportunity to search for new physics as the new particles may give rise to lower order contributions.

For instance, the rare decay $\mu \to e\gamma$ was not observed by the experiment so far $\mathcal{B}(\mu \to e\gamma) < 4.2 \cdot 10^{-13}$ [18] and can serve as a tight constraint on new physics scenarios. Within the SM the decay is mediated at one-loop by the W boson and neutrinos and is illustrated in figure 1.1. Processes of this type are referred to as charged lepton flavor violating.

A recent topic of interest are rare B-meson decays, in particular the decay of a B-meson into a kaon and two charged leptons, induced by the process $b \to sll$, which is generated at one-loop level in the SM, illustrated in figure 1.2. Within ratios of branching ratios of this process into different lepton pairs hadronic uncertanties cancel efficiently and result

in a SM prediction of the R_K observable close to one [19]:

$$R_K = \frac{\int_{q^2_{\min}}^{q^2_{\max}} \frac{dBr(B\to K\mu\mu)}{dq^2} dq^2}{\int_{q^2_{\min}}^{q^2_{\max}} \frac{dBr(B\to Kee)}{dq^2} dq^2} \overset{\text{SM}}{=} 1.00 \pm 0.01\,. \tag{1.3.10}$$

The LHCb collaboration, however, reported a $2.5\,\sigma$ deviation from the SM in this observable and found for the di-lepton mass squared range of $1.1\,\text{GeV}^2 < q^2 < 6.0\text{GeV}^2$ a best fit value of [20, 21]

$$R_K = 0.846^{+0.060+0.016}_{-0.054-0.014}\,. \tag{1.3.11}$$

Here, the coupling to the different lepton flavors is non-universal. Thus, these processes are categorized as lepton flavor universality violating. The most popular explanations of this anomaly involve BSM physics generating tree level contributions to $b \to sll$, such as leptoquark models, possibly emerging from a grand unified theory (GUT), or models involving additional $U(1)'$ gauge groups. Models employing one-loop solutions to the R_K anomaly are subject to chapter 6.

1.3.3. Dark Matter

Most of the content of this work is dedicated to models involving DM candidates. While a direct detection signal of particle DM has not been observed yet, there exist a number of observations indicating the existence of DM. In this section, some of these observations are summarized.

Historically, the first observations hinting at the existence of DM were made in the 1930's [22] and observed that part of the universe mass does not interact electromagnetically. Roughly fourty years later these measurements were supported by Vera Rubin [23], who investigated galaxy rotation curves and found that those could not be explained by the observed distribution of visible matter.

The most pressing evidence today, however, is given by the measurement of the CMB, which was released at the time of recombination, when photons were propagating freely from this point on. Before, the free propagation of the photons was not possible due to efficient photon-electron scattering. Since after recombination electrons are mostly bound in neutral hydrogen the interaction rate of photons is significantly suppressed. The CMB provides a map of the sky in terms of the photon temperature and is almost perfectly homogeneous. Only on small scales fluctuations in the temperature, that originate from density perturbations at the time of recombination, exist. Utilizing a perturbed form of the Boltzmann equation, the size of the temperature fluctuations gives rise to the size of the corresponding density fluctuations which, in return, allow to determine the amount of electromagnetically interacting (baryonic) and dark matter. Broadly speaking, baryonic matter, due to repulsive interactions between particles with a same sign charge, tends to delay the formation of structures in the universe. Since for DM electromagnetic interactions are absent, or at least significantly smaller, it can accelerate structure formation, thereby creating larger fluctuations in the CMB. The CMB provides the most precise measurement of the DM energy density today and the PLANCK collaboration [10] finds

$$\Omega_{\text{DM}} h^2 = 0.120 \pm 0.001\,, \tag{1.3.12}$$

where h is the dimensionless Hubble parameter $H = h \cdot 100 \frac{\text{km}}{\text{s Mpc}}$ and the PLANCK collaboration finds $h = 0.674 \pm 0.005$ today. In this sense, roughly 25% of the energy content of the universe today are made up of DM and approximately 5% of baryonic matter.

Another observation supporting the existence of DM is the measurement of the abundances of light elements in the universe. The formation of nuclei is commonly referred to as BBN and starts at the temperature T_N after the interaction rate for the dissociation of nuclei, e.g. $d + \gamma \to p + n$, becomes small compared to the Hubble parameter. At this point, however, the ratio of protons and neutrons can differ from one, if the temperature is comparable to the mass difference of proton and neutron, $T_N \lesssim m_n - m_p$. In addition, the neutron, in contrast to the proton, is not stable. Consequently, a part of the neutrons can decay into protons before they are bound in nuclei. Hence, the efficiency of nuclei formation, given by the ratio of its interaction rate compared to the Hubble parameter, has a significant impact on the ratios of light elements, for instance the ratio of hydrogen and deuterium. As the interaction rate is proportional to the square of the baryon density, $\Gamma_{bsf} \sim n_B^2$, and the Hubble parameter depends on both the baryon and DM density, the amount of light elements is determined by an interplay of both of these quantities. Measurements of the light elements in the universe find that only a fraction of the matter density in the universe can consist of baryonic matter [24], thereby indicating the existence of DM.

A different type of observation employs the effect of gravitational lensing. When light emitted from a distant source passes a massive object it can be bent depending on the mass distribution of the object. This effect allows to determine this distribution by inspecting the image of the source we receive on earth. Gravitational lensing is a purely gravitational effect and does not distinguish between baryonic matter and DM. Comparing these results with the mass distribution of visible matter, information about the DM distribution can be extracted. A famous example of such a measurement is the Bullet cluster [25], where gravitational lensing is induced by two colliding galaxy clusters. They find an offset between visible and gravitating matter, hinting at DM without any sizable self-interactions.

While there exist other observations, such as simulation of structure formation in the early universe, already the evidence reviewed above, indicates a universe whose matter density is dominated by a BSM particle, as the SM neutrinos are found to provide only a non-significant contribution. Although, theories of non-Newtonian gravity, e.g. MOND [26], provide a good explanation to observed rotation curves of galaxies they struggle to explain the CMB and gravitational lensing measurements without the introduction of particle DM. Within this thesis, we stick to the well motivated idea of DM consisting of one or more BSM particles. The different ways to produce DM and how its properties are constrained by various observations is subject to the Sections 2.3 and 2.4.

2. Relevant Concepts and Models

2.1. Neutrino Mass Models

In Section 1.3.1 we reviewed evidence for the existence of massive neutrinos. Here, we review the most common models for neutrino mass generation. For a more detailed discussion the reader is referred to [27–30].
In the SM, no renormalizable neutrino mass term exists due to the lack of a right-handed neutrino field ν_R. The simplest extension allowing for neutrino masses evolves in complete analogy to the rest of the SM fermions and requires the existence of a right-handed neutrino ν_R. In this case, a Dirac-type neutrino mass term is induced by the Yukawa coupling y_ν of the left-handed to the right-handed neutrino after EWSB

$$\mathcal{L}_{\nu-mass} = -\left(y_\nu\right)_{ij} \bar{L}_i \tilde{\phi} \nu_{Rj} + h.c. \overset{\text{EWSB}}{\supset} -\left(m_\nu\right)_{ij} \overline{\nu_L}_i \nu_{Rj} + h.c.\,, \tag{2.1.1}$$

with $\left(m_\nu\right)_{ij} = \left(y_\nu\right)_{ij} \frac{v}{\sqrt{2}}$, $i = 1,2,3$ and $j = 1,\ldots,n$. Already this simple model allows for an explanation of the observed neutrino mass squared differences and mixing angles if at least two right-handed neutrino fields ($n = 2$) are introduced. If all neutrino mass eigenstates have a non-zero mass, three right-handed neutrino fields are required, as pointed out in for instance [31]. To reproduce the observed neutrino masses, one expects $y_\nu \sim \mathcal{O}\left(10^{-12}\right)$, which is much smaller than the Yukawa couplings present in the SM.
In addition, the right-handed neutrino transforms as a singlet under the SM gauge groups, allowing for a Majorana mass term, which for a fermion field ψ generally is of the form

$$\mathcal{L}_{\text{majorana}} = -M\overline{\psi^c}\psi + h.c.\,, \tag{2.1.2}$$

where $\psi^c = i\gamma^2\psi^*$. If ψ transforms under a gauge transformation of the form $\psi \to \psi \exp\left(it_a\alpha^a\left(x\right)\right)$ the Majorana mass term is only gauge invariant if $t_a = 0$, meaning that ψ transforms as a gauge singlet. Thus, Majorana mass terms are not present in the SM at the renormalizable level. If, however, a right-handed neutrino is introduced, it naturally comes with a Majorana mass term if no further restrictions are imposed. The neutrino mass is then generated via an interplay of the Dirac and Majorana mass terms. If for instance the Majorana mass term is much larger than the Dirac mass term, neutrino mass generation is governed by the well known type-I seesaw scenario, described in more detail in Section 2.1.1.
Allowing for non-renormalizable operators, Majorana masses for neutrinos can be induced via higher-dimensional operators of odd dimension starting from dimension five. At dimension five there is only one unique operator, known as the Weinberg operator [32]

$$\mathcal{L}_{\text{dim-5}} = \frac{\kappa_{ij}}{\Lambda}\left(\overline{\left(L_L\right)_i^c}\tilde{\phi}^*\right)\left(\tilde{\phi}^\dagger\left(L_L\right)_j\right)\,. \tag{2.1.3}$$

Here, Λ is a large mass scale with $\Lambda \gg v$, where the effective description of the theory breaks down[1] and κ_{ij} is a coefficient function depending on the properties of the UV-

[1] In case of e.g. the type-I seesaw, this scale is given by the mass of the heavy neutrino mass state.

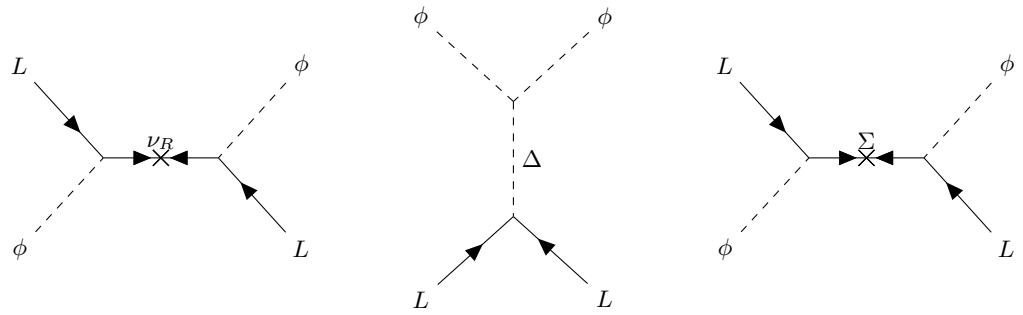

Figure 2.1.: Feynman diagrams associated with the type I (left), type II (middle) and type III (right) seesaw.

complete theory. After EWSB this operator generates a mass of

$$(m_\nu)_{ij} = \frac{(\kappa)_{ij}^2 \, v^2}{2\Lambda} \,, \tag{2.1.4}$$

for the active neutrinos. All models of Majorana neutrinos can be reduced to this operator. In the following we discuss various tree-level realizations of the Weinberg operator in the Sections 2.1.1 and 2.1.2 and possible extensions at one-loop level in Section 2.1.3.

2.1.1. Type I/II/III Seesaw

The minimal UV completions of the Weinberg operator are known as the type I-III seesaw. They are minimal in terms of their field content as only one additional field is introduced. In the type I seesaw [33], a SM singlet Weyl fermion ν_R is added, commonly referred to as the right-handed neutrino. The type II seesaw [34] employs a scalar $SU(2)$ triplet Δ with hypercharge $Y = 2$, while the type III seesaw [35] relies on a fermionic $SU(2)$ triplet Σ with hypercharge $Y = 0$. The Feynman diagrams associated with the neutrino mass generation within the different seesaw variations are given in Figure 2.1. The parts of the Lagrangian relevant to neutrino mass generation in the context of the type I seesaw after EWSB are given by

$$\mathcal{L}_{m_\nu} \supset -\overline{\nu_{Li}} \, (m_D)_{ij} \, \nu_{Rj} - \frac{1}{2} \overline{\nu_{Rj}} \, (M_M)_{jj'} \, \nu_{Rj'}^c + h.c. \,, \tag{2.1.5}$$

with the flavor indices $i = 1, 2, 3$ and $j, j' = 1, \ldots, n$ for n additional right-handed neutrinos. If not indicated differently by parentheses, the object $\psi_{L/R}^c$ is evaluated by first applying the projection operator and then charge conjugation. Thus, the object ψ_L^c is a right-handed field.
This expression can be conveniently rewritten in terms of the $(3+n)$ dimensional vector $n_L = (\nu_L, \nu_R^c)$, where we suppressed the flavor indices. It carries the index L, as only left-handed fields are present. With this definition we find

$$\mathcal{L}_{m_\nu} = -\frac{1}{2} \overline{n_L^c} \mathcal{M} n_L + h.c. \tag{2.1.6}$$

with

$$\mathcal{M} = \begin{pmatrix} 0 & m_D \\ m_D^T & M_M \end{pmatrix} . \tag{2.1.7}$$

The mass matrix $\mathcal{M}$ is quadratic and of dimension $(3+n)$. To arrive at the form given above, the following relations are useful

$$\overline{\nu_L^c} m_D \nu_R^c = \overline{\nu_R} m_D^T \nu_L \,, \tag{2.1.8}$$

$$(\nu_R^c M_M^* \nu_R)^\dagger = \overline{\nu_R} M \nu_R^c \,. \tag{2.1.9}$$

The mass matrix is diagonalized by a a rotation with the unitary matrix $\mathcal{U}$, which is defined as

$$\begin{pmatrix} \nu_L \\ \nu_R^c \end{pmatrix} = \underbrace{\begin{pmatrix} U_P & A \\ B & C \end{pmatrix}}_{\mathcal{U}} \begin{pmatrix} \chi_{\nu L} \\ \chi_{N L} \end{pmatrix} , \tag{2.1.10}$$

with $\chi_{\nu/N}$ representing the (light/heavy) neutrino *mass eigenstates* and U_P and C are quadratic matrices of dimension 3 and n respectively, while A and B are $(3 \times n)$ and $(n \times 3)$ matrices respectively. The explicit form of $\mathcal{U}$ can be extracted from the fact that it diagonalizes $\mathcal{M}$, i.e.

$$\mathcal{U}^T \mathcal{M} \mathcal{U} = \begin{pmatrix} M_\nu & 0 \\ 0 & M_N \end{pmatrix} , \tag{2.1.11}$$

and its unitarity. We choose the subscripts ν and N for the diagonal mass matrices, as we will refer to the light neutrino mass eigenstates as ν, while heavy neutrino mass eigenstates are referred to as N later in this thesis. In the limit of $M_M \gg {m_D}^2$ and in the basis of v_{Rj}, where M_M is diagonal, we find

$$A = m_D^* M_N^{-1} \,, \quad B = -A^\dagger U_P \,, \quad C = 1 - \mathcal{O}\left(\frac{m_D^2}{M_N^2}\right) , \tag{2.1.12}$$

and

$$M_N = M_M + \mathcal{O}\left(\frac{m_D^2}{M_N}\right) \qquad M_\nu = -U_P^T m_D M_N^{-1} m_D^T U_P \,. \tag{2.1.13}$$

In this sense, U_P can be identified with the PMNS matrix, as it diagonalizes the mass matrix of the light neutrinos. Note, however, that U_P is not exactly unitary anymore and deviates from unitarity by corrections of $\mathcal{O}\left(\frac{m_D^2}{M_N^2}\right)$. This has important consequences for the phenomenology of massive neutrinos, discussed in more detail in Section 2.2.
Examining eq. (2.1.6) in its diagonal form we find

$$\mathcal{L}_{m_\nu} = -\frac{1}{2}\left(\overline{\chi_{\nu L}^c} M_\nu \chi_{\nu L} + \overline{\chi_{N L}^c} M_N \chi_{N L}\right) + h.c. \tag{2.1.14}$$

[2] This has to be understood in the sense that the eigenvalues of the matrix M_M are much larger than the eigenvalues of m_D.

The entries of the diagonal matrices $M_{\nu/N}$ are real but not necessarily positive. This issue can be addressed by defining the Majorana fields χ_ν and χ_N as

$$\chi_\nu = \chi_{\nu L} + \eta_\nu \chi^c_{\nu L}\,, \quad \chi_N = \chi_{NL} + \eta_N \chi^c_{NL}\,, \tag{2.1.15}$$

where $\eta_{\nu/N}$ is a diagonal matrix with a phase factor for each field on its main diagonal. The phase factor is chosen according to the sign of the associated mass. More precisely it is $\left(\eta_{\nu/N}\right)_{ii} = \pm 1$ if sign $\left[\left(M_{\nu/N}\right)_{ii}\right] = \pm 1$. Hence we have

$$\mathcal{L}_{m_\nu} = -\left|(M_\nu)_{ij}\right| \overline{\chi_{\nu i}} \chi_{\nu j} - \left|(M_N)_{ij}\right| \overline{\chi_{Ni}} \chi_{Nj} + h.c.\,. \tag{2.1.16}$$

In the one generation scenario, we thus obtain the well known seesaw formula of $M_\nu = \frac{m_D^2}{M_N}$, which displays the origin of the seesaw label, as a heavier heavy neutrino state N implies a lighter light neutrino state ν.
Finally, we study the limiting case $M_M \to 0$, where the Dirac neutrino is recovered. In this case, we find $M_\nu = -M_N = m_D$ in eq. (2.1.14). In general, a Dirac type mass eigenstate arises if two Majorana mass eigenstates with a mass of opposite sign exist, i.e.

$$\mathcal{L}_{m_\nu} = -\frac{m}{2}\left(\overline{\chi^c_{1L}}\chi_{1L} - \overline{\chi^c_{2L}}\chi_{2L} + h.c.\right)\,. \tag{2.1.17}$$

Then, it is possible to define the Dirac state $\psi_D = \psi_L + \psi_R$ with

$$\psi_L = \frac{1}{\sqrt{2}}\left(\chi_{1L} + \chi_{2L}\right)\,, \quad \psi_R = \frac{1}{\sqrt{2}}\left(\chi^c_{1L} - \chi^c_{2L}\right)\,, \tag{2.1.18}$$

so that eq. (2.1.17) reads

$$\mathcal{L}_{m_\nu} = -m\left(\overline{\psi_D}\psi_D\right)\,. \tag{2.1.19}$$

Note, that this definition of the Dirac state is valid for any type of neutrino mass model that yields two Majorana states with a mass of opposite sign. In the case of the type I seesaw we recover the familiar result $\psi_L = \nu_L$ and $\psi_R = \nu_R$.
After this more detailed discussion of the type I seesaw, we briefly give the results for the type II/III seesaw. The type II seesaw scenario relies on the coupling of two neutrinos to the uncharged component of the scalar triplet Δ, which in turn couples to two Higgs fields

$$\mathcal{L}_{m_\nu} = (Y_\Delta)_{ij}\,\overline{\nu^c_{Li}}\Delta^0\nu_{Lj} + \mu\phi^T\left(i\sigma_2\right)\Delta^\dagger\phi + h.c.\,, \tag{2.1.20}$$

with

$$\Delta = \begin{pmatrix} \frac{\Delta^+}{2} & \Delta^{++} \\ \Delta^0 & -\frac{\Delta^+}{2} \end{pmatrix}\,. \tag{2.1.21}$$

Depending on the shape of the scalar potential $V(\phi, \Delta)$, both ϕ and Δ can acquire a vev. Each of these contributes to the neutrino mass and results in

$$M_\nu \sim (Y_\Delta)_{ij}\,\mu\frac{v_\phi^2}{M_\Delta^2}\,, \quad M_\nu \sim (Y_\Delta)_{ij}\,v_\Delta\,. \tag{2.1.22}$$

The vev of the scalar triplet, however, is tightly constrained from electroweak precision observables like the ρ parameter [36], measuring the mass ratio of the W and Z bosons, resulting in an upper bound of $v_\Delta \lesssim 4.8\,\text{GeV}$. This implies $v_\Delta \ll v_\phi$ and therefore the contribution of v_ϕ to the neutrino mass typically dominates.
The type III seesaw scenario is very similar to the type I seesaw. The mass terms of the Lagrangian read

$$\mathcal{L}_{m_\nu} = -\left(Y_\Sigma\right)_{ij} \overline{\Sigma}_i \tilde{\phi}^\dagger L_{Lj} + h.c. - \frac{1}{2}\text{Tr}\left[\overline{\Sigma} M_\Sigma \Sigma^c\right] + h.c\,. \tag{2.1.23}$$

After EWSB the neutrino mass term results in

$$M_\nu = \left(Y_\Sigma^T\right)_{ik} \left(Y_\Sigma\right)_{kj} \frac{v^2}{M_\Sigma}\,. \tag{2.1.24}$$

The main difference between the type I and type III seesaw scenarios is the coupling of Σ to the electroweak gauge bosons. However, we only discuss the phenomenology of the type I seesaw in Section 2.2, as the type II and type III seesaw are not subject to the models discussed in this work.

2.1.2. Inverse Seesaw

The inverse seesaw mechanism can be understood as an extension of the type I seesaw scenario. In addition to the introduction of a certain number of right-handed neutrinos ν_R, the model is enlarged by additional left-handed gauge singlet fermions s_L, typically matching the number of right-handed neutrinos. When considering the type I seesaw setup, electroweak signatures of the additional heavy neutrino states tend to be suppressed by either their large mass or the tiny Yukawa couplings in case of lighter heavy neutrinos. Models utilizing the inverse seesaw mechanism for neutrino mass generation typically allow for a larger mixing between the new states and the SM neutrinos, thus making it more accessible in experiments. In many of these models, a global or local $U\left(1\right)_L$, a lepton number symmetry, is imposed under which ν_L, ν_R and s_L all carry the charge $+1$. If this symmetry is unbroken, it forbids all possible Majorana mass terms, which in return leads to vanishing light neutrino masses. Only after the $U\left(1\right)_L$ is broken, e.g. by the vev of an additional scalar field often referred to as the Majoron, the induced Majorana masses allow to reproduce the observed neutrino masses.
Considering the the case of an unbroken $U\left(1\right)_L$ at first, the Lagrangian relevant to the neutrino mass generation via the inverse seesaw scenario after EWSB reads [37–40]

$$\mathcal{L}_{m_\nu} = -\frac{1}{2}\overline{n_L^c}\mathcal{M} n_L\,, \tag{2.1.25}$$

with

$$n_L = \begin{pmatrix} \nu_L \\ \nu_R^c \\ s_L \end{pmatrix}\,, \quad \mathcal{M} = \begin{pmatrix} 0 & m & 0 \\ m & 0 & M \\ 0 & M & 0 \end{pmatrix}\,. \tag{2.1.26}$$

For simplicity, we assumed only one generation of neutrinos as well as one additional ν_R and s_L. Diagonalizing $\mathcal{M}$ yields

$$\mathcal{L}_{\Downarrow_\nu} = -\frac{\sqrt{m^2+M^2}}{2}\left(\overline{\chi_{1L}^c} \quad \overline{\chi_{2L}^c} \quad \overline{\chi_{3L}^c}\right)\begin{pmatrix}0 & 0 & 0\\ 0 & -1 & 0\\ 0 & 0 & 1\end{pmatrix}\begin{pmatrix}\chi_{1L}\\ \chi_{2L}\\ \chi_{3L}\end{pmatrix}. \tag{2.1.27}$$

Thus we obtain one massless Majorana neutrino and two Majorana states with a mass of opposite sign, i.e. one Dirac neutrino. Now, we can define the Dirac state according to (2.1.18) as

$$N_L = \frac{1}{\sqrt{1+\theta^2}}\left(s_L + \theta\nu_L\right), \tag{2.1.28}$$

$$N_R = \nu_R, \tag{2.1.29}$$

with $\theta = \frac{m}{M}$. Thus, depending on the size of θ the new heavy neutral lepton state can have large admixtures of ν_L, which interacts via the electroweak gauge interactions. As discussed in Chapter 2.2, this mixing angle can be constrained by the experiment and is therefore known to be relatively small, hence motivating the simplifying limit $\theta \ll 1$. Up to linear order in θ we find

$$N_L = s_L + \theta\nu_L, \quad N_R = \nu_R, \quad \chi_{1L} = -\nu_L + \theta s_L. \tag{2.1.30}$$

Here, χ_{1L} forms the massless Majorana state $\chi_1 = \chi_{1L} + \chi_{1L}^c$, while N_L and N_R form a Dirac state with mass $m_N = M + \mathcal{O}\left(\theta^2\right)$.
Accounting for the observed light neutrino masses requires the existence of a Majorana mass term. Three possible Majorana mass terms are $\overline{\nu_R^c}\nu_R + h.c.$, $\overline{s_L^c}s_L + h.c.$ or $\overline{\nu_L^c}s_L + h.c.$. If we e.g. consider the presence of the mass term $\mu\overline{s_L^c}s_L$ and furthermore assume the hierarchies $\mu, m \ll M$, we find a non-zero mass $m_\nu \neq 0$ of the formerly massless Majorana mass state, which amounts to

$$m_\nu = \theta^2\mu. \tag{2.1.31}$$

A comparison of this formula with its counterpart in the type I seesaw scenario displays the key difference between the two mechanisms. Both expressions for the neutrino mass can be written in the form of mixing angle squared times a mass scale. However, in contrast to the type I seesaw the mass scale μ is unrelated to the mixing angle itself, allowing for sizable active-sterile neutrino mixing angles due to a small μ.
Additionally, the degeneracy in the absolute value of the mass of the remaining two Majorana mass states is lifted by a correction proportional to $\frac{\mu}{M}$, thereby spoiling the possibility to form a Dirac state. As the degeneracy is only slightly broken this case is often referred to as a pseudo-Dirac neutrino.
Moreover, the composition of the mass eigenstates receives a correction due to the small Majorana mass term μ. Expanding the heavy pseudo-Dirac states up to first order in both θ and $\frac{\mu}{M}$ yields

$$N_L = s_L + \theta\nu_L - \frac{1}{4}\frac{\mu}{M}\nu_R^c, \quad N_R = \nu_R + \frac{1}{4}\frac{\mu}{M}s_L^c. \tag{2.1.32}$$

This result indicates that the influence on the electroweak phenomenology is not sizable, as the leading order admixture of electroweak non-singlets, namely ν_L, remains approximately the same.

For a realistic version of the inverse seesaw, more than one pair of ν_R and s_L is mandatory. To accommodate the neutrino oscillation data, at least two ν_R and s_L are required [40]. Enlarging the vector n_L in Eq. (2.1.26) to describe three generations, allowing for a larger number of ν_R and s_L and promoting m, M and μ to matrices[3], we find the leading order contribution to the active neutrino mass to be

$$M_\nu = m^T M^{-1} \mu M^{T^{-1}} m \,. \tag{2.1.33}$$

Accordingly, Eq. (2.1.32) is still valid if the scalar parameters are promoted to matrices.

2.1.3. Radiative Neutrino Mass Models

The discussion of neutrino mass generation so far was limited to tree level realizations. The main motivation for the construction of models beyond the simplest tree level realizations of the Weinberg operator is the difficulty to falsify the latter. The inverse seesaw scenario already demonstrated one way to generate an additional suppression mechanism for the neutrino mass in the form of a small lepton number violation (LNV). Another possibility is to suppress the neutrino mass by only allowing contributions at loop level. There exists a large number of radiative neutrino mass models. A categorization of one-loop models is given in [41] and two-loop models were classified in [42]. A well known one-loop model is the scotogenic model [43], which we review briefly in the following, as it will be used for neutrino mass generation in some models subject to Chapter 6.

The model includes right-handed SM singlet fermions N_i, which, in contrast to the type I seesaw, are charged under an unbroken global symmetry. All SM fields are uncharged under this global symmetry. Consequently, Dirac masses for the new SM singlet fermions N_i and the SM neutrino fields are forbidden. Neutrino mass generation is allowed for via a second Higgs doublet η, which is also charged under the new global symmetry, such that a Yukawa coupling between the SM neutrinos and the singlet fermions is possible. The new scalar field interacts with the Higgs field via quartic interactions in the scalar potential, the so called Higgs portal couplings. Due to the global symmetry, the lightest particle charged under this symmetry is stable and, if electrically neutral, is a viable DM candidate.

The Lagrangian relevant for the neutrino mass generation is given by

$$\mathcal{L}_{m_\nu} = -h_{ij} \left(\overline{L_L}\right)_i \tilde{\eta} N_j + h.c. - V\left(\phi, \eta\right) \,, \tag{2.1.34}$$

with

$$\begin{aligned} V\left(\phi,\eta\right) = &- \mu_\phi^2 \phi^\dagger\phi + \mu_\eta^2 \eta^\dagger\eta + \lambda_1 \left(\phi^\dagger\phi\right)^2 + \lambda_2 \left(\eta^\dagger\eta\right)^2 + \lambda_3 \left(\phi^\dagger\phi\right)\left(\eta^\dagger\eta\right) \\ &+ \lambda_4 \left(\phi^\dagger\eta\right)\left(\eta^\dagger\phi\right) + \lambda_5 \left[\left(\phi^\dagger\eta\right)^2 + h.c.\right] \,. \end{aligned} \tag{2.1.35}$$

Due to the presence of the quartic coupling λ_5, the two neutral scalar fields resulting from the scalar doublet η differ in mass after EWSB

$$m_R^2 - m_I^2 = 2\lambda_5 v^2 \,, \tag{2.1.36}$$

[3] Note that the mass matrix must be symmetric.

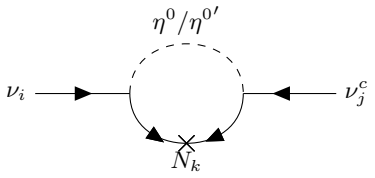

Figure 2.2.: Feynman diagram generating neutrino masses radiatively in the scotogenic model. Any combination of N_i and the real or imaginary part of the neutral component of η can propagate in the loop.

where $m_{R/I}$ refers to the mass of the real/imaginary part of the neutral η component. The neutrino mass is generated at one-loop via the diagram illustrated in Figure 2.2. Both, the particle associated with the real part and the one corresponding to the imaginary part of the neutral component of η can propagate in the loop. The diagrams contribute with a different sign and thus cancel exactly if λ_5 vanishes. In the limit of $\frac{m_R^2+m_I^2}{2} \approx M_{N_i}$ and $\frac{m_R^2+m_I^2}{2} \gg 2\lambda_5 v^2$ we find

$$M_\nu = \frac{\lambda_5 v^2}{16\pi^2} \sum_k \frac{h_{ik} h_{jk}}{M_{N_k}} \,. \tag{2.1.37}$$

This limit allows for a direct comparison with the corresponding type I seesaw formula and we find an additional suppression of $\frac{\lambda_5}{16\pi^2}$.

2.2. Phenomenological Implications of Neutrino Physics

The introduction of neutrino masses can also affect observables other than the neutrino mass itself. In this section, we sketch some important impacts of neutrino mass models on these observables. Note, however, that this list is not a complete catalogue of the possible phenomenological implications. A more detailed discussion can be found in e.g. [44, 45].
As we discussed in the section before, many neutrino mass models, e.g. the type I/III or inverse seesaw scenario, induce a mixing of the electroweakly charged left-handed neutrino states with BSM fermions, typically electroweak gauge singlets, that is encoded in the leptonic mixing matrix $\mathcal{U}$. The upper left 3×3 submatrix U_P of $\mathcal{U}$ is in general not unitary, which has an impact on the neutral and charged current interactions in the leptonic sector. The interactions with the W and Z take the form

$$\mathcal{L}_W \supset \sum_{i=1}^{3+n} \sum_{\alpha=e,\mu,\tau} \frac{g}{\sqrt{2}} \bar{l}_\alpha \gamma_\mu W^\mu P_L U_{\alpha i} \chi_i + h.c. \,, \tag{2.2.1}$$

$$\mathcal{L}_Z \supset \sum_{i,j=1}^{3+n} \sum_{\alpha=e,\mu,\tau} \frac{g}{2c_w} \overline{\chi}_i U^\dagger_{i\alpha} \gamma_\mu Z^\mu P_L U_{\alpha j} \chi_j \,. \tag{2.2.2}$$

Here, c_w is the cosine of the Weinberg angle, l_α are the charged leptons, χ_i are the neutrino mass eigenstates with $i = 1, 2, 3$ corresponding to the light active neutrinos and $i = 4, \ldots, 3+n$ correspond to the heavier neutrino states.

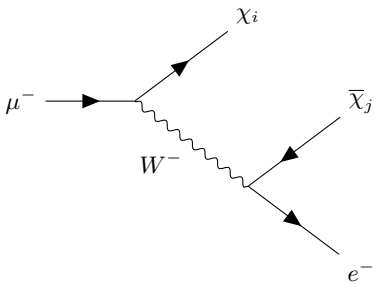

Figure 2.3.: Leading order Feynman diagram inducing the μ decay. Any kinematically allowed neutrino mass eigenstate can appear in the final state.

If we e.g. consider the $f_{ij}Z\overline{\nu}_i\nu_j$ vertex, where ν_i refers to one of the three light neutrinos within the type I seesaw scenario, we find

$$f_{\alpha\beta} \sim \left(1 - m_D^T M_N^{-2} m_D\right)_{\alpha\beta} , \tag{2.2.3}$$

using Eq. (2.1.12) and the unitarity of the complete leptonic mixing matrix $\mathcal{U}$.
In this sense, the non-unitarity of the 3×3 mixing matrix U_P induces lepton flavor non-universality and within the charged current allows for charged lepton flavor violation, which can exceed the SM predictions by many orders of magnitude. Moreover, electroweak precision variables like the Fermi constant G_F can be altered. In the following, we review the constraints from electroweak precision tests of the SM and charged lepton flavor violation.

2.2.1. Electroweak Precision Variables

The Fermi constant G_F can be extracted from μ decays, which are altered due to the effects of the new neutral heavy leptons. The tree level diagram contributing to the μ decay is illustrated in Figure 2.3. The final state includes all neutrino mass eigenstates χ_i that are kinematically allowed, i.e. $m_{\chi_i} + m_{\chi_j} < m_\mu - m_e$. If we order the neutrino mass eigenstates such that $m_{\chi_1} \leq m_{\chi_2} \leq \cdots \leq m_{\chi_{3+n}}$, there exists an $i = i_{\max}$ so that $\chi_{i_{\max}+1}$ is not kinematically allowed anymore. Then, Fermi's constant obtained from the μ decay including the effects of heavy neutrino states G_μ amounts to [46]

$$G_\mu^2 = G_F^2 \sum_{i,j=1}^{i_{\max}} |U_{\mu i}|^2 |U_{ej}|^2 , \tag{2.2.4}$$

where G_F is Fermis constant obtained assuming only three massless neutrino states. If $i_{\max} = 3 + n$, i.e. all neutrino states are light enough to contribute to the μ decay, the sums in Eq. (2.2.4) yield exactly 1 due to the unitarity of the complete leptonic mixing matrix. In this case, measurements of Fermis constant do not constrain the neutrino mass model in question. However, if e.g. in the type I seesaw, as discussed in Section 2.1, only the three light neutrino states are light enough to appear in the final state, we find

$$G_\mu^2 = G_F^2 \left(U_P^\dagger U_P\right)_{ee} \left(U_P^\dagger U_P\right)_{\mu\mu} = G_F^2 \left(1 - m_D^T M_N^{-2} m_D\right)_{ee} \left(1 - m_D^T M_N^{-2} m_D\right)_{\mu\mu} . \tag{2.2.5}$$

A similar expression can be found for the inverse seesaw scenario.
As a rough estimate for the corrections, we assume m_D and M_N to be proportional to the unit matrix. Hence, it is

$$\frac{G_\mu^2}{G_F^2} = (1-\theta)^2 = \left(1 - \frac{m_\nu}{M_N}\right)^2 , \tag{2.2.6}$$

where $\theta = \frac{m_D}{M_N}$. Thus, in the type I seesaw, the corrections to G_F are typically negligible. In scenarios like the inverse seesaw however, the mixing angle is potentially much larger and therefore constrained by electroweak precision tests, which involve also measurements of the Weinberg angle and the ρ parameter. Amongst others, these parameters are related via the Fermi constant and therefore also influenced by the altered leptonic mixing matrix.

2.2.2. Lepton Flavor Violation

The most prominent example for charged lepton flavor violation is the decay $\mu \to e\gamma$, as its branching ratio is tightly constrained by the MEG-experiment [18], more precisely $Br_{\mu\to e\gamma} < 4.2 \cdot 10^{-13}$. Furthermore, the SM prediction for this process, illustrated in Figure 1.1, is tiny. Due to the unitarity of the PMNS matrix, the contributions of the different neutrino mass eigenstates mostly cancel each other, as their mass is very small compared to the mass of the W. The decay width in the SM including three massive neutrinos is given by [47]

$$Br_{\mu\to e\gamma} = \frac{3\alpha}{32\pi}\left|\sum_i U_{\mu i}^* U_{ei} F\left(\frac{m_{\nu_i}^2}{M_W^2}\right)\right|^2 \sim 10^{-54} , \tag{2.2.7}$$

with

$$F(x) = \frac{10 - 43x + 78x^2 - 49x^3 + 4x^4 + 18x^3 \log(x)}{3(x-1)^4} . \tag{2.2.8}$$

Therefore, any measurable contribution to this process would be a clear signal for new physics.
Considering a new physics scenario, where the heavy neutrino states are roughly degenerate in mass allows to estimate the contribution to $\mu \to e\gamma$ in terms of the unitarity violation of the 3×3 submatrix U_P of the leptonic mixing matrix.

$$\begin{aligned} Br_{\mu\to e\gamma} &\approx \frac{3\alpha}{32\pi}\left(\left|\sum_{i=1}^{3} U_{\mu i}^* U_{ei} F(0)\right|^2 + \left|\sum_{i=4}^{3+n} U_{\mu i}^* U_{ei} F\left(\frac{M_N^2}{M_W^2}\right)\right|^2\right) \\ &= \frac{3\alpha}{32\pi}\left|\sum_{i=1}^{3} U_{\mu i}^* U_{ei}\right|^2 \left(F(0)^2 - F\left(\frac{M_N^2}{M_W^2}\right)^2\right) , \end{aligned} \tag{2.2.9}$$

where M_N is the mass scale of the heavy neutrino and we used $\sum_{i=1}^{3+n} U_{\mu i}^* U_{ei} = 0$ in the second step. Considering a scenario where $M_N \gg M_W$, the mixing matrix elements can be constrained to

$$\left|\sum_{i=1}^{3} U_{\mu i}^* U_{ei}\right| \leq 2.2 \cdot 10^{-5} . \tag{2.2.10}$$

Furthermore, the elements of the matrix $R_{\alpha\beta} = \sum_{i=1}^{3} U_{\alpha i}^{*} U_{\beta i}$ can be constrained by other observables, such as ratios of the decay width of the W into leptons of different flavor or lepton flavor violating three-body decays like $\mu \to eee$. The $R_{\tau\mu}$ element, e.g., is constrained by the ratio $\frac{\Gamma(W\to\tau\bar{\nu}_\tau)}{\Gamma(W\to\mu\bar{\nu}_\mu)}$ [46]. To conclude, the leptonic mixing matrix can be constrained by different measurements, while the element $R_{\mu e}$, typically, is subject to the tightest constraints resulting from the small upper bound on $\mu \to e\gamma$.

2.3. Dark Matter Production

A central part of any DM model is the underlying DM production mechanism. From astrophysical observations we know the DM energy density Ω_{DM} precisely and that it must have been present at the time of the creation of the CMB. In this work, we discuss production mechanisms relying on interactions of DM with SM particles or itself. These processes are usually described in terms of the evolution of the phase space densities of the different particle species. The dynamics of this evolution are governed by the Boltzmann equation.
In the following we introduce some relevant thermodynamical quantities and discuss the Boltzmann equation. Subsequently, we present various coupling regimes that can provide the observed DM relic density. The discussion of the thermodynamics in the early universe and the introduction of the Boltzmann equation can be found in various textbooks, e.g. [48]. The description of the four basic ways to produce DM and the figures included are based on [49, 50].

2.3.1. Thermodynamics in the Early Universe

The different particle species i in the universe are described by their *single particle phase space densities* $f_i(\vec{r}, \vec{p}, t)$. The Friedmann-Robertson-Walker universe is based on the assumption of isotropy and homogeneity. Thus, the phase space density cannot depend on $\vec{r}$ and the dependency on $\vec{p}$ reduces to dependency on $p = |\vec{p}|$ only. Often, we are only interested in global quantities such as the number or energy density of a certain particle species. These quantities can be obtained from the phase space density via

$$n_i(t) = \frac{g_i}{(2\pi)^3} \int \mathrm{d}^3 p \, f(p,t) \,, \tag{2.3.1}$$

$$\rho_i(t) = \frac{g_i}{(2\pi)^3} \int \mathrm{d}^3 p \, E(p) \, f(p,t) \,. \tag{2.3.2}$$

Here, g_i measures the internal degrees of freedom for a particle species, e.g. $g_i = 2$ for a fermion of spin $\frac{1}{2}$ due to the two spin degrees of freedom.
If a particle species is in kinetic equilibrium, i.e. energy is efficiently transferred between the particle species and the thermal bath, their phase space densities take the form of the so called equilibrium distributions

$$f_i^{\mathrm{eq}}(p,t) = \frac{1}{\exp\left(\frac{E-\mu}{T}\right) \pm 1} \,. \tag{2.3.3}$$

The $\pm$ in the denominator distinguishes between fermions and boson and yields the Fermi-Dirac and Bose-Einstein statistics respectively, and μ is the chemical potential. If a reaction $i_1 + i_2 + \cdots \leftrightarrow f_1 + f_2 + \ldots$ is in chemical equilibrium the corresponding chemical potentials fulfill

$$\sum_n \mu_{i_n} = \sum_n \mu_{f_n} \,. \tag{2.3.4}$$

Enforcing chemical equilibrium requires processes, that change the number of a certain particle species, to be efficient. Chemical potentials are associated with charges, such as the electric charge or the baryon number. Anti particles carry an opposite sign chemical potential with respect to the corresponding particle, as long as processes such as $e^+ + e^- \leftrightarrow \gamma\gamma$ are efficient, since $\mu_\gamma = 0$[4].
Furthermore, all chemical potentials can be set to zero to a good approximation as long as asymmetries such as that of the baryon number are negligible. In fact, in all studies of this work beside Chapter 5 the impact of asymmetries is negligible.
When in the following a process is classified to be in *thermal* equilibrium, it refers to a process which is in kinetic and chemical equilibrium. Moreover, if we refer to an equilibrium phase space or number density, we refer to (2.3.3) and the resulting number density (2.3.5) with $\mu = 0$, if not explicitly stated otherwise.
The integral in Eq. (2.3.1) cannot be solved for the general case of a Fermi-Dirac or Bose-Einstein statistics. However, in the common case of $E \gg T$ both statistics are well approximated by the Boltzmann distribution $f_i^{\mathrm{eq}} = \exp\left(-\frac{E}{T}\right)$, and the integral can be performed yielding [5]

$$n_i^{\mathrm{eq}}(T) = \frac{g_i}{2\pi^2} m_i^2 T K_2\left(\frac{m_i}{T}\right) \,, \tag{2.3.5}$$

where $K_j(x)$ is the Bessel-K function of the j-th kind.
In the relativistic case $T \gg m$, both Fermi-Dirac and Bose-Einstein statistics can be integrated and result in

$$\rho_i(T) = \begin{cases} \frac{7}{8}\frac{\pi^2}{30} g_i T^4 \\ \frac{\pi^2}{30} g_i T^4 \end{cases} \,, \quad n_i(T) = \begin{cases} \frac{3}{4}\frac{\zeta(3)}{\pi^2} g_i T^3, & \text{Fermions} \\ \frac{3}{4}\frac{\zeta(3)}{\pi^2} g_i T^3, & \text{Bosons} \end{cases} \tag{2.3.6}$$

This allows us to find the temperature dependence of the Hubble Parameter in the radiation dominated phase of the universe:

$$H \approx 1.66 \sqrt{g_{\mathrm{eff}}} \frac{T^2}{M_{Pl}} \,, \tag{2.3.7}$$

with g_{eff} counting the relativistic degrees of freedom with $T \gg m_i$ and defined as

$$g_{\mathrm{eff}} = \sum_{\mathrm{Bosons}} g_i \frac{T_i^4}{T^4} + \frac{7}{8} \sum_{\mathrm{Fermions}} g_i \frac{T_i^4}{T^4} \,, \tag{2.3.8}$$

where T is the temperature of the thermal bath and T_i the temperature of a certain species, which can deviate from T if this species has decoupled from the bath. For

[4] Consider for instance $e^- \to e^- + \gamma$ to be efficient. It follows directly $\mu_\gamma = 0$. This also holds true for any other gauge boson.
[5] The chemical potential would just enter as an overall factor of $\exp\left(-\frac{\mu}{T}\right)$.

$T \gtrsim 300\,\mathrm{GeV}$ all SM particles are relativistic and it is $g_{\mathrm{eff}} = 106.75$.
Finally, one finds that the entropy in a comoving volume a^3 within a thermal bath

$$S = a^3 \frac{\rho + p}{T}\,, \tag{2.3.9}$$

is a conserved quantity. Moreover, it is also dominated by the contribution of relativistic particles and thus the entropy density $s = Sa^{-3}$ can be expressed as

$$s = \frac{2\pi^2}{45} g_{\mathrm{eff}}^s T^3\,, \tag{2.3.10}$$

where g_{eff}^s counts the effective entropy degrees of freedom and is defined in complete analogy to g_{eff}. The conservation of S allows us to define the useful quantity

$$Y_i = \frac{n_i}{s}\,. \tag{2.3.11}$$

The advantage of Y compared to the number density n is that Y remains constant if the particle number in a comoving volume does not change. Thus, Y does not change if no particle-number-changing interactions are present.

2.3.2. The Boltzmann Equation

The Boltzmann equations play a crucial role in cosmology, as they describe the time evolution of the phase space densities of the different particle species. The relativistic version of the Boltzmann equation takes the form

$$\frac{df_X}{d\lambda} = \mathcal{C}^X\left[\{f\}\right]\,. \tag{2.3.12}$$

Here, $\mathcal{C}^X\left[\{f\}\right]$ is the collision term for the phase space density f_X, which includes effects from all possible interactions between the different particle species, $\{f\}$ is the set of the phase space distributions of all different particle species and λ is an affine parameter which can be taken proportional to the proper time τ.
Firstly, we examine the left-hand side and recall that the phase space densities are functions of only the time t and the absolute value of the momentum p or equivalently the energy E. Then, after expanding the total derivative $\frac{d}{d\lambda}$ and employing the geodesic equation $\frac{dp^\mu}{d\lambda} = \Gamma^\mu_{\alpha\beta} p^\alpha p^\beta$ in case of the Robertson-Walker metric we find

$$\frac{df_X}{d\lambda} = \left(E_X \frac{\partial}{\partial t} - H p_X^2 \frac{\partial}{\partial E_X}\right) f_X\left(p_X, t\right)\,. \tag{2.3.13}$$

This quantity can also be expressed in terms of the number density. Dividing by the energy E_X and integrating over d^3p_X results in

$$\frac{g_X}{(2\pi)^3} \int d^3p_X \frac{1}{E_X} \frac{df_X}{d\lambda} = \frac{dn_X}{dt} + 3Hn_X\left(t\right)\,. \tag{2.3.14}$$

If collisions are absent, i.e. $\mathcal{C}\left[\{f\}\right] = 0$, Eq. (2.3.14) implies the conservation of the particle number per comoving volume, $\frac{d}{dt}\left(a^3 n_X\right) = 0$.

Next, the collision term is given by

$$\begin{aligned}\mathcal{C}^X\left[\{f\}\right] = -\sum_{\text{Processes}}\prod_{i\in\mathcal{I}\cup\mathcal{F}} g_i\frac{d^3p_i}{2E_i\left(2\pi\right)^3}\left(2\pi\right)^4\delta^4\left(P_X+\sum_{j\in\mathcal{I}}P_j-\sum_{k\in\mathcal{F}}P_k\right)\\ \times\left[|\mathcal{M}_{X+\mathcal{I}\to\mathcal{F}}|^2 f_X\prod_{j\in\mathcal{I}}f_j\prod_{k\in\mathcal{F}}\left(1\pm f_k\right)\right.\\ \left.-|\mathcal{M}_{\mathcal{F}\to X+\mathcal{I}}|^2\left(1\pm f_X\right)\prod_{j\in\mathcal{F}}f_j\prod_{k\in\mathcal{I}}\left(1\pm f_k\right)\right],\end{aligned} \tag{2.3.15}$$

where $\mathcal{I}$ refers to the particles in the initial state except X, $\mathcal{F}$ are all particles in the final state, P_i is the four-momentum of the particle species i, $|\mathcal{M}_{X+\mathcal{I}\to\mathcal{F}}|^2$ is the squared matrix element averaged over initial and final state for the process under consideration and the factors $(1\pm f_i)$ are blocking and stimulated emission factors in the case of bosons(+) and fermions(−). Note that the matrix element includes symmetry factors $\frac{1}{n!}$ for identical particles in the initial and final state to avoid double counting from the integration over final and initial state momenta[6].
In general, the Boltzmann equations are a set of coupled integral-partial differential equations. In many cases, however, their form can be simplified significantly. If the process in question conserves CP and CPT invariance implies $|\mathcal{M}_{X+\mathcal{I}\to\mathcal{F}}|^2 = |\mathcal{M}_{\mathcal{F}\to\mathcal{X}+\mathcal{I}}|^2$. Moreover, typically one approximates $1\pm f_i\approx 1$, which holds true in the case of a small chemical potential and $E\gg T$. Furthermore, in this case, the phase space distributions of particle species in kinetic equilibrium can be assumed to be proportional to a Boltzmann distribution $f_i\sim\exp\left(-\frac{E_i}{T}\right)$. Then, the collision term reduces to

$$\begin{aligned}\mathcal{C}^X\left[\{f\}\right] = -\sum_{\text{Processes}}\prod_{i\in\mathcal{I}\cup\mathcal{F}} g_i\frac{d^3p_i}{2E_i\left(2\pi\right)^3}\left(2\pi\right)^4\delta^4\left(P_X+\sum_{j\in\mathcal{I}}P_j-\sum_{k\in\mathcal{F}}P_k\right)\\ \times|\mathcal{M}_{X+\mathcal{I}\leftrightarrow\mathcal{F}}|^2\left[f_X\prod_{j\in\mathcal{I}}f_j-\prod_{j\in\mathcal{F}}f_j\right].\end{aligned} \tag{2.3.16}$$

Often, we are not interested in the exact shape of the phase space distribution but only in the evolution of the number density. Then, as in Eq. (2.3.14), we can integrate the Boltzmann equation, including the collision term, over the three-momentum d^3p_X. Following the notation used in [51], we rewrite the collision term as

$$\frac{g_X}{(2\pi)^3}\int\frac{d^3p_X}{E_X}\mathcal{C}^X\left[\{f\}\right] = -\sum_{\text{Processes}}\gamma^{\text{eq}}\left(X+\mathcal{I}\leftrightarrow\mathcal{F}\right)\left(\frac{n_X}{n_X^{\text{eq}}}\prod_{i\in\mathcal{I}}\frac{n_i}{n_i^{\text{eq}}}-\prod_{j\in\mathcal{F}}\frac{n_j}{n_j^{\text{eq}}}\right), \tag{2.3.17}$$

[6]The situation differs from a particle collider where the initial state is known and therefore not integrated over.

with

$$\gamma^{\mathrm{eq}}\left(X+\mathcal{I}\leftrightarrow\mathcal{F}\right)=\int\frac{d^3p_X}{\left(2\pi\right)^3 2E_X}\prod_{i\in\mathcal{I}\cup\mathcal{F}}\frac{d^3p_i}{\left(2\pi\right)^3 2E_i}f_X^{\mathrm{eq}}\prod_{j\in\mathcal{I}}f_j^{\mathrm{eq}}$$
$$\left|\mathcal{M}_{X+\mathcal{I}\leftrightarrow\mathcal{F}}\right|^2\delta^4\left(P_X+\sum_{j\in\mathcal{I}}P_j-\sum_{k\in\mathcal{F}}P_k\right)\,. \tag{2.3.18}$$

In those steps, we assumed that every species is in kinetic equilibrium $f_i=\alpha_i\exp\left(-\frac{E_i}{T}\right)=\alpha_i f_i^{\mathrm{eq}}$ and CP-conserving interactions, which in combination with the δ-function implies $f_X^{\mathrm{eq}}\prod_{i\in\mathcal{I}}f_i^{\mathrm{eq}}=\prod_{j\in\mathcal{F}}f_j^{\mathrm{eq}}$. In the following, we refer to γ^{eq} as the thermal rate. The thermal rate for a CP-conserving decay results in

$$\gamma^{\mathrm{eq}}\left(X\leftrightarrow\mathcal{F}\right)=n_X^{\mathrm{eq}}\frac{K_1\left(x\right)}{K_2\left(x\right)}\Gamma_X\,, \tag{2.3.19}$$

while for a two-body initial state we find

$$\gamma^{\mathrm{eq}}\left(X+i\leftrightarrow\mathcal{F}\right)=\frac{T}{64\pi^4}\int\limits_{s_{\mathrm{min}}}^{\infty}\mathrm{d}s\,\sqrt{s}\hat{\sigma}\left(s\right)K_1\left(\frac{\sqrt{s}}{T}\right)\,, \tag{2.3.20}$$

where Γ_X is the decay width of X induced by the process $X\to\mathcal{F}$, $\hat{\sigma}\left(s\right)=2s\sigma\lambda\left(1,\frac{s}{m_X^2},\frac{s}{m_i^2}\right)$ is the reduced cross section, while σ is the cross section of the process $X+i\to\mathcal{F}$ summed over initial and final states, it is $\lambda\left(x,y,z\right)=\left(x-y-z\right)^2-4xy$ and $s_{\mathrm{min}}=\max\left\{\left(m_X+m_i\right)^2,\left(m_{f_1}+m_{f_2}\right)^2\right\}$ is the minimal center of mass energy and we defined $x=\frac{m_X}{T}$.
In certain cases, information about the shape of the phase space distribution is required, for example to estimate the impact of a DM model on structure formation. In these cases the momentum integration d^3p_X cannot be carried out, leading to a more complicated differential equation. Following the lines of [52, 53], we illustrate a solution strategy to obtain a solution to the Boltzmann equation at the level of phase space distributions.
We aim at rewriting the Liouville operator, the left-hand side of the Boltzmann equation, given in Eq. (2.3.13) such that it is a differential operator depending on one variable only. First we express the Liouville operator in terms of the absolute value of the momentum p_X and the time t

$$\frac{d}{d\lambda}f_X\left(p,t\right)=\frac{\partial}{\partial t}-Hp\frac{\partial}{\partial p}f_X\left(p,t\right)\,. \tag{2.3.21}$$

Then, we perform a transformation of variables $\left(t,p\right)\to\left(r,\xi\right)$ such that we have a differential operator depending on r only. This is the case if

$$r=F\left(t\right)\,,\quad\xi=G\left(\frac{a\left(t\right)}{a\left(t_0\right)}p_X\right)\,, \tag{2.3.22}$$

with F as an arbitrary function of the time only, G being an arbitrary function of a redshifted momentum and t_0 a reference time scale. In this work, we choose the

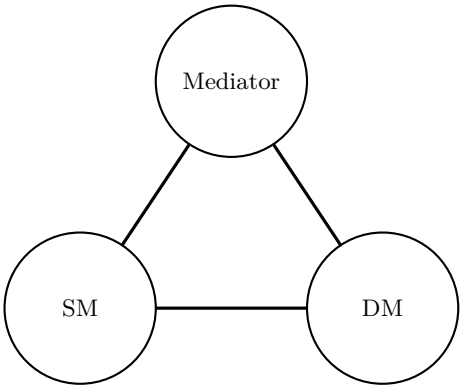

Figure 2.4.: Illustration of a portal DM model. The lines indicate the interactions between the different sectors. In the Figures 2.6, 2.8 and 2.10, a dotted line refers to a feeble interaction not sufficient to keep the to sectors in thermal equilibrium. A one headed arrow indicates a slow particle number transfer from one sector to another while a double headed arrow indicates that the corresponding two sectors are in thermal equilibrium.

functions F and G as in [53], i.e.

$$r = \frac{m_0}{T(t)}\,, \quad \xi = \frac{1}{T_0}\frac{a(t)}{a(t_0)}p_X\,, \tag{2.3.23}$$

with reference mass m_0 and reference temperature T_0. Note that r is a function of t in the sense that the time is directly related to the temperature via $T \sim t^{-1}$.[7] With that the Liouville operator reads

$$\frac{d}{d\lambda}f_X(p,t) = \frac{\partial r}{\partial t}\frac{\partial}{\partial r}f_X(\xi,r) = rH\left(\frac{T}{3g^s_{\text{eff}}}\frac{dg^s_{\text{eff}}}{dT}+1\right)^{-1}\frac{\partial}{\partial r}f_X(\xi,r)\,. \tag{2.3.24}$$

The operator simplifies further if we only consider temperature intervals where the entropy degrees of freedom are constant, which is the case for temperatures of $T \gtrsim 300\,\text{GeV}$. For the Boltzmann equation we eventually find

$$\frac{\partial}{\partial r}f_X(\xi,r) = \frac{1}{Hr}\left(1-\frac{r}{3}\frac{\partial}{\partial r}\log\left(g^s_{\text{eff}}\right)\right)\mathcal{C}^X\left[\{f\}\right]\,. \tag{2.3.25}$$

2.3.3. Production Mechanisms of Dark Matter via a Portal

In this section, we analyze several production regimes of DM coupled either directly or via a portal to the SM. In a portal model, DM does not necessarily couple to the SM directly but via one or multiple mediators. The different sectors of a DM model are illustrated in Figure 2.4 [49, 50]. We classify the interactions between the three sectors in three types. Consider first the case of a coupling sufficiently large to keep the two sectors in thermal equilibrium for a certain time. More precisely, this means that the interaction rate Γ of a particle-number-transferring process between two sectors, such as an annihilation $\bar{a}a \leftrightarrow \bar{b}b$ where the particles a and b belong to different sectors, is large

[7] The exact relation can be extracted from the fact that the entropy is conserved in a comoving volume.

compared to the Hubble parameter. Broadly speaking, if $\Gamma \ll H$ a particle interacts on average less than once during a time span of the order of the age of the universe, which scales as the inverse of the Hubble parameter. If, on the other hand, $\Gamma \gg H$, interactions occur rapidly, allowing for an efficient energy and particle number transfer between the two sectors. To estimate the coupling between two sectors required to keep them in thermal equilibrium, we define the interaction rate in thermal equilibrium Γ^{eq}, by inspecting the Boltzmann equation in a form obtained by combining the equations (2.3.14), (2.3.17) and (2.3.11). Then, one obtains

$$\frac{dY_X}{dt} = -\frac{\gamma^{\mathrm{eq}}\left(X + \mathcal{I} \leftrightarrow \mathcal{F}\right)}{s}\left(\frac{n_X}{n_X^{\mathrm{eq}}}\prod_{i\in\mathcal{I}}\frac{n_i}{n_i^{\mathrm{eq}}} - \prod_{j\in\mathcal{F}}\frac{n_j}{n_j^{\mathrm{eq}}}\right). \tag{2.3.26}$$

Comparing this expression with $\dot{Y}_X = \Gamma_X Y_X$, we find

$$\Gamma_X = \frac{\gamma^{\mathrm{eq}}\left(X + \mathcal{I} \leftrightarrow \mathcal{F}\right)}{n_X^{\mathrm{eq}}}\left(-\prod_{i\in\mathcal{I}}\frac{n_i}{n_i^{\mathrm{eq}}} + \frac{n_X^{\mathrm{eq}}}{n_X}\prod_{j\in\mathcal{F}}\frac{n_j}{n_j^{\mathrm{eq}}}\right). \tag{2.3.27}$$

Thus, if in thermal equilibrium the interaction rate for both directions results in

$$\Gamma_X^{\mathrm{eq}} = \frac{\gamma^{\mathrm{eq}}\left(X + \mathcal{I} \leftrightarrow \mathcal{F}\right)}{n_X^{\mathrm{eq}}}. \tag{2.3.28}$$

Given the mass scales of the considered sectors we can use the criterion $\Gamma_X^{\mathrm{eq}} H^{-1} = 1$ to find the coupling κ_{th} required to thermalize the two sectors. If this condition cannot be fulfilled, $\kappa < \kappa_{\mathrm{th}}$ must hold and we refer to the sectors as feebly coupled. In this case, we distinguish between two scenarios. First, the case where the coupling κ is large enough to transfer particle number in one direction (from a populated to an underpopulated sector) and second the case where the coupling is so tiny that no sizable particle number transfer in any direction takes place. Within the illustration of Figure 2.6 and 2.8, a coupling of $\kappa > \kappa_{\mathrm{th}}$ is indicated by a double-headed arrow, the slow particle number density transfer from one sector to another with a coupling of $\kappa < \kappa_{\mathrm{th}}$ is indicated by a one-headed arrow into the direction of the flow of particle number and the decoupled case is illustrated by a dashed line.
In the following, we discuss the various production regimes arising in a portal model. We assume a thermalized SM and negligible number densities of the mediators and the dark sector as our initial conditions after reheating. The dependence of the different production mechanisms on these initial conditions is discussed in the paragraph for the respective production mechanism. The different production regimes are displayed in Figure 2.5.

Freeze-Out production of DM

If DM is in thermal equilibrium with SM particles either directly or indirectly via the mediators[8], DM is produced via the freeze-out mechanism. More precisely this means that either the DM-SM coupling or the DM-mediator and SM-mediator coupling must

[8] In this case, DM is in thermal equilibrium with the mediator(s), which must be in thermal equilibrium with SM particles themselve(s).

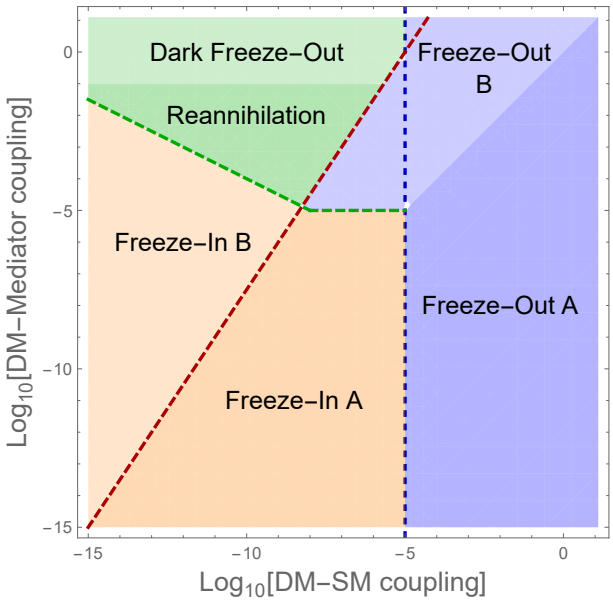

Figure 2.5.: A schematic 'phase space' diagram for DM production displaying the different DM production regimes in the plane spanned by the DM-SM coupling and the DM-mediator coupling as introduced in [49]. It is assumed that the DM-SM coupling is proportional to the product of the SM-mediator and mediator-DM coupling. The blue, green and red dashed lines indicate the coupling strength κ_{th}, that is sufficient to thermalize the two sectors, for the DM-SM, DM-mediator and SM-mediator interaction respectively. Constant values for the SM-mediator interaction follow lines parallel to the red dashed line and increase in value to the bottom right corner. Furthermore, the SM is assumed to be in thermal equilibrium initially, while the number densities in the dark sector and of the mediators are assumed to be negligible. This directly results in the kink within the green dashed line, since as soon as neither DM nor the mediators are not in thermal equilibrium with the SM(and therefore both sectors are underpopulated), a larger coupling is mandatory to thermalize the two sectors. The different production regimes, freeze-out, freeze-in, dark freeze-out and reannihilation, as well as the subcatogeries A and B, are discussed in the main text.

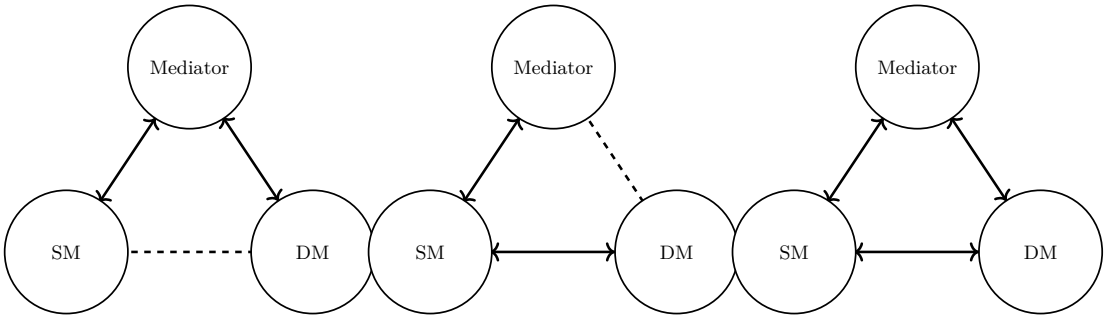

Figure 2.6.: Three coupling structures allowing for freeze-out production of DM. The double-headed arrow indicates a coupling of $\kappa > \kappa_{\mathrm{th}}$, while a dashed line or single-headed arrow corresponds to $\kappa < \kappa_{\mathrm{th}}$. In all cases, DM is in thermal equilibrium with the SM directly or indirectly.

exceed its thermalization value. The various coupling structures allowing for freeze-out production are illustrated in Figure 2.6.

Typically, DM freeze-out proceeds via pair annihilations of the DM candidate or pair annihilations of other dark sector particles, that are only slightly heavier than the DM candidate itself. The latter case is referred to as *coannihilation*. By definition the dark sector particles annihilate into particles that follow their equilibrium densities, i.e. $n_f = n_f^{\mathrm{eq}}$ if $f \in \mathcal{F}$. Consider first the case of pair annihilation of the DM candidate X itself only. Then, the Boltzmann equation for the evolution of the comoving number density Y_X in terms of the dimensionless variable $x = \frac{m_X}{T}$ reads

$$\frac{\mathrm{d}Y_X}{\mathrm{d}x} = -\frac{\gamma^{\mathrm{eq}}\left(\bar{X}X \to \mathcal{F}\right)}{sxH}\left[\left(\frac{Y_X}{Y_X^{\mathrm{eq}}}\right)^2 - 1\right]. \tag{2.3.29}$$

Qualitatively speaking, as long as the interaction rate Γ_X^{eq} exceeds the Hubble expansion H, DM tracks its equilibrium number density, i.e. $Y_X = Y_X^{\mathrm{eq}}$ and freezes out if $\Gamma_X^{\mathrm{eq}} \lesssim H$, therefore plummeting at a constant value. A typical evolution of the DM particle number is shown in Figure 2.7. When the temperature drops below the DM mass, DM can no longer be efficiently produced and the number density decreases exponentially. At some point the interaction rate of the DM annihilations is too strongly suppressed by the small number density and therefore also DM annihilation ceases, resulting in the well known freeze-out picture.

In general, Eq. (2.3.29) cannot be solved analytically. However, to a good approximation the relic density can be conveniently estimated in terms of the thermally averaged cross section

$$\langle \sigma v \rangle = \frac{\gamma^{\mathrm{eq}}\left(\bar{X}X \to \mathcal{F}\right)}{\left(n_X^{\mathrm{eq}}\right)^2}, \tag{2.3.30}$$

with σ referring to the cross section of the process $\bar{X}X \to \mathcal{F}$ summed over initial and final degrees of freedom and v the Møller velocity. Given the fact that after freeze-out the DM density is much larger than its equilibrium number density, the second term in Eq. (2.3.29) can be neglected for $x > x_f$, where x_f is defined by the condition $Y_X(x_f) = (c+1)\, Y_X^{\mathrm{eq}}(x_f)$. If we further assume the thermally averaged cross section

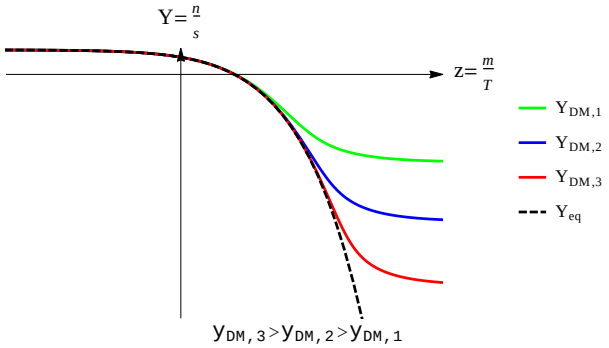

Figure 2.7.: The comoving number density of DM is plotted against the dimensionless variable $x = m_X T^{-1}$ in a generic freeze-out scenario. The dashed black line indicates the evolution of the particle number in thermal equilibrium. The colored lines refer to the evolution of the DM particle number given DM-SM couplings of different strengths. A larger coupling leads to a smaller DM density.

to be of the form $\langle \sigma v \rangle = \sigma_0 x^{-n}$, the equation can be integrated by parts [48, 54]. The choice $c\,(c+2) = n+1$ yields a result within 5% accuracy with the numerical result and yields

$$x_f = \ln\left[0.038\,(n+1)\,\frac{g_X}{\sqrt{g_{\text{eff}}}} M_{\text{Pl}} m_X \sigma_0\right] - \left(n+\frac{1}{2}\right)\ln\left(\ln\left[0.038\,(n+1)\,\frac{g_X}{\sqrt{g_{\text{eff}}}} M_{\text{Pl}} m_X \sigma_0\right]\right), \tag{2.3.31}$$

$$Y_\infty = \frac{3.79\,(n+1)\,x_f^{n+1}}{\frac{g^s_{\text{eff}}}{\sqrt{g_{\text{eff}}}} M_{\text{Pl}} m_X \sigma_0}. \tag{2.3.32}$$

Here, $Y_\infty = Y_X\,(x \to \infty)$ is the comoving DM number density today.
Note that the expansion of $\langle \sigma v \rangle$ in x can be related to an expansion in the velocity

$$\langle \sigma v \rangle = \left\langle a + b v^2 + c v^4 + \mathcal{O}\left(v^6\right)\right\rangle = a + \frac{3}{2} b x^{-1} + \frac{15}{8} c x^{-2} + \mathcal{O}\left(x^{-3}\right). \tag{2.3.33}$$

This expansion is suitable as the DM freeze-out typically takes place at temperatures at least one order of magnitude smaller than the DM mass. The case of a dominant zeroth order contribution in v is typically referred to as s-wave annihilation, while if the leading order contribution is of second order in v we have a p-wave annihilation. In Eq. 2.3.32 we observe the well known σ_0^{-1} dependence of the DM particle number today, neglecting the logarithmic contribution induced by the factor x_f^{n+1}. Given Y_∞, we find Ω_{DM} via

$$\Omega_{\text{DM}} = \frac{Y_\infty m_X s_{\text{today}}}{\rho_c} \sim \frac{x_f^{n+1}}{\sigma_0}, \tag{2.3.34}$$

where ρ_c and s_{today} are the critical energy density and entropy density measured today respectively.
Although the approximation discussed above provides accurate results for a large part of the parameter space of the freeze-out regime, there exist three well known exceptions [55] where the approximation breaks down: Resonances, threshold effects and

coannihilations. Resonances appear if the annihilation takes place near a pole in the cross section, threshold effects describe scenarios where the annihilation products are slightly heavier than the annihilating DM and coannihilations contribute to the annihilation cross section if annihilations of dark sector particles close in mass to the DM candidate are present. As coannihilations are essential to the discussion in the Chapters 4.3 and 6, we will review the effects of coannihilations in the following.
For our discussion we assume the dark sector consists of particles X_i with X_1 as the lightest particle and therefore the DM candidate. In case of a small mass splitting in the dark sector, in addition to the direct annihilation of the DM matter candidate X_1, $X_1\overline{X}_1 \to SM$, also annihilations with or of other dark sector particles such as $X_i\overline{X}_j \to SM$ can effectively contribute to the annihilation cross section. If conversions of different dark sector particles, such as $X_iSM \leftrightarrow X_jSM'$ remain efficient during the time of annihilation, the effective thermally averaged DM annihilation cross section σ_{eff} results in

$$\langle \sigma_{\text{eff}} v \rangle = \sum_{ij} \langle \sigma_{ij} v \rangle \, r_i r_j \,, \tag{2.3.35}$$

with

$$r_i = \frac{g_i}{g_{\text{eff}}^{\text{co}}} \left(\frac{m_{X_i}}{m_{X_1}} \right)^{\frac{3}{2}} \exp\left(\left[1 - \frac{m_{X_i}}{m_{X_1}} \right] \frac{m_{X_1}}{T} \right) , \tag{2.3.36}$$

where we defined $\sigma_{ij} = \sigma\left(\chi_i\overline{\chi}_j \to SM\right)$ and

$$g_{\text{eff}}^{\text{co}} = \sum_i g_i \left(\frac{m_{X_i}}{m_{X_1}} \right)^{\frac{3}{2}} \exp\left(\left[1 - \frac{m_{X_i}}{m_{X_1}} \right] \frac{m_{X_1}}{T} \right) . \tag{2.3.37}$$

Thus, for almost degenerate dark sector particles the annihilation cross section can even be dominated by the coannihilation contributions while for mass splittings larger than $\sim 20\%$ their contributions can be neglected.
Lastly, a few remarks on the dependence of freeze-out production on the initial conditions after reheating and the different freeze-out regimes depicted in Figure 2.5 are needed. As the couplings are large enough to guarantee a thermalization of the dark sector, freeze-out production is independent of the assumption of initially empty dark and mediator sectors. The two subregimes arising in Figure 2.5 distinguish between scenarios where an annihilation of DM into SM particles (Freeze-Out A) or into mediator particles (Freeze-Out B) decouples last.

Freeze-In production of DM

If DM is thermalized with neither the SM nor the mediator sector, DM production can proceed via the freeze-in mechanism. Therefore both the SM-DM and DM-mediator couplings are smaller than their thermalization value. Various coupling structures allowing for freeze-in production are illustrated in Figure 2.8. In freeze-in scenarios, the dark sector never reaches equilibrium with another sector and therefore $n_X \ll n_X^{\text{eq}}$ for dark sector particles. Due to this assumption contributions to the relic density of different production channels directly add up to a very good approximation. Inspecting the

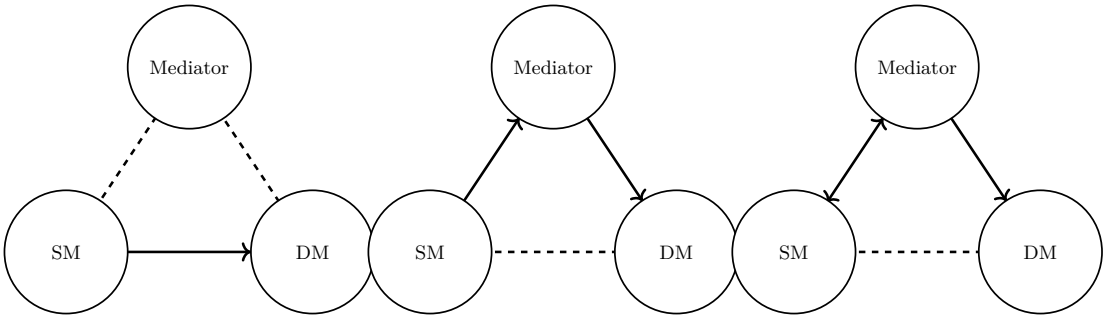

Figure 2.8.: Three coupling structures allowing for freeze-in production of DM. The double headed arrow indicates a coupling of $\kappa > \kappa_{\text{th}}$, while a dashed line or single-headed arrow corresponds to $\kappa < \kappa_{\text{th}}$. In case of a single-headed arrow the coupling is sufficiently large to transport number density from a populated sector to an underpopulated one. DM is never in thermal equilibrium with the SM directly or indirectly.

collision term in the form of Eq. (2.3.17), we find

$$\frac{\mathrm{d}Y_X}{\mathrm{d}x} = \frac{1}{sxH} \sum_{\text{processes}} \gamma^{\text{eq}} \left(\mathcal{F} \to X + \mathcal{I}\right) \prod_{f \in \mathcal{F}} \frac{n_f}{n_f^{\text{eq}}}\,, \tag{2.3.38}$$

for the evolution of the comoving number density of the DM candidate, where we neglect backreactions due the suppression induced by $n_X \ll n_X^{\text{eq}}$. Already at this point we can conclude that in case of no hierarchy in the thermal rates γ^{eq} for different production channels, the production is dominated by channels involving only non dark sector particles in the state $\mathcal{F}$. The resulting differential equation is much less complicated than in the case of freeze-out production and can be integrated for a given thermal rate γ^{eq}. Considering first the case of a (inverse) decay $1 \leftrightarrow n$ process (either the inverse decay into the DM candidate or the decay into n dark sector particles). Using Eq. (2.3.19) and assuming the initial state particles follow their equilibrium number densities, i.e. $n_f = n_f^{\text{eq}}$, we find

$$Y_X\left(x_f\right) = \frac{\Gamma_P}{K} \frac{g_P}{2\pi^2} \frac{m_P^2}{m_X^4} \int_{x_i}^{x_f} \mathrm{d}x\, x^3 K_1\left(x \frac{m_P}{m_X}\right)\,. \tag{2.3.39}$$

We use $K = sHT^{-5}$, $x = \frac{m_X}{T}$, Γ_P is the decay rate of the parent particle and m_P is the parent particle's mass. Note that also the DM candidate itself can be the parent particle so that $m_P = m_X$ and $g_P = g_X$. The integral boundaries are given by $x_i = \frac{m_X}{T_R}$, with T_R the reheating temperature, and $x_f = \frac{m_X}{T_0}$, with T_0 the temperature today. Assuming a large reheating temperature $T_R \gg m_X$ and $T_0 \ll m_X$ the expression for the comoving number density today simplifies to

$$Y_X\left(x_f \to \infty\right) = \frac{3 g_P}{4\pi K} \frac{\Gamma_P}{m_P^2}\,. \tag{2.3.40}$$

In case of a production channel involving a $2 \leftrightarrow n$ process, the thermal rate is given by Eq. (2.3.20) and the integration of the Boltzmann equation involves an additional

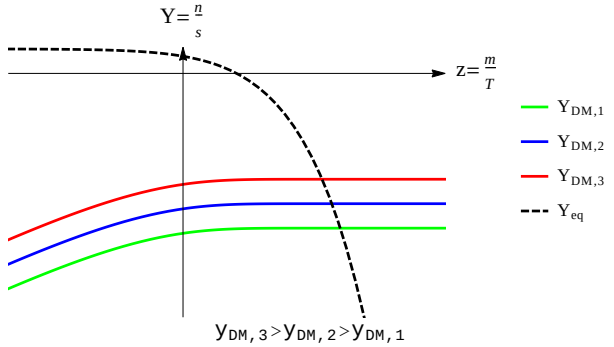

Figure 2.9.: The comoving number density of DM is plotted against the dimensionless variable $x = m_X T^{-1}$ in a generic freeze-in scenario. The dashed black line indicates the evolution of the particle number in thermal equilibrium. The colored lines refer to the evolution of the DM particle number given DM-SM/DM-mediator couplings of different strengths. A larger coupling leads to a larger DM density.

integration over the center of mass energy. Performing the integration over x results in

$$Y_X\left(x_f \to \infty\right) = \frac{3}{128 K \pi^3} \int\limits_{s_{\min}}^{\infty} \mathrm{d}s \, \frac{\hat{\sigma}\left(s\right)}{s^{\frac{3}{2}}} \,, \tag{2.3.41}$$

with $\hat{\sigma}$ the reduced cross section and $s_{\min}$ the minimal center of mass energy as defined below Eq. (2.3.20). If DM is produced via freeze-in out of a sector that is underpopulated itself, as for instance indicated in the second illustration in Figure 2.8, the formulas given above do not apply, since in this case we have $\frac{n_f}{n_f^{\mathrm{eq}}} < 1$ in Eq. (2.3.38), resulting in an additional suppression of the relic density. In the illustrations of the different production regimes in Figure 2.5, the freeze-in regime is separated into two areas distinguishing between freeze-in production with mediators in (Freeze-In A) and out (Freeze-In B) of thermal equilibrium with the SM. Inspecting the Eqs. (2.3.40) and (2.3.41), we find that, in contrast to freeze-out production, the DM density increases with an increasing coupling to the mediators or the SM. A typical time evolution in case of freeze-in production is displayed in Figure 2.9. Note that freeze-in production is sensitive to our initial conditions after reheating. In the expressions given in the Eqs. (2.3.40) and (2.3.41) we assume $Y_X\left(x_i\right) = 0$. Any non-zero initial contribution to the DM density must be added to the yield generated via freeze-in. In this sense any given freeze-in coupling that can reproduce the observed DM energy density for a vanishing initial abundance can be understood as an upper bound on the freeze-in coupling in case of a non-negligible initial density. Finally, we comment on an interesting scaling behavior that can be extracted out of the freeze-in yields given in Eq. (2.3.40) and (2.3.41). If the production process involves a dominant mass scale, the freeze-in yield will be inversely proportional to this mass scale. For the decay the dominant mass scale m_{Max} can only be set by the mass of the parent particle m_P and leads to $\Gamma_P \sim m_P$ directly resulting in the m_P^{-1} scaling in Eq. (2.3.40). For the scattering we have to investigate the integral over the center of mass energy in Eq. (2.3.41). The minimally allowed center of mass energy scales like $s_{\min} \sim m_{\max}^2$. After the s integration the term is of mass dimension -1 and the only available mass scale is $m_{\max}$, resulting in the $m_{\max}^{-1}$ scaling for the freeze-in yield.

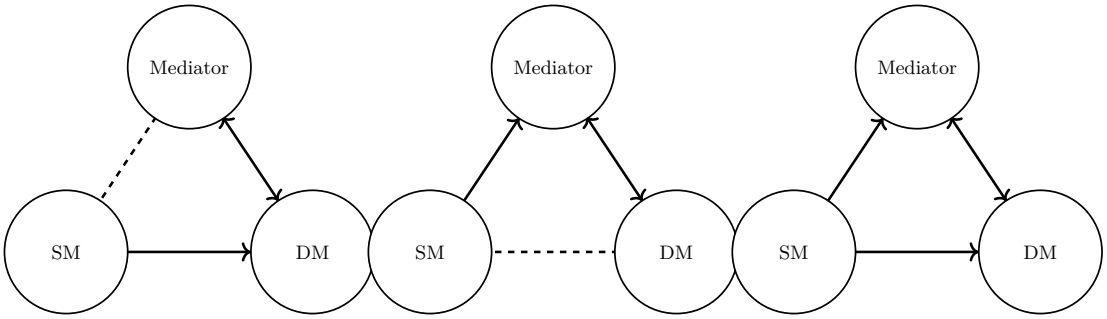

Figure 2.10.: Three coupling structures allowing for dark freeze-out or reannihilation production of DM. The double headed arrow indicates a coupling of $\kappa > \kappa_{\text{th}}$, while a dashed line or single headed arrow corresponds to $\kappa < \kappa_{\text{th}}$. In case of a single headed arrow the coupling is sufficiently large to transport number density from a populated sector to an underpopulated one. DM is never in thermal equilibrium with the SM but is in equilibrium with the mediators where it can undergo a freeze-out process.

Dark Freeze-Out and Reannihilation

The remaining regime is governed by a large DM-mediator interaction, while neither the dark sector nor the mediators reach thermal equilibrium with the SM. This regime combines elements of freeze-in and freeze-out production of DM. Assuming initially negligible abundances in the dark sector and for the mediators, either the dark sector, the mediators or both sectors become populated via freeze-in processes. Then however, in contrast to the freeze-in scenario, the DM-mediator coupling is sufficiently large to establish thermal equilibrium between the mediators and the dark sector. Various coupling structures that allow for a dark freeze-out or reannihilation scenario are presented in Figure 2.10. Within the equilibrium of the dark sector and the mediators, DM can now undergo a freeze-out process. If the freeze-out takes place after the freeze-in processes populating the dark sector and the mediators become inefficient the scenario is dubbed dark freeze-out. If, however, after the freeze-out in the dark sector freeze-in production is still efficient, the scenario is called reannihilation as DM is still being produced after its number density was decreased by annihilations. The evolution of the number densities is schematically illustrated in Figure 2.11. The calculation of the freeze-out temperature and the resulting yield can proceed similarly to the standard freeze-out picture, but with a different temperature T'. This is due to the fact that the SM equilibrates with neither the dark sector nor the mediators, causing $T = T_{SM} \neq T'$. The dark sector temperature can be obtained by solving the Boltzmann equations for the energy transfer from the SM to the dark sector via the freeze-in processes. The corresponding Boltzmann equation is obtained by multiplying both the Liouville operator in Eq. (2.3.13) and the collision term in Eq. (2.3.15) with the respective particle energy density and integrating over all three momenta. From the dark sector energy density ρ' the dark sector temperature T' can be extracted and allows to describe the equilibrium densities via $n^{\text{eq}}(T')$, where T' is a function of the SM temperature T. Eventually, the calculation of the freeze-out yield must be adjusted to the new equilibrium densities. Further details on the computation can be found in [49].

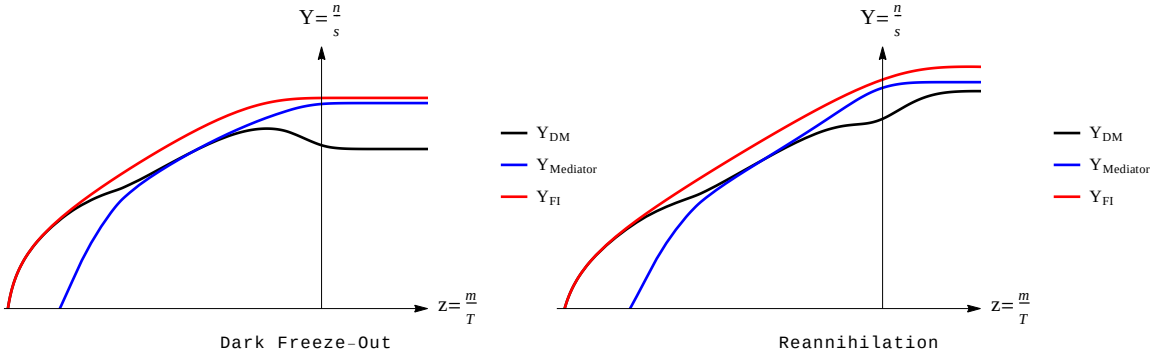

Figure 2.11.: The comoving number density of DM is plotted against the dimensionless variable $x = m_X T^{-1}$ in a generic dark freeze-out (left) and reannihilation (right) scenario. The red line indicates the freeze-in yield given a vanishing DM-mediator coupling. In both cases DM (black line) is produced from SM particles via freeze-in. The large DM-mediator coupling equilibrates the mediator (blue line) with the DM. The latter undergoes a freeze-out via annihilations into the mediator. On the left hand side the freeze-out takes place after the freeze-in production ceases to work, while on the right hand side it is the other way around.

Finally, the scaling behavior combines features from both freeze-in and freeze-out production of dark matter. A larger DM-mediator coupling decreases the relic density, while a larger SM-DM or SM-mediator coupling increases it.

2.4. Phenomenological Implications of Dark Matter

If DM couples to the SM non-gravitationally, it can lead to various different imprints, which we review in the following. There are three different ways to observe phenomenological implications of DM, that are schematically illustrated in Figure 2.12:

1. The idea of using sensitive detectors to search for DM recoiling with targets on earth is referred to as DM direct detection. Direct detection experiments can constrain the DM-SM coupling.

2. The production of DM via SM particle scattering on earth, as e.g. at the Large Hadron Collider (LHC). Again, the DM-SM interaction can be restricted from above. However, in contrast to direct detection experiments where due to the required instability of the non-DM candidates only DM can potentially scatter with the targets on earth, at colliders in addition to DM itself also other dark sector particles or particles of the mediator sector can be produced. Therefore, collider experiments have the potential to constrain large SM-mediator interactions.

3. The detection of DM annihilation or decay products from dense regions in the universe, that could be observed in for instance γ-rays from the galactic center. These types of experiments are referred to as indirect detection of DM.

In Figure 2.13, we illustrate how the different observational methods can constrain the parameter space of the various production mechanisms of a portal model for DM.
Beside these three main groups, various other methods to constrain the parameter space of a given DM model exist, including implications of the new dark sector particles for

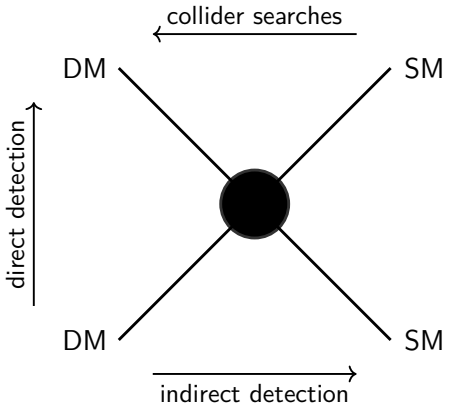

Figure 2.12.: An illustration of three different methods to observe DM. The arrows indicate the position of the initial and the final state and the blob in the middle refers to the interaction connecting DM and the SM. The figure is taken from [56].

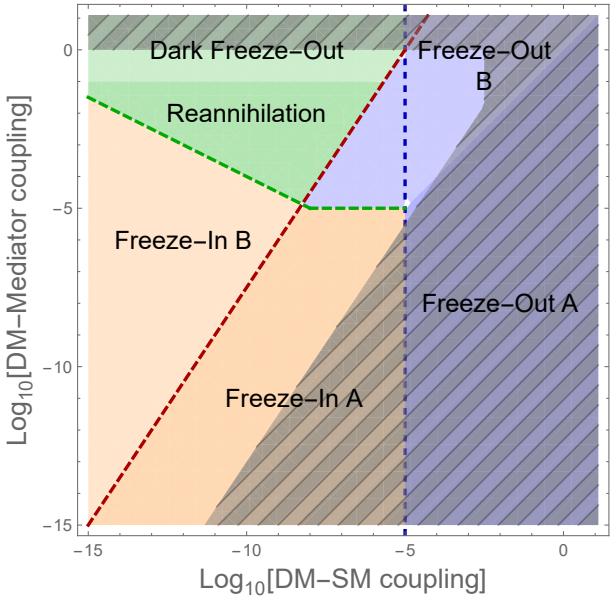

Figure 2.13.: The figure shows schematically how the different type of experiments can potentially constrain a given DM model. As elaborated on in the main text, direct detection experiments constrain the DM-SM interaction from above and therefore result in the vertical gray band on the right side. Collider experiments on the other hand not only constrain large DM-SM interaction but in addition provide the possibility to put upper bounds on the SM-mediator interactions, since also the mediators could be produced at colliders. Note that this also offers the possibility to constrain very small DM-SM interactions in the freeze-in regime via searches for collider-(meta)stable long lived particles, given a sizable SM-mediator interaction. For more details we refer the reader to [57]. Thus, collider experiments constrain the area indicated by the gray triangular shape in the bottom right. The gray excluded area on top is induced by gravitational lensing experiments resulting in an upper bound on the DM self interaction. Note that this bound only applies for light dark sectors, i.e. $m_{DM} \lesssim 1\,\mathrm{GeV}$.

the BBN, on the development of structures in the early universe or constraints on the DM self interaction from gravitational lensing experiments. In the following, we focus mainly on the particle physics of DM direct detection experiments and sketch a method to estimate the impact of a given DM candidate on the structure formation in the early universe.

2.4.1. Direct Detection

Direct detection experiments are one of the cornerstones of DM searches and aim to observe recoils of nuclei induced by scattering of nuclei with DM on earth, that are caused by the motion of the solar system through the milky way. In case of a small DM self interaction, where DM can be treated collisionless, the induced DM 'wind' has a typical velocity of roughly $v \sim 10^{-3}$ and its properties are set by its gravitational properties. The kinematics and therefore the expected nucleon-DM cross section depends on the DM velocity and thus the assumption about its velocity distribution. While we do not discuss the astrophysical properties of direct detection experiments here, they are addressed in e.g. [58, 59].
The particle physics determining the expected event rate in the detector can be tracked down to the effective nucleon-DM cross section. Typically, this quantity is split up into a (nucleon) spin independent (SI) and spin dependent (SD) part. In the non-relativistic limit, one finds

$$\sigma_0^{\mathrm{SI}} \sim \left(Z f_p + (A - Z)\, f_n\right)^2 , \tag{2.4.1}$$

for the DM-nuclei interaction. The number of protons in the nuclei is given by Z, while the total number of nucleons is given by A and $f_{p/n}$ describe the coupling strength of the proton and neutron to the mediator. For an isospin independent interaction, i.e. $f_n = f_p$, we find $\sigma_0^{\mathrm{SI}} \sim A^2$. Since the SD cross section does not increase as fast with the nucelon content, experiments with massive nuclei, as e.g. XENON1T, typically provide stronger limits for SI cross sections. Throughout this work we will employ the limits provided by XENON1T [60] on the SI cross section several times and therefore subsequently discuss, closely following the lines of [61], how the spin independent cross section can be derived from the DM interactions with quark and gluons.
Assuming a bosonic mediator, which is heavy compared to the transferred energy that typically ranges from a few keV to a few MeV, we can integrate out the heavy mediator

$$\mathcal{L}_{\mathrm{DD}} \supset \mathcal{O}_{\mathrm{DM}} \mathrm{Prop}_{\mathrm{med}} \mathcal{O}_q \to \frac{1}{m_{\mathrm{DM}}^2} \mathcal{O}_{\mathrm{DM}} \mathcal{O}_n \,, \tag{2.4.2}$$

where $\mathcal{O}_{\mathrm{DM}}$ encodes the DM current interacting with the mediator and $\mathcal{O}_q$ represents the interaction of the mediator with quarks, while O_n gives the interaction of the nucleons with the mediator. The main task is to relate the operators $\mathcal{O}_q$ and $\mathcal{O}_n$.
Consider first the case of a scalar mediator, so that scalar or pseudoscalar interactions can arise. The pseudoscalar interaction $\mathcal{O}_q = \tilde{t}_q \bar{q} \gamma^5 q$, leads to a SD and velocity suppressed interaction in the non-relativistic limit and therefore is not further investigated here. Note however, that a discussion of this case can be found in [61].
The scalar interaction $\mathcal{O}_q = \tilde{f}_q \bar{q} q$, results in a SI contribution to the DM-nucleon cross section and the resulting nucleon level operator is of the form $\mathcal{O}_n = \tilde{f}_n \bar{n} n$. Then, the

coupling to nucleons reads

$$\tilde{f}_n = m_n \sum_{q=u,d,s} f^n_{T_q} \frac{\tilde{f}_q}{m_q} + \frac{2}{27}\left(1 - \sum_{q=u,d,s} f^n_{T_q}\right) \sum_{q=c,b,t} \frac{\tilde{f}_q}{m_q}\,, \tag{2.4.3}$$

where the $f^n_{T_q}$ describe the nuclear quark content. Lattice calculations [62] find $f^p_{T_u} = 0.20$, $f^p_{T_d} = 0.026$ and $f^p_{T_s} = 0.043$ for the proton and the same values for the neutron but with the up and down quarks interchanged. In the case of a coupling to a scalar that is proportional to the quark mass itself, as in important case of the SM Higgs, we find with $\tilde{f}_q = \frac{m_q}{v}$

$$\tilde{f}_n = \frac{m_n}{v}\left[\frac{7}{9}\sum_{q=u,d,s} f^n_{T_q} + \frac{2}{9}\right]. \tag{2.4.4}$$

Next consider the case of a vector mediator, allowing for vector and axial-vector couplings. The axial-vector interaction leads to a SD interaction but, in contrast to a pseudoscalar interaction, is not velocity suppressed. Nevertheless, it is not further investigated here, as we will not employ limits on the SD DM-nucleon cross section.
The vector coupling, on the other hand, results in a contribution to the SI cross section and an operator of the form $\mathcal{O}_q = \tilde{b}_q \bar{q}\gamma^\mu q$ results in an nucleon level operator of the form $\mathcal{O}_n = \tilde{b}_n \bar{n}\gamma^\mu n$. The relation between the $\tilde{b}_q$ and $\tilde{b}_n$ is simply given by the summation over the valence quarks of the given nucleon, since in the case of an vector interaction only the valence quarks contribute

$$\tilde{b}_p = 2\tilde{b}_u + \tilde{b}_d\,, \quad \text{and} \quad \tilde{b}_n = \tilde{b}_u + 2\tilde{b}_d\,. \tag{2.4.5}$$

In the case of a SM Z boson mediating the interaction we find

$$\tilde{b}_u = g_2\left(\frac{1}{c_W} - \frac{2s^2_W}{3c_W}\right) \text{ and } \quad \tilde{b}_d = g_2\left(-\frac{1}{c_W} + \frac{s^2_W}{3c_W}\right), \tag{2.4.6}$$

with s_W and c_W corresponding to the sine and cosine of the Weinberg angle respectively. Now, given the interaction of DM with the mediator, we are able to find the SI DM-nucleon cross section. Following appendix B of [61] we summarize the non-velocity-suppressed contributions to the SI cross section for several relevant cases.

Fermionic DM: Scalar mediator
The interaction of Dirac DM via a scalar mediator S takes the form

$$\mathcal{L} \supset \left[\bar{\chi}\left(\lambda_{\chi s} + \lambda_{\chi p} i\gamma^5\right)\chi + \bar{f}\left(\lambda_{fs} + \lambda_{fp} i\gamma^5\right) f\right] S\,. \tag{2.4.7}$$

The mixed terms, more precisely the scalar-pseudoscalar or pseudoscalar-scalar interactions, are velocity suppressed with v^2, while the scalar-scalar and pseudoscalar-pseudoscalar interactions result in non-velocity suppressed contributions to both the SI and SD DM-nucleon cross section. We find

$$\sigma^{SI}_{s,s} = \frac{\mu_\chi N^2 \lambda^2_{\chi s}}{\pi m^4_S}\left(\frac{Z\tilde{f}_p + (A-Z)\,\tilde{f}_n}{A}\right)^2. \tag{2.4.8}$$

Here the $\tilde{f}_{n/p}$ are the dimensionless coupling constants to the neutron and proton given in Eq. (2.4.3) and $\mu_{\chi N}$ is the reduced mass of the χ-nuclei system. In case of Majorana DM the SI cross section takes the same form as in Eq. (2.4.8) but with the replacement $\lambda_{\chi s} \to \frac{1}{2}\lambda_{\chi s}$ in the Lagrangian.

Fermionic DM: Vector mediator
The interaction of Dirac DM with the vector mediator V_μ is given by

$$\mathcal{L} \supset \left[\bar{\chi}\gamma^\mu \left(g_{\chi s} + g_{\chi p}\gamma^5\right)\chi + \bar{f}\gamma^\mu \left(g_{fs} + g_{fp}\gamma^5\right) f\right] V_\mu \,. \tag{2.4.9}$$

Similarly to the case of a scalar mediator the vector-axialvector interactions are velocity suppressed and only the vector-vector interaction contributes to the SI cross section with

$$\sigma^{SI}_{v,v} = \frac{\mu\chi N^2 g^2_{\chi v}}{\pi m_V^4}\left(\frac{Z\left(2\tilde{b}_u + \tilde{b}_d\right) + (A-Z)\left(\tilde{b}_u + 2\tilde{b}_d\right)}{A}\right)^2 . \tag{2.4.10}$$

In case of Majorana DM the contribution to the SI cross section vanishes, as the vector coupling vanishes for a Majorana fermion, i.e. $g_{\chi v} = 0$.

Complex scalar DM: Scalar mediator
The interaction of complex scalar DM via a scalar mediator S is given by

$$\mathcal{L} \supset \left[\mu_\phi^2|\phi|^2 + \bar{f}\left(\lambda_{fs} + \lambda_{fp} i\gamma^5\right) f\right] S \,. \tag{2.4.11}$$

The scalar interaction contributes to the SI cross section with

$$\sigma^{SI}_s = \frac{\mu^2_{\phi N} m^2_\phi \mu^2_\phi}{4\pi m_S^4}\left(\frac{Z\tilde{f}_p + (A-Z)\,\tilde{f}_n}{A}\right)^2 , \tag{2.4.12}$$

while the pseudoscalar interaction contributes to the SD cross section. For the case of real scalar DM, the cross section takes the same form if μ_ϕ is replaced by $\frac{1}{2}\mu_\phi$ in the Lagrangian.

Complex Scalar DM: Vector mediator
The interaction is of the form

$$\mathcal{L} \supset \left[ig_\phi\left(\left(\partial_\mu\phi\right)\phi^\dagger + \phi\left(\partial_\mu\phi\right)^\dagger\right) + \bar{f}\gamma_\mu\left(g_{fs} + g_{fp}\gamma^5\right) f\right] V^\mu \,. \tag{2.4.13}$$

Again, the vector coupling contributes to the SI cross section with

$$\sigma^{SI}_s = \frac{\mu^2_{\phi N} g^2_\phi}{4\pi m_V^4}\left(\frac{Z\left(2\tilde{b}_u + \tilde{b}_d\right) + (A-Z)\left(\tilde{b}_u + 2\tilde{b}_d\right)}{A}\right)^2 . \tag{2.4.14}$$

For a real scalar the contribution vanishes.

The SI DM-nucleon cross section is constrained by multiple experiments. Current limits on the SI cross section are shown in Figure 2.14. The strongest limit for DM masses larger than 5 GeV is provided by the XENON1T experiment [65], that excludes

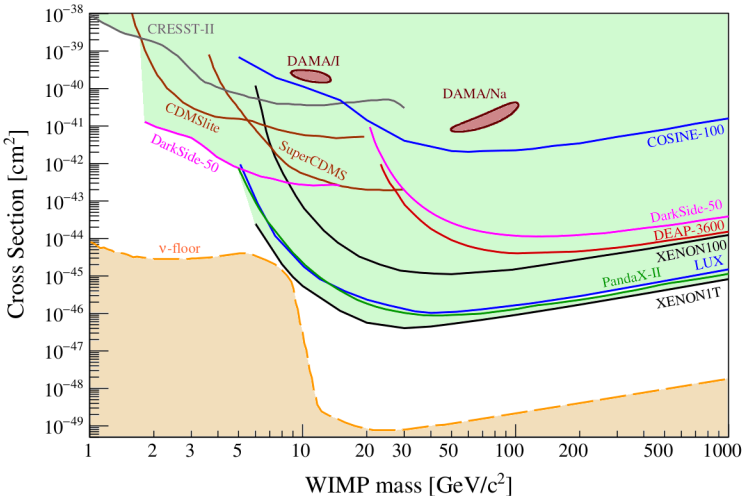

Figure 2.14.: Limits on the SI DM-nucleon cross section from various experiments. The figure is taken from [59]. For DM masses above 5 GeV the strongest limits come from the XENON1T experiment. The yellow area at the bottom indicates the so called neutrino floor, which describes the irreducible background induced by coherent neutrino nucleus scattering with neutrinos from the sun. The two red contours are two interpretations of the observed annual modulation signal by DAMA [63, 64] and are in contradiction with a large number of experiments.

cross sections as small as $10^{-46}\,\mathrm{cm}^2$ for DM masses of $\mathcal{O}\,(10 - 100\,\mathrm{GeV})$. In our later studies we will use the results of XENON1T on the SI cross section to constrain the parameters of our models.
The SD cross section is limited by several experiments and the results are summarized in Figure 2.15. However, the limits are roughly six orders of magnitude weaker than for the SI cross section, which is also the reason why we rely on the SI cross section to constrain our models.

2.4.2. Structure Formation

The addition of a DM candidate which is present during the time of structure formation, can alter the form and scale of structures that we expect to observe in the universe. If a DM particle travels, it might interfere with the gravitational collapse of structure [66], leading to a washout of structures below the free streaming length λ_{fs} of the DM candidate, as it is the case for light neutrinos. Hence structures at small scales would not expected to be seen. Thus, the observation of quasi-stellar objects (quasars) at high redshifts directly contradicts a hot DM candidate.
The observation of distant quasars manifests itself in the so called Lyman-α forest. Light emitted by these quasars excites the Lyman-α transition in neutral hydrogen atoms when passing by structures. This line is then missing in the quasar's spectrum. While propagating further, the photons are redshifted and by the time the next stricture is passed, the Lyman-α line can be absorbed again. In this way, light from distant quasars allows for a picture of the structures in the universe. From this data a one-dimensional matter-power spectrum can be extracted [67] and subsequently be compared to the

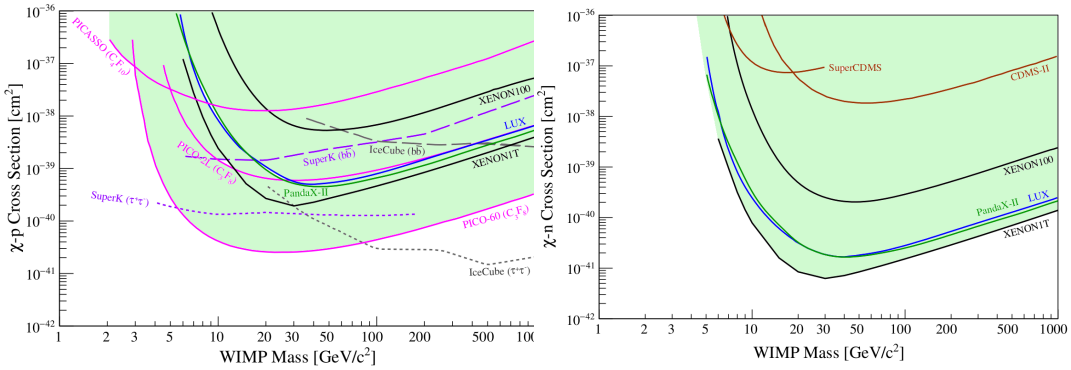

Figure 2.15.: Limits on the SD DM-proton (left) and DM-neutron cross section from various experiments. The constraints are several order of magnitude weaker than for the SI cross section.

matter-power spectrum predicted for a given DM model. This requires the usage of codes for solving the evolution of density fluctuations in the early universe, e.g. the CLASS code. We, however, follow a highly simplified but also less accurate approach. We employ the results of [68], who translated the analysis of the one-dimensional matter-power spectrum from [69] into an upper bound on the free streaming length. They find $\lambda_{fs} \lesssim 0.10\,\mathrm{Mpc}$ for a DM candidate that fully accounts for the observed DM relic density. This upper bound constrains the free streaming length of the DM candidate of a given model. The free streaming length of a particle produced at redshift $z = z_{\mathrm{prod}}$ is given by

$$\lambda_{fs} = \int_{z_{\mathrm{quasar}}}^{z_{\mathrm{prod}}} \mathrm{d}z \frac{v\,(z)}{H\,(z)}\,, \tag{2.4.15}$$

where v is the velocity of the particle and H the Hubble parameter. The lower bound of the integration typically is given by $z_{\mathrm{quasar}} \sim 2 - 5$. Note that in practice this lower bound can be set to zero, as the integral is usually dominated by contributions from larger redshifts, justifying the lower boundary of exactly zero. For the estimate of a typical free streaming length of the DM candidate we take z_{prod} at the temperature where most of the DM is produced or becomes freely propagating. For freeze-out production this temperature is given by the freeze-out temperature T_{fo} itself. At higher temperatures $T > T_{\mathrm{fo}}$, DM is even more abundant but does not stream freely as annihilations into e.g. SM particles occur rapidly before freeze-out. In a freeze-in scenario, DM gets produced over a large time period, but the production is most efficient at the freeze-in scale given by the largest mass scale involved in the production process. In the case of a particle decay, this scale would for instance be given by the mass of the parent particle. Lastly, we approximate the velocity in Eq. (2.4.15) with the average velocity of a DM particle at z_{prod}. After production in case of freeze-in production or decoupling in case of freeze-out production, the velocity becomes red shifted via

$$v\,(z) = \frac{p\,(z)}{\sqrt{p\,(z)^2 + m_{\mathrm{DM}}^2}}\,, \tag{2.4.16}$$

and

$$p\left(z\right) = p_{\text{prod}} \frac{1+z}{1+z_{\text{prod}}} \,. \tag{2.4.17}$$

The average momentum at the time of production p_{prod} is determined by

$$p_{\text{prod}} = \frac{\int \mathrm{d}p\, p^3 f_{\text{DM}}\left(p, T_{\text{prod}}\right)}{\int \mathrm{d}p\, p^2 f_{\text{DM}}\left(p, T_{\text{prod}}\right)} \,, \tag{2.4.18}$$

where $f_{\text{DM}}\left(p, T\right)$ describes the phase space density of the DM candidate. Finally, the Hubble parameter in terms of the redshift is given by

$$H\left(z\right) = H_0 \sqrt{\Omega_M \left(1+z\right)^3 + \Omega_R \left(1+z\right)^4 + \Omega_\Lambda} \,. \tag{2.4.19}$$

Using Eq. (2.4.15), we are now able to calculate the free streaming length of our DM candidate given its phase space distribution f_{DM}. In this sense, the limit derived from the upper bound of the free streaming length crucially depends on the production mechanism. For freeze-out production DM is following its equilibrium density, and therefore a Boltzmann distribution[9]. This does not apply to scenarios where DM does not reach thermal equilibrium with the SM, as for instance in freeze-in production of DM. In the latter instance, the Boltzmann equations have to be solved on the level of momentum distribution functions, as described in the end of Section 2.3.2.

2.4.3. Self Interactions, Indirect Detection, the BBN and Colliders

In this section, we briefly discuss the possibilities to constrain DM models from self interactions of DM, indirect detection probes, the BBN, and colliders.

Self Interactions
When a galaxy moves through a region of large DM density, for instance another galaxy, a separation between the DM halo and the visible matter of the galaxy can be caused due to the possibly smaller self interaction of DM compared to the electromagnetically charged SM particles. This separation can be observable via gravitational lensing effects. The most prominent astrophysical object that is used to constrain the self interactions of DM is the Bullet Cluster. Different groups analyzing the Bullet cluster [70–73] found an upper bound of order $\frac{\sigma_{\text{DM}}}{m_{\text{DM}}} \lesssim 1 \frac{\text{cm}^2}{\text{g}}$. Note however, that these results are still subject to an ongoing discussion. The authors of [74] for example can fit the observed separation of DM and visible matter in Abell 3827 with a DM self interaction of $\frac{\sigma_{\text{DM}}}{m_{\text{DM}}} \sim 1.5 - 3 \, \frac{\text{cm}^2}{\text{g}}$, which is in tension with the upper bound extracted from the Bullet cluster. Both observation could of course also be caused by an effect different from small DM self interactions. In the following, we assume an upper bound on the DM self interaction cross section of $\frac{\sigma_{\text{DM}}}{m_{\text{DM}}} \lesssim 1 \frac{\text{cm}^2}{\text{g}}$. The resulting limit on the couplings depends on the model itself but typically constrains the DM-mediator coupling to be smaller than an $\mathcal{O}\left(1\right)$ number for DM masses smaller than a few GeV.

[9] More precisely, it is following a Fermi-Dirac or Bose-Einstein distribution, that can be approximated with a Boltzmann distribution in most cases.

Indirect Detection
Indirect Detection probes rely on the detection of annihilation or decay products from DM emerging from dense regions of the universe. The decay or annihilation products depend on the DM model and can potentially involve any SM particle. The produced SM particles however will subsequently decay into lighter and eventually stable SM particles. Therefore, possibly detectable signatures involve photons, electrons, positrons, protons, antiprotons, and neutrinos.
From these candidates the neutral particles, the neutrino and the photon, have the advantage that they are not influenced by the cosmic magnetic fields and travel to earth in basically straight lines. Collecting information about their directionality and origin much easier than in case of charged particles. Additionally, charged particles are more likely to lose large amounts of energy on their way to earth, making their signals more difficult to model. Let us consider a DM candidate that annihilates into photon or neutrinos with the thermally averaged cross section $\langle \sigma v_{\mathrm{rel}} \rangle$ and the energy spectrum $\left(\frac{\mathrm{d}N_\gamma}{\mathrm{d}E}\right)_0$. In this scenario, we expect to observe the following spectrum on earth (see [75] for a more detailed and pedagogical discussion):

$$\frac{\mathrm{d}N_\gamma}{\mathrm{d}E\mathrm{d}t} = \frac{A}{4\pi}\left(\frac{\mathrm{d}N_\gamma}{\mathrm{d}E}\right)_0 \frac{\langle \sigma v_{\mathrm{rel}} \rangle}{2m_{\mathrm{DM}}^2} \int \mathrm{d}r\, \mathrm{d}\Omega\, \rho\left(r\right)^2 \,, \tag{2.4.20}$$

where A is the surface area of the detector and $\rho\left(r\right)$ describes the distribution of the DM mass density of the source. Typically, the expression above is factorized into two contributions

$$\frac{1}{A}\frac{\mathrm{d}N_\gamma}{\mathrm{d}E\mathrm{d}t} = \left(\frac{\mathrm{d}N_\gamma}{\mathrm{d}E}\right)_0 \frac{\langle \sigma v_{\mathrm{rel}} \rangle}{m_{\mathrm{DM}}^2} J_{\mathrm{ann}} \,, \tag{2.4.21}$$

with $J_{\mathrm{ann}} = \frac{1}{8\pi}\int \mathrm{d}r\, \mathrm{d}\Omega\, \rho\left(r\right)^2$, the J-factor, encoding the astrophysical contribution to the predicted spectrum. The J-factor depends crucially on the presumed density profile ρ, that can be obtained from gravitational probes or via numerical multi particle simulations. Given the J-factor and the experimentally observed neutrino or photon spectrum the particle physics component $\left(\frac{\mathrm{d}N_\gamma}{\mathrm{d}E}\right)_0 \frac{\langle \sigma v_{\mathrm{rel}} \rangle}{m_{\mathrm{DM}}^2}$ can be constrained. Typically J-factors, e.g. for the satellite dwarf galaxies of the milky way can range over multiple orders of magnitude, $J_{\mathrm{ann}} \sim 10^{17-20}\frac{\mathrm{GeV}^2}{\mathrm{cm}^5}$. Note that the formulas given above assume the absence of redshift effects in the produced neutrinos or photons during their way to earth, which is only a good approximation for nearby sources like milky way satellites or the galactic center.
The observation of neutral annihilation products proves to be especially powerful, if the annihilations are s-wave and therefore not suppressed by the small velocities of $v \sim 10^{-3}$, and if the resulting annihilation products are photon rich. This is the case for any annihilation into gauge boson or quarks. For example, in a DM model with a dominant annihilation into a $b\bar{b}$ pair, DM masses of $m_{\mathrm{DM}} \lesssim 100\,\mathrm{GeV}$ are excluded by the γ-rays from the Milky Ways dwarf galaxies observed by Fermi [76].
For cosmic rays of charged particles the analysis is, as mentioned above, more elaborated and therefore not further discussed here. Lastly, we mention the possibility to search for indirect probes of DM in the CMB via investigating its anisotropies, which could be affected by a larger ionization fraction induced by DM annihilation products during the

time when the CMB formed.

Big Bang Nucleosynthesis
The introduction of a DM candidate that remains in thermal equilibrium with the SM during the time of the BBN can alter the predictions for the amount of light elements in the universe by the injection of its energetic annihilation or decay products. As already mentioned in Section 1.3.3, this is caused by the interplay of multiple factors. Firstly, new degrees of freedom can alter the expansion rate of the universe, especially if they are relativistic since $H \sim \sqrt{\rho}$. The expansion rate plays a crucial role in determining the time when certain nuclear processes, such as $n\nu_e \leftrightarrow pe^-$, cease to work efficiently and therefore freeze-out which in turn alters the time window in which the various elements are produced. In this way additional relativistic degrees of freedom take a direct influence on the observed abundances of light elements. Secondly, depending on their coupling strength to electrons and neutrinos, they can alter the photon to neutrino temperature ratio, which in return changes the proton to neutron conversion rates. Lastly, light and therefore relativistic particles can significantly increase the entropy and thus dilute the number densities of light elements if this entropy is injected after or during BBN. If we for example consider a weakly interacting massive particle (WIMP) DM that directly annihilates electrophilic (into electrons) or neutrinophilic (into neutrinos), the authors of [77] find the following constraints in different mass regions:
Light (below 10 MeV) neutrinophilic DM potentially increases the neutron to proton and therefore deuterium to hydrogen ratio. Electrophilic DM in this mass range tends to inject sizable amounts of entropy, leading to a dilution of the baryon to photon density. Furthermore, they find that for DM masses of $m_{\mathrm{DM}} \gtrsim 30\,\mathrm{MeV}$ the parameter space of the model remains unconstrained from the BBN, as the annihilations freeze-out before the BBN takes place. Note that similar effects can also occur due to the late decay of a mediator or metastable DM particle if it decays efficiently during the time of the BBN. In the models discussed in this work, we take the approach to only consider WIMP DM of large enough masses so that the BBN is not perturbed or ensure that any annihilation or decay decouples before the onset of the BBN. If this was not the case, we would be required to solve the Boltzmann equations governing the density evolution of the light elements utilizing BBN codes like PRIMAT [78] and compare the results to the experimental observations.

Collider Constraints
In particle colliders DM or mediators can be produced via SM particle scattering if the coupling to the SM is large enough. Therefore in addition to the SM-DM coupling, the SM-mediator coupling can be constrained. As DM particles in many cases do not carry a SM charge, typical signatures involve signals with missing energy that come along with the radiation of a photon or a jet from the initial state, such as Mono-jet or Mono-photon searches. If the final state consists of both DM and SM particles, depending on the model also Mono-W/Z, Mono-Higgs or Mono-Top searches can be employed. In cases that involve a SM-charged mediator or dark sector particle, typically masses up to the TeV range and couplings within the freeze-out regime are subject to constraints. Consider for instance the effective four fermion operator $\bar{\chi}\Gamma^{\mu}\chi\bar{q}\Gamma'_{\mu}q$, with χ as the DM candidate, $\Gamma^{(\prime)}_{\mu}$ a given Lorentz structure and q a SM quark that is also constrained by

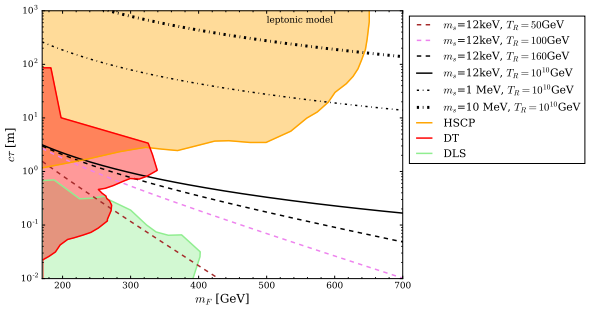

Figure 2.16.: Exclusion plot for a DM candidate coupling to the SM leptons via a mediator of mass m_F and with a lifetime τ. For masses below 650 GeV large lifetimes and therefore arbitrarily small couplings can be excluded.

direct detection experiments. Typically the results of the ATLAS and CMS collaborations can compete with the limits of the direct detection experiments for the Lorentz structures resulting in a SD DM-nucleon cross section, but they cannot reach the sensitivity of direct detection experiments in case of operators yielding a SI cross section. In a simple Higgs portal model, however, with a SM singlet scalar as the DM candidate, the CMS limits on the invisible decay width of the Higgs [79] exceed the ones of XENON1T for masses below 20 GeV.
A complementary approach is the search for long-lived particles. Given a large SM-mediator interaction, these searches can constrain tiny DM-mediator interactions of the freeze-in regime. The idea is to pair produce the mediator, which exclusively decays into final states involving DM. This approach applies to models that involve a SM-charged mediator that also carries a charge under the DM stabilizing symmetry, a scenario that was investigated in [57]. Various analysis methods can be employed, including the search for the track of heavy (collider) stable charged particles, disappearing tracks in case of a particle that decays within the collider, as well as the search for displaced leptons and vertices with missing energy. The constraints are given in plane spanned by the mediator mass m_F and its lifetime, which is directly correlated to its coupling to DM. In Figure 2.16 we show the results obtained in [57] for a DM candidate coupling to SM leptons. Interestingly the search for charged collider stable particles results in an upper bound on the mediator particle's lifetime and, in return, in a *lower* bound on the freeze-in coupling to DM, hence excluding tiny couplings for a given mass range. Note that these kind of searches can only be applied for models involving a SM-charged mediator or large SM-mediator couplings.

3. An Extradimensional Seesaw Model

This chapter contains material that was already part of the author's master thesis. This applies to most of the content in Section 3.1. It is presented for the sake of a better understanding of the follow up in Section 3.2 which mainly consists of results obtained during the PhD.

The problem of the small non-zero neutrino masses observed in neutrino oscillation experiments has been addressed widely in the literature over the past decades. Some of the most common model building approaches were addressed in Section 2.1. In this chapter, we investigate the leptonic flavor structure of an extra dimensional model generating light neutrino masses via a type-I seesaw variant with one SM singlet neutrino propagating in an extra dimension.
A key feature of this extra dimensional setup is the suppression of the five dimensional neutrino Yukawa coupling in the effective four dimensional theory, resulting from a reduced wave function overlap, as the SM particles, in contrast to the bulk neutrino, are confined to a (3+1) dimensional subspace. Furthermore, when integrating out the extra dimension, a infinite number of Kaluza-Klein (KK) excitations with masses $\sim R^{-1}$ appears, with R the radius of the compactified extra dimension.
The model was originally introduced in [80,81] but only studied in a one generation scenario. Here, we investigate a realistic three generation setup and focus on the question if the observed neutrino oscillation data can be realized and study the phenomenological implications of this model, such as rare lepton decays.

3.1. The Model

In this section, we briefly introduce the particle content of the model [1,80,81] and discuss the interactions arising in the effective 4D theory. The 5D SM singlet bulk neutrino and the SM lepton fields are described by

$$N\left(x^{\mu},y\right)=\begin{pmatrix}\Psi_1\left(x^{\mu},y\right)\\ \bar{\Psi}_2\left(x^{\mu},y\right)\end{pmatrix},\qquad L\left(x\right)=\begin{pmatrix}\nu_l\left(x^{\mu}\right)\\ l\left(x^{\mu}\right)\end{pmatrix},\qquad l_R\left(x^{\mu}\right). \tag{3.1.1}$$

$L\left(x\right)$ and $l_R\left(x\right)$ are the SM lepton fields with $l=e,\mu,\tau$. The x^{μ} are the usual coordinates, with $\mu=0,1,2,3$, y is the extra dimensional coordinate and Ψ_1 and Ψ_2 are 5D two component spinors. [1] The extra dimension is compactified on an $S_1/\mathbb{Z}_2$ orbifold and Ψ_1 is is even and Ψ_2 is odd under a $y\to -y$ transformation. While we only consider a setup with a bulk neutrino propagating in one extra dimension, this is not necessarily the case

[1] Here the notation, $\bar{\psi}_2$ for a particle transforming under the $(0,\frac{1}{2})$ representation of the Lorentz algebra is chosen in analogy to earlier works on this model. One might be more familiar with the $\psi_2^{\dagger}$ notation that is used in [82] which is a useful reference for the two component spinor notation.

for gravity that can experience the presence of n extra dimensions[2]. The Planck scale $M_{\rm Pl}$ is related to the new fundamental scale of gravity M_F via $M_P = (2\pi M_F R)^{\frac{n}{2}} M_F$. The Lagrangian of the model is given by [81, 85]:

$$\mathcal{L} = \int_0^{2\pi R} dy \left\{ \bar{N} \left(i\gamma^\mu \partial_\mu + \gamma^5 \partial_y \right) N - \frac{M}{2} \left(N^T C^{(5)-1} N + h.c. \right) \right.$$
$$\left. + \delta\left(y-a\right) \left[\frac{h_1^l}{M_F^{1/2}} L\tilde{\Phi}^* \Psi_1 + \frac{h_2^l}{M_F^{1/2}} L\tilde{\Phi}^* \Psi_2 \right] + \delta\left(y-a\right) \mathcal{L}_{SM} \right\} . \tag{3.1.2}$$

Here $\tilde{\Phi} = i\sigma_2 \Phi^*$ is the hypercharge conjugate of the SM Higgs doublet Φ and $\mathcal{L}_{SM}$ is the SM Lagrangian. The 5D γ matrices and the charge conjugation operator are defined as [85]:

$$\gamma^\mu = \begin{pmatrix} 0 & \sigma^\mu \\ \bar{\sigma}^\mu & 0 \end{pmatrix} \qquad \gamma^5 = \begin{pmatrix} -1_2 & 0 \\ 0 & 1_2 \end{pmatrix} \qquad C^5 = -\gamma_1\gamma_3 = \begin{pmatrix} -i\sigma_2 & 0 \\ 0 & -i\sigma_2 \end{pmatrix} ,$$

where $h_{1,2}^l$ are fundamental 5D Yukawa couplings, $\sigma^\mu = (1_2, \sigma)$ and $\bar{\sigma}^\mu = (1_2, -\sigma)$ with σ being the usual 4D Pauli matrices and C^5 is the 5D analog to charge conjugation in 4D while, as discussed in [85], the gauge invariant mass term $N^T C^{(5)-1} N$ is not a true Majorana mass term. However, after integrating out the extra dimension a Majorana mass term in the effective 4D theory is obtained.
Note, that the SM brane is not necessarily located at one of the orbifold fixed points but at positions $y = a$, with a being a free parameter of the model parameterizing the *brane shift*. The fields Ψ_1 and Ψ_2 are symmetric and antisymmetric, respectively, under the y to $-y$ transformation and therefore can be expanded in a Fourier series:

$$\Psi_1\left(x^\mu, y\right) = \frac{1}{\sqrt{2\pi R}} S_0\left(x^\mu\right) + \frac{1}{\sqrt{\pi R}} \sum_{k=1}^{\infty} S_k\left(x^\mu\right) \cos\left(\frac{ky}{R}\right) \tag{3.1.3}$$

$$\Psi_2\left(x^\mu, y\right) = \frac{1}{\sqrt{\pi R}} \sum_{k=1}^{\infty} A_k\left(x^\mu\right) \sin\left(\frac{ky}{R}\right) . \tag{3.1.4}$$

With this expansion, we can perform the y integration the Lagrangian (3.1.2). After introducing the weak basis for Kaluza-Klein spinors

$$\chi_{\pm k} = \frac{1}{\sqrt{2}} \left(S_k \pm A_k\right) , \tag{3.1.5}$$

we find the kinetic term in the effective 4D theory after EWSB:

$$\mathcal{L} = \bar{\chi} i\bar{\sigma}^\mu \partial_\mu \chi - \left(\frac{1}{2} \chi^T \mathcal{M} \chi + h.c. \right) , \tag{3.1.6}$$

[2]Such a scenario can be realized by embedding the SM 3-brane into a 4-brane which itself is embedded into a $3+n$ dimensional space. The bulk neutrino is confined to the 4-brane while gravity feels the entire $4+n$ dimensional spacetime. The realization of such scenarios is discussed e.g. in [83] or [84]

with

$$\mathcal{M} = \begin{pmatrix} 0 & 0 & 0 & m_0^e & m_{+1}^e & m_{-1}^e & \cdots \\ 0 & 0 & 0 & m_0^\mu & m_{+1}^\mu & m_{-1}^\mu & \cdots \\ 0 & 0 & 0 & m_0^\tau & m_{+1}^\tau & m_{-1}^\tau & \cdots \\ m_0^e & m_0^\mu & m_0^\tau & M & 0 & 0 & \cdots \\ m_{+1}^e & m_{+1}^\mu & m_{+1}^\tau & 0 & M+\frac{1}{R} & 0 & \cdots \\ m_{-1}^e & m_{-1}^\mu & m_{-1}^\tau & 0 & 0 & M-\frac{1}{R} & \cdots \\ \vdots & \vdots & \vdots & \vdots & \vdots & \vdots & \ddots \end{pmatrix} = \begin{pmatrix} 0 & Y^T \\ Y & \mathcal{M}_{\mathrm{KK}} \end{pmatrix}, \tag{3.1.7}$$

and $\chi^T = (\nu_l^e, \nu_l^\mu, \nu_l^\tau, \chi_0, \chi_{+1}, \chi_{-1}, \ldots)$. The m_k are a combination of the Yukawas $h_1^{(k)}$ and $h_2^{(k)}$:

$$m_k^l = \frac{v}{\sqrt{2}} \left[\bar{h}_1^l \cos\left(\frac{ka}{R}\right) + \bar{h}_2^l \sin\left(\frac{ka}{R}\right) \right] = A^l \cos\left(\frac{ka}{R} + \Phi^l\right). \tag{3.1.8}$$

where $A^l = \frac{v}{\sqrt{2}} \sqrt{\left(\bar{h}_1^l\right)^2 + \left(\bar{h}_2^l\right)^2}$, $\Phi^l = -\arctan\left(\frac{h_2^l}{h_1^l}\right)$, v is the vev of the Higgs and $\bar{h}_i^l = \left(\frac{M_F}{M_P}\right)^{\frac{1}{n}} h_i^l$. At this point, we can observe the suppression of the maximal possible value for the effective Yukawa coupling A^l relative to the 5D Yukawa couplings h_i^l, which results in a factor $\left(\frac{M_F}{M_P}\right)^{\frac{1}{n}}$.
We further rewrite the Lagrangian by introducing the four component spinor vector

$$\Psi_\nu^T = \left(\begin{pmatrix} \nu_l \\ \bar{\nu}_l \end{pmatrix}, \begin{pmatrix} \chi_{k_0} \\ \bar{\chi}_{k_0} \end{pmatrix}, \begin{pmatrix} \chi_{k_0+1} \\ \bar{\chi}_{k_0+1} \end{pmatrix}, \begin{pmatrix} \chi_{k_0-1} \\ \bar{\chi}_{k_0-1} \end{pmatrix}, \cdots \right), \tag{3.1.9}$$

with k_0 chosen in a way such that $M_0 = M + \frac{k_0}{R}$ is the minimum of $|M + \frac{k}{R}|$. This reordering causes a redefinition of the phases Φ^l to

$$\Phi^l = -\arctan\left(\frac{h_2^l}{h_1^l}\right) - \frac{k_0 a}{R}. \tag{3.1.10}$$

Eventually, we find the Lagrangian in the familiar form

$$\mathcal{L}_{kin} = \frac{1}{2} \bar{\Psi}_\nu \left(i\partial\!\!\!/ - \mathcal{M} \right) \Psi_\nu, \tag{3.1.11}$$

but with the replacement $M \to M_0$ in the matrix $\mathcal{M}$. In this form we can find the masses of the light and heavy neutrino states by diagonalizing the matrix $\mathcal{M}$. The three light neutrino masses are given by the solution to the equation $\sum_{i=0}^{3} K_i \lambda^i = 0$, with

$$K_2 = \sum_F S_1(F, F, \lambda), \quad K_1 = \sum_{F_1 > F_2} S_1(F_1, F_1, \lambda) S_1(F_2, F_2, \lambda) - S_1(F_1, F_2, \lambda)^2,$$
$$K_3 = 1, \qquad K_0 = -\sum_{F_1, F_2, F_3} \varepsilon_{F_1 F_2 F_3} S_1(\mathrm{e}, F_1, \lambda) S_1(\mu, F_2, \lambda) S_1(\tau, F_3, \lambda) = 0,$$

and

$$\frac{S_1(F_1,F_2,\lambda)}{\pi R A^{F_1} A^{F_2}} = \Big[\cot(\pi R[M_0-\lambda])\cos\left(\Phi^{F_1}-a[M_0-\lambda]\right)\cos\left(\Phi^{F_2}-a[M_0-\lambda]\right) - \frac{1}{2}\sin\left(\Phi^{F_1}+\Phi^{F_2}-2a[M_0-\lambda]\right)\Big] . \tag{3.1.12}$$

A more detailed discussion of the derivation can be found in [1]. Examining the coefficients of the polynomial, we see that we always find one zero mass eigenstate due to $K_0 = 0$. Furthermore, the linear coefficient vanishes, if the Dirac like masses m_k^f factorize in the sense that $m_k^f = g(k)\,h(f)$. This is the case if we find $\Phi^e = \Phi^\mu = \Phi^\tau$ and/or $a = 0, \frac{\pi R}{2}, \pi R$. Consequently, it is not possible to generate two neutrino mass differences without a brane shift away from the orbifold fixed points, resulting in $a \neq 0, \pi R$.
Let us consider first the case of equal phases $\Phi^l = \Phi$ and thus only one non-vanishing light neutrino mass. Then, this mass is given by

$$\begin{aligned}\lambda_3 &\approx \pi R \sum_F \left(A^F\right)^2 \frac{\cos(aM_0-\Phi)\cos(aM_0-M_0\pi R-\Phi)}{\sin(M_0\pi R)} \\ &= \pi R \sum_F \left(A^F\right)^2 f(a,M_0,R,\Phi) .\end{aligned} \tag{3.1.13}$$

We find a formula comparable with the well known type-I seesaw result. The mass scale of the right-handed neutrino is substituted by the inverse of the radius of the extra dimension R^{-1} and the Dirac mass contribution is given by $\left(A^l\right)^2$. Additionally, we find a factor of the form of the extra dimension f. As pointed out before, the A^l are suppressed by a volume factor emerging from the reduced wave function overlap. Therefore, we expect smaller mass scales R^{-1} compared to the typical type-I seesaw scales given a non-divergent f. In this sense, the extra dimensional seesaw mechanism provides a natural realization of a low scale type-I seesaw.
To accommodate for the observed two neutrino mass differences, we allow for small changes in the phases Φ^l, which we parametrize with

$$\Phi^e = \Phi \qquad \Phi^\mu = \Phi + \delta\Phi \qquad \Phi^\tau = \Phi + r\delta\Phi . \tag{3.1.14}$$

Expanding the masses in $\delta\phi$, we find the following leading order result for the three lightest eigenvalues of $\mathcal{M}$

$$\lambda_1 = 0 , \tag{3.1.15}$$

$$\lambda_2 = -\frac{\pi R Y^2}{4}\frac{w(c_\mu,c_\tau,r)}{s(c_\mu,c_\tau)\,f(a,M_0,R,\Phi)}\delta\Phi^2 , \tag{3.1.16}$$

$$\lambda_3 = \pi R Y^2 s(c_\mu,c_\tau)\,f(a,M_0,R,\Phi) , \tag{3.1.17}$$

with

$$s(c_\mu,c_\tau) = 1 + c_\mu^2 + c_\tau^2 , \tag{3.1.18}$$

$$w(c_\mu,c_\tau,r) = c_\mu^2 + c_\tau^2 r^2 + c_\mu^2 c_\tau^2 (r-1)^2 , \tag{3.1.19}$$

and we define $A^F = c_F Y$, with $c_e = 1$.
To conclude our discussion about the neutrino mass, we comment on current collider

bounds on large extra dimensions [86]. The ATLAS collaboration found an lower bound on the fundamental scale of gravity M_F of $\frac{M_F}{\text{TeV}} \geq (5.25, 4.11, 3.57, 3.27, 3.06)$ for $n = (2, 3, 4, 5, 6)$ extra dimensions. These limits can be translated into upper bounds on the radius. The limits are compatible with the observed neutrino masses within the presented framework. The correct neutrino mass scale can be achieved by either choosing a small R (corresponding to a larger M_F) or a small $\delta\phi$ since $\lambda_2\lambda_3 \sim \pi R Y^2 \delta\phi^2$, while the correct ratio for the eigenvalues can be accommodated for by choosing a suitable $f(a, M_0, R, \Phi)$ since $\frac{\lambda_2}{\lambda_3} \sim \left(\frac{\delta\phi}{f(a,M_0,R,\Phi)}\right)^2$.
Next we discuss the constraints imposed by the observed neutrino mixing parameters (see Table 3.1) [87]. In total we find six distinct orderings of the mass eigenvalues λ_i, two

Param.	NO Best Fit	NO 3σ	IO Best Fit	IO 3σ
$\sin^2(\Theta_{12})$	0.304	$0.270 \to 0.344$	0.304	$0.270 \to 0.344$
$\sin^2(\Theta_{23})$	0.452	$0.382 \to 0.643$	0.579	$0.389 \to 0.644$
$\sin^2(\Theta_{13})$	0.0218	$0.0186 \to 0.0250$	0.0219	$0.0188 \to 0.0251$
$\Delta m^2_{21}/10^{-5}\,\text{eV}^2$	7.50	$7.02 \to 8.09$	7.50	$7.02 \to 8.09$
$\Delta m^2_{31}/10^{-3}\,\text{eV}^2$	2.457	$2.317 \to 2.607$	-2.449	$-2.590 \to -2.307$

Table 3.1.: Three-flavor oscillation parameters from [87]

corresponding to a normal ordering while the other two generate an inverse ordering. The two remaining cases are already excluded since it is $\lambda_1 = 0$ and $m_2^2 > m_1^2$ has to be satisfied. The four viable cases are:

- Case I: $m_1 = |\lambda_1| < m_2 = |\lambda_2| < m_3 = |\lambda_3|$ (NO)
- Case II: $m_1 = |\lambda_1| < m_2 = |\lambda_3| < m_3 = |\lambda_2|$ (NO)
- Case III: $m_1 = |\lambda_2| < m_2 = |\lambda_3| > m_3 = |\lambda_1|$ (IO)
- Case IV: $m_1 = |\lambda_3| < m_2 = |\lambda_2| > m_3 = |\lambda_1|$ (IO)

For each of them we have to compare the resulting prediction for the mixing matrix with the observed values to extract the viable parameter space. Remarkably, the mixing matrix in leading order in $\delta\Phi$ is only dependent on three (complex) parameters c_μ, c_τ and r. In this work, we considered only the case of a vanishing CP phase δ and therefore real Yukawa couplings. In the light of the hint for a non-vanishing $\delta \approx -\frac{\pi}{2}$, it might be interesting to investigate the influence of a non-zero CP phase on the parameter space of the model and therefore on the lepton flavor violating (LFV) observables discussed in Section 3.2. For the case of a vanishing CP phase, the 3σ ranges for the parameters relevant to the mixing matrix are given in Table 3.2.

3.2. Lepton Flavor Violation

In the previous section, we gave an approximated unitary mixing matrix for the SM neutrinos. However, including the additional degrees of freedoms in form of the Kaluza-Klein excitations, the 3×3 submatrix identified with the PMNS matrix is not unitary anymore. As it was pointed out in Section 2.2, the unitarity violation of the PMNS matrix causes several phenomenological implications, such as deviations of electroweak

Case	c_μ^2 BF	c_μ^2 3σ	c_τ^2 BF	c_τ^2 3σ	r BF	r 3σ
I	20.3	$14.9 \to 33.9$	24.6	$13.9 \to 32.6$	1.6	$1.45 \to 1.80$
I	20.3	$14.9 \to 33.9$	24.6	$13.9 \to 32.6$	0.64	$0.55 \to 0.69$
II	0.59	$0.31 \to 0.74$	1.78	$1.52 \to 2.28$	-0.12	$-0.14 \to -0.04$
II	0.46	$0.16 \to 0.62$	1.91	$1.64 \to 2.48$	-0.48	$-0.59 \to -0.20$
II	1.08	$0.41 \to 1.33$	1.29	$1.10 \to 2.09$	-1.62	$-1.84 \to -0.52$
II	1.63	$0.86 \to 1.97$	0.73	$0.61 \to 1.51$	-1.17	$-1.18 \to -0.41$
III	1.22	$0.89 \to 1.97$	1.14	$0.55 \to 1.62$	1.22	$1.18 \to 1.28$
III	1.22	$0.89 \to 1.97$	1.14	$0.55 \to 1.62$	0.82	$0.78 \to 0.85$
IV	0.30	$0.23 \to 0.45$	0.17	$0.07 \to 0.25$	1.56	$1.45 \to 1.80$
IV	0.30	$0.23 \to 0.45$	0.17	$0.07 \to 0.25$	0.62	$0.45 \to 0.68$

Table 3.2.: Allowed Parameter regions which reproduce the observed neutrino mixing for the different possible orderings of the mass eigenvalues. The first two cases correspond to the NO and the last two to the IO. The values are obtained by using the best fit values for the mixing angles and the 3σ regions, respectively.

precision variables or the presence of rare LFV decays. In this section, we discuss the implications for the latter in detail and point out the predictions of the model for the correlations between different rare decays. Eventually, we give a lower bound on the fundamental scale of gravity induced by the upper bounds on rare lepton decays in case of 5D Yukawa couplings of $\mathcal{O}(1)$.
The deviation of unitarity is given by (for a detailed calculation see appendix B):

$$\begin{aligned}(\mathcal{E})_{F_1F_2} &= -\left(Y^T\mathcal{M}_{\mathrm{KK}}^{-2}Y\right)_{F_1F_2} = -\sum_{k=-\infty}^{\infty}\frac{m_k^{F_1}m_k^{F_2}}{\left(M_0+\frac{k}{R}\right)^2}\\ &=: -S_2(F_1,F_2) = \frac{d}{dM_0}S_1(F_1,F_2,0)\,.\end{aligned} \tag{3.2.1}$$

The decay width of rare lepton decays $l_\alpha \to l_\beta\gamma$, mediated at one-loop level, strongly depends on the unitarity violation. Furthermore, the ratio of its decay width to the decay width of $l_\alpha \to \nu_\alpha\bar{\nu}_\beta l_\beta$ is given by [45, 46]:

$$\frac{\Gamma(l_\alpha \to l_\beta\gamma)}{\Gamma(l_\alpha \to l_\beta\bar{\nu}_\beta\nu_\alpha)} = \frac{3\alpha}{32\pi}\frac{|\sum_{k=1}^{\infty}U_{\alpha k}U_{k\beta}^\dagger F(x_k)|^2}{(UU^\dagger)_{\alpha\alpha}(UU^\dagger)_{\beta\beta}}. \tag{3.2.2}$$

The matrix U is the mixing matrix as defined in Section 2.1.1. In the sum over k, $k = 1,2,3$ correspond to the mass eigenvalues of the active neutrinos. The ones corresponding to $k > 3$ are the ones close to the masses of the KK excitations. The function $F(x_k)$ is a loop function with $x_k = \frac{m_{\nu_k}^2}{m_W^2}$, where m_{ν_k} is the mass of the k-th neutrino mass eigenstate and $F(x_k)$ is given by:

$$F(x) = \frac{10-43x+78x^2-49x^3+4x^4+18x^3\ln(x)}{3(x-1)^4}\,. \tag{3.2.3}$$

If the sum $\sum_{k=1}^{\infty} U_{\alpha k} U_{k\beta}^{\dagger} F(x_k)$ is split into $\sum_{k=1}^{3} U_{\alpha k} U_{k\beta}^{\dagger} F(x_k) + \sum_{k=4}^{\infty} U_{\alpha k} U_{k\beta}^{\dagger} F(x_k)$, it is reasonable to assume $F(x_k) \approx \frac{10}{3}$ for $k = 1, 2, 3$, since $m_{\nu_k} \ll m_W$. Thus, we find

$$\sum_{k=1}^{3} U_{\alpha k} U_{k\beta}^{\dagger} F(x_k) \approx \frac{10}{3} \left(U_P U_P^T\right)_{\alpha\beta} \approx \frac{10}{3} (\mathcal{E})_{\alpha\beta} \,. \tag{3.2.4}$$

Since the complete mixing matrix is unitary, $\sum_{k=4}^{\infty} U_{\alpha k} U_{k\beta}^{\dagger} = -(\mathcal{E})_{\alpha\beta}$ holds for $\alpha \neq \beta$. Assuming $m_W \ll M_0$ and using the fact that $F(x)$ decreases monotonously, allows to find an upper bound on the branching ratio by setting $F(x_k) = \frac{4}{3}$ for $k \geq 4$:

$$\frac{\Gamma(l_\alpha \to l_\beta \gamma)}{\Gamma(l_\alpha \to l_\beta \bar{\nu}_\beta \nu_\alpha)} \approx \frac{3\alpha}{32\pi} \left| \sum_{k=1}^{3} U_{\alpha k} U_{k\beta}^{\dagger} F(x_k) + \sum_{k=4}^{\infty} U_{\alpha k} U_{k\beta}^{\dagger} F(x_k) \right|^2 \leq \frac{3\alpha}{8\pi} (\mathcal{E})_{\alpha\beta}^2 \,. \tag{3.2.5}$$

Next, we derive lower bounds on the decay rate for $M_0 \approx m_W$ and $M_0 \ll m_W$. To this end we assume $F(x_k) = F\left(\frac{M_0^2}{m_W^2}\right)$ for $k \geq 4$. This is justified since the loop function $F\left(\frac{m_i^2}{m_W^2}\right)$ is decreasing with an increasing m_i. Thus, by choosing $m_i = M_0$, which is the lowest KK mass, for all $i \geq 4$, a lower bound on the decay rate is obtained. We discuss the following cases:

- $M_0 \approx m_W$
  With $F(1) = \frac{17}{6}$, the lower bound results in:

  $$\frac{\Gamma(l_\alpha \to l_\beta \gamma)}{\Gamma(l_\alpha \to l_\beta \bar{\nu}_\beta \nu_\alpha)} \geq \frac{3\alpha}{128\pi} (\mathcal{E})_{\alpha\beta}^2 \tag{3.2.6}$$

  In comparison with the upper bound, a factor $\frac{1}{16}$ is multiplied to the upper bound.

- $M_0 \ll m_W$
  A series expansion for small arguments of $F(x_k)$ up to first order yields $F\left(\frac{M_0^2}{m_W^2}\right) \approx \frac{10}{3} - \frac{M_0^2}{m_W^2}$. Thus, the lower bound results in:

  $$\frac{\Gamma(l_\alpha \to l_\beta \gamma)}{\Gamma(l_\alpha \to l_\beta \bar{\nu}_\beta \nu_\alpha)} \geq \frac{3\alpha}{32\pi} \frac{M_0^2}{m_W^2} (\mathcal{E})_{\alpha\beta}^2 \,. \tag{3.2.7}$$

  In this case, the lower bound is additionally suppressed by the small factor $\frac{M_0^2}{m_W^2}$.

Using the experimental values for the branching ratios of the processes $l_\alpha \to l_\beta \bar{\nu}_\beta \nu_\beta$, see e.g. [88], we find an expression for the branching ratios of the three LFV decays:

$$\mathcal{B}_{\mu e} \leq \frac{3\alpha}{8\pi} (\mathcal{E})_{\mu e}^2 \,, \qquad \mathcal{B}_{\tau e} \leq \frac{1}{5.6} \frac{3\alpha}{8\pi} (\mathcal{E})_{\tau e}^2 \quad \text{and} \quad \mathcal{B}_{\tau \mu} \leq \frac{1}{5.9} \frac{3\alpha}{8\pi} (\mathcal{E})_{\tau \mu}^2 \,. \tag{3.2.8}$$

In the limit of a small $\delta\Phi$, $\mathcal{E}_{\alpha\beta}$ is given in leading order in $\delta\Phi$ by:

$$\frac{\mathcal{E}_{\alpha\beta}}{c_\alpha c_\beta} = \frac{(\pi R Y)^2}{2\sin(y)^2} \left[1 - (q-1)\cos(2yq - 2\Phi) + q\cos(2[y - qy + \Phi])\right] \tag{3.2.9}$$

$$= (\pi R Y)^2 h(q, y, \Phi) \,, \tag{3.2.10}$$

Case	$\frac{\mathcal{B}_{\tau\mu}}{\mathcal{B}_{\mu e}}$ analytic	3σ	$\frac{\mathcal{B}_{\tau e}}{\mathcal{B}_{\mu e}}$ analytic	3σ
I	$\frac{\cot(\Theta_{13})^2\cos(\Theta_{23})^2}{5.9}$	$[2.36, 5.53]$	$\frac{\cot(\Theta_{23})^2}{5.6}$	$[0.10, 0.29]$
II	No analytic expression	$[0.10, 0.42]$	No analytic expression	$[0.06, 2.77]$
III	$\frac{\cos(\Theta_{23})^2[\sin(\Theta_{13})\tan(\Theta_{13})-\tan(\Theta_{23})]}{5.9\cos(\Theta_{13})^2\tan(\Theta_{12})^2}$	$[0.09, 0.27]$	$\frac{1}{5.6}\left(\frac{\tan(\Theta_{23})-\sin(\Theta_{13})\tan(\Theta_{12})}{1+\sin(\Theta_{13})\tan(\Theta_{12})\tan(\Theta_{23})}\right)^2$	$[0.07, 0.23]$
IV	$\frac{\cos(\Theta_{23})^2[\sin(\Theta_{13})-\tan(\Theta_{12})\tan(\Theta_{23})]^2}{5.9\cos(\Theta_{13})^2}$	$[0.01, 0.04]$	$\frac{1}{5.6}\left(\frac{\sin(\Theta_{13})-\tan(\Theta_{12})\tan(\Theta_{23})}{\tan(\Theta_{12})+\sin(\Theta_{13})\tan(\Theta_{23})}\right)^2$	$[0.03, 0.15]$

Table 3.3.: Analytic expressions (LO in $\delta\Phi$) for the ratios of the branching ratios of the rare lepton decays in terms of the mixing angles and their 3σ regions for the different cases. Case I and II correspond to NO and Case III and IV to IO.

where $q = \frac{a}{\pi R}$ and $y = \pi M_0 R$. Remarkably, the only dependence on the flavor is given by the factors c_α, c_β. Thus, the ratio of two different branching ratios of rare lepton decays is to leading order in $\delta\Phi$ given by $\frac{\mathcal{B}_{\alpha\beta}}{\mathcal{B}_{\gamma\delta}} = \frac{c_\alpha^2 c_\beta^2}{c_\gamma^2 c_\delta^2}$.
Note that the ratios of the LFV decays in leading order $\delta\phi$ are independent of any simplifications of the loop function, for instance $F(x_k) = F\left(\frac{M_0^2}{m_W^2}\right)$ for $k \geq 4$. This is the case since $U_{\alpha k}U_{k\beta}^\dagger \sim c_\alpha c_\beta + \mathcal{O}(\delta\phi)$ holds. Consequently, the only flavor dependent terms, the factors $c_\alpha c_\beta$, can be pulled out of the sum in Eq. (3.2.2) and therefore the ratios of the decay rates in leading order $\delta\phi$ are independent of the approximations adopted in the loop functions. The results for all four cases for the ratios $\frac{\mathcal{B}_{\tau\mu}}{\mathcal{B}_{\mu e}} = \frac{c_\tau^2}{5.9}$ and $\frac{\mathcal{B}_{\tau e}}{\mathcal{B}_{\mu e}} = \frac{c_\tau^2}{5.6 c_\mu^2}$ are presented in Table 3.3. This implies that all of the LFV rare lepton decay branching ratios can be expected within two orders of magnitude and that their ratios are directly related to the mixing angles and the mass ordering in the neutrino sector.

However, for a scenario generating branching ratios close to the experimental limits, a certain configuration of phases is mandatory, as the branching ratio is suppressed by the ratio of the neutrino mass to the mass of the W. As we elaborated on above, the branching ratio is highly dependent on the mass of the lightest KK excitation M_0. A numerical analysis shows that the branching ratio is maximized for $M_0 \sim m_W$ and results in

$$\mathcal{B}_{\mu e} \approx \frac{3\alpha}{128\pi}\frac{c_\mu^2}{s(c_\mu, c_\tau)^2}\left(\frac{m_\nu}{m_W}\right)^2 y^2 \frac{h(q,y,\Phi)^2}{f(q,y,\Phi)^2} \approx 2\times 10^{-31} y^2 \frac{h(q,y,\Phi)^2}{f(q,y,\Phi)^2}\,. \tag{3.2.11}$$

In the last step, we adopted the best fit values for scenario I for c_μ and c_τ (see Table 3.2). Thus, an observation of a rare lepton decay requires an enhancement by the factor $\frac{h(q,y,\Phi)^2}{f(q,y,\Phi)^2}$, which can be realized for three different special cases, which are displayed in table 3.4. Since the factor diverges for these three configurations of the parameters q, y and Φ, a small deviation ϵ from these configurations is needed concerning a large $\mathcal{B}_{\mu e}$. The dependence on ϵ is shown in table 3.4. Additionally, the influence of these configurations on the value for the phase shift $\delta\Phi$ is presented, which is required to be small to reproduce the observed neutrino masses. The ϵ dependence of the phase shift can be estimated by the ratio of the non-vanishing eigenvalues λ_2 (3.1.16) and λ_3 (3.1.17), which has to be ~ 1 for the IO and ~ 5 or ~ 0.2 for the NO, respectively.
To conclude, the extra dimensional setup allows for $\mathcal{B}_{\mu e}$ close to experimental limits if the phases of the Yukawa couplings are close to $\Phi^F \approx \frac{2n+1}{2}\pi + qy$ or $\Phi = \frac{2n+1}{2}\pi + qy - y$.

Configuration	$h^2 f^{-2}$	$\delta\Phi$
$y = 0$	ϵ^{-2}	$\cos(\Phi)^2 \epsilon^{-1}$
$\Phi = \frac{2n+1}{2}\pi + qy$	$q^2\epsilon^{-2}$	ϵ
$\Phi = \frac{2n+1}{2}\pi + qy - y$	$(q-1)^2 \epsilon^{-2}$	ϵ

Table 3.4.: Dependence of $h^2 f^{-2}$ and $\delta\Phi$ on the deviation ϵ of the presented configurations. Since $h^2 f^{-2}$ is always $\sim \epsilon^{-2}$, $\epsilon \approx 10^{-7}$ is required to generate $\mathcal{B}_{\mu e} \approx 10^{-13} - 10^{-14}$. Consequently, this would lead to a large $\delta\Phi$ for the first case, which is not desirable since $\delta\Phi \ll 1$ was assumed before. The remaining two cases have $\delta\Phi \sim \epsilon$, thus leading to a very small $\delta\Phi$ for a large $\mathcal{B}_{\mu e}$. The ϵ dependence of $\delta\Phi$ is calculated by taking the ratio of λ_2 and λ_3, leading to $\delta\Phi \sim f$.

n	2	6	10	20	50
Lower Limit on M_F	1.5 EeV	3.4 PeV	660 TeV	166 TeV	68 TeV
Lower Limit on R^{-1}	5.6 GeV	2.4 TeV	12.7 TeV	50.3 TeV	123 TeV

Table 3.5.: Lower Limits for the fundamental scale of gravity M_F for different number of extra dimensions n.

Furthermore, it predicts a correlation between different decay channels depending on the present mass hierarchy in the neutrino sector and its mixing angles.

If we furthermore assume 5D Yukawa couplings of $h_i^l \sim 1$, we can use the tight constraints on the branching ratio for the decay $\mu \to e\gamma$ to constrain the fundamental scale of gravity M_F for a given number of extra dimensions. In the case of $M_0 \gg m_W$, using $M_P = (2\pi M_F R)^{\frac{n}{2}} M_F$ and the expression for the neutrino mass scale given in Eq. (3.1.16), we find

$$M_F = \left(\sqrt{\frac{3\alpha c_\mu^2}{512\pi \mathcal{B}_{\mu e}}} v^2 M_P^{\frac{2}{n}} \right)^{\frac{n}{2(n+1)}} \geq \left(1.33 \times 10^9 \,\mathrm{GeV}^2 M_P^{\frac{2}{n}} \right)^{\frac{n}{2(n+1)}} . \tag{3.2.12}$$

For some values of n, the lower limit of M_F is presented in table 3.5. For a small number of extra dimensions the fundamental scale of gravity is constrained more severely than by the LHC limits provided by the ATLAS collaboration [86], given the case of 5D Yukawa couplings of $\mathcal{O}(1)$. Note, however, that the limit can easily be relaxed by allowing for smaller 5D Yukawa couplings h, as the lower bound is proportional to $h^{1+\frac{1}{n}}$. For example, the ATLAS limit of 5.25 TeV for $n = 2$ becomes more constraining as soon as the 5D Yukawa couplings are below $h \lesssim 10^{-5}$.

3.3. Conclusion

In this work, we have studied an extra dimensional seesaw mechanism with a single right-handed bulk neutrino. The SM particles are confined to a four dimensional brane. Shifting the brane away from the orbifold fixed points allows to generate two non-vanishing mass-squared differences as required by neutrino oscillation experiments.

In particular, we have worked out the flavor structure without adopting a unitary approximation of the 3×3 submatrix. This allows us to study the phenomenological consequences of the bulk neutrino.

In a first step, we studied the neutrino mass generation and mixing. We further simplified the analysis by assuming CP conversation and that the ratios of the Yukawa

coupling of the Z_2 even component and Z_2 odd component of the right-handed neutrino to the SM neutrinos $\frac{h_2^l}{h_1^l}$ are almost the same for all three generations, resulting in nearly degenerated phases Φ^l in the Dirac-masses between the KK states and the left-handed neutrinos of the SM. The allowed parameter space is presented in table 3.2.
It is pointed out that the model is capable of generating $\mathcal{B}_{\mu e}$ close to the experimental bounds. As discussed in section 3.2, the contribution to $l_i \to l_j\gamma$ is maximized if the lightest KK excitation has roughly the W-Boson mass. Due to the suppression of the Yukawa coupling by the extra dimension it is still possible to generate the observed neutrino mass with a Yukawa coupling of order one in this case. However, this effect is not strong enough to produce $\mathcal{B}_{\mu e}$ close to 10^{-13}. Therefore, some fine tuning of the brane shift, the ratio of the lowest KK mass to R^{-1} and $\frac{h_2^l}{h_1^l}$ is necessary. Note that this behavior is not an exclusive feature of the brane shifted model and is also possible without a brane shift. In this case, M_0 close to $\frac{1}{2}R^{-1}$ is required to generate a sizable $\mathcal{B}_{\mu e}$. However, the brane shift is mandatory to generate two neutrino mass squared differences.
A strong prediction of the model within the approximations mentioned above are the ratios of flavor violating charged lepton decay branching ratios which are correlated with the neutrino mixing angles and the neutrino mass hierarchy. Thus, the model could be tested by the next generation of experiments looking for charged LFV. Furthermore, it could allow for a distinction of the neutrino mass hierarchies by the measurement of lepton flavor violating processes.
In the following chapter, we will discuss a class of DM models built around additional right-handed SM singlet neutrinos as the mediators to DM. In the first study, we focus on models that are only feebly coupled to the SM. The work presented in this chapter provides a natural realization of a feebly coupled model, as already the coupling of the bulk neutrino to the SM is suppressed as soon the lightest KK excitation has a mass below the Planck scale. The coupling of DM to the bulk neutrino could easily be suppressed in the same manner if the DM candidate itself is confined to a lower dimensional subspace.

4. The Neutrino Portal to Dark Matter

In the Sections 2.3 and 2.4, we gave an overview of the DM production and phenomenology of models involving a portal to DM. Such a scenario typically arises if the DM candidate is a SM singlet and therefore does not interact with the SM via gauge interactions. This, in turn, necessitates an additional particle to mediate the interactions between DM and the SM. If we are about to construct renormalizable operators including a non-SM field that can couple to singlet DM, we are left with three possible choices:

1. *Higgs Portal*
   The Higgs portal arises if an additional scalar η is introduced. This allows for the quartic scalar interaction $\lambda_3 \left(\eta^\dagger \eta\right) \left(\phi^\dagger \phi\right)$, where ϕ is the SM Higgs doublet. In its simplest realization η itself can contain the DM candidate. In more elaborated Higgs portal models η can couple to a larger dark sector, a topic that is extensively covered in the literature [89].

2. *Vector Portal*
   If an additional $U(1)$ gauge group is added to the model, it introduces an additional vector boson, which can mix with the gauge boson of the $U(1)_Y$ of the SM via $\epsilon B^{\mu\nu} V_{\mu\nu}$. Here, $V_{\mu\nu}$ and $B_{\mu\nu}$ refer to the field strength tensor of the new and the SM $U(1)$ respectively. If DM is charged under the new $U(1)$ gauge group, the mixing induces a electric charge for the DM candidate, which is tightly constrained by the experiment. Therefore, the mixing between the two gauge bosons must be small, motivating the term *milicharged* DM. An analysis of a vector portal with fermionic milicharged DM can be found in [49, 50].

3. *Neutrino Portal*
   If a SM singlet fermion N is added to the SM, it can couple to the SM neutrinos and the Higgs via a Yukawa coupling $y_\nu \bar{N} \tilde{\phi} \nu_L$. In addition to the potential coupling to a DM candidate this term generates masses for the SM neutrinos after EWSB.

This chapter is dedicated to the analysis of the neutrino portal to dark matter (NPDM). It is based on the publication [2] and the forthcoming publication [4]. We start our discussion by introducing the model and its particle content and give an overview over the different interactions that can arise. Subsequently, in Section 4.2, we give a detailed analysis of the feebly coupled regime of the NPDM and determine the parameter space in agreement with the DM energy density measurement of the Planck satellite and the phenomenological consequences of the model. In Section 4.3, we enlarge the analysis to already existing strongly coupled freeze-out solutions of the NPDM and test their robustness against certain consistency conditions, such as the stability of the scalar vacuum and perturbativity at high scales.

4.1. The Model

The NPDM arises if an additional singlet fermion is added to the particle content of the SM. Already at this stage a potential DM candidate is introduced to the model. After EWSB, the new fermion mixes with the SM neutrinos. If the resulting heavy neutrino N' fulfills $M_{N'} < 2m_e$, it can be cosmological stable, as the decay $N' \to \nu\gamma$ only arises at one-loop level and is suppressed by the small mixing angle resulting from the tiny Yukawa coupling. This scenario is typically referred to as sterile neutrino DM. The simplest realization of sterile neutrino dark matter involving direct production via the feeble coupling (or equivalently the small mixing angle) is already excluded due to a combination of the Lyman-α measurement and indirect detection experiments, looking for the decay products of the decay $N' \to \nu\gamma$ in γ-rays from the galactic center. However, there exist more elaborated production mechanisms, for instance via the decay of an additional heavy scalar particle as discussed in [53, 90]. Sterile neutrino DM is subject to an ongoing discussion and a review on this topic can be found in [91].
In this work, however, we take a different approach. We assume that the heavy neutrino is not the DM candidate itself, as for instance in the case of $M_{N'} > 2m_e$. In this case, due to its singlet nature, the additional fermion is perfectly suited to couple to a dark sector. In the following, we consider a dark sector consisting of a fermion χ and a scalar η. Both are singlets under the SM gauge groups but must be charged under a global or local symmetry to guarantee the stability of the DM candidate. Here, we consider a global symmetry, in turn implying the absence of any vector portal contribution and thereby allowing for a more clear picture of the effects of the neutrino portal itself. To this end, we additionally assume in Section 4.2 that the Higgs portal coupling $\lambda_3 \left(\eta^\dagger\eta\right)\left(\phi^\dagger\phi\right)$ only has subleading effects compared to the neutrino portal. The implied limits on the Higgs portal coupling are specified later on and we assume $\lambda_3 = 0$ during the first part of the discussion. Note that we do not employ this assumption during the analysis of the consistency conditions within Section 4.3.
The singlet fermion N couples to the dark sector via a Yukawa coupling $y_\chi \bar{\chi}\eta N$ and due to the stabilizing symmetry, the lightest particle of the dark sector constitutes the DM candidate. Due to the mixing of the new fermion state with the SM neutrinos, the neutrino portal allows for neutrino mass generation. In the following, we consider the type-I seesaw, as it requires the smallest number of additional particles, more precisely two right-handed singlet fermions $(N)_i$. However, in analogy to the three generation present in the SM, we consider the presence of three right-handed fermions $(N)_i$. For the moment, we specify on the type-I seesaw NPDM[1] with the Lagrangian

$$\begin{aligned}\mathcal{L} = \mathcal{L}_{\text{SM}} &+ (Y_\nu)_{ij}\,\overline{N}_i\tilde{\phi}^\dagger L_j + (Y_\chi)_{ij}\,\overline{N}_i\eta\,\chi_{Lj} \\ &- \frac{1}{2}(M_N)_{ij}\,\overline{N}_i N_j^{\mathcal{C}} - (M_\chi)_{ij}\,\overline{\chi}_{Ri}\,\chi_{Lj} + \text{h.c.} - V\,,\end{aligned} \tag{4.1.1}$$

and with the potential

$$V = m_H^2\,\phi^\dagger\phi + m_\eta^2\,\eta^\dagger\eta + \frac{\lambda_1}{2}\,(\phi^\dagger\phi)^2 + \frac{\lambda_2}{2}\,(\eta^\dagger\eta)^2 + \lambda_3\,(\phi^\dagger\phi)(\eta^\dagger\eta)\,. \tag{4.1.2}$$

[1] For the consistency conditions discussed in Section 4.3.2, we additionally consider a simplified one generation version of the inverse seesaw mechanism, involving one Dirac fermion N

After EWSB the active neutrino masses are generated via the type-I seesaw, as discussed in Section 2.1.1. To ensure that the observed neutrino masses and mixing angles are reproduced we utilize the following parametrization of the Yukawa coupling matrix Y_ν [92]:

$$Y_\nu = \frac{\sqrt{M_N}}{v} R \sqrt{m_\nu} U_{\text{PMNS}}^\dagger = \underbrace{\frac{\sqrt{M_N \Delta m_\nu}}{v}}_{\equiv y_\nu} R \underbrace{\frac{1}{\sqrt{\Delta m_\nu}} \sqrt{m_\nu}}_{\equiv R'} U_{\text{PMNS}}^\dagger \,, \tag{4.1.3}$$

where we assumed the Majorana mass matrix M_N to be diagonal with degenerated eigenvalues, that is $M_N = \text{diag}\,(M_N, M_N, M_N)$. Here, U_{PMNS} is the PMNS matrix, v is the vev of the Higgs field, $\sqrt{m_\nu}$ is a diagonal matrix with the square root of the neutrino masses as eigenvalues, R is an orthogonal complex 3×3 matrix and Δm_ν is the square root of the large mass squared difference $\Delta m_\nu = \sqrt{\Delta m_\nu^2}$. Note that after EWSB, the singlet fermion N is not a mass eigenstate anymore. The resulting neutrino mass eigenstates, ν and N' are given by

$$\begin{pmatrix} \nu_L \\ N \end{pmatrix} = U \begin{pmatrix} \nu \\ N' \end{pmatrix} \approx \begin{pmatrix} U_{\text{PMNS}} & Y_\nu^T v M_N^{-1} \\ -Y_\nu U_{\text{PMNS}}\, v M_N^{-1} & 1 \end{pmatrix} \begin{pmatrix} \nu \\ N' \end{pmatrix} , \tag{4.1.4}$$

and the masses of the heavy states are in leading order given by M_N. For the sake of a simpler notation, we refer to the heavy mass eigenstate N' as N in the following.
The mixing between the left and right-handed neutrinos causes an interaction between ν, N and the Higgs as well as a coupling of N to the $SU(2)_L$ gauge bosons. As presented in [29], the resulting interactions between the heavy and the light neutrinos are given by:

$$\mathcal{L}_W \supset -\frac{g_W}{2\sqrt{2}} l_i W_\mu^- \gamma^\mu \left(1 - \gamma_5\right) B_{l_i N_j} N_j + h.c. \,, \tag{4.1.5}$$

$$\begin{aligned} \mathcal{L}_Z \supset & -\frac{g_W}{4\cos\left(\Theta_W\right)} Z_\mu^0 \left\{ \bar{\nu_i} \gamma^\mu \left[i \text{Im}\left(C_{\nu_i N_j}\right) - \gamma_5 \text{Re}\left(C_{\nu_i N_j}\right) \right] N_j \right. \\ & \left. \bar{N_i} \gamma^\mu \left[i \text{Im}\left(C_{N_i N_j}\right) - \gamma_5 \text{Re}\left(C_{N_i N_j}\right) \right] N_j + h.c. \right\} , \end{aligned} \tag{4.1.6}$$

$$\begin{aligned} \mathcal{L}_H \supset & -\frac{g_W}{4 M_W} h \left\{ 2\bar{\nu_i} \left[\left(m_{\nu_i} + M_{N_j}\right) \text{Re}\left(C_{\nu_i N_j}\right) + i\gamma_5 \left(M_{N_j} - m_{\nu_j}\right) \text{Im}\left(C_{\nu_i N_j}\right) \right] N_j \right. \\ & \left. + \bar{N_i} \left(M_{N_i} + M_{N_j}\right) \text{Re}\left(C_{N_i N_j}\right) N_j \right\} . \end{aligned} \tag{4.1.7}$$

The matrices B and C are defined as in [29]. In case of real Yukawa couplings, as we will assume no CP violation from now on, they are given by:

$$B_{l_i N_j} \approx \frac{v}{M_N} \left(Y_\nu^T\right)_{ij} , \quad C_{\nu_i N_j} \approx \frac{v}{M_N} \left(U_{\text{PMNS}}^T Y_\nu^T\right)_{ij} , \quad C_{N_i N_j} \approx \frac{v^2}{M_N^2} \left(Y_\nu Y_\nu^T\right)_{ij} . \tag{4.1.8}$$

Thus, the couplings relevant for heavy neutrino production are given by

$$\mathcal{L}_W \supset -\frac{M_W y_\nu}{\sqrt{2} M_N} \left(U_{\text{PMNS}} R'^T\right)_{ij} \bar{l}_i W_\mu^- \gamma^\mu \left(1-\gamma_5\right) N_j + h.c.\,, \tag{4.1.9}$$

$$\mathcal{L}_Z \supset \frac{M_W y_\nu}{2\cos\left(\Theta_W\right) M_N} \left(R'^T\right)_{ij} Z_\mu^0 \bar{\nu}_i \gamma^\mu \gamma_5 N_j\,, \tag{4.1.10}$$

$$\mathcal{L}_H \supset -y_\nu h \left(R'^T\right)_{ij} \bar{\nu}_i N_j - y_\nu^2 \frac{v}{M_N} h \left(R'^T R'\right)_{ij} \bar{N}_i N_j\,, \tag{4.1.11}$$

whereas the coupling of the heavy neutrino to the dark sector is governed by:

$$\mathcal{L}_\chi \supset -y_\chi \eta \bar{\chi} N_i + h.c \quad . \tag{4.1.12}$$

Note that the parameters y_ν and M_N are not independent and related by the seesaw mechanism requiring $y_\nu = \sqrt{\Delta m_\nu M_N} v^{-1}$. Therefore, the couplings in Eq.(4.1.9)-(4.1.11), excluding the flavor dependent matrices, can be rewritten as:

$$\begin{array}{ll} g_{h\nu N} = y_\nu = \frac{\sqrt{m_\nu M_N}}{v} & g_{WlN,Z\nu N} = y_\nu \frac{M_W}{M_N} = \sqrt{\frac{m_\nu}{M_N}} \frac{M_W}{v} \\ g_{hNN} = y_\nu^2 \frac{v}{M_N} = \frac{m_\nu}{v} & g_{ZNN} = g_{Z\nu N} \frac{y_\nu v}{M_N} = \frac{m_\nu}{M_N} \frac{M_W}{v} \end{array} \tag{4.1.13}$$

Thus, for $M_N \geq M_W$, the coupling $g_{h\nu N}$ can be expected to be the largest and the $h\nu N$ vertex is the most relevant one for DM production. On the other hand, for $M_N \leq M_W$, the WlN and $Z\nu N$ vertices are expected to provide the dominant contribution to the DM production processes as long as $M_N \gtrsim m_\nu$.

4.2. A feebly interacting Neutrino Portal to Dark Matter

In this section, we study the part of the parameter space of the model specified above leading to a freeze-in production of DM. Thus, we require small couplings y_ν and y_χ. In the context of the type-I seesaw, the coupling y_ν takes small values for heavy neutrino masses in the GeV and TeV ranges, as $y_\nu \sim 4 \cdot 10^{-8} \sqrt{M_N/\text{GeV}}$. On the other hand, the dark Yukawa y_χ is completely unconstrained. In the following, we determine its value by matching the freeze-in yield to the experimentally observed DM relic density. The different production channels contributing to the DM abundance are illustrated in Figure 4.1. The production channels can be classified into two categories: *SM Particle Scattering* and *Heavy Neutrino Scattering*. The SM particle scattering processes involve two SM particles in the initial state, have χ and η in the final state and are mediated by the heavy neutrino. As a consequence, the cross section scales as $\sigma \sim y_\nu^2 y_\chi^2$.
The heavy neutrino scattering processes involve two heavy neutrinos in the initial state and produce a pair of χ or η. Hence the cross section only depends on the dark Yukawa, $\sigma \sim y_\chi^4$.
As a first approach, we derive analytic one generation results for the relic density in different limiting cases before solving the Boltzmann equation numerically in a realistic three generation scenario. Note that the one generation results can be easily translated to the three generations setup due to the assumption of degenerated heavy neutrino masses $M_{N_i} = M_N$ and the universal coupling of the singlet fermions to the dark sector. In the case of dominant SM particle scattering process $\nu_i h \to \chi\eta$ mediated by N_j, the one generation result, utilizing a neutrino Yukawa coupling of $y_\nu = \sqrt{\Delta m_\nu M_N} v^{-1}$, has

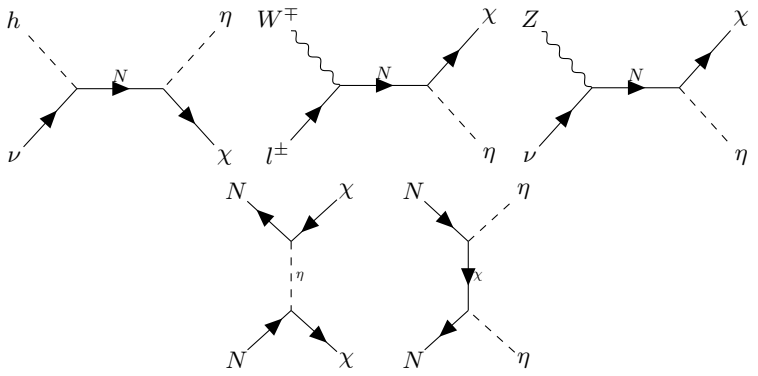

Figure 4.1.: Feynman diagrams for the DM production processes. The upper row shows processes with SM particles in the initial state, while the lower row displays DM production from heavy neutrino states.

to be multiplied by $\sum_i |\sum_j \left(R'^T\right)_{ij}|^2 = f_1(\theta)$. Here, θ is a vector containing the in our case three real angles parameterizing the orthogonal matrix R. Choosing the standard parametrization for an orthogonal three by three matrix we find $10^{-16} \lesssim f_1(\theta) \leq 3$. Note that on average we find $f_1(\theta) \sim 1$ and roughly 1 % of the θ configurations generate $f_1(\theta) < 10^{-2}$.
The $Z\nu_i N_j$-vertex has the same flavor structure as the $h\nu_i N_j$-vertex, thus the one generation result for the $Z\nu$ initial state is multiplied by the same factor as the $h\nu$ initial state.
For the Wl initial state, the factor encoding the effects of three generations of singlet fermions N_j differs and results in $f_2(\theta) = \sum_i |\sum_j \left(U_{\text{PMNS}} R'^T\right)_{ij}|^2$. Here, we find $10^{-18} \lesssim f_2(\theta) \lesssim 7.65$. A scan over various randomly chosen configurations of the angles θ for both f_1 and f_2 shows that on average $f_2 \approx 2.5 f_1$. Nevertheless, excluding the rare cases where f_1 is close to its lower bound, the contribution of the $h\nu_i$ initial state is still dominating the DM production due to the following reason: The production via the scattering of the SM gauge bosons is only viable for temperatures below the critical temperature, where the $SU(2)_L \times U(1)_Y$ symmetry of the SM is broken. At larger temperatures initial states involving the Z and W do not contribute to DM production, as the new fermionic singlet state does not mix with the SM neutrinos. Hence, the time period of DM production via those initial states is small compared to one of the Higgs neutrino scattering. Additionally, before EWSB, the Higgs contributes with four degrees of freedom to the Higgs neutrino scattering. Therefore, we only consider the production via $h\nu_i \to \chi\eta$ and the heavy neutrino scattering for the analytic estimates, while all production channels are taken into account in the numerical solution.

4.2.1. The Relic Density in the case of feeble Interactions

For the rest of the discussion of the freeze-in regime of the NPDM, we assume that the dark sector particles have roughly the same mass and thus replace $m_\eta = M_\chi$. Therefore, the relic density is given by the sum of the relic density of η and χ. If one of the particles is heavier, the relic density is still given by the sum of both quantities, as

the heavier particle will eventually decay into the lighter one, for instance via $\eta \to N\chi$, if $m_\eta > M_N + M_\chi$ or via a multi-body decays mediated by an off-shell N otherwise. Firstly, we present the resulting freeze-in yields for the SM particle scattering followed by the results from the heavy neutrino scattering. Subsequently, the implications of the results are discussed.

SM Particle Scattering
The reduced cross section for the dominant production channel is given by:

$$\hat{\sigma}_{vh\leftrightarrow\chi\eta}(s) = y_\chi^2 y_\nu^2 \frac{\left(1-\frac{m_h^2}{s}\right) s^2 \sqrt{\left(1-4\frac{M_\chi^2}{s}\right)}}{16\pi\left[\left(s-M_N^2\right)^2+\Gamma_N^2 M_N^2\right]}\,. \tag{4.2.1}$$

Here, Γ_N is the total decay width of the propagating neutrino. There are two cases to be distinguished:

- The resonant case with $M_N \geq 2M_\chi$, where $M_N^2 \geq s_{\min}$.
- The non-resonant case with $M_N < 2M_\chi$, where $M_N^2 < s_{\min}$.

First, we discuss the non-resonant case. In the case of $m_h \ll M_\chi$, we can use Eq.(2.3.41) to determine the relic density analytically. We find

$$Y_{\rm DM} = Y_\chi + Y_\eta = \frac{3^4}{2^{11}\pi^5}\frac{y_\nu^2 y_\chi^2}{\sqrt{g_{\rm eff}}g_{\rm eff}^s}\frac{M_{\rm pl}}{\sqrt[4]{\left[4M_\chi^2-M_N^2\right]^2+\Gamma_N^2 M_N^2}} \tag{4.2.2}$$

$$\overset{M_N\ll M_\chi}{=} \frac{3^4}{2^{12}\pi^5}\frac{y_\nu^2 y_\chi^2}{\sqrt{g_{\rm eff}}g_{\rm eff}^s}\frac{M_{\rm pl}}{M_\chi}\,, \tag{4.2.3}$$

where $g_{\rm eff}^{(s)}$ are the number of effective relativistic (entropy) degrees of freedom which are both assumed to be constant during this calculation with $g_{\rm eff}^{(s)} = 106.75$. This is a good approximation as long as the production is mainly efficient for temperatures above 100 GeV. Note that in the process of obtaining this result the reduced cross section was multiplied by an additional factor of four arising from the four degrees of freedom of the Higgs doublet before the electroweak phase transition.
Before we proceed with the discussion of the resonant production we want to comment on the validity of the approximation of $m_h \ll M_\chi$ taken in order to arrive at the result in Eq.(4.2.2). In principle, the z integral appearing in the derivation of Eq.(2.3.41) has to be split into two parts, namely from $z = 0$ to $z(T_c)$ with $m_h \neq 0$ and from $z(T_c)$ to $z \to \infty$ with $m_h = 0$. Here, T_c is the critical temperature where the $SU(2) \times U(1)$ symmetry is broken and the Higgs and the gauge bosons become massive. For $M_\chi > \frac{1}{2}m_h$ and $M_\chi \gg M_N$ the integration is still solvable analytically and shows that the deviation of the approximated result (4.2.3) is 6% at $M_\chi = \frac{m_h}{2}$ and goes to zero for $M_\chi \gg m_h$. Thus, the result is trustworthy as long as $M_\chi > \frac{m_h}{2}$.
Next, we discuss the resonant case, that is $M_N \geq 2M_\chi$. As it was pointed out in [93], it is useful to approximate the Breit-Wigner peak in Eq.(4.2.1) with:

$$\int_c^\infty dx\,\frac{f(x)}{(x-a)^2+b^2} \approx \frac{f(a)}{b}\,, \tag{4.2.4}$$

which is valid as long as $b \ll a$, i.e. $\Gamma_N \ll M_N$.
Then, the integration in Eq.(2.3.41) results in:

$$Y_{DM}\left(z \to \infty\right) = \frac{27}{4\pi^5 g_{\text{eff}}^s \sqrt{g_{\text{eff}}}} \frac{\left(y_\nu y_\chi\right)^2}{y_\nu^2 + y_\chi^2} \frac{M_{\text{pl}}}{M_N}\,, \tag{4.2.5}$$

where we already used $M_N \gg M_\chi$ to simplify the result.
Comparing the results given in the Eqs. (4.2.3) and (4.2.5) we find that the DM relic density scales with M_χ^{-1} in the non-resonant production regime, while in the resonant production regime we find $Y_{\text{DM}} \sim M_N^{-1}$.

Heavy Neutrino Scattering
The cross sections for heavy neutrino scattering in the case of $M_N \ll M_\chi$ result in

$$\sigma_{NN\to\chi\chi} = y_\chi^4 \frac{\sqrt{1-\frac{4M_\chi^2}{s}}}{8\pi s}\,, \tag{4.2.6}$$

$$\sigma_{NN\to\eta\eta} = \frac{y_\chi^4}{2\pi}\left[\left(1+4\frac{M_\chi^2}{s}\right)\log\left(\frac{s-2M_\chi^2-\sqrt{s^2-sM_\chi^2}}{2M_\chi^2}\right)+2\sqrt{1-4\frac{M_\chi^2}{s}}\right]\,. \tag{4.2.7}$$

By employing Eq.(2.3.41) again we find:

$$Y_{\text{DM}} = Y_\chi + Y_\eta = \frac{35\cdot 3^3 y_\chi^4}{2^{13}\pi^5 \sqrt{g_{\text{eff}}} g_{\text{eff}}^s} \frac{M_{\text{Pl}}}{M_\chi}\,. \tag{4.2.8}$$

As for the SM particle scattering in the limit of $M_N \ll M_\chi$, the DM density is inversely proportional to its mass.
In the case where the SM scattering processes are in the resonant regime we cannot find an analytic estimate for the DM relic density. In terms of masses and couplings it scales as

$$Y_{\text{DM}} \sim \frac{y_\chi^4 M_{\text{Pl}}}{\sqrt{g_{\text{eff}}} g_{\text{eff}}^s M_N}\,. \tag{4.2.9}$$

Although the factor of proportionality is unknown we expect this contribution to be much smaller compared to the contribution of the SM particle scattering. This is due to the resonance enhancement of the production via SM particle scattering. Hence, we neglect this contribution for the discussion of the analytic results.

Discussion of the Analytic Results
In the limit of $M_N \ll M_\chi \sim m_\eta$ we found analytic solutions for the DM relic density for both SM particle scattering and heavy neutrino scattering. Combining the results given in the Eqs. (4.2.3) and (4.2.5) yields:

$$Y_{DM}\left(z \to \infty\right) = \frac{3^3}{2^{13}\pi^5 g_{\text{eff}}^s \sqrt{g_{\text{eff}}}} \frac{M_{\text{Pl}}}{M_\chi} \left(6 y_\nu^2 y_\chi^2 + 35 y_\chi^4\right)\,. \tag{4.2.10}$$

This prediction has to be compared to the experimentally observed DM energy density by the PLANCK satellite, that results in

$$Y_{DM,\mathrm{exp}} = \frac{\Omega_{DM}}{\Omega_B}\frac{m_B}{m_{DM}}Y_B = (4.6 \pm 0.1)\,10^{-10}\frac{m_B}{M_\chi}\,. \tag{4.2.11}$$

The experimental data is taken from [10,94] and in the following, m_B, the average baryon mass, is taken as the mass of the proton.
Since in the non-resonant production regime the DM mass itself is the dominant mass scale, the relic density scales like M_χ^{-1}. In turn, generating the observed DM energy density is independent of the DM mass. By comparing the Eqs. (4.2.10) and (4.2.11), we find

$$\left(6y_\nu^2 y_\chi^2 + 35 y_\chi^4\right) = (3.9 \pm 0.1)\cdot 10^{-21}\,. \tag{4.2.12}$$

Since the coupling y_ν is a function of M_N only, the coupling y_χ is fixed by the heavy neutrino mass M_N. Moreover, we find $y_\chi \lesssim 10^{-5}$ in order not to overproduce DM. Note, however, that the latter statement must be relaxed if we consider the fact that the heavy neutrinos can be out of equilibrium at the time of DM production. In return, this allows for a larger y_χ. The effects of this sequential freeze-in process are investigated during the discussion of the numerical solution to the Boltzmann equations.
In principle, the couplings y_χ and y_ν are unrelated otherwise. However, both describe a coupling to the new fermionic singlet and - if the heavy neutrino is lighter than $\mathcal{O}\left(10^{15}\,\mathrm{GeV}\right)$ - both couplings are required to be relatively small. This motivates the idea that they might be suppressed by the same mechanism, resulting in $y_\nu \approx y_\chi$.[2] Considering a model that generates $y_\chi \sim y_\nu$ allows for constraining the mass of the heavy neutrino since in such a scenario Eq.(4.2.12) reads

$$41 y_\nu^4 = 41\left(\frac{m_\nu M_N}{v^2}\right)^2 = (3.9 \pm 0.1)\cdot 10^{-21}\,. \tag{4.2.13}$$

Thus, in order to generate the observed DM density (4.2.11), $M_N \sim 10\,\mathrm{TeV}$ is required. Due to the requirement of $M_N < 2m_{\mathrm{DM}}$ in the non-resonant regime we find a lower bound on the DM mass of $m_{\mathrm{DM}} \gtrsim 5\,\mathrm{TeV}$, if we naively assume the behavior for large DM masses to be also correct for parameters close to the transition of the non-resonant to the resonant regime.
We arrived at the results discussed above by assuming $n_N = n_N^{\mathrm{eq}}$, $M_\chi \gg M_N$ and by taking only the dominant process of the SM particle scattering into account. From Eq.(4.2.10), we see that in the case of $y_\chi = y_\nu$ the contribution of the heavy neutrino scattering processes accounts for roughly eighty percent of the produced DM. Thus, the result will be altered significantly if the heavy neutrinos are out of equilibrium during the time when the production of DM via heavy neutrino scattering is efficient. Also, we expect a significant change in areas of the parameter space when $M_\chi \sim M_N$. On the other hand, taking the subdominant processes into account is not expected to have a significant impact, as they are suppressed by $\frac{M_W^2}{M_N^2}$ and are only accessible after EWSB.

[2] As an example, such a mechanism could be the extra dimensional model, that we discussed in Chapter 3, where the fermionic singlet in contrast to all other particles propagates in an extra dimension. Thereby, its coupling gets suppressed by the reduced wave function overlap [1, 95]. However, a one on one correspondence with the model presented in Chapter 3 would require $R^{-1} \gg T_{\mathrm{Reheating}}$, as otherwise all Kaluza-Klein excitations needed to be considered in the calculation of the relic density.

For these reasons, we solve the Boltzmann equations numerically for various coupling structures and present the results in a later discussion.
Additionally, we found an analytic solution for the DM relic density in the limit $M_N \gg M_\chi$, where the SM particle scattering processes are in the resonant regime:

$$Y_{DM}\left(z \to \infty\right) = \frac{27}{4\pi^5 g_{\text{eff}}^s \sqrt{g_{\text{eff}}}} \frac{\left(y_\nu y_\chi\right)^2}{y_\nu^2 + y_\chi^2} \frac{M_{\text{pl}}}{M_N} \,. \tag{4.2.14}$$

In the case of $y_\chi \ll y_\nu$, the observed DM energy density is reproduced if $y_\chi \approx 10^{-12} \sqrt{\frac{M_N}{M_\chi}}$. Such a tiny coupling is necessary to remain in the freeze-in regime since the production cross section is significantly enhanced by the resonance.
However, if $y_\chi \ll y_\nu$ does not hold, the approximation of $Y_\chi \ll Y_\chi^{\text{eq}}$ which we used to derive (4.2.10) does not apply anymore. To illustrate this we inspect the case $y_\chi = y_\nu$, yielding

$$Y_{DM}\left(z \to \infty\right) \approx \frac{3^3}{2^2 \pi^5 g_{\text{eff}}^s \sqrt{g_{\text{eff}}}} \frac{m_\nu M_{\text{Pl}}}{v^2} \approx 10^{-1} \,, \tag{4.2.15}$$

for Eq.(4.2.10). Using Eq.(2.3.5), we find $Y_{DM}^{\text{eq}} \lesssim 10^{-2}$. Therefore, $Y_\chi \ll Y_\chi^{\text{eq}}$ cannot be satisfied. Hence, the freeze-in scenario does not apply here. Nevertheless, it is still possible to account for the correct amount of DM. In this configuration, we recover a freeze-out like scenario. Due to the resonance enhancement of the interaction even small couplings suffice to equilibrate DM with the SM for temperatures where the resonance is accessible. Thus, DM comes into equilibrium with the SM at large T and freezes out as soon as the interaction becomes inefficient. This occurs approximately at $T = M_N$.[3] Consequently, the number density can be estimated by the equilibrium density at the freeze-out temperature

$$Y_{\text{DM}}\left(z \to \infty\right) = Y_\chi^{\text{eq}}\left(T \approx M_N\right) \overset{M_N \gg M_\chi}{=} \frac{45 g_\chi}{2\pi^4 g_{\text{eff}}^s} \approx 10^{-3} \,. \tag{4.2.16}$$

Equating this result with Eq.(4.2.11) yields a DM mass of $M_\chi = \mathcal{O}\left(100\,\text{eV}\right)$. In contrast to the non-resonant case, this DM mass violates the Tremaine–Gunn bound, that restricts fermionic DM to have a mass of at least roughly a keV [96]. Therefore, in this case DM must be bosonic. However, this case is in tension with observations of the Lyman-α forest, which allows to probe structures in the universe that are of the size $10^{0-2} h^{-1}\,\text{Mpc}$ [97]. This issue is addressed in more detail in Section 4.2.2.
We summarized our results for the case $y_\chi = y_\nu$ in a schematic plot illustrated in Fig. 4.2.

Numerical Analysis
In this section, we present the results of a numerical solution to the Boltzmann equations in the non-resonant production regime for different coupling structures $y_\chi = (0.1, 1, 10) y_\nu$ and DM masses of $M_\chi \in [10^2, 10^{10}]\,\text{GeV}$ assuming different flavor structures, that is $f_1\left(\theta\right) = (10^{-1}, 1)$ and $f_2\left(\theta\right) = 2.46$ and a normal mass hierarchy in the neutrino sector,

[3] This is due to the fact that the main contribution to the interaction rate comes from the resonance at $s = M_N^2$. Hence, as soon as the temperature drops below M_N the resonance cannot be reached efficiently anymore and therefore the interaction rate decreases significantly.

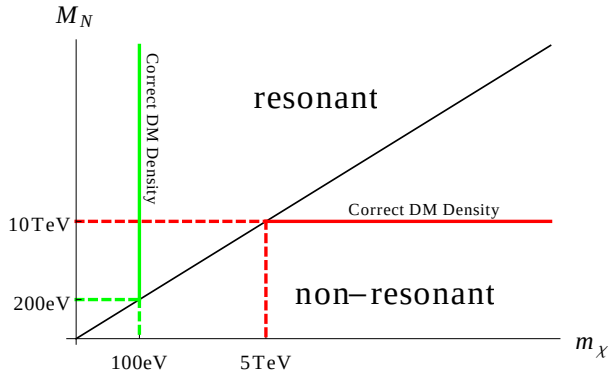

Figure 4.2.: Parameter space for $y_\chi = y_\nu$: The black line divides the plane spanned by the DM mass M_χ and the mediator mass M_N into two halves. The upper (lower) half corresponds to the resonant (non-resonant) DM production regime. The red and green line show where the correct amount of DM is produced for the non-resonant and the resonant regime, respectively. In the non-resonant regime, producing the correct density only depends on the mediator mass, whereas it only depends on the DM mass in the resonant region.

$m_{\nu_1} < m_{\nu_2} < m_{\nu_3}$. Additionally, we set $m_{\nu_1} = 0$ in the results presented in figure 4.3. Since we investigate a feebly coupled sector, the back reactions in the DM production processes can be neglected. Only for the processes $N \leftrightarrow \nu h$, which produce the mediator N, the back reactions are relevant, since for most of the parameter space N equilibrates with the SM.
Therefore, we solve the Boltzmann equation in two steps:

1. The N production via $N \leftrightarrow \nu h$ is solved at the level of the momentum distribution function, thereby taking into account the non-thermal shape of the distribution. The details of solving the Boltzmann equations at the level of momentum distribution functions are given in the end of Section 2.3.2. The collision term for the process in question is given in Eq.(A.23). Eventually, this procedure results in the quantity $\frac{n_N}{n_N^{\text{eq}}}(T)$[4]. We take $\frac{n_N}{n_N^{\text{eq}}}(T \to \infty) = 0$ as our initial condition.

2. Next, we solve the Boltzmann equations for the DM production via heavy neutrino and SM particle scattering employing the formalism described in Section 2.3.2. We take vanishing number densities for the DM particles as our initial conditions. The SM particles are assumed to follow their equilibrium densities throughout the production process. The heavy neutrino number density is given by the quantity $\frac{n_N}{n_N^{\text{eq}}}(T)$ which we found in step one. The final result is given by $Y_{\text{DM}} = Y_\chi + Y_\phi$ for $T \to 0$. Note that the independent solution of the Boltzmann equations for the dark sector particles and the heavy neutrino is only possible due to the tiny interaction rate, which allows to neglect the back reactions from DM production via heavy neutrino scattering.

The results are summarized in Figure 4.3. From our earlier considerations in this section, we expect the setup to reproduce the experimental observations for a constant mediator

[4]Note that we defined the quantity n_N as the sum over all three heavy neutrinos, i.e. $n_N = \sum_j n_{N_j}$.

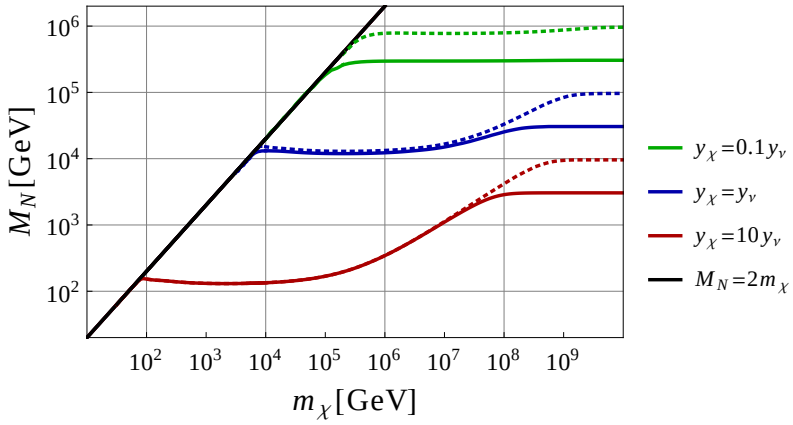

Figure 4.3.: The numerically obtained DM density Y_{th} is compared to the observed DM density Y_{exp} for different values of the DM mass M_χ and the mediator mass M_N: The different colored solid lines represent the points where the observed DM density is reproduced for a certain coupling structure. A parameter point above a specific line overproduces DM for the corresponding coupling structure while points below do not generate enough DM. Lines of the same color have the same coupling structure. A solid line represents a scenario with of $f_1(\theta) = 1$, while a dotted represents a scenario with $f_1(\theta) = 0.1$. The black line separates the plane into the non-resonant (lower right) and resonant (upper left) regime. The latter one was not scanned. We assumed normal ordering and one massless neutrino.

mass M_N as long as $M_\chi \gg M_N$. This constant value can be obtained by solving Eq.(4.2.12) for a given coupling structure. Consider, for instance, the case $y_\nu = y_\chi$, where Eq.(4.2.12) results in $M_N \sim 10\,\text{TeV}$. This case is illustrated by the solid blue line in Figure 4.3. For $10\,\text{TeV} \leq M_\chi \leq 10^4\,\text{TeV}$ the prediction is met by the numerical solution. However, for larger DM masses a larger mediator mass is required to accommodate the observed relic density. This is due to the following reason: The freeze-in mechanism produces DM efficiently down to temperatures around the heaviest mass scale involved in the production process. For the non-resonant regime this mass scale is given by the DM mass itself. Therefore, DM production is efficient for $T \gtrsim M_\chi$. The mediator mass, and thereby the neutrino Yukawa coupling y_ν, required to generate the observed DM relic density start to increase as soon as $\frac{n_N}{n_N^{\text{eq}}}(T) \ll 1$ for $T \gtrsim M_\chi$, since this suppresses DM production via heavy neutrino scattering. In the case of $y_\nu = y_\chi$ heavy neutrino scattering accounts for $\frac{35}{41}$ of the produced DM if the heavy neutrinos are following their equilibrium density during the time of production. If this contribution is missing, it has to be compensated by a larger neutrino Yukawa coupling resulting in a larger mediator mass M_N.

The heavy neutrinos reach thermal equilibrium with the SM via the inverse decay $\nu_i h \to N_j$ for a temperature $T_{\text{eq}} \sim cM_N$. The factor c is independent of the neutrino Yukawa coupling y_ν and the parameters θ, which encode the flavor structure of the neutrino Yukawas. However, it depends on the sum of the three active neutrino masses since the decay rate is proportional to this sum. The evolution of the heavy neutrino number density is shown in Figure 4.4. Here, the heavy neutrinos reach equilibrium for $T \approx 10^{-3} M_N$. Therefore, the lines in Figure 4.3 indicating the observed value of the relic

density start to deviate significantly from a constant value of M_N for $M_\chi > 10^3 M_N$, since in this case $\frac{n_N}{n_N^{\text{eq}}}(T) < 1$ for the complete time of production taking place for $T \gtrsim M_\chi$. A constant value of M_N is reached again when the contribution of the heavy neutrino scattering becomes negligible.
For $f_1(\theta) = 0.1$, the contribution of SM particle scattering is suppressed by a factor of 10. Thus, a larger coupling compared to the case of $f_1(\theta) = 1$ is required. This effect can be seen in Figure 4.3 where all dotted lines lie above the solid line of the same color. The effect is more pronounced for large DM masses, as the SM particle scattering dominates the DM production for $M_\chi \gtrsim 10^3 M_N$.
The different couplings structures result in larger (smaller) mediator masses for a small (large) dark Yukawa coupling compared to the neutrino Yukawa. Additionally, the effect of a small $f_1(\theta)$ differs for a small (large) dark Yukawa. While the increase of the mediator mass with a larger DM mass becomes less significant for a small dark Yukawa, the absolute difference between the small and large f_1 cases becomes stronger. This is due to the varying relative contributions to the DM production from heavy neutrino and SM particle scattering for the different coupling structures. For instance, the coupling structure $y_\chi = 0.1 y_\nu$ has a larger contribution to the DM production from the SM scattering and therefore results in a larger discrepancy between the dotted and solid green line.
For small DM masses close to the transition to the resonant regime, the correct DM relic density is obtained for values of M_N very close to $M_N = 2M_\chi$. In Figure 4.3, all lines follow the black line down to small DM masses until the enhancement close to the resonance is not strong enough to generate a sufficient amount of DM. However, the numerical solution is not trustworthy in this area due to numerical instabilities and therefore not presented here. We estimate the lower bound on M_χ by evaluating Eq.(4.2.2) in the limit $M_N \to 2M_\chi$. In the case of $y_\chi = \alpha y_\nu$, we obtain $M_\chi \gtrsim \alpha^{-\frac{4}{3}}\,\text{MeV}$.

4.2.2. Constraints on the feebly coupled Neutrino Portal to Dark Matter

In this section, we discuss several constraints on the model, arising from structure formation and direct detection experiments. We also comment on rare lepton decays as well as indirect detection experiments.

Structure Formation
As briefly discussed in Section 2.4.2, DM interacts only weakly with the SM and thus can escape from gravitational wells formed in the early universe, thereby delaying structure formation below their free-streaming scale. Given the redshift z_{prod} and the average momentum p_{prod} at the production time, the average the free-streaming scale is given by

$$\lambda_{fs} = \int_0^{z_{\text{prod}}} dz \frac{v(z)}{H(z)}\,, \tag{4.2.17}$$

where $v(z)$ is the DM velocity at a given redshift z. Here, we use the upper bound on the free streaming length, $\lambda_{fs} \lesssim 0.1\,\text{Mpc}$, derived in [68] to constrain the DM mass. As

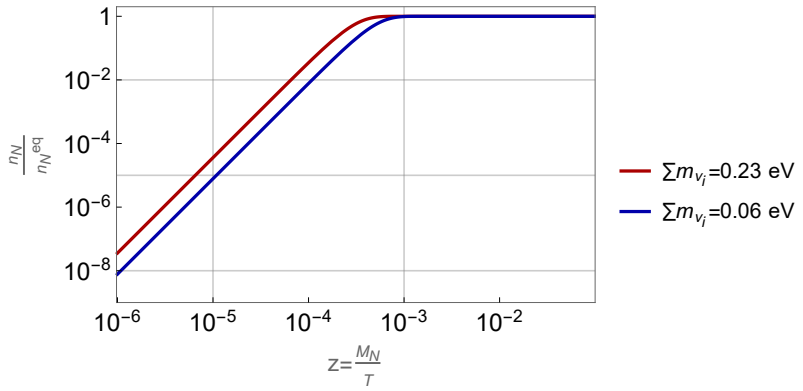

Figure 4.4.: The ratio of the heavy neutrino density to its equilibrium density against the dimensionless quantity $z = M_N T^{-1}$ for $\sum_i m_{\nu_i} = 0.06\,\text{eV}$ ($\sum_i m_{\nu_i} = 0.23\,\text{eV}$) [94], corresponding to the lower (upper) bound on the sum of the three active neutrino masses. Since the production rate of N is proportional to the sum of the active neutrino masses this choice shows the earliest and latest point of equilibration. The heavy neutrinos reach equilibrium for $T \approx 10^{-3} M_N$ in both cases. In Figure 4.3, the lower bound on the sum of the neutrino masses was used, but the results are negligibly different when considering the upper bound.

it was pointed out in [53], the free-streaming scale should be understood as an order-of-magnitude estimate in the case of a non-thermal DM momentum distribution and may differ up to $\mathcal{O}(1)$ factors from results obtained with dedicated tools like the CLASS-code. The latter computes the linear-matter-power spectrum resulting from the addition of the DM candidate.

For the purposes of this work, a rough estimate of the free-streaming length suffices, firstly because the non-thermal momentum distribution produced by the resonant freeze-in process, Eq.(A.21), is close to a thermal shape and secondly because the resonantly produced DM for the freeze-out case will be excluded by this method by roughly two orders-of-magnitude.

In the case of resonant production with $y_\nu \lesssim y_\chi$, we can assume DM to have a Boltzmann like momentum distribution, that is $f(p,T) = \exp\left(-E_p T^{-1}\right)$. We take the time of production as the freeze-out temperature since the interactions of DM with the SM cease to be efficient from this point on. For this momentum distribution the average momentum is given by

$$p_{\text{prod}} = \frac{M_\chi^2 + 3M_\chi T_{\text{prod}} + 3T_{\text{prod}}^2}{M_\chi + T_{\text{prod}}}\,. \tag{4.2.18}$$

Comparing the interaction rate Γ of the process $vh \to \chi\phi$ in the resonant regime to the Hubble parameter we find $T_{\text{prod}} \sim M_N$. For mediator masses $M_N \gtrsim$ MeV, the free-streaming scale becomes insensitive to the mediator mass itself. In this case, we find a lower bound on the DM mass of $M_\chi \gtrsim 10\,\text{keV}$. However, we found in Section 4.2 that a DM mass of 0.1 keV is required in order not to overproduce DM within this scenario. This is two orders of magnitude below the estimated lower bound. Therefore, the resonant production regime with $y_\nu \lesssim y_\chi$ is excluded by the Lyman-α measurement. On the other hand, if $y_\chi \ll y_\nu$, DM does not equilibrate with the SM even in the reso-

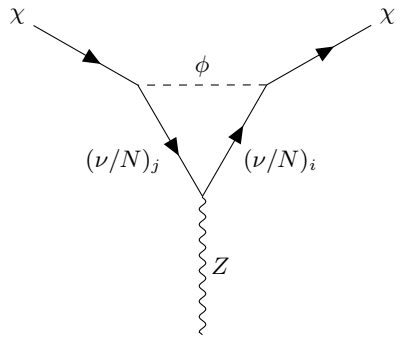

Figure 4.5.: 1-Loop diagram generating the effective coupling of DM to the Z. The indices i, j run from 1 to 3.

nant production regime. Therefore the spectrum is non-thermal and given by Eq.(A.21). We take $z_{\text{prod}}\,(T_{\text{prod}})$ as the temperature where the derivative of the total particle number with respect to the time is maximized. We find $T_{\text{prod}} = 3.36 M_N$, which results in $p_{\text{prod}} = 0.4 T_{\text{prod}}$. Again, for $M_N \gg M_\chi$, the free-streaming scale is insensitive to the mediator mass and the lower bound on the mass results in $M_\chi \gtrsim 3\,\text{keV}$.
To summarize, the Lyman-α measurement strongly constraints the resonant production regime of this model. While the case where the resonant enhancement of the production cross section is strong enough to equilibrate DM with the SM is completely ruled out, the freeze-in regime remains accessible for couplings $y_\chi \lesssim 10^{-12}\sqrt{\frac{M_N}{\text{keV}}}$, with $M_\chi \gtrsim 3\,\text{keV}$. Note that recently the free-streaming length has been constrained by a comprehensive study of the Milky Way's satellite galaxies and the DES collaboration [98] finds $\lambda_{fs} \lesssim 0.01 h^{-1}\,\text{MPc}$. If we consider this upper limit on the free streaming length instead, we find $M_\chi \gtrsim 35\,\text{keV}$ for the case of resonantly produced DM with $y_\chi \lesssim 10^{-12}\sqrt{\frac{M_N}{\text{keV}}} \ll y_\nu$. The case of resonantly produced DM with $y_\chi \gtrsim y_\nu$ remains excluded.

Direct Detection
Direct detection experiments search for interactions of DM with nuclei. In this model, a coupling of DM to the Z boson is generated at one-loop level. The corresponding Feynman diagram is shown in Figure 4.5. The coupling to the Z is then given by $\mathcal{L} \supset g_{Z\chi\chi}\bar{\chi}\gamma^\mu P_L \chi Z_\mu$ with [99]

$$g_{Z\chi\chi} = -\frac{y_\chi^2}{16\pi^2}\frac{g_w}{4\cos\theta_w}\frac{\Delta m_\nu}{M_N} 2.3 \cdot g\left(\frac{M_N^2}{m_\phi^2}\right), \tag{4.2.19}$$

and

$$g\,(x) = \frac{x\left[(x+2)\log\,(x) + 3\,(1-x)\right]}{2\,(1-x)^2}, \tag{4.2.20}$$

where we have used the best fit values of [100] for the parameters of the PMNS matrix in the case of normal ordering yielding $\sum_{k,m=1}^{3}\left(Y_\nu^T Y_\nu\right)_{km} \approx 2.3 \cdot y_\nu^2$. As DM couples to the SM quarks via the Z, we can use the results from Section 2.4.1 for the vector mediated

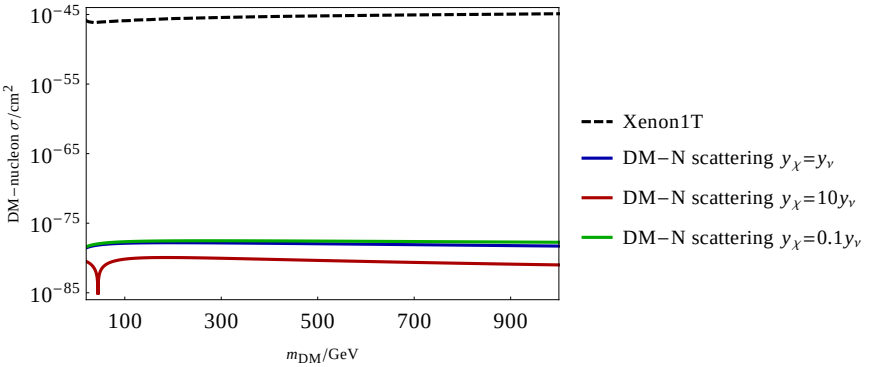

Figure 4.6.: The expected direct detection signals for the coupling structures investigated within chapter 4.2 are compared to the current bounds from XENON1T [60] (dashed black curve). The dip in the red curve is due to a cancellation appearing in the loop function.

SI cross section, given in Eq.(2.4.10), to compare the predicted DM-nucleon cross section to the experimental constraints from the XENON1T [60]. The results are illustrated in Figure 4.6. The model is clearly not constrained by direct detection experiments, which is typically the case for DM produced via freeze-in. There exist scenarios which allow for a large direct detection signature even in a freeze-in scenario [101]. In [101], the cross section is enhanced by a resonance induced by a light mediator.[5] Since the interaction in our model is mediated by a Z boson, this does not apply here.

Indirect Detection and Lepton Flavor Violation
Prospects for indirect detection of DM, such as the observations of γ-rays from the galactic center or the precise measurement of the CMB, all rely on the efficient annihilation of DM into SM particles. In the case of neutrino portal DM this usually occurs via DM first annihilating into heavy neutrinos which subsequently decay or annihilate into SM particles. Several prospects for indirect detection were investigated in [102] in the case of freeze-out production of DM. For the freeze-in scenario investigated in this work, the process is efficient only in the direction of DM production due to tiny couplings involved. This leads to a suppression of the annihilation cross section $< \sigma v >$ which enters all observables of indirect detection considered in [102], since the couplings y_ν and y_χ are required to be feeble. For this reason we do not study indirect detection observables within this work. Note however, that decays of a meta-stable slightly heavier dark sector scalar, $\eta \to \chi\nu$ could potentially constrain parts of the parameter space, as was shown in [103].
The minimal version of the type-I seesaw mechanism employed here induces couplings of the SM gauge bosons and the Higgs to the heavy neutrino states. This can modify electroweak precision observables and induce charged LFV as well as additional Higgs decay channels in the case of a light heavy neutrino [46, 104]. The strongest constraints come from the decay $\mu \to e\gamma$ with $\mathcal{B}(\mu \to e\gamma) \leq 4.2 \cdot 10^{-13}$ [94]. Within this setup the decay is mediated at one-loop level by a W boson and a neutrino. The branching ratio

[5] More precisely this refers to a case where the mediator is not more massive than the typical recoil energies involved in DM-nuclei scattering.

of this process results in [45]:

$$\frac{\Gamma\left(\mu \to e\gamma\right)}{\Gamma\left(\mu \to \nu_\mu e \bar{\nu}_e\right)} = \frac{3\alpha}{32\pi} \frac{|\sum_{k=1}^{6} U_{\mu k} U_{ek}^{\dagger} F\left(x_k\right)|^2}{\sum_{k,j=1}^{3} U_{\mu k} U_{\mu k}^{\dagger} U_{el} U_{el}^{\dagger}}\,, \tag{4.2.21}$$

where $F\left(x_k\right)$ is a loop function with $x_k = m_k^2 M_W^{-2}$. Since we assumed the heavy neutrinos to be mass-degenerate and the light neutrino mass is tiny compared to m_W we split the sum in the numerator into two parts with $F\left(0\right) = \frac{10}{3}$ and $F\left(\frac{M_N^2}{M_W^2}\right)$. Additionally we neglect the small deviation from one in the diagonal elements of $U_{\text{PMNS}} U_{PMNS}^{\dagger}$ in the denominator. Since the mixing matrix U is unitary we find

$$\frac{\Gamma\left(\mu \to e\gamma\right)}{\Gamma\left(\mu \to \nu_\mu e \bar{\nu}_e\right)} = \frac{3\alpha}{32\pi} \frac{\Delta m_\nu^2}{M_N^2} \left(F\left(0\right) - F\left(\frac{M_N^2}{M_W^2}\right)\right)^2 \left| \left(U_{\text{PMNS}} \frac{m_\nu}{\Delta m_\nu} U_{\text{PMNS}}^{\dagger}\right)_{\mu e} \right|^2 . \tag{4.2.22}$$

Taking the best fit values from [100] we find $\left(U_{\text{PMNS}} \frac{m_\nu}{\Delta m_\nu} U_{\text{PMNS}}^{\dagger}\right)_{\mu e} = 0.12$. Thus, we can give the branching ratio as a function of the heavy neutrino mass only since the free parameters of the orthogonal matrix R cancel within this setup [92]. This expression is maximized for $M_N = 1.36 M_W$ and results in

$$\frac{\Gamma\left(\mu \to e\gamma\right)}{\Gamma\left(\mu \to \nu_\mu e \bar{\nu}_e\right)} = \frac{3\alpha}{32\pi} \frac{\Delta m_\nu^2}{M_W^2} 0.12^2 \cdot 0.266 \approx 10^{-31}\,, \tag{4.2.23}$$

which is far below the experimental limit. For this reason, we also expect other LFV and electroweak precision observables not to significantly constrain the scenario.
Another imprint of this model could be found in additional decay channels of the Higgs if $M_N < \frac{m_h}{2}$. In this case the decays $h \to \nu_i N_j$ and $h \to N_i N_j$ are kinematically accessible. As pointed out in [105, 106], the dominant contribution of those to decay comes from the decay into a heavy and a light neutrino. However, branching ratios of this process larger than 10^{-2} are already ruled out and are typically much smaller due to the tiny Yukawa coupling [106]. Therefore, the contribution is negligible.

4.2.3. Conclusion

In this section, we have investigated a minimal NPDM model. The SM is extended by three SM singlet fermions which generate the neutrino masses via a type I seesaw mechanism and, furthermore, act as mediators between the SM and DM. The dark sector consists of a boson η and fermion χ coupled to the singlet fermions N via a Yukawa coupling y_χ. In the light of the small couplings arising in type-I seesaw scenarios in case of small heavy neutrino masses of $M_N \lesssim \mathcal{O}\left(\text{PeV}\right)$, we studied DM production via the freeze-in mechanism.
We derived analytic solutions for the number density in the resonant ($M_N > M_\chi + m_\eta$) and non-resonant ($M_N < M_\chi + m_\eta$) DM production regime. Depending on the coupling structure, more precisely the ratio of the dark Yukawa coupling to the neutrino Yukawa

coupling $\alpha = \frac{y_\chi}{y_\nu}$, we can predict the heavy neutrino mass in the non-resonant regime. For instance, we find $M_N \sim 10\,\text{TeV}$ in the case of $\alpha \sim 1$ or $M_N \sim 10\,\text{TeV} \cdot \alpha^{-1}$ in case of $\alpha \gg 1$. The non-resonant regime was studied in more detail numerically and the results are illustrated in Figure 4.3.
In the resonant regime, for $\alpha \gtrsim 1$, the resonant enhancement of the DM production cross section brings the dark sector into equilibrium with the SM. Thus, the freeze-out mechanism is recovered although the couplings between DM and the SM are feeble. Moreover, in this scenario we can predict a DM mass of $M_\chi \sim 100\,\text{eV}$. This result directly contradicts measurements of the Lyman-α forest that put a lower bound on of $M_\chi \gtrsim 10\,\text{keV}$ on the DM mass in this scenario. Hence, resonant DM production via the neutrino portal with $\alpha \gtrsim 1$ is excluded by the experiment. For $\alpha \ll 1$, nonetheless, DM production can still proceed via freeze-in production within the resonant regime. To satisfy the observed DM energy density the coupling of the fermionic singlets to DM must be of order $y_\chi \sim 10^{-12}\sqrt{\frac{M_N}{M_\chi}}$. Additionally, the Lyman-α measurement requires $M_\chi \gtrsim 3\,\text{keV}$ in this scenario and limits on the free-streaming length derived from a recent study of the Milky Way's satellite galaxies result in the more restrictive lower bound of $M_\chi \gtrsim 35\,\text{keV}$. Charged LFV, Higgs decays, indirect detection and direct detection have little impact on our parameter space due to the feeble coupling of the SM to the dark sector and the singlet nature of the mediator. The resonant production regime and the non-resonant production regime with $\alpha \gg 1$ require heavy neutrino states in the GeV mass range that could be potentially probed by upcoming hidden-sector searches, such as SHIP [107]. This possibility, however, will be addressed in a future work.
In the next Section, we generalize our analysis to a more strongly interacting version of the NPDM, as studied for example in [105, 108].

4.3. Consistency Conditions on the strongly coupled Neutrino Portal to Dark Matter

In this Section, we discuss several consistency conditions on the class of NPDM models utilizing the type-I seesaw mechanism. The corresponding Lagrangian is given in Eq.(4.1.1). In addition to the feebly coupled version investigated in the previous section, we devote the largest part of our discussion to the freeze-out regime of the NPDM, as it will be more severely constrained by the considered consistency conditions. Please note that the results presented in this section are part of an ongoing project.
Whereas the DM and LHC phenomenology of those models has been partially addressed in the literature and allows to constrain the parameter space [2, 102, 105, 108], an important theoretical consistency check is missing so far. Already the type-I seesaw can render the scalar vacuum unstable, as it introduces a new fermion loop as a correction to the Higgs self-energy [109]. Since the NPDM introduces an additional scalar, the form of the scalar potential is altered. This scalar mediates the DM-heavy neutrino interaction. Thus, its mass term and quartic coupling receive negative contributions from a fermion loop consisting of the dark fermion and the heavy neutrino. The corresponding Feynman diagrams are illustrated in Figure 4.7. At high scales this contribution can flip the sign of the mass term or the quartic coupling of the dark scalar. While the former can break a potential DM stabilizing symmetry, the latter leads to an unstable vacuum. Note that

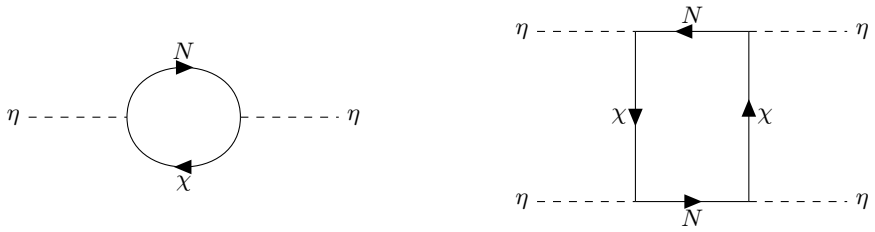

Figure 4.7.: One-loop diagrams contributing with a negative sign to the β function of m_η^2 (left hand side diagram) and λ_2 (right hand side diagram). Both contributions are more significant for a larger dark Yukawa coupling y_χ, as they scale like y_χ^2 and y_χ^4, respectively.

we do not include an analysis of metastable regions of the scalar potential in our study and only investigate if absolute stability criteria of the scalar vacuum are violated. Similar effects are observed in the scotogenic model where either the stabilizing $\mathcal{Z}_2$ symmetry can be broken [110] or the vacuum becomes unstable [111]. The renormalization group equations (RGE) for the scotogenic model were first discussed in [112, 113] and in [114] an extension of the scotogenic model avoiding $\mathcal{Z}_2$ breaking was presented. While the $\mathcal{Z}_2$ symmetry is restored at large temperatures the quartic coupling remains unaffected by thermal corrections at leading order [115, 116]. Thus, the unstable vacuum remains problematic.

In the following, we randomly generate a set of data points reproducing the observed relic density and satisfying the bounds from direct detection and collider experiments. We take those data points as the initial condition at the DM scale, which is defined below, for a numerical solution of the RGE. Afterwards, we check if the solution satisfies the following criteria:

1. Stability of the scalar vacuum: In the case of the scalar potential given in Eq. 4.1.2, this requirement directly translates to lower bounds on the quartic couplings of the scalar potential, namely

$$\lambda_1 > 0\,, \quad \lambda_2 > 0\,, \quad \lambda_3 > -\sqrt{\lambda_1 \lambda_2}\,. \tag{4.3.1}$$

2. Perturbative couplings: This for instance requires $\lambda_i < (4\pi)^2$ for quartic couplings and $y_i < 4\pi$.

4.3.1. Dark Matter Phenomenology in the strongly interacting Type-I Seesaw Neutrino Portal to Dark Matter

The Lagrangian of the model is given in Eq. (4.1.1). The new parameters relevant for the DM phenomenology and the RGE running are the Yukawa matrices $(Y_\chi)_i$ and $(Y_\nu)_{ij}$, the quartic coupling of the new scalar λ_2, the Higgs portal coupling λ_3, the masses of the dark sector particles M_χ and m_η and the masses of the new heavy neutrino states $(M_N)_i$. We assume the different generations of heavy neutrinos to be of the same mass and to couple universally to the dark sector, that is $(Y_\chi)_i = y_\chi$. The neutrino Yukawa matrix is again parametrized by Eq.(4.1.3) and therefore given in terms of the parameters y_ν and θ which is a vector of three (complex) angles. Thus, a data point contains the following

parameters

$$(M_N, M_\chi, m_\eta, y_\nu, \theta, y_\chi, \lambda_3, \lambda_2, \mu_{\rm DM}) \,, \tag{4.3.2}$$

where $\mu_{\rm DM}$ is the energy scale of DM production.
The available parameter space for the freeze-in production of DM in the context of the type-I seesaw NPDM was at length discussed in Section 4.2. We generate the data points using the approximated analytic solutions given Section 4.2.1 and check if the point satisfies the Lyman-α constraints. We further require that the dominant contribution to the relic density comes from the neutrino portal and therefore set the Higgs portal coupling to $\lambda_3 = 0$ in all freeze-in data points.
In the context of freeze-out production of DM, the model was investigated in [105, 117]. We repeat and improve their analysis in the following by discussing the constraints on the parameter space from invisible Higgs decays, direct detection experiments and the observed relic density.

Higgs Decays
All new particles couple at tree or one-loop level to the Higgs. Thus, if $M_N \leq \frac{m_h}{2}$, $M_\chi \leq \frac{m_h}{2}$ or $m_\eta \leq \frac{m_h}{2}$, invisible Higgs decays into a pair of the new particles might provide sizable contributions to the Higgs decay width. The branching ratio of invisible Higgs decays is constrained by the CMS collaboration to $\mathcal{B}\,(H \to \text{inv}) < 0.19$ with $\Gamma_H = 4.1\,\text{MeV}$ [79].
If $H \to \eta\eta$, $H \to \chi\chi$ and $H \to \nu N$ are kinematically allowed, the decay width for invisible Higgs decays results in

$$\begin{aligned}\Gamma_{H\to\text{inv}} = &\frac{\lambda_3^2}{8\pi}\frac{v^2}{m_H^2}\sqrt{1-4\frac{m_\eta^2}{m_H^2}}m_H + \frac{\lambda_{\text{eff}}^2}{8\pi}\left(1-4\frac{M_\chi^2}{m_H^2}\right)^{\frac{3}{2}} m_H \\ &+ \frac{M_N^2}{8\pi v^2}|\sum_{\alpha,i,j} U_{\alpha i}U_{\alpha j}^*|^2\left(1-\frac{M_N^2}{m_H^2}\right)^2 m_H \,,\end{aligned} \tag{4.3.3}$$

with

$$\lambda_{\text{eff}} = \frac{3y_\chi^2\lambda_3}{32\pi^2}\frac{M_\chi^2 - \left(m_\eta^2 - 3M_\chi^2\right)\log\left(\frac{m_\eta^2}{m_\eta^2 - M_\chi^2}\right)}{M_\chi^2} \,, \tag{4.3.4}$$

the effective $\bar{\chi}\chi\Phi$ coupling at one-loop, $U_{\alpha i}$ are elements of the leptonic mixing matrix and the sum is evaluated for all combinations for i, j that refer to one light and one heavy neutrino. Note that the expression for λ_{eff} assumes $M_N = 0$ and does not include contributions stemming from light neutrinos propagating in the loop, which come with an mixing angle suppression compared to the heavy neutrino contribution. In our numerical calculation we include the full loop integral with $M_N \neq 0$. Furthermore, the effective coupling differs from the one given in [117], as $M_\chi = 0$ was assumed in their work. We consider the case $M_\chi \neq 0$ since the masses of the dark sector particles χ and η are comparable in many scenarios, for instance in a setup allowing for efficient coannihilation.

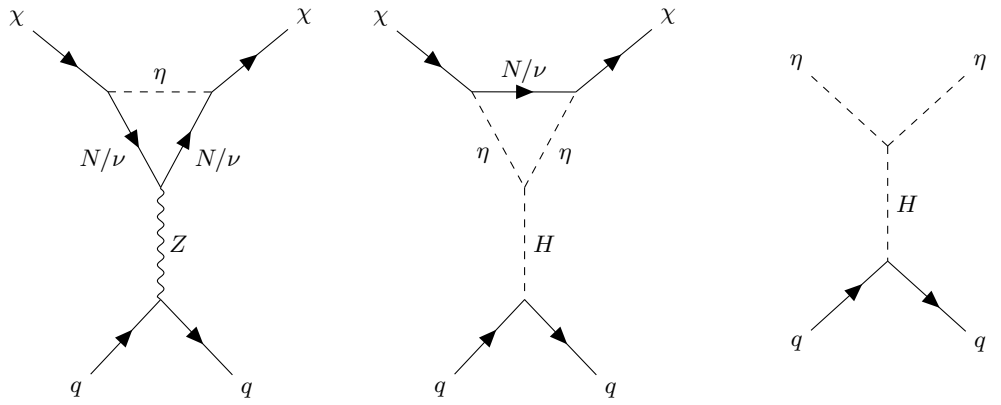

Figure 4.8.: Different contributions to the SI direct detection cross section. For fermionic DM the interaction is mediated at one-loop level, while for scalar DM a tree level contribution exists, which is generated by the Higgs portal coupling.

In addition, we neglected any contributions to the Higgs invisible decay width from final states involving either two light or two heavy neutrinos, as they are subdominant compared to the mixed decay. Within the type-I seesaw setup, the decay width into a heavy and a light neutrino scales as $\Gamma_H \sim \frac{m_\nu}{v} \sim 10^{-11}$ and is thus negligible as well.
For $m_\eta \ll m_H$ the $H \to \eta\eta$ channel alone yields the constraint $\lambda_3 \lesssim 7 \cdot 10^{-3}$. Hence the Higgs portal contribution is expected to be small for light dark sectors. For our numerical analysis we use the decay width given in Eq.(4.3.3).

Direct Detection
The XENON1T experiment provides stringent limits on the DM nucleon scattering cross sections for $m_{\rm DM} \gtrsim$ GeV. In the case of scalar DM η, DM-nucleon scattering is induced at tree-level by a t-channel exchange of a SM Higgs. For fermionic DM χ, interactions with quarks arise at one-loop level via Higgs or Z boson exchange. The various contributing diagrams are displayed in Figure 4.8.

Using the result for the spin-independent cross section in case of a scalar mediated coupling of scalar DM to quarks given in Eq.(2.4.8) and (2.4.4), we find for the SI DM-nucleon cross section in case of scalar DM η

$$\sigma_{SI} = \frac{\mu_{\eta N}^2 \lambda_3^2 v^2}{8\pi m_H^4 m_\eta^2} \left(\frac{Z\tilde{f}_p^2 + (A-Z)\,\tilde{f}_n^2}{A} \right)^2 , \tag{4.3.5}$$

where $\mu_{\eta N}$ is the reduced mass of the DM-XENON system, Z is the number of protons in XENON and A its number of nucleons. Therefore, direct detection directly constraints the Higgs portal coupling λ_3 in the case of scalar DM and we find that for $10\,\text{GeV} \lesssim m_\eta \lesssim 3\,\text{TeV}$ a dominant Higgs portal contribution to DM annihilations is excluded by the XENON experiment.
For fermionic DM, on the other hand, the interaction is mediated at one-loop level via Z or Higgs exchange. The Higgs mediated diagram can again be evaluated by means of

Eq.(2.4.8) and (2.4.4) and results in

$$\sigma_{SI} = \frac{\mu_{\eta N}^2 \lambda_{\text{eff}}^2 v^2}{2\pi m_H^4} \left(\frac{Z\tilde{f}_p + (A-Z)\,\tilde{f}_n}{A} \right)^2 . \tag{4.3.6}$$

In this case, direct detection constrains the coupling combination $y_\chi^2 \lambda_3$ and due to the one-loop suppression the constraints are significantly weaker.
The contribution of the Z mediated diagram can be derived from Eq.(2.4.10) and yields

$$\sigma_{SI} = \frac{\mu_{\chi N}^2 g_v^2}{\pi m_Z^4} \frac{\left[Z\tilde{b}_p + (A-Z)\,\tilde{b}_n \right]^2}{A^2} . \tag{4.3.7}$$

In the limit of zero outer momentum, the effective vector coupling of χ to the Z is given by

$$g_V \approx \frac{1}{\sqrt{2}} \frac{y_\nu v}{M_N} \frac{y_\chi^2}{16\pi^2} \frac{\frac{m_\eta^2}{M_N^2} - 1 - \log\left(\frac{m_\eta^2}{M_N^2}\right)}{4\left(1 - \frac{m_\eta^4}{M_N^4}\right)} . \tag{4.3.8}$$

Due to the typically small values for y_ν in the context of the type-I seesaw, this contribution is subdominant compared to the contribution arising from the Higgs exchange. Thus, for fermionic DM the Higgs portal potentially provides a sizable contribution to the DM annihilation rate, given a small dark Yukawa coupling y_χ. Note, however, that for a dominant Higgs portal contribution, in the case of fermionic DM, coannihilation effects must be efficient and therefore require a mass degenerate dark sector $M_\chi \sim m_\eta$.

Relic Density
In a freeze-out scenario and in the absence of coannihilations, the relic density is determined by the thermally averaged annihilation cross section of the annihilation channel that decouples latest. Within the type-I seesaw the neutrino Yukawa matrix Y_ν is given by Eq.(4.1.3), and its entries are of order $y_\nu = \frac{\sqrt{M_N \Delta m_\nu}}{v}$. This requirement already rules out a scenario in which the heavy neutrinos are heavier than the DM candidate, more precisely $M_N > \min[m_\eta, M_\chi]$. Given this mass hierarchy, DM annihilations into a pair of heavy neutrinos are kinematically suppressed and the dominant annihilation channel, annihilations into light neutrinos $\bar{\chi}/\bar{\eta}\,\chi/\eta \to \bar{\nu}\nu$, arises at one-loop level. Therefore, the annihilation cross section is suppressed by the loop factor and the small neutrino Yukawa[6] and we find $\sigma \sim y_\nu^4$ [118]. In such a scenario, DM would be far too abundant in the universe, as thermal freeze-out would occur too early. Thus, we restrict our study to cases where the heavy neutrino is lighter than the DM candidate. Additionally, we do not take into account effects stemming from resonant enhancement in s-channel production via the Higgs portal, for example in case of $m_{DM} = \frac{m_H}{2}$.
We distinguish two scenarios, namely fermionic and scalar DM. The dark fermion mainly annihilates via $\bar{\chi}\chi \to \bar{N}N$, while the dark scalar has two competing annihilation channels: $\eta^*\eta \to \bar{N}N$ via the dark Yukawa y_χ and $\eta^*\eta \to \Phi^\dagger\Phi$ via the Higgs portal coupling λ_3. Additionally, in the case of $m_\eta < m_H$, contributions from Higgs mediated s-channel

[6] A large neutrino Yukawa coupling requires very massive heavy neutrinos, which as well would suppress the annihilation cross section as the heavy neutrino propagates in the loop.

annihilations into SM fermions with a mass smaller than the DM candidate, $\eta^*\eta \to \bar{f}f$, arise.
As discussed in Section 2.3.3, the relic density in the case of an s-wave annihilation can be estimated by the inverse of the leading order contribution σ_0 in the relative velocity v of $< \sigma_A v >$. Using the results of [105], we arrive at

$$\Omega_{\rm DM} = \frac{\sqrt{g_{\rm eff}}}{g_{\rm eff,s}} \frac{3.79 x_f}{M_{\rm Pl} m_B \sigma_0} \frac{\Omega_B}{Y_B}\,, \tag{4.3.9}$$

with

$$x_f = \ln\left[0.038 \frac{g_{\rm eff,s}}{\sqrt{g_{\rm eff}}} M_\chi M_{\rm Pl} \sigma_0\right] - \frac{1}{2}\ln\left(\ln\left[0.038 \frac{g_{\rm eff,s}}{\sqrt{g_{\rm eff}}} M_\chi M_{\rm Pl} \sigma_0\right]\right)\,, \tag{4.3.10}$$

and σ_0 is the zeroth order contribution to the thermally averaged annihilation cross section. In the case of fermionic DM it is [105]

$$\sigma_0\left(\bar{\chi}\chi \to \bar{N}N\right) = \frac{y_\chi^4}{\pi M_\chi^2}\left(1 + \frac{M_N}{M_\chi}\right)^2 \frac{\sqrt{1 - \left(\frac{M_N}{M_\chi}\right)^2}}{\left(1 + \frac{m_\eta^2}{M_\chi^2} - \frac{M_N^2}{M_\chi^2}\right)^2}\,, \tag{4.3.11}$$

while for scalar DM the two contributing annihilations result in [105]

$$\sigma_0\left(\eta^*\eta \to \bar{N}N\right) = \frac{y_\chi^4}{2\pi m_\eta^2}\left(1 + \frac{M_N}{m_\eta}\right)^2 \frac{\sqrt{1 - \left(\frac{M_N}{m_\eta}\right)^2}}{\left(1 + \frac{M_\chi^2}{m_\eta^2} - \frac{M_N^2}{m_\eta^2}\right)^2}\,, \tag{4.3.12}$$

and

$$\sigma_0\left(\eta^*\eta \to \Phi^\dagger\Phi\right) = \lambda_3^2 \frac{\sqrt{m_\eta^2 - m_h^2}}{64\pi m_\eta^3}\,. \tag{4.3.13}$$

Further we include the Higgs mediated s-channel annihilations $\eta^*\eta \to W^+W^-/ZZ/\bar{f}f$ that scale as $\lambda_3^2 g_2^2$ and $\lambda_3^2 y_f^2$ respectively. The corresponding thermally averaged cross section are given in [119]. In our numerical analysis all of these contributions are included.
Next, we estimate the minimally allowed neutrino portal coupling in the case of a vanishing λ_3. Aiming for an analytic lower bound on y_χ in the case of fermionic DM, we neglect the logarithmic mass dependence in the freeze-out temperature given in Eq.(4.3.10) and assume $x_f = x_{f,0} \sim 30$. CMB measurements indicate $\Omega_{DM} = 0.265$ and here we shall rule out a model if it exceeds this value.[7] Using Eq.(4.3.9), we find

$$\sigma_0 > \frac{\sqrt{g_{\rm eff}}}{g_{\rm eff,s}} \frac{3.79 x_{f,0}}{M_{\rm Pl} m_B} \frac{\Omega_B}{Y_B} \frac{1}{0.265} \equiv K \approx 6.72 \cdot 10^{-11} x_{f,0}\,. \tag{4.3.14}$$

[7] A lower value is not in disagreement with the measurement in the sense that the missing energy density could be accommodated for by another DM component.

The right-hand side of this equation is independent of the dark Yukawa and the dark sector masses. In the case of fermionic DM, $\lambda_3 = 0$ and $m_\eta \gg M_\chi$, σ_0 amounts exactly to the contribution given in Eq.(4.3.11) and therefore we find

$$\frac{y_\chi^4}{M_\chi^2} \cdot f\left(\frac{M_N}{M_\chi}, \frac{m_\eta}{M_\chi}\right) > K\,. \tag{4.3.15}$$

To find a lower bound on y_χ in terms of M_χ we need to find the maximum of f, which is given by $f\,(0.82, 1) \approx 0.10$. Thus we expect

$$y_\chi \gtrsim 0.012\sqrt{\frac{M_\chi}{\mathrm{GeV}}}\,. \tag{4.3.16}$$

However even in the case $\lambda_3 = 0$, this value can potentially be further decreased by coannihilations if $M_\chi \sim m_\eta$. In such a scenario, annihilations of the dark scalar can effectively enhance the annihilation cross section resulting in

$$\sigma_0^{\mathrm{eff}} = \sigma_0\left(\bar{\chi}\chi \to \bar{N}N\right) + r_{12}^2\sigma_0\left(\eta^*\eta \to \bar{N}N\right)\,, \tag{4.3.17}$$

where r_{12} is given in Eq.(2.3.36) and the indices 1 and 2 refer to χ and η respectively. Evaluating Eq.(4.3.17) at $T = T_{fo}$, so that $\frac{M_\chi}{T} = x_{f,0} \sim 30$, again employing Eq.(4.3.9) and determining the mass ratios $\frac{M_N}{M_\chi}$ and $\frac{m_\eta}{M_\chi}$ so that σ_0^{eff} is maximized, results in the minimally allowed dark Yukawa y_χ. The changes due to coannihilations in the case of $\lambda_3 = 0$ are small and the effect on the lower bound presented in Eq.(4.3.16) is negligible. Note that, for a sizable λ_3, coannihilations via Higgs-portal-mediated annihilations can dominate the effective annihilation cross section. This, however, requires a small mass splitting in the dark sector, as the scalar annihilation contribution is suppressed by $\exp\left(-\frac{m_\eta - M_\chi}{M_\chi}x_{\mathrm{f},0}\right)$.
Similarly, for scalar DM with $\lambda_3 = 0$ we find

$$y_\chi \gtrsim 0.012\sqrt{\frac{m_\eta}{\mathrm{GeV}}}\,, \tag{4.3.18}$$

which resembles the case of fermionic DM. To sum up, we expect viable data points for sets of DM masses and y_χ that satisfy the lower bounds given in the Eqs. (4.3.16) and (4.3.18). In a scalar DM scenario, we do not expect sizable Higgs portal contributions for $m_\eta \lesssim 3\,\mathrm{TeV}$ due to the tight constraints on λ_3 from the XENON1T experiment. For $m_\eta \gtrsim 3\,\mathrm{TeV}$, however, large Higgs portal contributions may generate viable data points with a smaller y_χ than allowed for by the lower bound that assumed a vanishing λ_3.
On the other hand, fermionic DM is not as tightly constrained by direct detection experiments due to the one-loop suppression of its coupling to the Higgs. Thus, even for $M_\chi \lesssim 3\,\mathrm{TeV}$ Higgs portal contributions might be sizable given a small y_χ. For $M_\chi < \frac{m_h}{2}$, the constraints on the Higgs invisible decay width still rule out any sizable Higgs portal contribution.

4.3.2. Analytic and Numerical Results to the Renormalization Group Equations

In this section, we present analytic and numerical solutions to the RGEs for the randomly generated data points that are in agreement with the DM phenomenology discussed in

the previous section.
We take the generated values as the initial conditions for the couplings and masses at the scale $\mu_{\rm DM}$ that determines the scale of DM production. In the case of freeze-in production of DM, this mass scale is given by the maximal mass scale involved in the production process. Conversely, for freeze-out production $\mu_{\rm DM}$ is set by the freeze-out temperature, which is given by $m_{\rm DM}x_f^{-1}$ and x_f is determined during the numerical computation of the relic density. A typical value is $x_f \sim 30$. Thus

$$\mu_{\rm DM} = \begin{cases} \text{Max}\left[M_\chi, m_\eta, M_N\right], & \text{for freeze-in production.} \\ \text{Min}\left[M_\chi, m_\eta\right] x_f^{-1}, & \text{for freeze-out production.} \end{cases} \tag{4.3.19}$$

We computed the RGEs for the type-I seesaw NPDM with ARGES at one-loop level and the relevant β-functions are given in Appendix C.
Consider first the Higgs quartic λ_1, and assume that the renormalization group flow of the gauge and Yukawa couplings of the SM is approximately unaltered. This approximation is justified in the fact that the running of these couplings is typically logarithmic with the energy. Hence, β_{λ_1} is then only modified by a term proportional to λ_3^2, which is positive, and thus can only help to stabilize the vacuum. The remaining new terms are proportional to $\text{Tr}[Y_\nu^\dagger Y_\nu]$ and $\text{Tr}[(Y_\nu^\dagger Y_\nu)^2]$, which are typically small in the context of the type-I seesaw. Thus, we expect the new sector not to introduce important deviations in λ_1.
In the case of λ_2, the contribution from the dark Yukawa, proportional to $\text{Tr}[(Y_\chi^\dagger Y_\chi)^2]$, may drive the coupling to negative values; an analogous effect was described in [111] for the scotogenic model. Taking y_χ to be approximately constant, the scale μ_{λ_2} at which λ_2 approaches negative values may be estimated by only considering the contributions from the term quartic in the dark Yukawa. We obtain

$$\ln \frac{\mu_{\lambda_2}}{\mu_{\rm DM}} \sim \frac{4\pi^2 \lambda_2(\mu_{\rm DM})}{y_\chi^4}\,, \tag{4.3.20}$$

Demanding the vacuum to be stable up to the Planck scale, that is $\mu_{\lambda_2} > M_{\rm Pl}$, places constraints on y_χ for a given $\mu_{\rm DM}$.
Next we consider y_χ, the running of which depends only on the neutrino Yukawa Y_ν and y_χ itself. If we assume $y_\chi \gg y_\nu$, the beta function for y_χ β_{y_χ} can be integrated and $|y_\chi|$ increases with the energy scale. Thus, we can estimate the scale μ_{y_χ} at which y_χ becomes unperturbative, more precisely $|y_\chi\left(\mu_{y_\chi}\right)| = 4\pi$. We find

$$\ln \frac{\mu_{y_\chi}}{\mu_{\rm DM}} \sim \frac{16\pi^2 - y_{\chi,0}^2}{8 y_{\chi,0}^2}\,, \tag{4.3.21}$$

with $y_{\chi,0} = y_\chi\left(\mu_{\rm DM}\right)$. Using this result allows for a more precise estimate of the scale μ_{λ_2}. In addition to $\text{Tr}[(Y_\chi^\dagger Y_\chi)^2]$, we include the terms proportional to λ_2^2 and $\lambda_2 \text{Tr}[(Y_\chi^\dagger Y_\chi)]$ in β_{λ_2} to account for the stabilizing effects of a sizable λ_2. While we cannot find an expression for $\ln \frac{\mu_{\lambda_2}}{\mu_{\rm DM}}$, we can determine a lower bound on y_χ above which the sign of λ_2 can be potentially flipped at some energy scale. We obtain

$$y_{\chi,0} \geq \sqrt{\frac{16+\sqrt{31}}{3\left(1+\sqrt{31}\right)}}\sqrt{\lambda_2(\mu_{\rm DM})}\,. \tag{4.3.22}$$

If this condition is not fulfilled λ_2 can become unperturbative $\lambda_2 > (4\pi)^2$. In the case of $y_\chi = 0$ we find an estimate for the maximal value of λ_2 such that it remains perturbative up to $M_{\rm Pl}$:

$$\lambda_2\left(\mu_{\rm DM}\right) \lesssim \frac{16\pi^2}{1 + 10\ln\left(\frac{M_{\rm Pl}}{\mu_{\rm DM}}\right)}\,. \tag{4.3.23}$$

Hence we can estimate the maximal value of $y_{\chi,0}$ which does not lead to an unstable vacuum while $\lambda_2\left(\mu_{DM}\right)$ is small enough to remain perturbative up to $M_{\rm Pl}$. We find

$$y_{\chi,0} \leq \sqrt{\frac{16+\sqrt{31}}{3\left(1+\sqrt{31}\right)}}\frac{4\pi}{\sqrt{1 + 10\ln\left(\frac{M_{\rm Pl}}{\mu_{\rm DM}}\right)}}\,. \tag{4.3.24}$$

For instance, in the case of $\mu_{\rm DM} \sim 1\,\text{TeV}$ the upper bound results in $y_{\chi,0} \lesssim 0.7$. In combination with the lower bound on the dark Yukawa derived from the DM phenomenology given in the Eqs (4.3.16) and (4.3.18), we can find an upper limit on the DM mass. Assuming $x_f \sim 30$, we find an order of magnitude estimate of

$$M_{\rm DM} \lesssim 3\,\text{TeV}\,. \tag{4.3.25}$$

In the following, we present the results of our numerical analysis for different data sets demonstrating some of the properties of the model discussed above. Each point represents a certain configuration of parameters and is additionally assigned a mass scale $\Lambda_{\rm max}$ corresponding to the highest scale at which no consistency conditions are violated by the numerical solution to the RGE. If, for instance, λ_2 became negative at 100 TeV while all other consistency condition were fulfilled, we would assign $\Lambda_{\rm max} = 100\,\text{TeV}$. The color of each point refers to the consistency condition that is violated first. In the case of a purple data point, the model is consistent at least up to $M_{\rm Pl}$. Our example of a negative λ_2 would result in a yellow point and therefore unstable vacuum. For the case of freeze-out production we consider four different data sets. For both fermionic and scalar DM we create one data set with $\lambda_3 = 0$ and another one with $\lambda_3 \neq 0$ where the former only includes contributions from the neutrino portal, while the latter illustrates where Higgs portal contributions can arise. We generate data points for the parameter ranges given in Table 4.1. All values are drawn logarithmically.

	$M_{\rm DM}$	$M_{\rm DS}$	M_N	y_i	λ_a
Lower Bound	10 GeV	$M_{\rm DM}$	$10^{-2}M_{\rm DM}$	10^{-5}	10^{-5}
Upper Bound	1000 TeV	$10^2 M_{\rm DM}$	$M_{\rm DM}$	4π	$(4\pi)^2$

Table 4.1.: Parameter ranges for the randomly generated data sets. All parameters are drawn logarithmically. The mass $m_{\rm DS}$ refers to the mass of the heavier dark sector particle. The coupling y_i refers to the Yukawa couplings y_χ and y_ν while λ_a gives the parameter ranges for λ_2 and λ_3.

Scatter Plots in the $\mu_{DM} - y_\chi$ Plane

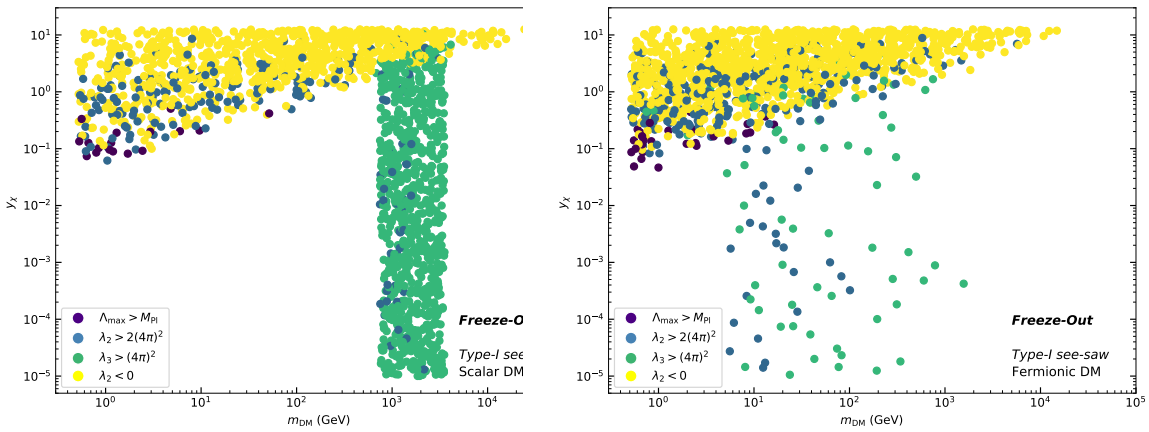

Figure 4.9.: Phenomenologically viable data points of the NPDM colored according to their behavior at high energy scales. The data points are presented in the $\mu_{\rm DM} - y_\chi$ plane where $y_\chi = y_\chi(\mu_{\rm DM})$. The color code indicates if the data set leads to a model that is consistent up to the Planck scale (purple), an unstable vacuum (yellow) or results in a non-perturbative coupling (green and blue). The left (right) panel shows the results for data points involving scalar (fermionic) DM. The corresponding plots for the case of a vanishing λ_3 are given in Figure D.1 in Appendix D.

In Figure 4.9, the data points are scattered in the $\mu_{\rm DM} - y_\chi$ plane. We clearly observe the distinct features of scalar (left panel) and fermionic (right panel) DM described in Section 4.2.1. Both scenarios feature a triangle-like shape that contains the largest part of the viable data points. The boundaries of these triangles are set by the lower bounds for the dark Yukawa coupling given in the Eqs. (4.3.16) and (4.3.18) for fermionic and scalar DM respectively. Data points above this line can be understood by an suppression of the annihilation cross section by, for instance, a large mass of the other dark sector particle. Points that lie outside of this area involve scenarios where the annihilation cross section is dominated by Higgs portal contributions, thereby allowing for a smaller y_χ. In the case of scalar DM this effect only arises for large DM masses and therefore large $\mu_{\rm DM}$ due to the tight constraints from the XENON1T collaboration on the interaction of DM with the Higgs. For fermionic DM this interaction is loop suppressed and thus Higgs portal contributions can be sizable as long as the Higgs decays into dark sector particles are kinematically forbidden. Note that nevertheless the points with sizable λ_3 are far more abundant in the scalar DM scenario. This results from the necessity of a nearly mass-degenerate dark sector in the case of fermionic DM to allow for efficient coannihilation, which, in that case, is a requirement for a sizable Higgs portal contribution. This does not apply to scalar DM. As seen in Figure 4.9, no data points were found with a sizable Higgs portal contribution that run up the Planck scale without violating any consistency condition (purple points).

Scatter Plots in the $y_\chi - \lambda_2$ Plane

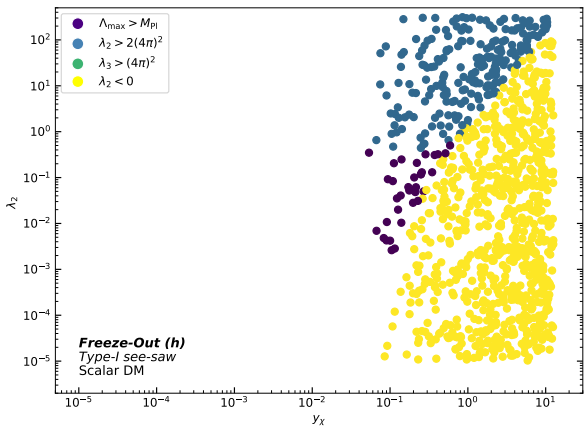

Figure 4.10.: The data set for the case of scalar DM with a vanishing λ_3 is displayed in the $y_\chi - \lambda_2$ plane. The values of both λ_2 and y_χ are given at the scale $\mu_{\rm DM}$. The cases of non-zero λ_3 for fermionic and scalar DM are depicted in Figure D.3 in Appendix D, while the case of $\lambda_3 = 0$ for fermionic DM is shown in Figure D.2.

In Figure 4.10, we show the data set with vanishing λ_3 and fermionic DM in the $y_\chi - \lambda_2$ plane. There, the upper bound on y_χ in order to provide a consistent model up to the Planck scale can be clearly seen. The crucial parameter in this case is the dark scalar quartic λ_2, which can become non-perturbative or negative leading to an unstable vacuum. A sizable λ_2 tends to create unperturbative λ_2 at high energy scales. This, in turn, requires a sizable y_χ to safe the perturbativity of λ_2. If however, y_χ becomes too large it drives λ_2 towards negative values. For large values of y_χ this balance cannot be found anymore. Thus, if y_χ exceeds a certain value the model becomes inconsistent. For fermionic DM with $\lambda_3 = 0$, we find $y_\chi \lesssim 0.8$.

Scatter Plots in the $\mu_{DM} - \Lambda_{max}$ Plane

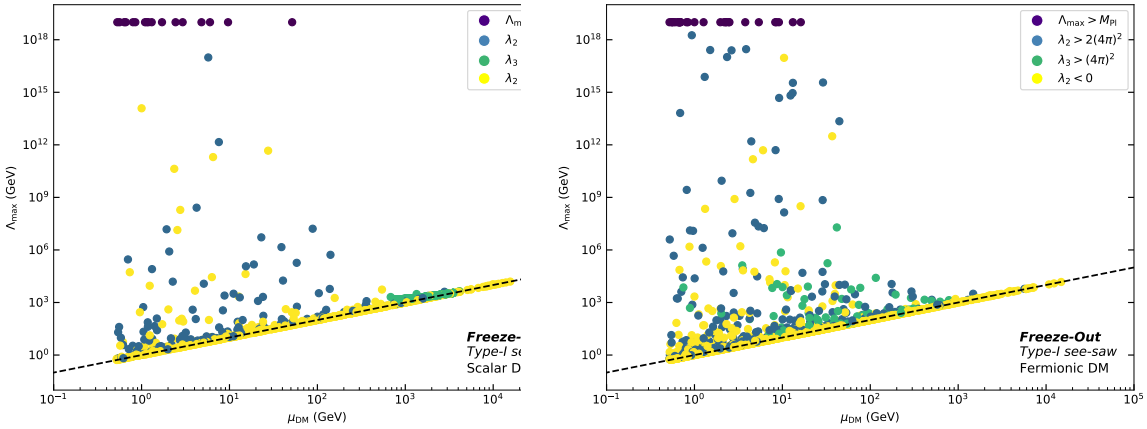

Figure 4.11.: The data sets for scalar (left panel) and fermionic (right panel) DM with $\lambda_3 \neq 0$ are displayed in the $\mu_{\mathrm{DM}} - \Lambda_{\mathrm{max}}$ plane. The scale Λ_{max} describes the scale where the first inconsistency appears. The color code again denotes which specific inconsistency arises or if the model is safe up to the Planck scale. The dotted line indicates where $\Lambda_{\mathrm{max}} = \mu_{\mathrm{DM}}$, which is the starting point for the numerical solution of the RGE. The corresponding figures for the case of $\lambda_3 = 0$ are given in Figure D.4.

In Figure 4.11, we illustrate for the fermionic and scalar DM $\lambda_3 \neq 0$ data sets at which energy scale a certain data point runs into its first inconsistency. It is apparent that most of the previously viable data points run into inconsistencies. We observe a DM energy scale above which we do not find any points that do not develop inconsistencies. In the case of fermionic DM this is the case for $\mu_{\mathrm{DM}} \gtrsim 20\,\mathrm{GeV}$, which translates into an upper bound on the DM mass of roughly 600 GeV.
For a majority of the data points the first inconsistency is reached within one or two orders magnitude. This result makes the inconsistencies even more concerning. For data points that develop inconsistencies for energy scales $\mu \gg \max[m_\eta, M_\chi]$, one might argue that the model could be extended by additional field content that does not interfere with the DM phenomenology but cures the arising inconsistencies by altering the RGEs above the mass scale of this new physics. However, this approach does fail if the inconsistency arises for scales that are comparable to the largest mass scale involved in the model. In such a scenario, the model as considered in this chapter is not consistent and would have to be extended with particle content of the same or even smaller mass. Considering that the scale μ_{DM} is at least one order of magnitude smaller than the DM mass itself rules out parts of the previously viable parameter space of the NPDM. This in particular holds true for $\mu_{\mathrm{DM}} \gtrsim 100\,\mathrm{GeV}$, where we only find data points with $\Lambda_{\mathrm{max}} \lesssim \max[m_\eta, M_\chi]$. This implies that all phenomenologically viable data points develop inconsistencies at mass scales that appear in the formulated model itself.

4.3.3. Conclusion and further Studies

We presented results of an analysis of the type-I seesaw NPDM that checked if phenomenological viable data points are consistent. We classified a data point inconsistent if it leads to an unstable vacuum or non-perturbative couplings at energy scales below $M_{\rm Pl}$. We generated data points in agreement with collider and direct detection limits while reproducing the observed DM relic density and numerically solved the RGEs from the DM production scale, given by the freeze-out temperature, up to the Planck scale. We found that the dark Yukawa coupling y_χ tends to destabilize the scalar vacuum, which yields the approximate upper limit on y_χ given in Eq.(4.3.24). For instance, in the case of $\mu_{\rm DM} = 1\,\text{TeV}$ we find $y_\chi \lesssim 0.7$. On the other hand, the requirement to fit the observed relic density makes a relatively large dark Yukawa coupling mandatory in order to sufficiently deplete the DM relic abundance. This statement is quantified in the Eqs. (4.3.16) and (4.3.18). Those required minimal values for the Yukawa couplings increase with the mass and in combination with the necessity of a consistent model rule out large DM mass scales. For the case of fermionic DM we did not find consistent data points with $\mu_{\rm DM} \gtrsim 20\,\text{GeV}$, while for scalar DM this is the case for $\mu_{\rm DM} \gtrsim 80\,\text{GeV}$.
Furthermore, the scan allows for contributions from the Higgs portal as well as from the neutrino portal. However, we found that all consistent data points are dominated by the neutrino portal coupling, as Higgs-portal-dominated data points tend to generate an unperturbative λ_3 for scales that are comparable to the mass scales of the model itself. Thus, we conclude that the type-I seesaw neutrino portal can provide parameter space that allows for producing the observed relic density while satisfying collider and direct detection constraints. The applied consistency conditions rule out sizable Higgs portal contributions and further exclude heavy DM realizations above a TeV. In ongoing studies we work towards extending this analysis to the case of inverse seesaw NPDM. The RGE for the model [102, 108] can be found in in Appendix C.
We, however, plan to address the consistency conditions in the version of the model discussed in [102,108] where the SM is extended by a right-handed and a left-handed singlet fermion. Such a model, however, as elaborated on in Section 2.1, cannot reproduce the observed neutrino oscillation parameters, since only one non-zero mass difference is generated. Nevertheless, the study proves interesting as it indicates where potential signals of (a realistic version of) the model can be expected. As shown in Section 2.1, the inverse seesaw does allow for much larger neutrino Yukawa couplings Y_ν and therefore also a richer phenomenology. In the context of the consistency conditions addressed in the previous sections, the larger neutrino Yukawa might drive the Higgs quartic λ_1 towards negative values and alters the running of the dark Yukawa, which indirectly influences the running of λ_2.
The potentially large neutrino Yukawa opens up an additional annihilation channel of DM into light SM neutrinos, for instance $\bar{\chi}\chi \to \bar{\nu}\nu$, which typically dominates the thermally averaged annihilation cross section. Further the mixing angle of the SM neutrinos and the resulting heavy pseudo-Dirac neutrino can be sizable and allow for constraints from several sterile neutrino observables such as from μ/τ decays, rare meson decays involving dark sector particles or from invisible Z or Higgs decays. Thus, the model is expected to be more tightly constrained compared to the type-I seesaw neutrino portal. However, both rely on large Yukawa couplings to match the observed relic density.

Consequently, we expect the effects on the scalar vacuum to be sizable and allow for a further restriction of this model. These effects are subject of ongoing studies [4].
Finally, we would like to outline several directions in which the analysis presented in this section can be improved in future works. Firstly, the vacuum stability analysis carried out here involves only tree-level interactions, while effects arising from the effective scalar potential could be included. Secondly, the absolute stability criteria used here could be refined by considering metastability regions, which might open up part of the parameter space. Next, here the RGE running was computed including one relevant scale, the scale of DM production. A more detailed analysis with matching at the potentially different scales featured by each particular data point would be beneficial. Lastly, one could study the impact of including 2-loop effects in the RGEs of the scalar couplings, which were here computed at 1-loop.

5. Effects of a long-lived Yukawa Bound State on Dark Matter Production

In this chapter, we investigate the effects of a Yukawa bound state formed in the dark sector. In contrast to a Coulomb potential, which is repulsive for particle-particle or antiparticle-antiparticle interactions, the Yukawa potential is always attractive. Thus, if the Yukawa interaction of the form $\bar{\psi}\phi\psi$ is mediated by a light scalar ϕ, in addition to $\psi\bar{\psi}$ bound states, also $\psi\psi$ and $\bar{\psi}\bar{\psi}$ bound states can form, as long as a potential repulsive gauge interaction can be overcome.
Some effects of bound state formation (BSF) in a dark sector were already studied. The existence of bound states among the DM candidates gives rise to the so called Sommerfeld enhancement [120, 121], which effectively increases the annihilation rate of DM, thereby leading to a smaller relic density. Additionally, the bound state itself can assist in depleting the relic density via bound state annihilations or decays and this effect was considered in the context of coannihilation scenarios [122–125]. Such BSF can even be mediated by the SM Higgs if it is significantly lighter than the particles forming the bound state [126, 127].
In this work, we examine the effect of a bound state in a heavy dark sector that is only feebly coupled to the SM or another hidden sector. In many scenarios, the interaction rates of processes transferring particle number from the dark sector to the SM or another hidden sector are suppressed by both the tiny portal coupling and the a potentially small number density of the dark sector partic les. We consider a scenario where due to a large Yukawa interaction within the dark sector bound states can form efficiently. Broadly speaking, the bound state confines two particles close to each other, thereby effectively erasing the suppression by the small dark sector number density for two dark sector particle annihilation. This, in turn, can allow for efficient particle number transfer from the dark sector to another sector by the decay of the bound state. This effect, as we will demonstrate later on, can take place although the transfer by direct annihilations of dark sector particles is not efficient by many orders of magnitude.
In a DM portal model involving symmetric[1] DM, as for instance described in Section 2.3.3, this effect might be impactful if the couplings to the SM are small but the DM-mediator interaction is sizable, corresponding to a reannihilation or dark freeze-out scenario, or at the transition region to a freeze-in scenario. In such scenarios, the efficient BSF might significantly increase the annihilation into SM particles or mediators, thereby depleting the relic density. This issue might be addressed in a future project. In this work, however, we consider the case of asymmetric DM where either more particle or antiparticle DM exists. We demonstrate how the existence of a bound state of heavy DM can shift an existing asymmetry from one sector into another although the coupling connecting these two sectors is feeble. For this purpose, we investigate a model where

[1] The case of symmetric DM describes a scenario where the relic density consists of equal contributions of DM particles and antiparticles, while the scenario of asymmetric DM refers to a setup where the relic density is dominated by either particles or antiparticles.

two feebly coupled dark sectors share an asymmetry generated by an unspecified mechanism in Section 5.2. Before we proceed with the discussion of this model, we review how to obtain an approximated BSF cross section in case of a Yukawa interaction in Section 5.1.

5.1. Bound State Formation and Dissociation

In this section, we discuss the computation of the bound state dissociation (BSD) cross section for a bound state $R_{\psi\psi}$, which consists of a pair of fermions ψ, and is formed via the attractive Yukawa potential arising from an interaction with a light scalar ϕ that is of the form $\mathcal{L} \supset y\bar{\psi}\phi\psi$. In our calculation we are closely following the formalism described in Ref. [128], where the BSD for the hydrogen atom is derived. The bound state is broken via a scattering with the mediator ϕ that results in two free ψ. The thermal rate for the BSF can be obtained from the thermal rate of the BSD via $\gamma^{\mathrm{eq}}\left(\psi\psi \to R_{\psi\psi}\phi\right) = \gamma^{\mathrm{eq}}\left(R_{\psi\psi}\phi \to \psi\psi\right)$, which holds true as long as the interactions under consideration are CP-conserving.
The computation of the amplitude for the process of BSD requires the wave function overlap between the initial and final states. Therefore, the wave function of the bound ψ particles in the presence of a Yukawa potential is required. In general, this problem is not solvable analytically, as discussed for example in [129, 130]. To simplify the calculation, we focus on regions of the parameter space where the Yukawa potential can be well approximated by a Coulomb potential, of which the resulting wave function for a bound particle is well known. In the following, we derive the BSD cross section for a non-relativistic and ultra-relativistic free ψ, which are matched for the subsequent numerical solution of the Boltzmann equations.

Non-Relativistic Case
We start our discussion with the case of a non-relativistic ψ. The Yukawa potential is given by

$$V(r) = -\frac{y^2}{4\pi}\frac{\exp\left(-m_\phi r\right)}{r} = -\frac{y^2}{4\pi}\frac{1}{r}\left[1 - m_\phi r + \mathcal{O}\big((m_\phi r)^2\big)\right], \tag{5.1.1}$$

where y is the Yukawa coupling and m_ϕ is the mass of the scalar mediator ϕ. In case the mediator mass is much smaller than the inverse of the Bohr radius a_0 ($= 8\pi/(y^2 m_\psi)$), the Yukawa potential will be dominated by the leading term since $m_\phi r \sim m_\phi a_0 \ll 1$, resulting in a Coulomb potential. Under this approximation, we can solve the Schrödinger equation for the Coulomb potential and obtain the ground state wave function

$$\Psi_i(r) = \frac{m_\psi^{3/2} y^3}{16\sqrt{2}\pi^2}\exp\left(-\frac{m_\psi y^2}{8\pi}r\right), \tag{5.1.2}$$

where the subscript i refers to the initial state. Further, for the binding energy of the ground state, we find

$$E_B = -\frac{m_\psi y^4}{64\pi^2} + \frac{m_\phi y^2}{4\pi}. \tag{5.1.3}$$

The differential cross-section for the process of $R_{\psi\psi} + \phi \to \psi + \psi$ is given by

$$\frac{d\sigma}{d\Omega} = \frac{|V_{fi}|^2}{(2\pi)^2}\mu_\psi |\mathbf{p}|\,, \tag{5.1.4}$$

where $\mathbf{p} \equiv \mu_\psi(\mathbf{p}_{\psi,1}/m_\psi - \mathbf{p}_{\psi,2}/m_\psi)$ is the relative momentum between the two ψ particles. Conservation of energy requires $|\mathbf{p}| = \sqrt{2\mu_\psi(E_B + E_\phi)}$ and the matrix element V_{fi} is defined as:

$$V_{fi} = y\sqrt{\frac{2\pi}{E_\phi}}\int \Psi_i^* \exp(ikr)\,\Psi_f \equiv y\sqrt{\frac{2\pi}{E_\phi}}M_{fi}\,, \tag{5.1.5}$$

where k is the momentum of ϕ. The form of the matrix element differs from the one presented in Chapter 56 of [128]. This is due to the presence of a Yukawa-type interaction, $\mathcal{L} \supset y\phi\bar{\psi}\psi$, instead of the Coulomb interaction that is mediated by the photon, $\mathcal{L} \supset e\bar{\psi}\gamma_\mu\psi A^\mu$. Since we assume the unbound ψ to be non-relativistic, it is sufficient to use the solution of the Schrödinger equation with a positive energy eigenvalue in the description of the unbound final state Ψ_f:

$$\Psi_f = \frac{m_\psi y^2}{4\sqrt{2\pi}|\mathbf{p}|}\frac{\exp(-i|\mathbf{p}|r)}{\sqrt{v\left[1-\exp(2\pi v)\right]}}{}_1F_1\left(1+iv,2,2i|\mathbf{p}|r\right). \tag{5.1.6}$$

Here, we use $v = y^2 m/(8\pi|\mathbf{p}|)$ and only the $l = 0$ component contributes due to the conservation of angular momentum. Furthermore, we assume $\exp(ikr) \approx 1$, which is a good approximation as long as the Yukawa potential can be approximated with a Coulomb potential, which is the case for $m_\phi \ll y^2 m_\psi/(8\pi)$. From Eqs. (5.1.2) and (5.1.6), the integral in Eq. (5.1.5) becomes

$$V_{fi} = -\frac{y^6\sqrt{m_\psi}}{2\sqrt{2}\pi E_\phi^{\frac{5}{2}}}\sqrt{\frac{v}{1-\exp(-2\pi v)}}\frac{\exp\left(2v\arctan\left[v^{-1}\right]\right)}{1+v^2}. \tag{5.1.7}$$

Note that we have made a replacement of $r \to 2r$ in the wave functions ψ_i and ψ_f in the integral (5.1.5), since dr is defined as the position relative to the center of mass of the bound state, whereas the relative position is used before in the bound state wave functions (5.1.2) and (5.1.6). Since we are dealing with a bound state consisting of two particles of equal mass, there is a factor of 2 difference between these two quantities.

Finally, by integrating Eq. (5.1.4) over the solid angle and employing the conservation of the kinetic energy, $E_\phi = \frac{|\mathbf{p}|^2}{2\mu} + \frac{my^2}{64\pi^2} = \frac{|\mathbf{p}|^2}{m_\psi}\left(1+v^2\right)$, the cross section for the non-relativistic BSD is obtained:

$$\sigma = \frac{y^{12}m_\psi^{\frac{5}{2}}\sqrt{E_B+E_\phi}}{2\pi^3 E_\phi^5}\frac{v\exp\left(4v\arctan\left[v^{-1}\right]\right)}{(1-\exp(-2\pi v))\left(1+v^2\right)^2}. \tag{5.1.8}$$

For the BSD of $R_{\bar{\psi}\psi}$, we have to include an additional factor[2] of 1/2 to Eq. (5.1.8). Moreover, it is convenient to rewrite the result in terms of the center-of-mass energy s

[2]The symmetry factor for $R_{\psi\psi}$ is $\frac{1}{2}(2\times 2)^2$, where 1/2 comes from the identical outgoing particles (phase-space integral reduced by 1/2) and (2×2) is owing to the different ways for the Yukawa interaction to annihilate the initial state and create the final state: $<\psi\psi|\phi\bar{\psi}\psi|\phi\psi\psi>$. By contrast, $R_{\bar{\psi}\psi}$ only has a symmetry factor of $(2)^2$ coming from two ways of annihilating and creating the initial state and final state: $<\bar{\psi}\psi|\phi\bar{\psi}\psi|\phi\bar{\psi}\psi>$. As a consequence, there is a relative factor of 2 between the cases of $R_{\psi\psi}$ and $R_{\bar{\psi}\psi}$.

in order to apply Eq. (2.3.20). In the rest frame of the bound state the center of mass energy is $s = m_R^2 + 2m_R E_\phi + m_\phi^2$. Thus, the cross section becomes:

$$\sigma(s) = \frac{2^4 y^{12} m_\psi^{\frac{5}{2}} m_R^5}{\left(s - m_R^2 - m_\phi^2\right)^5} \sqrt{\frac{s + m_R(m_R - 4m_\psi) - m_\phi^2}{2m_R}} \frac{v \exp\left(4v \arctan\left[v^{-1}\right]\right)}{(1 - \exp(-2\pi v))(1 + v^2)^2}, \tag{5.1.9}$$

with

$$v = \frac{y^2 m_\psi}{8\pi |\mathbf{p}|} = \frac{y^2}{8\pi} \sqrt{\frac{2m_\psi m_R}{s + m_R(m_R - 4m_\psi) - m_\phi^2}}\,.$$

Relativistic Case
For the case of relativistic ψ, we follow Chapter 57 of Ref. [128], where results of the hydrogen atom have to be adapted for the Yukawa coupling as above. To calculate the matrix element M_{fi}, defined in Eq. (5.1.5), again the initial and final state wave functions are required. The unbound, outgoing ψ is assumed to be highly relativistic. Therefore, the wave function is taken to be a plane wave:

$$\psi_f = \sqrt{\frac{1}{2E_\psi}} u_f \exp(ipr)\,. \tag{5.1.10}$$

Since the initial state is also relativistic now, the first-order relativistic correction should be included:

$$\psi_i = \left(1 - \frac{i}{2\mu_\psi} \gamma^0 \vec{\gamma} \vec{\bigtriangledown}\right) \frac{u_i}{\sqrt{2\mu_\psi}} \psi_{nr}\,, \tag{5.1.11}$$

where the wave function is derived in Chapter 39 of Ref. [128] and ψ_{nr} is simply the ground state wave function in Eq. (5.1.2). Substituting these equations into (5.1.5) yields

$$M_{fi} = \frac{1}{2\sqrt{\mu E_\psi}} \int d^3x\, \bar{u}_f \left(\gamma^0 - \frac{i}{2\mu_\psi} \vec{\gamma} \vec{\bigtriangledown}\right) u_i \psi_{nr} e^{-i(\mathbf{p}-\mathbf{k})\mathbf{r}}\,, \tag{5.1.12}$$

that results in

$$|M_{fi}|^2 = \frac{y^{10} m_\psi^4}{256\pi^4 E_\psi (\mathbf{p} - \mathbf{k})^4} \bar{u}_f A u_i \left(\bar{u}_f A u_i\right)^\dagger\,, \tag{5.1.13}$$

with

$$A = \frac{\gamma^0}{(\mathbf{p} - \mathbf{k})^2} + \boldsymbol{\gamma} \frac{\mathbf{k} - \mathbf{p}}{2\mu_\psi (\mathbf{k} - \mathbf{p})^2}\,. \tag{5.1.14}$$

Here $\mathbf{k}$ corresponds to the momentum of ϕ and $\mathbf{p}$ stands for the momentum of the unbound ψ in the rest frame of the bound state before the collision. After summing over the final spins and averaging over the initial ones, we obtain

$$\frac{d\sigma}{d\Omega} = \frac{y^{12} m_\psi^5 |\mathbf{p}|}{256\pi^5 E_\phi (\mathbf{p} - \mathbf{k})^6} \left(\frac{E_\psi + m_\psi}{(\mathbf{p} - \mathbf{k})^2} + \frac{E_\psi}{m_\psi^2} - \frac{\mathbf{p}^2 - \mathbf{k}^2}{m_\psi (\mathbf{p} - \mathbf{k})^2}\right)\,. \tag{5.1.15}$$

In contrast to the case of the hydrogen atom, neither of the two particles forming the bound state can be treated at rest in this system. We have to first calculate $\mathbf{k}'$ and $\mathbf{p}'$ in the center-of-mass system of the collision, and then perform a Lorentz boost back into the rest frame of the bound state afterwards. The procedures are lengthy but straightforward, and will not be shown here. Additionally, the integral over the solid angle $d\,\Omega$ in Eq. (5.1.15) can only be computed numerically. The resulting cross section is a function of the center-of-mass energy ($s = m_R^2 + 2m_R E_\phi + m_\phi^2$), the mass of ψ and the Yukawa coupling.

5.2. Asymmetry Transfer between feebly coupled sectors via a Bound State

In this section, we consider a model of two-component asymmetric DM where the two DM components are of very different mass. These kind of models are attractive in the sense that the heavy component that can accumulate in the galactic center or the center of the sun can annihilate in the highly relativistic light component. This, in turn, can enhance the DM-nuclei cross section in direct detection experiments [131–133].
The idea of asymmetric DM [134] is to connect the origin of the DM relic density and the baryon asymmetry of the universe, neither of which can be generated without BSM physics. In such a scenario, only DM particles or antiparticles remain in the universe due to a (broken) global or local symmetry, which is analogous to the procedure of baryogenesis. If the generation mechanisms of those asymmetries are interwoven, they typically lead to comparable amounts of asymmetries in the dark sector and the SM baryons. This, in turn, implies a DM mass of roughly 5 GeV.
If we consider a scenario where we meld those two ideas of asymmetric and two-component DM of different mass, for instance $\sim 1\,\text{GeV}$ and $\gtrsim 100\,\text{GeV}$, we will generate an excessive relic density if the light and heavy component share the same amount of asymmetry as the SM baryons. The problem can be circumvented if the asymmetry generation mechanisms for the two DM species are not related or the amounts of asymmetry are controlled by independent parameters. For instance, they could be generated by decays of two different heavy bosons or of the same heavy boson but with different couplings [3]. In this situation, the number density of the heavy component can be arbitrarily small without exceeding the observed DM density.
In this work, however, we investigate an alternative scenario demonstrating that BSF via a long-ranged mediator can efficiently transfer the asymmetry from the heavy to the light DM sector even in a scenario where the two sectors are only feebly coupled.
In our setup, we have two dark sectors separately containing the heavy DM component ψ and the light DM component χ. Further, we assume that a particle-antiparticle asymmetry was generated by an unspecified mechanism at early times that is shared by χ, ψ and the SM baryons. Realizing a scenario that does not overproduce DM, relies on a long-range interaction among the heavy DM ψ, induced by the Yukawa coupling to a light scalar ϕ. The resulting ψ-$\bar{\psi}$ bound state facilitates the depletion of the symmetric DM component and the remaining asymmetric part is composed of free ψ and the ψ-ψ bound state $R_{\psi\psi}$. As we detail below, the ratio of bound states $R_{\psi\psi}$ to free ψ crucially

[3] It has been demonstrated that asymmetric DM can have a very different mass from GeV in the context of two-sector leptogenesis [135, 136], where the right-handed neutrinos decay both into the SM and DM particles with dissimilar amounts of asymmetry. Models of asymmetric DM with a much heavier mass can also be realized in the context of bosonic technicolor [137].

depends on the binding energy of the bound state. Due to the tiny coupling connecting the two sectors, the bound state is long-lived but eventually decays into a pair of χ via annihilations of the constituents of the bound state. In case of a large Yukawa coupling, a large part of the asymmetry is stored in bound states, leading to a disparity in the number densities $n_\psi \ll n_\chi$. Hence, the corresponding energy densities can be of the same order $\Omega_\chi \sim \Omega_\psi$.

Both DM components are charged under a global $U(1)'$ symmetry to ensure their stability, as all SM particles are singlets under the $U(1)'$. Both χ and ψ are individually in thermal equilibrium with the SM via annihilations into SM fermions that are assumed to be sufficiently efficient to deplete the symmetric components of χ and ψ.

Additionally, there is a real scalar ϕ and complex scalar ϕ'. The particle ϕ is a pure singlet, and mediates the long-range interactions among ψ and $\bar{\psi}$. This interaction results in BSF, $i + j \to R_{ij} + \phi$, where i and j are referring to ψ and/or $\bar{\psi}$, and R_{ij} is the bound state composed of the fields i and j, and BSD, which is the inverse process. On the other hand, ϕ' has a $U(1)'$ charge of -2 and induces an interaction that can shift asymmetry between χ and ψ [4]. The particle content is summarized in Table 5.1. The relevant Lagrangian reads

$$\begin{aligned}\mathcal{L} \supset & - y\,\phi\bar{\psi}\psi - y'\,\phi\bar{f}f - \kappa_\chi\,\phi'\overline{\chi^c}\chi - \kappa_\psi\,\phi'\overline{\psi^c}\psi + \frac{\bar{\chi}\gamma^\mu\chi\bar{f}\gamma_\mu f}{\Lambda_\chi^2} + \frac{\bar{\psi}\gamma^\mu\psi\bar{f}\gamma_\mu f}{\Lambda_\psi^2} \\ & - m_\chi\bar{\chi}\chi - m_\psi\bar{\psi}\psi - \frac{1}{2}m_\phi^2\phi^2 - m_{\phi'}^2\phi'^*\phi' \end{aligned} \tag{5.2.1}$$

where the superscript c denotes charge conjugation. This explicitly indicates that the ϕ'-Yukawa interactions allow for an asymmetry transfer via $\chi\chi\,(\bar{\chi}\bar{\chi}) \leftrightarrow \psi\psi\,(\bar{\psi}\bar{\psi})$. Note that we consider a scenario where the couplings $\kappa_{\chi/\psi}$ are small and therefore do not allow for an efficient direct asymmetry transfer. The two four-fermion effective operators characterize interactions between DM and SM fermions, mediated by an unspecified heavy gauge boson. These interactions not only keep both χ and ψ in the thermal bath but also eliminate the symmetric components of χ and ψ [5] when $T \lesssim m_\chi\,, m_\psi$. In case of $m_\chi \sim$ GeV and $m_\psi \sim$ TeV, one requires $\Lambda_\chi \lesssim 350\,\text{GeV}$ and $\Lambda_\psi \lesssim 6.5\,\text{TeV}$ to annihilate away the symmetric components. To avoid potential experimental constraints on the underlying gauge boson, one can simply assume the gauge boson only couples to the third-generation SM fermions. We do not specify the identity of the gauge boson, as the details of the interactions are not relevant to our discussions as long as the resulting cut-off scales Λ_χ and Λ_ψ are small enough to keep the interactions in equilibrium.

The real scalar ϕ decays into SM fermions via the Yukawa coupling y' [6] if kinematically allowed. Those decays keep ϕ in thermal equilibrium with the SM until T drops well below m_ϕ. As mentioned above, the bound states form in the ψ sector due to the Yukawa interaction with ϕ. Since the interaction is always attractive among particles

[4] Instead of including ϕ', one can assume feeble $\psi\psi \to \bar{f}f$ which breaks the $U(1)'$ symmetry and makes the bound state decay at a later time, reducing Y_ψ to achieve $\Omega_\psi \sim \Omega_\chi$. In this case, the stability of ψ is still protected by a residual Z_2 symmetry. Notwithstanding, the freeze-in process of $\psi\psi \to \chi\chi$ under consideration can give rise to boosted χ which entails rich phenomenological consequences.

[5] The heavy component ψ has an additional annihilation channel $\bar{\psi}\psi \to \phi\phi$.

[6] The coupling can arise, e.g., via the mixing between the SM Higgs boson and ϕ, leading to $y' \approx y_f^{\text{SM}} \sin\theta$, where θ is the mixing angle and y_f^{SM} is the SM Yukawa coupling. To ensure ϕ is in the thermal bath for $T \lesssim m_\phi \sim$ GeV (scale of interest in this work), we have $y' \gtrsim 10^{-9}$, indicating $\sin\theta \gtrsim 10^{-7}$, depending on the final state fermions. Such a small mixing angle is well below the current experimental sensitivity.

	χ	ψ	ϕ	ϕ'
Mass	$\mathcal{O}$ (GeV)	$\mathcal{O}$ ($\gtrsim$ 100 GeV)	$\lesssim$ GeV	$>$ TeV
$U(1)_D$	$+1$	$+1$	0	-2

Table 5.1.: The particle contents in the dark sectors where all particles are singlets under the SM gauge groups. See the text for details.

and antiparticles, there exist three types of the bound states: $R_{\psi\psi}$, $R_{\bar{\psi}\bar{\psi}}$ and $R_{\bar{\psi}\psi}$. We only consider the ground state with a binding energy given in Eq. (5.1.3). The bound state mass results in $m_R = 2m_\psi + E_B$, with $m_{R_{\psi\psi}}$=$m_{R_{\bar{\psi}\bar{\psi}}}$=$m_{R_{\bar{\psi}\psi}} \equiv m_R$. The three types of bound states are not stable. The $R_{\bar{\psi}\psi}$ bound state decays quickly into either a pair of ϕ or SM fermions. The $R_{\psi\psi}$ and $R_{\bar{\psi}\bar{\psi}}$ bound states decay into a pair of χ or $\bar{\chi}$ mediated by the $U(1)'$ charged scalar ϕ'. Due to the asymmetry in the ψ sector and the efficient annihilation $\bar{\psi}\psi \to \bar{f}f$, for temperatures $T < m_\psi$ only $R_{\psi\psi}$ exists if $n_\psi > n_{\bar{\psi}}$ initially.
In the following, we first detail how the asymmetry is shifted between the free ψ, bound states $R_{\psi\psi}$ and χ in Section 5.2.1. Afterwards, in Section 5.3, we present the results of a numerical solution of the Boltzmann equation for the species ϕ, ψ, $\bar{\psi}$, $R_{\psi\psi}$, $R_{\bar{\psi}\bar{\psi}}$ and $R_{\bar{\psi}\psi}$ considering the interactions of BSF, BSD, $\bar{\psi}\psi \leftrightarrow \bar{f}f$, $\bar{\psi}\psi \leftrightarrow \phi\phi$, $R_{\bar{\psi}\psi} \leftrightarrow \phi\phi$, $R_{\psi\psi} \leftrightarrow \chi\chi$ ($R_{\bar{\psi}\bar{\psi}} \leftrightarrow \bar{\chi}\bar{\chi}$) and $\phi \leftrightarrow \bar{f}f$.

5.2.1. Asymmetry Transfer

In this Section, we give a qualitative discussion of the asymmetry transfer between the different sectors, which is schematically illustrated in Figure 5.1. Further, the time evolution of the densities of the relevant species are shown in Fig. 5.2, in which for demonstration we choose $(m_\psi, m_{\phi'}, \Lambda_\psi) = (1, 10, 10)$ TeV with a massless ϕ and f, and $(y, \kappa_\chi, \kappa_\psi) = (1, 10^{-4}, 10^{-4})$, implying a binding energy of $|E_B| = 1.58$ GeV. The solid green (red, blue) line corresponds to Y_ϕ (Y_ψ, $Y_{R_{\psi\psi}}$), while the dashed red (blue) line represents $Y_{\bar{\psi}}$ ($Y_{R_{\bar{\psi}\bar{\psi}}}$ and $Y_{R_{\bar{\psi}\psi}}$[7]). The vertical dashed grey lines mark the absolute value of the binding energy and the catch-up temperature, defined below. For $T \lesssim 10^{-2}$ GeV, the light (dark) blue line refers to the case of stable (decaying) $R_{\psi\psi}$. Subsequently, we describe the different phases and effects taking place in the time evolution of the system illustrated in Figure 5.2.

1. At a high temperature $T \gg m_\psi$, both χ and ψ are in thermal equilibrium with the SM. An unspecified mechanism is presumed to generate asymmetries in χ, ψ and the SM baryons, for instance by the out-of-equilibrium decays of heavy gauge or Higgs bosons [138–141]. In addition, we assume that the total initial asymmetry of the three sectors adds up to zero:

$$\Delta Y_B + \Delta Y_\psi^i + \Delta Y_\chi^i = 0\,, \tag{5.2.2}$$

where the superscript i refers to the initial values and $\Delta Y_f \equiv Y_f - Y_{\bar{f}}$. Furthermore, it is assumed that the generated baryon asymmetry accounts for the observed value, i.e. $\Delta Y_B = (8.6 \pm 0.7) \times 10^{-11}$ [10] and remains constant once being created[8]. In

[7] The lines corresponding to $Y_{R_{\bar{\psi}\bar{\psi}}}$ and $Y_{R_{\bar{\psi}\psi}}$ are on top of each other.
[8] In fact, our conclusions do not rely on these assumptions.

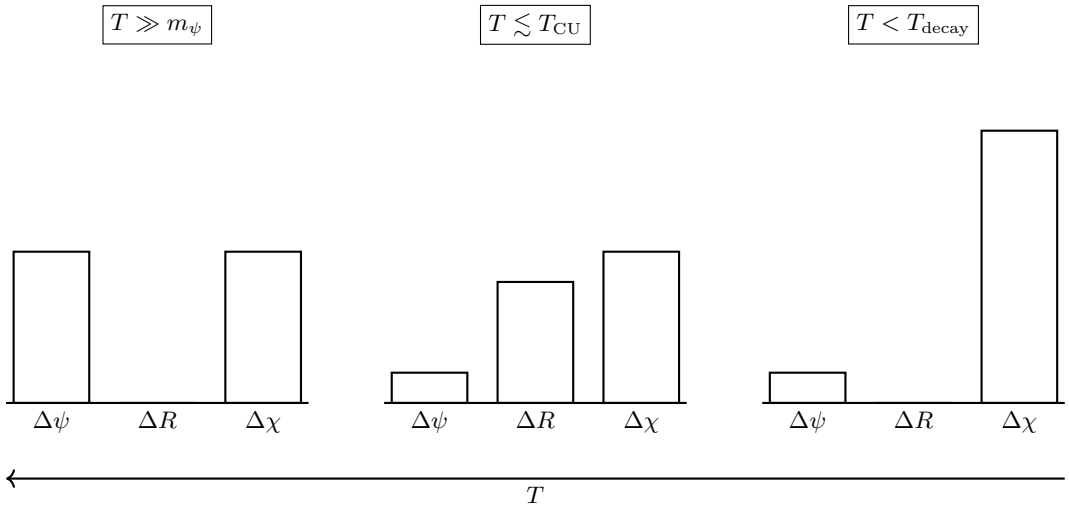

Figure 5.1.: Illustration of the asymmetry transfer between the heavy (ψ) and light (χ) DM components with the help of the bound state R. At a high temperature, an asymmetry is generated and shared by both the dark and SM sectors. Below the temperature $T_{\rm CU}$ (catch-up temperature at which $Y_R = Y_\psi/2$), more than half of the ψ asymmetry has been stored in the bound states. The bound states later decay into χ, thereby transferring the majority of the asymmetry from ψ into χ, leading to $Y_\chi \gg Y_\psi$ but with $\Omega_\chi \approx \Omega_\psi$ as $m_\psi \gg m_\chi$.

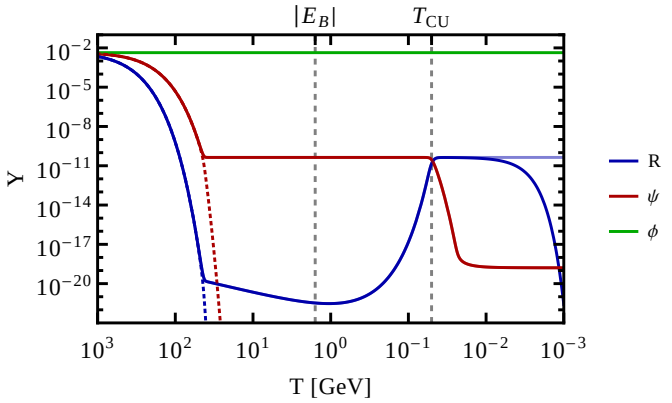

Figure 5.2.: The time evolution of the densities for particles in the dark sectors, where $(m_\psi, m_{\phi'}, \Lambda_\psi) = (1, 10, 10)$ TeV with a massless ϕ and $(y, \kappa_\chi, \kappa_\psi) = (1, 10^{-4}, 10^{-4})$ are assumed. The solid green (red, blue) line represents Y_ϕ (Y_ψ, $Y_{R_{\psi\psi}}$). The dashed red (blue) line refers to $Y_{\bar\psi}$ ($Y_{R_{\bar\psi\bar\psi}}$ and $Y_{R_{\bar\psi\psi}}$), demonstrating that the symmetric components are annihilated away. The horizontal light blue line at small T stands for the case of a stable $R_{\psi\psi}$, while the final density of ψ (red line) is unaffected by the decay, as BSF already ceases before the onset of the decay.

the following, we set $\Delta Y_\psi^i \sim \Delta Y_\chi^i > 0$, which directly implies that there exist more ψ (χ) than $\bar{\psi}$ ($\bar{\chi}$).

2. The processes of BSF and BSD are efficient for a large part of the time period of interest. In this case, Eq. (2.3.17) implies

$$\frac{n_\psi^2}{\left(n_\psi^{\mathrm{eq}}\right)^2} \approx \frac{n_{R_{\psi\psi}}}{n_{R_{\psi\psi}}^{\mathrm{eq}}} \frac{n_\phi}{n_\phi^{\mathrm{eq}}} \,. \tag{5.2.3}$$

   Hence, R follows its equilibrium density when $T \gtrsim m_\psi$, as both ψ and ϕ are in thermal equilibrium with the SM.

3. For $|E_B| \lesssim T \lesssim m_\psi$, the production of $\bar{\psi}$ and ψ out of ϕ and SM fermions is kinematically suppressed compared to the annihilation of $\bar{\psi}$ and ψ into SM particles. Thus, the number density of ψ experiences a Boltzmann suppression. At a certain point in time, when the equilibrium number density of ψ becomes smaller than the asymmetry stored in ψ, the symmetric component of ψ has been mostly obliterated. Hence only the asymmetric component remains, which in our case are ψ particles. The depletion of the symmetric component of the bound states takes place at roughly the same time, since the number densities, due to the efficient BSF, are connected by Eq. (5.2.3). In our example, this occurs around $T = 41\,\mathrm{GeV}$ but with $Y_{R_{\psi\psi}} \ll Y_\psi$ because the bound state density experiences a double Boltzmann suppression due to $\exp(-m_R/T) \approx \exp(-2m_\psi/T) \ll \exp(-m_\psi/T)$. The relative suppression can alternatively be understood by inspecting Eq. (5.2.3), which results in $n_R \sim (m_\psi T)^{-3/2}(n_\psi)^2 \ll n_\psi$, given $n_\phi = n_\phi^{\mathrm{eq}}$.

4. For $T \lesssim |E_B| + m_\phi$, we observe a sharp increase in the density $Y_{R_{\psi\psi}}$, leading to catch-up with the density Y_ψ, as shown in Fig. 5.2. The catch-up behavior can be perceived via the interplay between the BSF and the conservation of the total asymmetry. While the process $\psi\psi \leftrightarrow R_{\psi\psi}\,\phi$ changes the number densities of $R_{\psi\psi}$ and ψ individually, the total asymmetry remains constant before $R_{\psi\psi}$ decays:

$$\Delta Y_\psi^i = Y_\psi + 2Y_R \,. \tag{5.2.4}$$

   Furthermore, if the interactions caused by $\phi\bar{f}f$ in Eq. (5.2.1) are faster than the expansion rate of the universe, ϕ is in equilibrium with the SM, resulting in $n_\phi = n_\phi^{\mathrm{eq}}$. As a consequence, combining Eq. (5.2.3) and (5.2.4), we can extract the number density of $R_{\psi\psi}$, provided that BSF and BSD are effective:

$$Y_R = \frac{\Delta Y_\psi^i}{2} + \mathcal{R}\left(1 - \sqrt{1 + \frac{\Delta Y_\psi^i}{\mathcal{R}}}\right) , \tag{5.2.5}$$

   with

$$\mathcal{R} = \frac{\left(n_\psi^{\mathrm{eq}}\right)^2}{8 n_R^{\mathrm{eq}} s_{\mathrm{en}}} \,. \tag{5.2.6}$$

For small temperatures we find $\mathcal{R} \sim (m_\psi/T)^{-\frac{3}{2}} \exp\left(-\frac{|E_B|}{T}\right) \to 0$ in the limit of $T \to 0$, and consequently $Y_R \overset{T\to 0}{=} \frac{\Delta Y_\psi^i}{2}$. Thus, BSF is favored over BSD and the asymmetry would be transferred completely to the bound states if the BSF was efficient for all times. The reason behind this effect is that when the temperature falls below $|E_B|$, it becomes less and less likely that a ϕ particle has a sufficiently large energy to overcome the binding energy, which is a requirement to break the bound state. A larger Yukawa coupling and hence a larger $|E_B|$, will therefore cause a larger fraction of ψ particles to be converted into $R_{\psi\psi}$. This eventually leads to more asymmetry being stored in χ after $R_{\psi\psi}$ decays. In this sense, the existence of the bound states allows for two-component asymmetric DM of very different mass scales but with comparable energy densities. In fact, the situation here is comparable to the period of recombination at which electrons and protons started to form neutral hydrogen atoms. In case of a massive ϕ, its number density also experiences an exponential suppression at $T < m_\phi$ such that the absence of ϕ particles renders BSD ineffective.

5. We define the catch-up temperature $T_{\rm CU}$ as the temperature when the asymmetry is equally shared by $R_{\psi\psi}$ and free ψ, which translates to $Y_\psi/2 = Y_{R_{\psi\psi}}$ at $T = T_{\rm CU}$. By setting $Y_R = \Delta Y_\psi^i/4$ in Eq. (5.2.5), the value of $T_{\rm CU}$ can be numerically calculated. In our exemplary case shown in Fig. 5.2, we find $T_{\rm CU} = 0.05$ GeV. Assuming $m_\phi = 0$, we found an empirical expression for $T_{\rm CU}$ that results in

$$T_{\rm CU} \approx 0.03\,|E_B|\,y^{1/5}\,, \tag{5.2.7}$$

and has an accuracy above 90 % for $0.1 \lesssim y \lesssim 5$.

6. During the catch-up of the bound state, the ψ density decreases and it becomes harder and harder for them to find each other to form a bound state. Eventually, below a certain temperature, denoted by $T_{\rm D}$, BSF ceases to work, similar to the freeze-out of thermal DM. The temperature T_D depends on the parameters m_ϕ and y and in our example T_D is around 12 MeV, below which Y_ψ stops decreasing and levels off as shown in Fig. 5.2. The asymmetry stored in the bound states after the asymmetry transfer is given by $Y_{R_{\psi\psi}}(T_{\rm D})$, while the final asymmetry stored in ψ, represented by ΔY_ψ^f, is simply $Y_\psi(T_{\rm D})$. After the decay of $R_{\psi\psi}$, the final χ asymmetry is given by

$$\Delta Y_\chi^f = -\Delta Y_B - \Delta Y_\psi^f\,, \tag{5.2.8}$$

where we have used Eq. (5.2.2) and

$$\Delta Y_\chi^i + \Delta Y_\psi^i = \Delta Y_\chi^f + \Delta Y_\psi^f\,. \tag{5.2.9}$$

As a result, the ratio of the total energy density of DM to that of the SM baryons reads

$$\frac{\Omega_{\rm DM}}{\Omega_B} = \left|\frac{\Delta Y_\psi^f}{\Delta Y_B}\right| \frac{m_\psi - m_\chi}{m_B} + \frac{m_\chi}{m_B}\,, \tag{5.2.10}$$

and in order to reproduce the observed relic density

$$\left|\frac{\Delta Y_\psi^f}{\Delta Y_B}\right| = \frac{m_B}{m_\psi - m_\chi}\left(\frac{\Omega_{\rm DM}}{\Omega_B} - \frac{m_\chi}{m_B}\right) \overset{m_\psi \gg m_\chi}{=} \frac{m_\chi}{m_\psi}\left[\frac{m_B}{m_\chi}\frac{\Omega_{\rm DM}}{\Omega_B} - 1\right], \tag{5.2.11}$$

must be met. If we further require that the energy densities of ψ and χ are comparable ($m_\psi \Delta Y_{\psi,f} \sim m_\chi \Delta Y_{\chi,f}$), the mass of χ can be inferred

$$m_\chi \sim \frac{m_\psi m_B}{2m_\psi - m_B \frac{\Omega_{\rm DM}}{\Omega_B}} \frac{\Omega_{\rm DM}}{\Omega_B} \overset{m_\psi \gg m_B}{=} m_B \frac{\Omega_{\rm DM}}{2\,\Omega_B} = 2.66\,\text{GeV}\,. \tag{5.2.12}$$

This implies

$$\left|\frac{\Delta Y_\psi^f}{\Delta Y_B}\right| \sim \frac{m_\chi}{m_\psi}, \tag{5.2.13}$$

given $\Omega_{\rm DM} = 5.4\,\Omega_B$ and $m_B \approx 1$ GeV. Therefore, the final density of ψ (solid red line) in Fig. 5.2 is too small to have any impact on the relic density.

To summarize, when the temperature falls below m_ψ, the symmetric components of ψ and R will be destroyed by the processes of $\bar{\psi}\psi \to \phi\phi\,, \bar{f}f$ and $R_{\bar{\psi}\psi} \to \phi\phi$, and only the asymmetric component remains. Further, we find $Y_\psi \gg Y_{R_{\psi\psi}}$ due to the larger Boltzmann suppression of the bound state. At $T \lesssim |E_B|$, $Y_{R_{\psi\psi}}$ begins to catch-up with Y_ψ caused by the lack of energetic ϕ that are mandatory to dissociate the bound state, resulting in BSF being kinematically preferred over BSD. With the continuous decrease in Y_ψ, the BSF eventually becomes ineffective since the BSF rate is proportional to Y_ψ^2. Afterwards, the density Y_ψ stays constant, while the bound state decays into a pair of χ. The Yukawa coupling y determines when BSF stops and therefore the final value of Y_ψ. In the following, we discuss the conditions for realizing two-component asymmetric DM with comparable energy densities in case of different mass scales for the two DM components. Throughout our analyses, we always assume $m_\chi = 2.66$ GeV unless stated otherwise.

5.3. Numerical Solution to the Boltzmann Equation

In this Section we present numerical solutions of the coupled Boltzmann equations involving the (anti)particles of ψ and R as well as ϕ. Firstly, we discuss the individual effects of the Yukawa coupling y, the mediator mass m_ϕ and the decay width $\Gamma_{R_{\psi\psi}}$ on the amounts of asymmetry that are stored in ψ and $R_{\psi\psi}$ (χ) eventually. Subsequently, we present four benchmark scenarios, where the correct relic density is reproduced with $\Omega_\chi \sim \Omega_\psi$.

5.3.1. Effect of the Yukawa coupling y

The effect of a varying Yukawa coupling y on the final number densities of ψ and $R_{\psi\psi}$ is illustrated in Fig. 5.3, where we present numerical solutions to the Boltzmann equation for the Yukawa couplings $y = (0.2, 0.3, 0.4)$, while assuming a massless ϕ, a TeV ψ and a stable bound state with an initial condition of $\Delta Y_\psi^i = \Delta Y_B$ at high T. The final

abundance of ψ decreases as y increases. As the BSF cross section is proportional to y^{12}, a larger Yukawa coupling corresponds to a significantly larger BSF rate. Hence more ψ form bound states, which implies a smaller final density for ψ. Besides, from Eq. (5.2.7) we know that the catch-up temperature scales as $|E_B| y^{1/5} \sim y^{21/5}$. Thus, a larger Yukawa coupling causes an earlier catch-up as shown in Figure 5.3. For $y = 0.2$, the BSF processes cease to work for a temperature $T > T_{\mathrm{CU}}$. Thus, in this scenario only a negligible amount of asymmetry is transferred to the bound states. However, given a mass of the heavy DM component m_ψ that exceeds multiple GeVs, a sizable asymmetry transfer is required to not overproduce DM energy density. Consequently, for a given m_ψ, a lower bound on the value of y is implied.

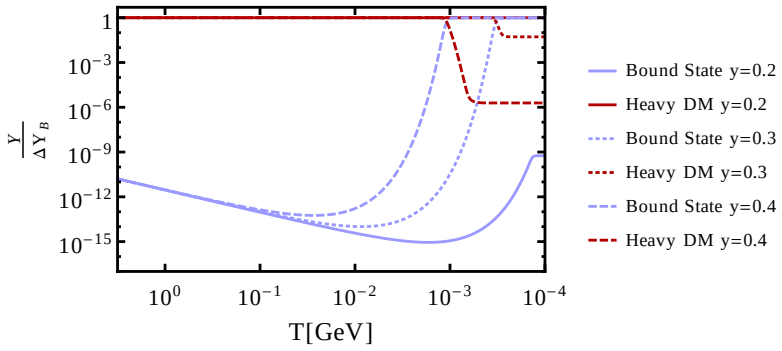

Figure 5.3.: The numerical solutions of the Boltzmann equations for the Yukawa couplings $y = (0.2, 0.3, 0.4)$, given $m_\chi = 2.66\,\mathrm{GeV}$, $m_\psi = 1\,\mathrm{TeV}$ and $\Gamma_{R_{\psi\psi}} = 0$ with a massless ϕ. The red (blue) lines represent the number density of ψ ($R_{\psi\psi}$) normalized to the baryon density. The different line styles correspond to the different values of y. Comparable energy densities $\Omega_\chi \approx \Omega_\psi$ can be accommodated by taking $y \approx 0.33$. The initial condition of $\Delta Y_\psi^i = \Delta Y_B$ at large T is presumed.

For instance, in case of $m_\chi = 2.66$ GeV and $m_\psi = 1$ TeV, the Yukawa coupling must satisfy $y \sim 0.33$ to reproduce a correct value of ΔY_ψ^f that fulfills Eq. (5.2.13) and additionally attains $\Omega_\psi \sim \Omega_\chi$. The corresponding plummet of Y_ψ for the cases of $y = 0.3$ and $y = 0.4$ takes place around $T \lesssim 1$ MeV. The bound states eventually decay and potentially create highly energetic χ particles below the scale of the BBN that occurs at temperatures of roughly 1 MeV. Moreover, if the presumed asymmetry generation mechanism instead creates more $\bar{\chi}$ than χ, then annihilations of the χ resulting from the bound state decay with pre-existing $\bar{\chi}$ into the SM fermions will potentially inject a sizable amount of entropy into the thermal bath. Thus, as described Section 2.4.3, the model possibly disturbs the BBN [142–144].

Since most of the bound states are produced around $T = T_{\mathrm{CU}}$, we have to raise T_{CU} above temperatures of a MeV such that the subsequent decay of the bound state takes place before the onset of the BBN. Naively thinking, one may enlarge y, which in return leads to an earlier catch-up and also puts an end to BSF above the BBN scale. The increase on y, nonetheless, will also decrease significantly the final density Y_ψ. Note, for instance that there is a difference of more than four orders of magnitude in Y_ψ^f between the cases of $y = 0.3$ and $y = 0.4$, resulting in $\left|\Delta Y_\psi^f / \Delta Y_B\right| \ll m_\chi / m_\psi$ and hence

$\Omega_\psi \ll \Omega_\chi$. One possibility to avoid this issue is to allow for a massive mediator ϕ in combination with a large value of y as discussed below.

5.3.2. Effect of a non-zero mediator mass

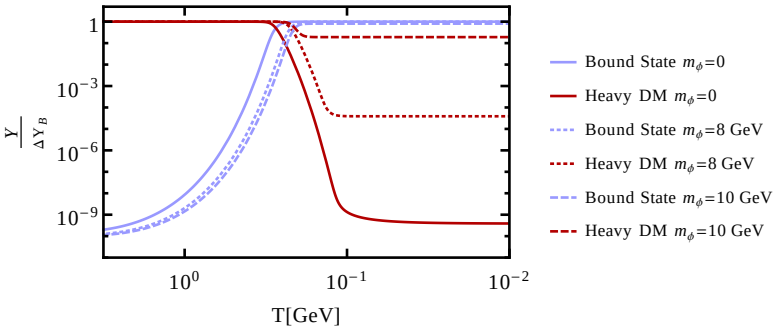

Figure 5.4.: The solutions of the Boltzmann equations for $m_\psi = 1\,\text{TeV}$, $y = 1.5$ and the different values of $m_\phi = (0, 8, 10)$ GeV. We find a binding energy, which partially depends on m_ϕ as shown in Eq. (5.1.3), of roughly 8 GeV. The red (blue) lines represent the number density of ψ ($R_{\psi\psi}$) normalized to the baryon asymmetry. The different styles of the lines correspond to the different mediator masses. The density Y_ψ^f increases with a larger m_ψ, and the mass dependence is striking.

The final densities of ψ and $R_{\psi\psi}$ depend on the value of the decoupling temperature T_D below which BSF stops. In case of a massless ϕ, the BSF process $\psi\psi \to R_{\psi\psi}\phi$ is always kinematically allowed since $2\,m_\psi > m_R$. However, it becomes ineffective when Y_ψ is diminutive, as the interaction rate scales with y_ψ^2. Increasing Y_ψ^f requires to halt BSF earlier. Considering $m_\phi > |E_B|$, in addition to the suppression induced by the small number density of free particles, BSF also suffers from a kinematical suppression by virtue of $2\,m_\psi < m_R + m_\phi$ when $T < m_\phi$, leading to a higher T_D and hence a larger Y_ψ^f. Figure 5.4 illustrates that a larger mass of ϕ gives rise to a larger final density of ψ. For the density evolution displayed in Figure 5.4, we fixed $y = 1.5$ and $m_\psi = 1$ TeV with the same initial condition $\Delta Y_\psi^i = \Delta Y_B$ as above. The dependence of the final density Y_ψ^f on the mass m_ϕ is quite remarkable. An increase of m_ϕ from 8 to 10 GeV is accompanied by a factor of nearly 10^4 on the final density of ψ. Conversely, the catch-up temperature T_CU decreases in the presence of massive ϕ, as shown in Fig. 5.4. This effect can be understood by noticing that $Y_{R_{\psi\psi}}$ begins to rise when ϕ no longer has enough energy to break apart the bound states. As the mass of ϕ itself can also be used to destroy the bound states, involving a massive ϕ delays the catch-up and in turn lowers T_CU. As a result, a large value of y together with a nonzero mass of ϕ with $m_\phi \gtrsim |E_B|$ is necessary to increase both T_CU and T_D. In this way, it can be ensured that the majority of the bound states decays before the BBN, while attaining a sizable final density of free ψ.

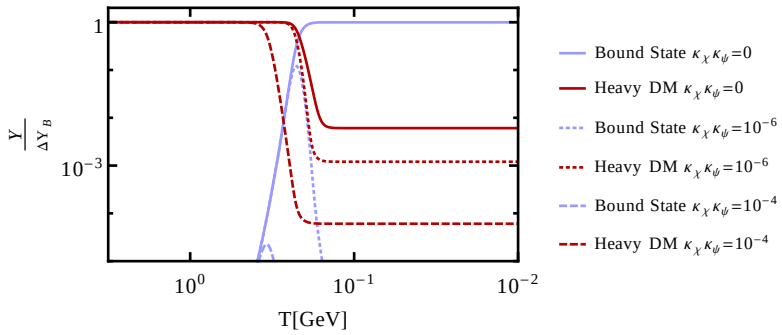

Figure 5.5.: The results of the Boltzmann equations, given $m_\psi = 1\,\text{TeV}$, $m_\phi = 9\,\text{GeV}$, $y = 1.5$ and different values of $\kappa_\chi\kappa_\psi = \left(0, 10^{-6}, 10^{-4}\right)$, that correspond to different decay widths $\Gamma_{R_{\psi\psi}}$ as $\Gamma_{R_{\psi\psi}} \sim (\kappa_\psi\kappa_\chi)^2$. The red (blue) lines represent the number density of ψ ($R_{\psi\psi}$) normalized to the baryon density.

5.3.3. Effect of a non-zero Decay Width

Lastly, we study the influence of the bound state decay width on the final densities of ψ and χ. The effect is illustrated in Fig. 5.5, again using the same initial condition $\Delta Y_\psi^i = \Delta Y_B$. The decay eliminates the bound state population and stops BSD at an earlier time, which in turn leads to a larger T_{CU}, when compared to the situation of a stable $R_{\psi\psi}$, since there are fewer bound states left to dissociate. That is to say, only BSF is active and causes more ψ being converted into the bound states that subsequently decay into χ. Note that if the bound state decays only after BSF ceases to work, the final ψ density will not be affected by the decay as displayed in Fig. 5.2.

The decay width of $R_{\psi\psi}$ is partially controlled by the product of the couplings κ_χ and κ_ψ. In Fig. 5.5, the decay takes place during the catch-up period, and a larger decay width corresponds to fewer ψ but more χ particles – increasing the product $\kappa_\chi\kappa_\psi$ from 10^{-6} to 10^{-4} makes Y_ψ^f more than ten times smaller. Again, we focus on feebly coupled scenarios where $\psi\psi \leftrightarrow \chi\chi$ was not in thermal equilibrium at high T and therefore cannot transfer asymmetry from one sector into the other.

5.3.4. Benchmark Scenarios

To conclude, we present four benchmark sets of the parameters, listed in Table 5.2, which are capable of reproducing the observed Ω_{DM} with $\Omega_\chi \approx \Omega_\psi$. The corresponding

m_χ[GeV]	m_ψ[GeV]	m_ϕ[GeV]	$m_{\phi'}$[GeV]	y	κ_ψ	κ_χ
2.66	10000	5.7	10000	0.75	$3 \cdot 10^{-4}$	$3 \cdot 10^{-4}$
2.66	1000	9	1000	1.5	$1.2 \cdot 10^{-4}$	$1.2 \cdot 10^{-4}$
2.66	500	8.25	500	1.75	$1.5 \cdot 10^{-4}$	$1.5 \cdot 10^{-4}$
2.66	100	5.75	100	2.5	$7 \cdot 10^{-5}$	$7 \cdot 10^{-5}$

Table 5.2.: Sets of parameters reproducing the observed relic density with comparable energy densities for ψ and χ, assuming the initial condition $\Delta Y_\chi^i = \Delta Y_\psi^i = -\Delta Y_B/2$.

time evolution of the particle densities is shown in Fig. 5.6. The mass of χ is fixed

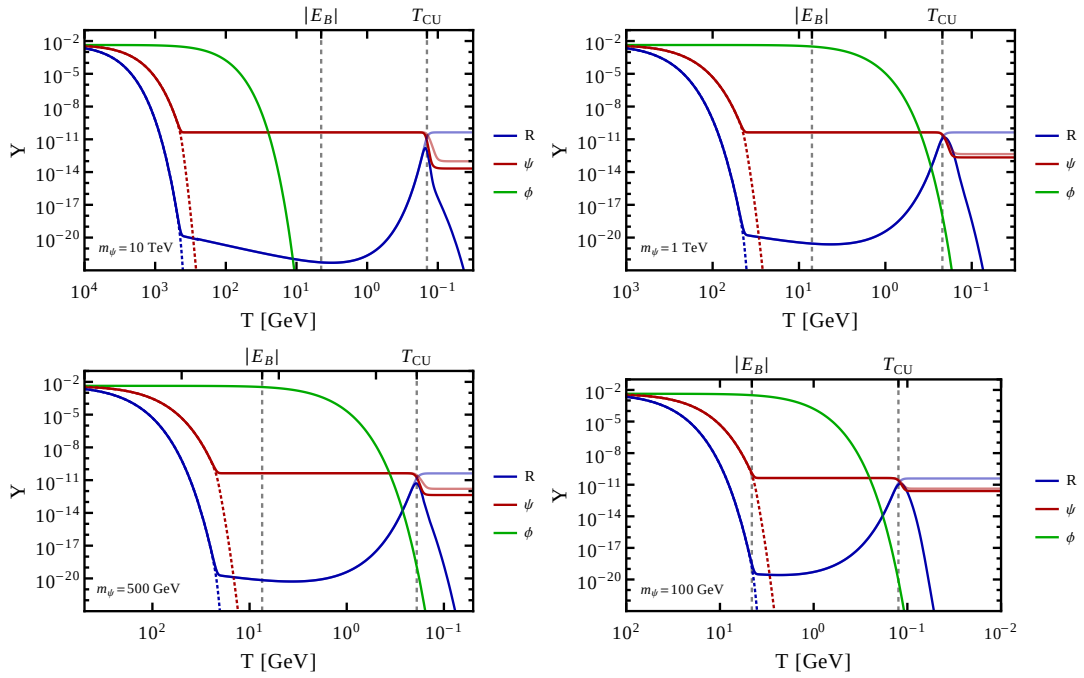

Figure 5.6.: The results of the Boltzmann equations with $m_\psi = 10\,\text{TeV}$ (upper left panel), $m_\psi = 1\,\text{TeV}$ (upper right), $m_\psi = 500\,\text{GeV}$ (bottom left) and $m_\psi = 100\,\text{GeV}$ (bottom right). These plots are similar to Fig. 5.2 but with $\Omega_\chi \approx \Omega_\psi$. We choose $\Delta Y_{\psi_i} = \Delta Y_{\chi_i} = -\Delta Y_B/2$ as the initial condition at large T. The symmetric components of ψ and R are rapidly depleted via the annihilations into ϕ and the SM fermions. The relative distribution of the final asymmetric components of ψ and R is determined by when BSF and BSD decouple. Finally, the bound state decay shifts asymmetry into χ.

at 2.66 GeV, while m_ψ ranges from 100 GeV to 10 TeV. It is assumed that the initial asymmetry created at $T \gg m_\psi$ is initially distributed as $\Delta Y_\chi^i = \Delta Y_\psi^i = -\Delta Y_B/2$. The rest of parameters are chosen to fulfill $\Omega_\chi \approx \Omega_\psi$. To ensure that $R_{\psi\psi}$ decays before the onset of the BBN, $T_{\rm CU} \gtrsim 1\,\text{MeV}$ is mandatory. As the catch-up temperature $T_{\rm CU}$ scales as $|E_B|\, y^{1/5} \sim m_\psi\, y^{21/5}$, a smaller m_ψ requires a larger value of y, as demonstrated in Table. 5.2. However, due to the fact that the density Y_ψ^f is extremely sensitive to y, as illustrated in Fig. 5.3, a considerable value of y will often make the final density of ψ vanishingly small. Therefore, as discussed in Section 5.3.2, a massive ϕ with $m_\phi \gtrsim |E_B|$ is involved to disrupt the BSF, preventing an utter depletion of ψ. In fact, we have found that for $m_\psi \lesssim \mathcal{O}(\text{TeV})$, a massive ϕ is requisite to obtain $\Omega_\chi \sim \Omega_\psi$.
Lastly, the product $\kappa_\chi \kappa_\psi$, that determines the decay width of $R_{\psi\psi}$, has to be chosen such that the correct relic density is obtained and the bound states decay before the onset of the BBN.

5.4. Conclusion

In this Chapter, we investigated the dynamics of a long-lived Yukawa bound state that can form in a dark sector. The setup is comparable to the one of recombination where

hydrogen was formed out of protons and electrons. However, there are some key differences. Firstly, the underlying interaction allowing for BSF is a Yukawa interaction instead of the Coulomb interaction. Hence in addition to particle-antiparticle bound states, particle-particle bound states can arise. Further, in contrast to neutral hydrogen, the resulting bound states are not stable and decay eventually due to feeble interactions with less massive particles. Lastly, the particle mediating the interaction can be massive.

We demonstrated that the presence of a Yukawa bound state in a heavy dark sector can compensate a feeble portal coupling and efficiently transfer particles from a heavy sector into a less massive one, given a sizable Yukawa coupling and hence efficient BSF. The basic reason for this phenomenon is that the bound state confines its constituents close to each other, thereby eliminating the number density suppression that otherwise renders the direct annihilation of these particles inefficient. In this sense, a large DM self interaction can eliminate the barrier of a small DM coupling to a different less massive sector. In the context of the DM portal models discussed in Section 2.3, the effects discussed in this Chapter are especially interesting for models that utilize DM production mechanisms that rely on a large DM-mediator interaction, hence the reannihilation and the dark freeze-out regime.

We applied this variant of particle number transfer to a model of two-component asymmetric DM. A common feature of existing asymmetric DM models is that the baryon asymmetry is closely correlated with that of DM, and quite often the amounts of asymmetry stored in the DM and SM sectors are of the same order, implying the DM mass is of order $\mathcal{O}(\mathrm{GeV})$ given $\Omega_{\mathrm{DM}} = 5.4\,\Omega_B$. In the framework of two-component asymmetric DM, if an asymmetry created at an early time is equally shared among a light DM component χ, a heavy DM component ψ and the SM baryons, the energy density of the heavy ψ alone will certainly exceed the observed DM energy density. The ψ and χ sectors are only feebly coupled and therefore a direct asymmetry transfer is not efficient. The ψ however, can form bound states due to a Yukawa interaction via a light mediator ϕ. Depending on the value of the bound state forming Yukawa coupling y, the asymmetry partially gets stored in the bound states and is eventually transferred to the χ sector via late decays. The process of asymmetry transfer is illustrated in Figure 5.1. Moreover, we found several benchmark points, summarized in Table 5.2, that succeed in creating a scenario of asymmetric two-component DM of different mass but comparable energy densities. Such a setup might have interesting phenomenological implications in the context of boosted DM searches that are not investigated here but can serve as a subject of future work.

6. A Systematic Analysis of One-Loop Solutions to R_K in the Light of Dark Matter

In this chapter, we present the first results of the analysis of a class of models addressing the observed 2.6σ discrepancy [20] with the SM in the observable R_K [145] in the light of the observed DM relic density. More precisely we investigate if the anomaly in R_K and the relic density can be simultaneously explained by the considered class of models without contradicting the current direct detection limits provided by XENON1T [10, 146]. While we only present the results of one specific model in this work, the complete study will be given in the forthcoming publication [5].
The anomaly in R_K has been addressed extensively in the past, including very different approaches, for instance the tree level exchange of leptoquarks [17, 147–149], possibly emerging from a grand unified theory, or via the introduction of a new $U(1)$ gauge group [150, 151].
Our work builds on a class of models introduced in [152]. The authors analyze a scenario where contributions to $b \to s\mu\mu$ are realized at one-loop level via three new particles charged under the SM gauge groups. Allowing for representations up to the adjoint of each SM gauge group, they find and analyze 48 different models. Several of those models include an electrically neutral color singlet, which if stabilized by a symmetry[1], can be a valid DM candidate. In this work, we enlarge the analysis of this class of models and address the question if both the R_K anomaly and the observed DM relic density can be explained within this framework, provided the models include a bosonic or fermionic singlet.
Typically, in this setup, explaining the R_K anomaly requires a relatively large coupling of the new particles to μ's, since, in comparison to tree level realizations, the one-loop suppression has to be compensated. Additionally, the coupling of the new particles to the b and the s quark is constrained by B-$\overline{B}$ mixing. This, in return, can lead to an underpopulated dark sector, as the strong coupling to μ's delays the thermal freeze-out. Moreover, the large coupling to μ's can generate a large vector coupling of DM to the Z at one-loop level that is subject to the constraints from the XENON1T experiment [146]. However, in models with a fermionic singlet DM candidate, DM can be either a Dirac or Majorana particle, where the latter forbids the vector coupling to the Z and weakens the constraints from B-$\overline{B}$ mixing. Thus, these models seem especially promising and are the main subject of our ongoing studies. In these cases, we also check if the observed light neutrino masses can be generated at one-loop level. The exemplary model we present in this thesis, contains a SM singlet fermion as its DM candidate.
The chapter is structured as follows: In Section 6.1, we briefly review the class of models presented in [152] and consider the model addressed in this work in more detail. Fur-

[1] In many of those models, couplings of a new dark sector particle to for instance the SM up-type quarks must be forbidden as they would lead to a mixing of the SM quarks with the new state. A symmetry that forbids this type of couplings could serve as the DM stabilizing symmetry. In the simplest scenario, all new particles are odd under a $\mathcal{Z}_2$ symmetry.

thermore, we give the constraints on the model parameters from the requirement to fit the R_K anomaly and to produce a stable scalar potential. In Section 6.2, we present our analysis strategy and sketch the procedure to obtain the relic density and direct detection cross sections. In Section 6.3, we analyze the DM phenomenology of the exemplary model. We conclude in Section 6.4.

6.1. Model and Constraints from Lepton Flavor Universality Violation

The model classes proposed by [152] as a one-loop solution to the $b \to s\mu^-\mu^+$ anomalies are distinct in their particle content. In either of the two model realizations the SM is enlarged by three additional fields. In realization a), two heavy scalar fields, ϕ_Q and ϕ_L, and a vector-like fermion field ψ are present, whereas in realization b) there exist two vector-like fermion fields, ψ_Q and ψ_L, and a scalar field ϕ. The indices Q and L denote their coupling to quarks and leptons respectively. The corresponding Lagrangians for each realization are

$$\mathcal{L}_{int}^{a)} = \Gamma_{Q_i} \bar{Q}_i P_R \psi \phi_Q + \Gamma_{L_i} \bar{L}_i P_R \psi \phi_L + \text{h.c.} \tag{6.1.1}$$

$$\mathcal{L}_{int}^{b)} = \Gamma_{Q_i} \bar{Q}_i P_R \psi_Q \phi + \Gamma_{L_i} \bar{L}_i P_R \psi_L \phi + \text{h.c.}\,, \tag{6.1.2}$$

where Q_i and L_i denote the left-handed quark/lepton doublets, while i is a flavor index. The Eqs. (6.1.1) and (6.1.2) reveal that the additional heavy particles couple only to left-handed SM fermions. This is a phenomenologically driven feature, implemented to ensure that the Wilson coefficients C_9 and C_{10} fulfill $C_9 = -C_{10}$, which is the preferred scenario to fit the b anomalies. The Wilson coefficients belong to the operators $\mathcal{O}_9$ and $\mathcal{O}_{10}$ that are part of the flavor changing $|\Delta B| = |\Delta S| = 1$ effective Hamiltonian

$$\mathcal{H}_{\text{eff}} = -4\frac{G_F}{\sqrt{2}} V_{tb} V_{ts}^* \frac{\alpha_e}{4\pi} \sum_i C_i \mathcal{O}_i\,, \tag{6.1.3}$$

that is obtained by integrating out the heavy degrees of freedom, namely the

$$t$$

, H, Z and W. The operators $\mathcal{O}_9$ and $\mathcal{O}_{10}$ are given by

$$\mathcal{O}_9 = [\bar{s}\gamma^\mu P_L b]\left[\bar{l}\gamma_\mu l\right]\,, \tag{6.1.4}$$

$$\mathcal{O}_{10} = [\bar{s}\gamma^\mu P_L b]\left[\bar{l}\gamma_\mu \gamma_5 l\right]\,. \tag{6.1.5}$$

For the sake of simplicity, we assume vanishing couplings to the first generation.
The model classification up to the adjoint representation can be extracted from Table 6.1, where the representations of the new particles under the SM gauge groups are presented. The arising contributions to the decay $b \to s\mu^+\mu^-$ and $b \to s\nu\nu$ are illustrated in Figure 6.1.

In the context of Table 6.1, X is defined as the hypercharge of ψ in model class a), while it is defined as the negative hypercharge of ϕ in model realization b). The parameter X can be freely chosen in units of $1/6$ in the interval $X \in (-1, 1)$.
In this work, we want to analyze whether the model classes presented above contain a viable DM candidate, while still being able to explain the b anomalies. A DM candidate

$SU(2)$	ϕ_Q, ψ_Q	ϕ_L, ψ_L	ψ, ϕ
I	**2**	**2**	**1**
II	**1**	**1**	**2**
III	**3**	**3**	**2**
IV	**2**	**2**	**3**
V	**3**	**1**	**2**
VI	**1**	**3**	**2**
$SU(3)$			
A	**3**	**1**	**1**
B	**1**	$\overline{\mathbf{3}}$	**3**
C	**3**	**8**	**8**
D	**8**	$\overline{\mathbf{3}}$	**3**
Y			
	$1/6 \mp X$	$-1/2 \mp X$	$\pm X$

Table 6.1.: All possible choices for the combinations of representation of the new particles such that they allow for a one-loop contribution to $b \to s\mu^+\mu^-$. The first (second) subtable gives the possible combination of representations of the new particle content under the $SU(3)$ ($SU(2)$) gauge group. The last line summarizes the possible hypercharge assignment and X is a free parameter. The upper (lower) sign applies to the a)(b)) type models.

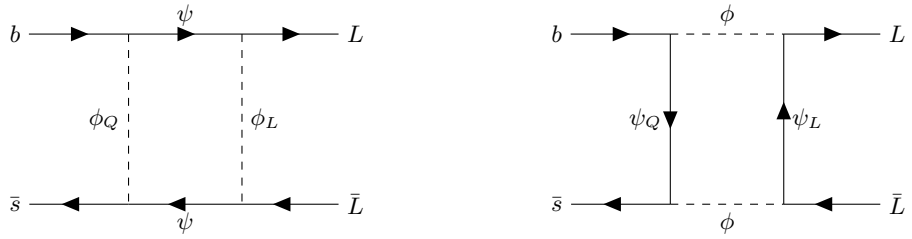

Figure 6.1.: Box diagram contribution to the decay $b \to s\mu^+\mu^-(\nu\nu)$ for model type (a) on the left and model type (b) on the right.

is constrained to be a colorless, electrically neutral, massive particle [2]. This statement alone eliminates half of the 48 possible model configurations, since in the categories C and D there is not a single colorless particle. The remaining 24 models can be classified in terms of the properties of their DM candidates. In the upcoming article [5], we limit ourselves to models with a singlet dark matter candidate. All singlet DM models are categorized in Table 6.2. In the context of this thesis, we further specify on the model b)IIA.

[2] In fact, DM could be colored and exist in form of eventually colorless bound states. We, however, only consider single particle DM. Please also note, that in principle DM could possess a small electric charge, such as in scenarios of millicharged DM.

fermionic singlet	scalar singlet
a)IA	a)IIA
b)IIA	a)IIB
b)IIB	a)VA
b)VA	a)VIB
b)VIB	b)IA

Table 6.2.: Models containing at least one singlet DM candidate. The model discussed in this thesis is highlighted in blue.

Following [152], we obtain constraints on the couplings Γ_μ relevant for the DM production cross section from constraints on the Wilson coefficients C_9 and $C_{B\bar{B}}$, which are obtained from fitting the R_K observables and the observed B-$\bar{B}$ oscillations. Additionally, the new Yukawas must be chosen small enough to evade limits from B-$\bar{B}$-mixing. In this work, we use the updated constraints from [153]. The contributions to C_9 and C_{10} from the box diagrams illustrated in Figure 6.1 and the Wilson coefficients relevant to the B-$\bar{B}$-mixing are given in Appendix E. We neglect the influence of photon penguin diagram contributions to C_9 and therefore assume $C_9 \approx C_9^{\text{box}}$. The current 2σ bounds on C_9 and $C_{B\bar{B}}$ are

$$C_9 \in [-0.62, -0.17] \tag{6.1.6}$$

$$C_{B\bar{B}} \in [-2.1, 0.6] \cdot 10^{-5}\,\text{TeV}^{-2}\,. \tag{6.1.7}$$

Starting from these premises we can construct an upper bound on $\Gamma_s\Gamma_b^*$ from B-$\bar{B}$ mixing and use this to construct a lower bound on Γ_μ by taking into account the bounds on C_9. In the following, we specify on the model b)IIA and only give results concerning this model. We choose $X = 1/2$, such that ψ_L constitutes the DM candidate. We assume mass degeneracy between the new non-dark matter particles ψ_Q and ϕ. For convenience, we introduce the dimensionless parameter

$$\kappa = \frac{m_{\psi_Q}}{m_{\psi_L}} = \frac{m_\phi}{m_{\psi_L}} > 1\,. \tag{6.1.8}$$

Moreover, we introduce a global $\mathcal{Z}_2$ under which all SM particles are even, while the three BSM particles are odd. This renders ψ_L stable if it is the lightest of the new particles, which is the case for $\kappa > 1$. Note, that this symmetry also forbids Yukawa couplings of the ψ_Q to the SM up-type quarks which would be present otherwise, as the field ψ_Q transforms like a right-handed SM up-type quark. This coupling would lead to a mass mixing of the new state with SM quarks.
From the bounds on C_9 and $C_{B\bar{B}}$ we find

$$\Gamma_s \cdot \Gamma_b^* \leq 1.508 \cdot 10^{-4} \kappa \frac{m_{\psi_L}}{\text{GeV}}\,, \tag{6.1.9}$$

$$\Gamma_\mu \geq 0.608 \cdot \left(\kappa \frac{-230.91 + 307.88\kappa^2 - 76.97\kappa^4 - 153.94 \cdot \log\left(\kappa^2\right)}{\left(\kappa^2 - 1\right)^3} \right)^{-\frac{1}{2}} \sqrt{\frac{m_{\psi_L}}{\text{GeV}}}\,. \tag{6.1.10}$$

Additionally, we enlarge the scalar sector of the theory, thereby altering the form of the scalar potential. In addition to the SM Higgs doublet H, there exists another scalar

doublet ϕ in the considered model. The most general form (again respecting a stabilizing symmetry) of the scalar potential in this scenario is

$$\begin{aligned} V_{\text{scalar}} =& m_H^2 H^\dagger H + m_\phi^2 \phi^\dagger \phi + \lambda_H \left(H^\dagger H\right)^2 + \lambda_\phi \left(\phi^\dagger \phi\right)^2 \\ &+ \lambda_{\phi,H,1} \left(\phi^\dagger \phi\right)\left(H^\dagger H\right) + \lambda_{\phi,H,2} \left(\phi^\dagger H\right)\left(H^\dagger \phi\right) + \left[\lambda_{\phi,H,3} \left(\phi^\dagger H\right)^2 + \text{h.c.}\right] . \end{aligned} \tag{6.1.11}$$

To ensure the stability of the scalar vacuum on tree-level, we adopt the limits of [111,154], leading to

$$\lambda_H > 0, \tag{6.1.12}$$

$$\lambda_\phi > 0, \tag{6.1.13}$$

$$\lambda_{\phi,H,1} > -2\sqrt{\lambda_\phi \lambda_H}, \tag{6.1.14}$$

$$\lambda_{\phi,H,1} + \lambda_{\phi,H,2} - |2\lambda_{\phi,H,3}| > -2\sqrt{\lambda_\phi \lambda_H} \, . \tag{6.1.15}$$

Note that for the model b)IIA discussed in this thesis, the coupling $\lambda_{\phi,H,3}$ vanishes as the new scalar has a different hypercharge than the SM Higgs field. This also implies the absence of non-zero neutrino masses in this model. While the fermion ψ_L is a SM singlet and could potentially couple to the SM Higgs and neutrino via a Yukawa coupling, this coupling is forbidden by the $\mathcal{Z}_2$ charge assignment that ensures the stability of the DM candidate. However, neutrino masses could still be generated via the scotogenic mass mechanism described in Section 2.1, if $\lambda_{\phi,H,3} \neq 0$ which, however, does not apply here.

6.2. Analysis Strategy and DM Phenomenology

We intend to examine whether the aforementioned models, in addition to providing an explanation to the R_K anomaly, can simultaneously create the correct DM relic density $\Omega_{DM} h^2 = 0.120 \pm 0.001$ (at 68% CL) observed by Planck [10] and withstand the bounds set by DM direct detection experiments like XENON1T [146]. For our phenomenological analysis we use FeynRules [155, 156] and its interface with FeynArts [157] and FormCalc [158] and/or FeynCalc to calculate contributions to direct detection cross sections up to one-loop level. We also operate another FeynRules interface with CalcHEP [159] to compute direct detection cross sections with micrOMEGAs, which uses said CalcHEP output. We also use micrOMEGAs to numerically solve Boltzmann's equations [160, 161] and obtain the relic density. Since the Yukawa coupling required to generate the observed R_K is sizable, DM production can only proceed via the *freeze-out* mechanism.

The model features two regions of parameters space for $\kappa \gtrsim 1.2$ and $\kappa \lesssim 1.2$ that are distinct in terms of DM production. For $\kappa \gtrsim 1.2$, coannihilations of the heavier dark sector particles, an effect described in Section 2.3.3, are not efficient due to the sizable mass difference between the DM candidate ψ_L and the other dark sector particles ψ_Q and ϕ. Thus, the annihilation cross section is typically dominated by direct annihilation of ψ_L into a pair of μ's or neutrinos.

On the other hand, for $\kappa \lesssim 1.2$, coannihilations are efficient and annihilations of ψ_Q and

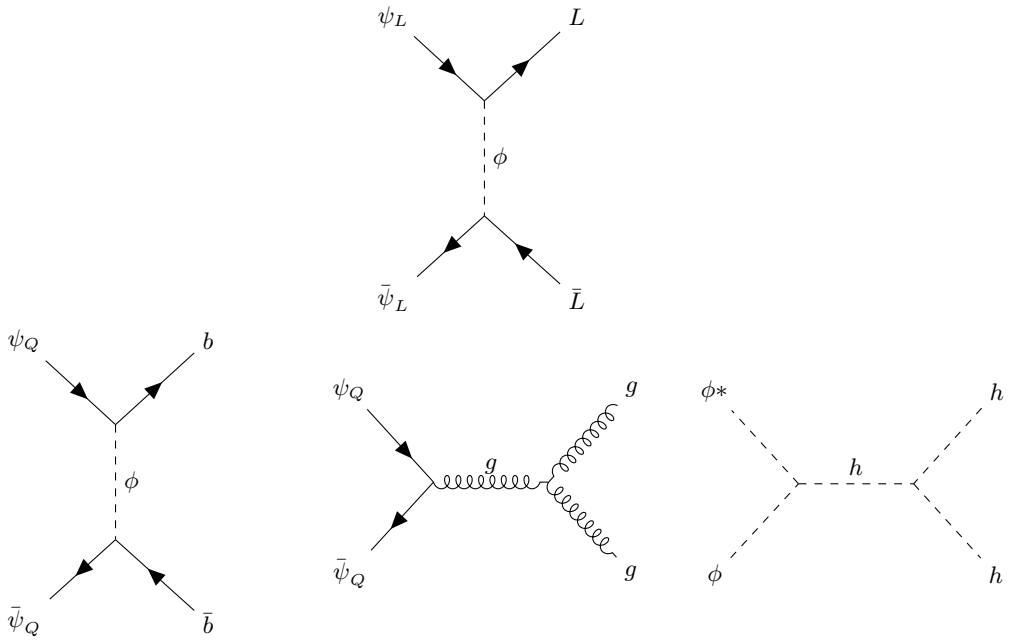

Figure 6.2.: The first line shows the dominant DM annihilation channel for a non-coannihilating scenario. The second line gives three exemplary annihilation channels that can contribute in a scenario involving coannihilation, that is $\kappa \lesssim 1.2$.

ϕ can effectively dominate the annihilation cross section of ψ_L. Typically, the annihilations of ψ_Q mediated by the couplings $\Gamma_{s/b}$ to the second and third quark generation and the strong gauge coupling g_3 provide larger contributions to the annihilation cross section than the annihilation of the dark scalar ϕ via the Higgs portal couplings $\lambda_{\phi,H,1}$. Various Feynman diagrams of the contributions to the annihilation cross section are illustrated in Figure 6.2. In case of $\kappa \gtrsim 1.2$, we can find a simple estimate for the relic density using Eq. (2.3.32), as the matrix element of the dominant annihilation channel $\psi_L \bar{\psi}_L \to \bar{L}L$ only depends on Γ_μ, m_{ψ_L} and κ. The thermally averaged cross section $\langle \sigma v \rangle$ of this process expanded in powers of the relative velocity v to leading order results in

$$\langle \sigma v \rangle = 2 \frac{\Gamma_\mu^4}{8\pi M_{\psi_L}^2} (1+\kappa^2)^{-2} + \mathcal{O}(v^1) = \sigma_0 + \mathcal{O}(v^1)\,. \tag{6.2.1}$$

As in Section 4.3, we can relate σ_0 to the observed relic density Ω_{DM} via

$$\Omega_{\mathrm{DM}} = \frac{\sqrt{g_{\mathrm{eff}}}}{g_{\mathrm{eff,s}}} \frac{3.79 x_f}{M_{\mathrm{Pl}} m_B \sigma_0} \frac{\Omega_B}{Y_B}\,. \tag{6.2.2}$$

If we simultaneously want to provide an explanation for the anomaly in R_K, the coupling of ψ_L to muons must satisfy Eq. (6.1.10). Both the lower bound on Γ_μ as well as the value for Γ_μ required to reproduce the measured relic density scale like $\sqrt{M_{\psi_L}}$. Thus, we can find an upper bound on the relic density that only depends on the parameter κ besides the logarithmic mass dependence of x_f. A numerical evaluation reveals that only for $\kappa \gtrsim 12$, the model can account for both the relic density and an explanation to R_K. We illustrate the behavior in Figure 6.3.

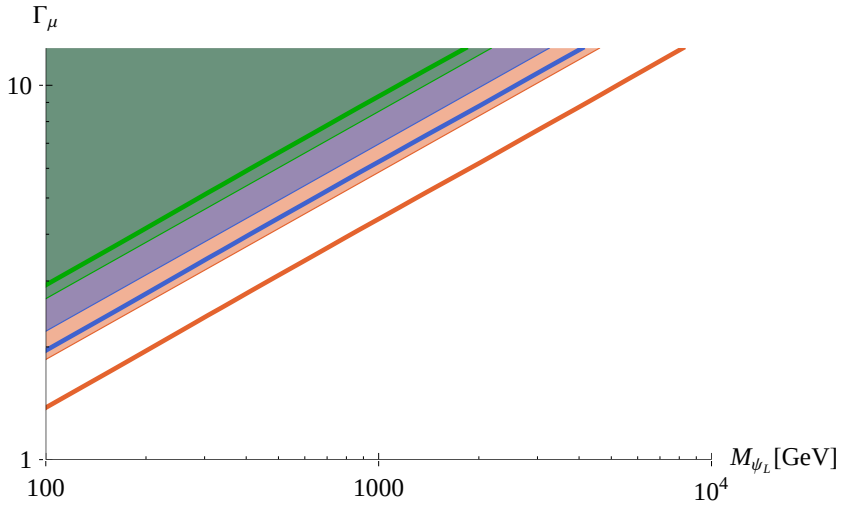

Figure 6.3.: Approximation of the correct relic density requirement in the non-coannihilation scenario with $\kappa \in (7, 10, 15)$ in (red,blue,green). The shaded areas show the configurations, where R_K can potentially be explained. The solid lines indicate where the correct relic density is reproduced. Only the $\kappa = 15$ configuration can explain the observed Ωh^2 and R_K simultaneously.

Beside the relic density, we check if a certain data point violates the limits on the SI DM-nucleon cross section provided by XENON1T. In this model, the leading order contributions to the direct detection cross section σ_{DD} are one-loop processes. Sizable contributions to σ_{DD} mainly arise from $Z/\gamma/H$-penguin diagrams. The corresponding amplitudes of these diagrams are proportional to Γ_μ^2. Further contributions arise from box diagrams that induce scattering with the quarks of the second and third generation. The different contributions are illustrated in Figure 6.4. For our numerical results we compute the effective vertices $\bar{\psi}_L Z^\mu \psi_L$ and $\bar{\psi}_L H \psi_L$ at zero outer momentum utilizing FeynArts [157] and FormCalc [158] and/or FeynCalc. The DM cross sections with nucleons are calculated with micrOMEGAs. The resulting cross sections have to be compared to the limits provided by XENON1T illustrated in Figure 2.14. However, these limits must be rescaled according to the relic density of the respective data point. The limits from XENON1T on the DM-nucleon cross section assume that for a given DM mass the particle species fully accounts for the measured relic density. This, however, is not the case for the majority of our data points. If for instance the data point underproduces DM, a lower number density of DM particles than the one assumed for the exclusion plot from XENON1T is implied. As the scattering process involves one DM particle, we naively rescale the bound from XENON1T, in the following referred to as Xe1T (M_{ψ_L}), inversely linear with the relic density predicted by the model. Thus, a data point must fulfill

$$\frac{\Omega_0}{\Omega} \text{Xe1T}(M_{\psi_L}) \geq \sigma_{\text{DD}}^{\text{SI}} \,, \tag{6.2.3}$$

not to be excluded by the experiment. In the formula above, Ω_0 refers to the measured DM energy density, while Ω corresponds to the DM energy density predicted by the specific data point.

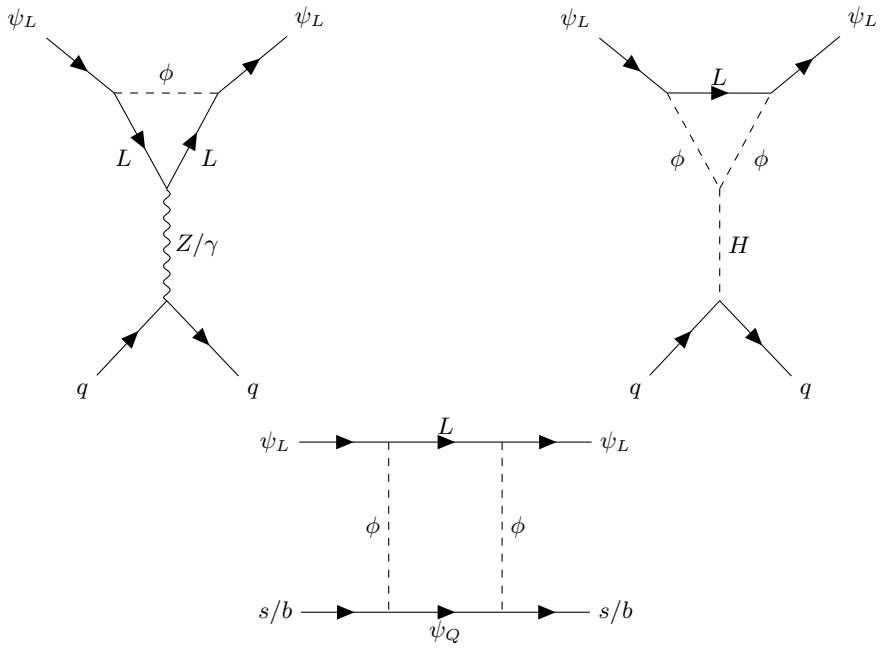

Figure 6.4.: The three types of one-loop contributions to direct detection arising in this model.

6.3. Results

For our scan we either randomly generate data points or only vary the parameters M_{ψ_L} and Γ_μ, allowing for a compact presentation in the M_{ψ_L}-Γ_μ plane. For the randomly generated data sets we scan over the parameters given in Table 6.3 but with a constant coannihilation parameter. For all data sets, we take $\lambda_\phi = 1$ as it is irrelevant for the DM phenomenology. We further assume $\lambda_{\phi,H,2} = 0$, which directly results in mass-degenerate components of the scalar doublet ϕ, that is $m_{\eta^0} = m_{\eta^-}$. As mentioned in Section 6.1, the coupling $\lambda_{\phi,H,3}$, given in the general scalar potential in Eq. (6.1.11), is absent in this model, as the two scalar doublets have a different hypercharge.

	M_{ψ_l}	Γ_μ	Γ_b	$\lambda_{\phi,H,1}$
Lower Bound	$100\,\text{GeV}$	10^{-4}	$\max\left[10^{-4}, \frac{1.5}{4\pi}10^{-4}\sqrt{\kappa\frac{M_{\psi_L}}{\text{GeV}}}\right]$	10^{-4}
Upper Bound	$\min\left[10^5\,\text{GeV}, \frac{16\pi^2}{1.5\kappa}10^4\,\text{GeV}\right]$	4π	4π	$2\frac{M^2_{\psi_L}}{v^2}\kappa^2$

Table 6.3.: Parameter ranges for the scatter plots given in Appendix F. The lower bound on Γ_b and the upper bound on M_{ψ_L} result from the requirement of perturbative couplings Γ_s and Γ_b, while still fulfilling Eq. (6.1.9). The upper bound on $\lambda_{\phi,H,1}$ ensures that the DM stabilizing symmetry is not broken by a vev of ϕ.

The main result is summarized in Figure 6.5, where we present four data sets with $\kappa = (1.01, 1.1, 5, 15)$, constant $\lambda_{\phi,H,1} = 0.1$ and $\Gamma_b = \Gamma_s = \sqrt{1.5}\cdot 10^{-2}\sqrt{\kappa\frac{M_{\psi_L}}{\text{GeV}}}$ while varying M_{ψ_L} and Γ_μ in the ranges $M_{\psi_L} \in \left(100, 3\cdot 10^4\right)$ GeV and $\Gamma_\mu \in \left(10^{-4}, 4\pi\right)$.

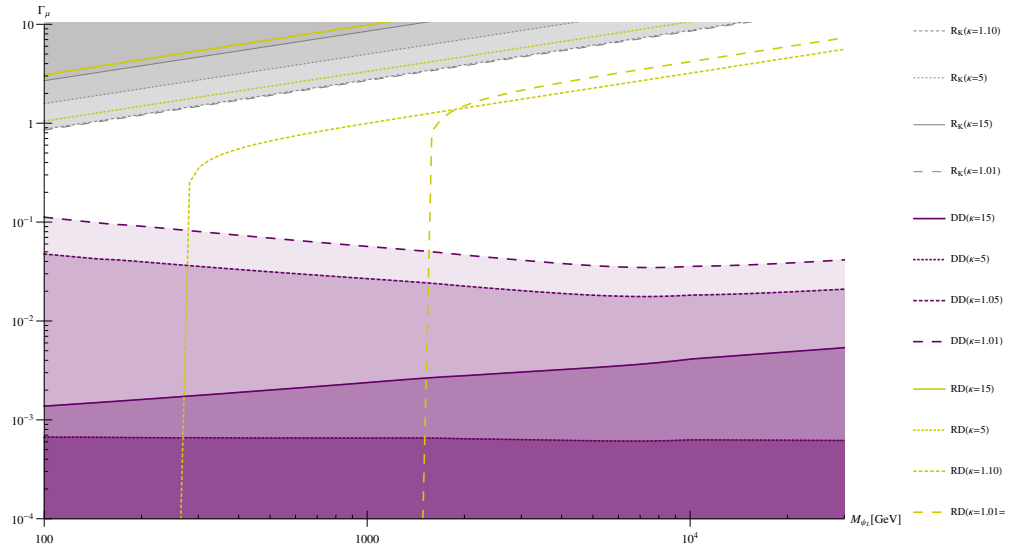

Figure 6.5.: The regions that respect the current XENON1T limits (purple), allow for an explanation of R_K (gray) and reproduce the observed relic density (yellow) are presented in the $M_{\psi_L} - \Gamma_\mu$ plane for data sets with four different coannihilation parameters. Note that below a given yellow line, DM is overproduced thereby excluding the model. Above a yellow line DM is underproduced. The different boundary lines correspond to the different data sets, namely: $\kappa = 15$ (solid), $\kappa = 5$ (dotted), $\kappa = 1.1$ (finely dashed) and $\kappa = 1.01$ (roughly dashed). Only the case $\kappa = 15$ allows for an simultaneous explanation of R_K and the correct relic density. However, this scenario is excluded by direct detection experiments. Additionally, we do not find a region that explains the R_K anomaly and is not excluded by direct detection, as we do not observe an overlapping gray and purple area. In this sense, direct detection tests if this model can explain the anomaly in R_K. Thus, in the form presented here, the model cannot serve as an explanation to R_K. Further, we find that only coannihilating scenarios allow to reproduce the observed relic density, while being in agreement with direct detection experiments.

For large κ, we observe the feature described in the previous subsection. Both the boundary of the region that provides an explanation to R_K (gray) and the line representing the observed relic density (yellow) shift to larger Γ_μ for an increasing κ. The relic density, however, increases in a higher rate with increasing κ, such that at a given $\kappa_0 \sim 12$ both lines overlap. Thus, we find that the correct relic density can be reproduced in a model with $\kappa = 15$ while also allowing for a solution to R_K. Note that for the other three cases, the scenarios providing a solution to R_K are not excluded by the measurement of the relic density, as above the yellow lines DM is underproduced due to the larger coupling to the SM. The missing DM energy density could be accommodated by an additional DM component.
However, we do not observe any overlap between the purple regions that indicate the parts of the parameter space in agreement with direct detection experiments and the gray regions allowing for an explanation to R_K. Thus, direct detection experiments exclude this version of the model as an explanation to R_K. Although DM tends to be underproduced in these regions, thereby relaxing the exclusion limit from XENON1T, the coupling of ψ_L to muons is too sizable to evade those constraints. Note that the

direct detection limits only apply if a DM stabilizing symmetry is imposed on the model. However, such a symmetry also forbids mass mixing of the new fermion ψ_Q with the SM quarks. Without this symmetry the couplings inducing the mass mixing would have to be set to zero or a tiny value by hand.
Note that we also did not find any data points that allow for an explanation of R_K that are in agreement with direct detection in a scan using a randomly generated data set with parameters that were varied within the ranges given in Table 6.3, although the limits arising from direct detection experiments are weaker, when $\Gamma_s \neq \Gamma_b$. In Appendix F, we provide the same type of plot as illustrated in Figure 6.5 but with $\Gamma_s = 4\pi$ and Γ_b chosen such that the model is not excluded by B-$\bar{B}$ mixing. This scenario provides the weakest limits from direct detection experiments, as discussed in Appendix F.
Moreover, we find that coannihilations are mandatory in this model to fully account for the observed relic density. This can be seen in Figure 6.5 from the fact that the only yellow lines that enter the purple colored areas belong to coannihilating scenarios. For large masses and couplings, the coannihilating scenarios behave in the same way as non-coannihilating configurations. However, we find a lower bound on the DM mass in coannihilating scenarios in case they account for the observed relic density. This stems from the fact that in those sets we did not vary the couplings $\Gamma_{s/b}$ and $\lambda_{\phi,H,1}$ that in combination with the strong gauge coupling g_3 determine the strength of the coannihilation channels. This contribution is independent of Γ_μ and even exists in case of $\Gamma_\mu = 0$. Thus, as the effective annihilation cross section is bounded from below, we find a lower bound on the DM mass. This lower bound also exists for $\Gamma_{s/b} = \lambda_{\phi,H,1} = 0$, due to the contribution from the strong gauge coupling.
The dependence of the lower bound on the mass ratio κ, can be understood by means of the formula for the effective cross section given in Eq. (2.3.35). Since the contribution of the coannihilation channels to the effective annihilation cross section is suppressed by a factor of $\exp(-x_\mathrm{f}[\kappa - 1])$, the lower bound on the effective annihilation cross section, and thus the lower bound on the DM mass, are relaxed for a larger κ.
The tight constraints from direct detection stem from the vector coupling of ψ_L to the Z boson. The discussed b)IIA model, however, also allows ψ_L to be a Majorana fermion. This forbids the vector coupling to the Z and therefore might relax the constraints from direct detection. Again we calculated the contributions of the model to the effective vertices $\bar{\psi}_L Z^\mu \psi_L$ and $\bar{\psi}_L H \psi_L$ at zero outer momentum utilizing FeynArts [157] and FormCalc [158] and/or FeynCalc but for a Majorana fermion ψ_L instead of a Dirac fermion. Due to the absence of the vector coupling, the contribution to the SI DM-nucleon cross section is much smaller than in the case of Dirac DM. As a consequence, the constraints from XENON1T and IceCube on the SD DM-nucleon cross section, arising from the axial-vector coupling, are more restricting than the ones on the SI cross section despite being several orders of magnitude less stringent. Therefore, we use the bounds on the DM-proton cross section from IceCube [162] and on the DM-neutron cross section from XENON1T [146] to constrain the model in case of Majorana DM.
In Figure 6.6, we show the results of a scan with fixed $\Gamma_{s/b}$ and $\lambda_{\phi,H,1}$ as in the case of Dirac DM for coannihilation parameters $\kappa = (1.01, 1.1, 5, 15)$. Beside the relaxed constraints from direct detection experiments, the results in the case of Majorana DM are similar to the findings for Dirac DM. The observed relic density and R_K can be reproduced simultaneously for $\kappa \gtrsim 5$. The value differs from the case of Dirac DM,

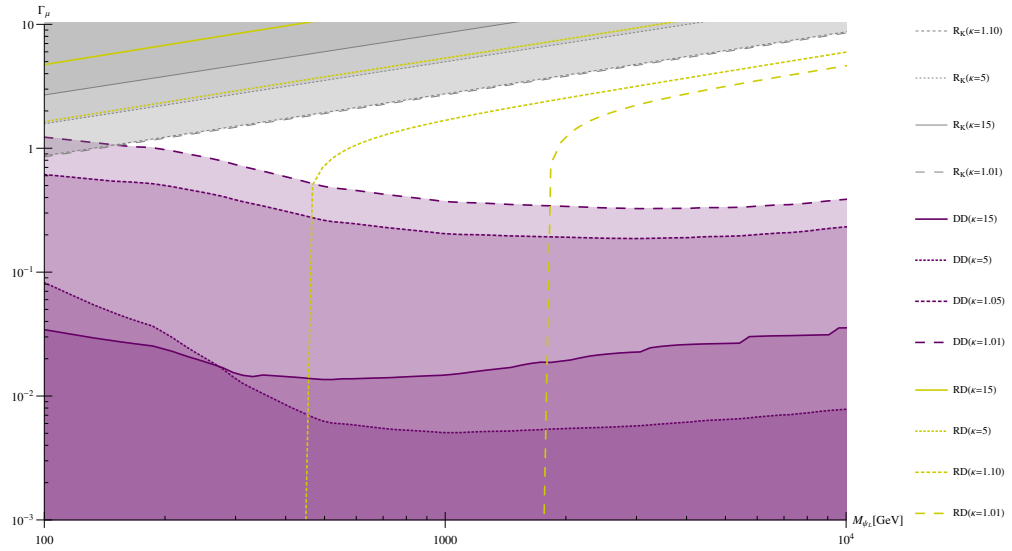

Figure 6.6.: The regions that respect the current limits on the SD DM-nucleon cross section (purple), allow for an explanation of R_K (gray) and reproduce the observed relic density (yellow) are presented in the $M_{\psi_L} - \Gamma_\mu$ plane for data sets with four different coannihilation parameters in the case of Majorana DM. The purple regions arise from a combination of the constraints from IceCube [162] and XENON1T [146]. The constraints from direct detection are much weaker than in the case of Dirac DM. Nevertheless, only the strongly coannihilating scenario with $\kappa = 1.01$ allows for an explanation of R_K in agreement with direct detection experiments. Even in this scenario small masses of $M_{\psi_L} \lesssim 110\,\text{GeV}$ are mandatory, implying ψ_Q in a similar mass range. Those masses can be in contradiction with collider bounds on vector-like quarks [163]. As in the case of Dirac DM, only coannihilating scenarios allow for the observed relic density in agreement with direct detection experiments.

since the s-wave annihilation is suppressed in case of Majorana DM. Thus, the leading order contribution of the annihilation cross section is velocity suppressed, resulting in larger required values for Γ_μ compared to the case of Dirac DM. This, in turn, allows for a simultaneous explanation of R_K and the relic density for $\kappa \gtrsim 5$ instead of $\kappa \gtrsim 13$. However, such a scenario is still excluded by direct detection experiments.
In contrast to the case of Dirac DM, the relaxed direct detection constraints allow for an explanation of R_K in the case of a strongly coannihilating scenario with $\kappa = 1.01$ if $M_{\psi_L} \lesssim 110\,\text{GeV}$. As shown in Appendix F, this region can extend up to 850 GeV in the case of a hierarchical coupling structure with $\Gamma_s = 4\pi$. However, the model also introduces a vector-like fermion with the quantum numbers of a right-handed up quark. As this particle couples to the SM gluons, it can be constrained from collider searches, for instance by mono-jet searches. While a collider analysis is planned to be part of the future work [5], it is not presented in this thesis. If we adopt an estimated lower bound on the mass of a $SU(2)$ singlet vector-like up-type quark of 600 GeV taken from [163], we would directly exclude the only working scenario for an explanation of R_K in agreement with direct detection experiments for democratic coupling structures $\Gamma_s \sim \Gamma_b$.

6.4. Conclusion

In this chapter, we have analyzed the b)IIA version of a class of models introduced in [152] to address the observed anomaly in the R_K observable. The model adds a singlet fermion ψ_L, a color triplet and $SU(2)_L$ singlet fermion ψ_Q with hypercharge $Y = \frac{2}{3}$ and a scalar doublet ϕ with hypercharge $Y = -\frac{1}{2}$ to the SM. All new particles are odd under a $\mathcal{Z}_2$ symmetry, while the SM fields are even. Thus, the electrically neutral fermion ψ_L is a DM candidate if it is the lightest particle in the dark sector. We found that coannihilations are necessary to reproduce the observed relic density in agreement with current direct detection experiments. Coannihilations only take place if the mass ratio of the dark sector particles, parametrized by $\kappa = \frac{M_{\psi_Q}}{M_{\psi_L}}$, fulfills $\kappa \lesssim 1.2$.
The model relies on a large coupling of ψ_L to muons to explain the R_K anomaly. This leads to an underproduction of DM in most of the cases capable of explaining the anomaly in R_K. Only for the case of heavy dark sector partner particles, more precisely $\kappa \gtrsim 13$ for Dirac DM and $\kappa \gtrsim 5$ for Majorana DM, scenarios explaining R_K can provide the observed relic density. Those scenarios, however, are excluded by direct detection experiments. Remarkably, direct detection experiments even prove to be more powerful in this setup. Although DM is underproduced in most scenarios providing an explanation to R_K, the large coupling to muons still leads to an exclusion by the XENON1T experiment. Even if, as in the case of Majorana DM, the vector coupling to the Z boson is forbidden the constraints on the SD DM-nucleon cross section, taking into account the lower bound on the mass of the vector-like up-type quark ψ_Q, might be sufficient to exclude the b)IIA model as an explanation of the anomaly in R_K. For the case of Dirac DM the model in this form is excluded as an explanation for the R_K anomaly. For the case of Majorana DM the collider study, which is a subject of an ongoing study, is mandatory to make a definite statement about the capability of the model to serve as an explanation to the R_K anomaly.
The study of the remaining models including a singlet DM candidate, summarized in Table 6.2, is still ongoing and will be discussed in [5].

7. Conclusion

The measurement of the CMB provides strong and precise evidence for the existence of energy density in the universe in form of DM. In this thesis, we invesitgated several SM model extensions including a DM candidate and their connection to neutrino and flavor physics.
In Chapter 2, we reviewed several neutrino mass generation mechanism, as the models investigated in the Chapters 3 and 4, and partially in Chapter 6, are constructed to generate the observed neutrino masses and mixing parameters. Furthermore, we provided an overview of different DM production mechanisms and pointed out various phenomenological implications of DM models.
Chapter 3 was dedicated to a model involving a SM singlet fermion propagating in an extra dimension. The resulting suppression of couplings to the SM particle conent, confined on a (3+1) dimensional subspace, allows for a neutrino mass generation via the type-I seesaw involving heavy neutrino masses down to a few GeV.
Motivated by the small couplings arising in the type-I seesaw for heavy neutrinos with masses around the electroweak scale, we constructed a feebly coupled neutrino portal to DM model in Chapter 4. We found two distinct DM production regimes: non-resonant and resonant production of DM. The latter is strongly constrained by the measurement of the Lyman-α forest and a large part of the parameter space can be ruled out. Conversely, the non-resonant production regime remains basically unconstrained but provides a prediction of the heavy neutrino mass scale, given the coupling structure of the model. If for instance the coupling of the heavy neutrino to DM is significantly larger than the one to the SM, heavy neutrinos in the GeV range are predicted. These could potentially be probed by future hidden sector searches such as SHIP.
In the second part of Chapter 4, we extended our analysis to more strongly coupled version of the neutrino portal to DM and checked if phenomenolgical viable data points provide a model that is theoretically consistent in the sense that the scalar vacuum remains stable and couplings are perturbative also at large energy scales. The freeze-out realizations of the neutrino portal to DM are severly constrained by the applied consistency conditions. We find that sizable contributions of the Higgs portal are excluded, as they would lead to non-perturbative couplings. Further we find an upper bound on the DM mass of a few hundred GeV for a fermionic DM candidate and an upper bound of 2 TeV for a scalar DM candidate. In the future, we plan to analyze an inverse seesaw realization of the neutrino portal to DM concerning the consistency conditions given above.
While freeze-in scenarios are unconstrained by the consistency conditions, the renormalization group running of the model parameters provides an interesting prospect for future work. As freeze-in production can be efficient for very different energy scales, the effects induced by the running of the coupling relevant for DM production can change the prediction for the generated relic density.
In Chapter 5, we investigated the effect of a Yukawa bound state that can form in a

heavy dark sector. We found that the bound state can facilitate the interaction of the heavy dark sector with a lighter dark sector or the SM. The bound state can even generate an efficient particle transfer between to sectors if the connecting interaction is too small to provide a direct particle transfer. The bound state effectively enhances the annihilation cross section by confining its constituents close to each other.
Eventually, in Chapter 6, we discussed the capability of one-loop solutions to the R_K anomaly to additionally generate the observed relic density. We specified on the model version b)IIA and found that this model cannot explain R_K and DM in agreement with current DM direct detection experiments. Furthermore, we found that direct detection experiments are even more restrictful in this case. As long as the lightest dark sector particle is stable, direct detection experiments exclude this model as an explanation for the R_K anomaly for Dirac DM. The analyis will be extended to the remaining one-loop solutions to the R_K anomaly including a singlet DM candidate.

A. Momentum Distribution Function of resonantly produced DM in the Neutrino Portal to Dark Matter

A common simplifying assumption (e.g. in [51]) to solve the Boltzmann equation is to perform the momentum integration by assuming that if a particle distribution deviates from its equilibrium density it differs only by a momentum-independent factor, i.e. $f_i = \alpha_i f_i^{\mathrm{th}}$ with $\frac{\partial \alpha_i}{\partial p_i} = 0$. Furthermore, the equilibrium densities of bosons and fermions are approximated by a Boltzmann distribution.
Following the lines of [53, 164] we solve the Boltzmann equations at the level of momentum distribution functions. This has the advantage of a more accurate solution and the exact shape of the momentum distribution allows for more insights into the process of structure formation. Throughout the calculation we approximate the equilibrium densities of any particle species by a Boltzmann distribution. The Boltzmann equation is given by:

$$\left(\frac{\partial}{\partial t} - Hp\frac{\partial}{\partial p}\right) f\left(p, T\left(t\right)\right) = \mathcal{C}\left(p, T\right) . \tag{A.1}$$

Here t is the time, H the Hubble parameter, f is the momentum distribution function of the particle species whose evolution is described by this Boltzmann equation, p is their momentum and $\mathcal{C}\left(p, T\right)$ is the collision term which describes the impact of interactions. For the integration of this equation it is convenient to perform a coordinate transformation $(t, p) \to (r, x)$ such that the differential operator on the left-hand side contains a derivative with respect to one of the new variables only. If r only depends on t and

$$\frac{\partial x}{\partial t} - Hp\left(r, x\right)\frac{\partial x}{\partial p} = 0\,, \tag{A.2}$$

the left-hand side of Eq. (A.1) results in

$$\frac{\partial r}{\partial t}\frac{\partial}{\partial r}\,. \tag{A.3}$$

The condition (A.2) is fulfilled if

$$x\left(p, t\right) = x\left(\frac{a\left(t\right)}{a\left(t_0\right)}p, t_0\right) \tag{A.4}$$

A convenient choice for x is

$$x\left(p, t\right) = \frac{1}{T_0}\frac{a\left(t\right)}{a\left(t_0\right)}p = \left(\frac{g_s\left(T_0\right)}{g_s\left(T\right)}\right)^{\frac{1}{3}}\frac{p}{T}\,. \tag{A.5}$$

For the last equality we used the conservation of entropy $s(T_0)a(T_0) = s(T)a(T) = \text{const.}$ and g_s are the entropy degrees of freedom. The conservation of entropy also allows us

to relate the temperature T to the time t via

$$\frac{dT}{dt} = -HT\left(1 + \frac{T}{3}\frac{dg_s}{dT}g_s^{-1}\right)^{-1} . \tag{A.6}$$

Since T is only a function of t and not of p we can choose

$$r\left(T\right) = \frac{m_0}{T} , \tag{A.7}$$

with m_0 as an arbitrary mass scale. Combining these results, the Boltzmann equation reads

$$rH\left(1 - \frac{T}{3}\frac{\partial}{\partial r}\ln\left(g_s\right)\right)^{-1}\frac{\partial}{\partial r}f\left(p\left(r,x\right),T\left(r\right)\right) = \mathcal{C}\left(p\left(r,x\right),T\left(r\right)\right) . \tag{A.8}$$

Since in this work DM production is mainly governed by $2 \leftrightarrow 2$ scattering processes, we discuss the collision term for these type of processes in more detail. For a $A + B \rightarrow C + DM$ scattering the collision term for the evolution of the momentum distribution function of DM is given by:

$$\begin{aligned}\mathcal{C}_{\mathcal{DM}}\left(p\right) = \frac{g_A g_B g_C}{2E_{DM}}\int\frac{d^3\mathbf{p}_A}{2E_A\left(2\pi\right)^3}\frac{d^3\mathbf{p}_B}{2E_B\left(2\pi\right)^3}\frac{d^3\mathbf{p}_C}{2E_C\left(2\pi\right)^3}\left(2\pi\right)^4\delta^4\left(p_A + p_B - p_C - p_{DM}\right)\times \\ \times\left|\mathcal{M}\right|^2\left(f_A f_B - f_C f_{DM}\right) .\end{aligned} \tag{A.9}$$

Here, $E_i = \sqrt{\mathbf{p}_i^2 + m_i^2}$, $\mathcal{M}$ is the matrix element for the process $A + B \rightarrow C + DM$ which is the same in both directions since we are assuming CP invariant interactions and f_i is the distribution function of particle species i. We assume that $f_C f_{DM} \ll f_A f_B$ which is justified in the context of freeze-in production of DM, as discussed in Chapter 4. Furthermore, we take $f_{A/B} = f_{A/B}^{th}$ assuming the interactions of A and B are efficient enough to keep them in thermal equilibrium. Moreover, taking $f_{A/B}^{\mathrm{eq}}$ to be a Boltzmann distribution, shifting the integration over $\mathbf{p}_c$ to $\mathbf{p}_C + \mathbf{p}_{DM} = \mathbf{P}$ and multiplying the equation by $1 = \int dP_0\delta\left(P_0 - E_C - E_{DM}\right)$ yields

$$\begin{aligned}\mathcal{C}\left(p_{DM}\right) = \frac{g_A g_B g_C}{4E_{DM}}\int\frac{d^4P}{\left(2\pi\right)^3}\frac{exp\left(-P_0/T\right)}{E_C}\delta\left(P_0 - E_C - E_{DM}\right)\times \\ \times\int\frac{d^3\mathbf{p}_A}{2E_A\left(2\pi\right)^3}\frac{d^3\mathbf{p}_B}{2E_B\left(2\pi\right)^3}\left(2\pi\right)^4\delta^4\left(p_A + p_B - p_C - p_{DM}\right)\left|\mathcal{M}\right|^2\end{aligned} \tag{A.10}$$

The equation above can be simplified by rewriting it in terms of the reduced cross section [165]:

$$\begin{aligned}&g_A g_B g_C g_{DM}\int\frac{d^3\mathbf{p}_A}{2E_A\left(2\pi\right)^3}\frac{d^3\mathbf{p}_B}{2E_B\left(2\pi\right)^3}\left(2\pi\right)^4\delta^4\left(p_A + p_B - p_C - p_{DM}\right)\left|\mathcal{M}\right|^2 \\ =&\frac{\hat{\sigma}\left(s\right)}{\sqrt{\left[1 - \frac{\left(m_C + m_{DM}\right)^2}{s}\right]\left[1 - \frac{\left(m_C - m_{DM}\right)^2}{s}\right]}} .\end{aligned} \tag{A.11}$$

Moreover, we change the variables of integration from d^4P to an integration over the zeroth component of the center of mass momentum vector P_0, the center of mass energy

s and the angle θ between center of mass momentum $\mathbf{P}$ and the momentum of the DM candidate $\mathbf{p}_{DM}$, $d^4P = 2\pi\mathbf{P^2}dP_0d\mathbf{P}d\cos(\theta) = 2\pi\sqrt{P_0^2 - s}dP_0dsd\cos(\theta)$. To eliminate the remaining δ function we express its argument in terms of $\cos(\theta)$:

$$\begin{aligned}\delta\left(E_C + E_{DM} - P_0\right) &= \delta\left(\sqrt{\mathbf{P}^2 + \mathbf{p}_{DM}^2 - 2\mathbf{P}\mathbf{p}_{DM}\cos(\theta) + m_C^2} + E_{DM} - P_0\right) \\ &= \frac{E_C}{\mathbf{P}\mathbf{p}_{DM}}\delta\left(\cos(\theta) - \cos(\theta_0)\right) , \end{aligned} \tag{A.12}$$

where $\cos(\theta_0)$ is the value required for $\cos(\theta)$ for a vanishing argument of the δ function. Therewith, Eq. (A.10) results in

$$\begin{aligned}\mathcal{C}(p_{DM}) = \frac{1}{4g_{DM}E_{DM}\mathbf{p}_{DM}}\int\limits_{s_{\min}}^{\infty} ds \frac{\hat{\sigma}(s)}{\sqrt{\left[1 - \frac{(m_C+m_{DM})^2}{s}\right]\left[1 - \frac{(m_C-m_{DM})^2}{s}\right]}} \times \\ \times \int\limits_{\sqrt{s_{\min}}}^{\infty} \frac{dP_0}{(2\pi)^2}\exp\left(-\frac{P_0}{T}\right) \underbrace{\int\limits_{-1}^{1} d\cos(\theta)\,\delta\left(\cos(\theta) - \cos(\theta_0)\right)}_{=1,\ \text{if}\ \cos(\theta_0)\in[-1,1]}\end{aligned} \tag{A.13}$$

The last integral basically restricts the boundaries of either P_0 or s in the sense that if

$$\sqrt{\mathbf{P}^2 + \mathbf{p}_{DM}^2 - 2\mathbf{P}\mathbf{p}_{DM}\cos(\theta_0) + m_C^2} + E_{DM} - P_0 = 0 \tag{A.14}$$

is fulfilled $|\cos(\theta_0)| \leq 1$ must hold. This requirement yields the inequality

$$\left(s + m_{DM}^2 - m_C^2 - 2P_0E_{DM}\right)^2 \leq 4\mathbf{p}_{DM}^2\left(P_0^2 - s\right) . \tag{A.15}$$

In case of $m_C = m_{DM}$ [1] this results in a lower (relative minus sign) and upper bound (relative plus sign) of the P_0 integration of

$$P_0^{\pm} = \frac{E_{DM}s}{2m_{DM}^2}\left[1 \pm \frac{p_{DM}}{E_{DM}}\sqrt{1 - 4\frac{m_{DM}^2}{s}}\right] \overset{m_{DM}=0}{=} \begin{cases} P_0^+ \to \infty \\ P_0^- = \frac{s}{4p_{DM}} + p_{DM} \end{cases} . \tag{A.16}$$

The last equality shows that in case of $m_{DM} = 0$ only a lower bound exists, as was shown in [164], while for finite DM masses there is also an upper bound. Thus, we have

$$\mathcal{C}(p_{DM}) = \frac{1}{4g_{DM}E_{DM}\mathbf{p}_{DM}}\int\limits_{s_{\min}}^{\infty} ds \frac{\hat{\sigma}(s)}{\sqrt{1 - 4\frac{m_{DM}^2}{s}}}\int\limits_{P_0^-}^{P_0^+}\frac{dP_0}{(2\pi)^2}\exp\left(-\frac{P_0}{T}\right) . \tag{A.17}$$

The s integral and the following integration of the differential equation for an arbitrary cross section cannot be performed analytically. However, in case of a light DM candidate ($m_{DM} \approx 0$) and a resonant production process with $\Gamma_{\text{mediator}} \ll M_{\text{mediator}}$ the integral can be evaluated analytically. Moreover, this case is of special interest for this thesis since for resonant production discussed in Chapter 4 the DM mass can be considered as

[1] This is a good approximation for this work since we assume the dark sector to be almost degenerate in mass.

small. Therefore, the exact shape of the momentum distribution is required to quantify the impact of DM on structure formation. In this case, we have $P_0^+ \to \infty$ and

$$\hat{\sigma}(s) \approx \delta\left(s - M_N^2\right) \sqrt{1 - 4\frac{m_{DM}^2}{s}} \hat{\sigma}_{BW}(s) \ . \tag{A.18}$$

Hence the collision term yields

$$\mathcal{C}(p_{DM}) = \frac{T}{32\pi^2 g_{DM} \mathbf{p}_{DM}^2} \hat{\sigma}_{BW}\left(M_N^2\right) \exp\left(-\frac{M_N^2}{4\mathbf{p}_{DM} T} - \frac{\mathbf{p}_{DM}}{T}\right) . \tag{A.19}$$

Transforming the variables according to Eq. (A.7) and Eq. (A.5) and taking g_s to be a constant, i.e. $x = \frac{\mathbf{p}_{DM}}{T}$, leads to

$$\mathcal{C}(p_{DM}) = \frac{1}{32\pi^2 g_{DM}} \frac{r}{x^2 m_0} \hat{\sigma}_{BW}\left(M_N^2\right) \exp\left(-\frac{M_N^2 r^2}{4x m_0^2} - x\right) . \tag{A.20}$$

A collision term of this form can be integrated and results in the following momentum distribution function:

$$f(p,T) = \frac{M_{pl}\hat{\sigma}_{BW}\left(M_N^2\right)}{64\pi^2 g_{DM} c_H} \frac{\exp(-p/T)}{M_N^3} \frac{T^2}{p^2} \left[\sqrt{\frac{\pi p}{T}} \operatorname{erf}\left(\frac{M_N}{\sqrt{pT}}\right) - 2\frac{M_N}{T} \exp\left(-\frac{M_N^2}{Tp}\right)\right] , \tag{A.21}$$

where $\operatorname{erf}(x)$ is the error function. Therewith, the number density is given by the integration over the momentum

$$n(T) = 4\pi g_{DM} \int_0^\infty p^2 f(p,T) \overset{T \ll M_N}{=} \frac{M_{pl}\hat{\sigma}_{BW}\left(M_N^2\right)}{8 c_H} \frac{T^3}{M_N^3} . \tag{A.22}$$

In the last step, we assumed that the temperature where we observe the DM density is much smaller than the mass of the resonant particle. As mentioned above, to derive this analytic result we took the effective entropy degrees of freedom to be a constant. Hence the formula given above is only a good approximation as long as T is large enough to allow for a constant value of $g_s(T) \approx 100$ during the time of DM production. The result remains a good approximation if the main part of the production has been finished before $g_s(T)$ starts to vary significantly since for a collisionless particle species the quantity $Y = \frac{n}{s}$ is a constant.
By comparing the number of produced DM particles at temperature T to the number of particles for $T \to 0$, $\frac{n(T)T^3}{\lim\limits_{T\to 0} n(T)T^3}$, with an unapproximated $n(T)$ we find that for $T \approx \frac{M_N}{4}$ already over 0.99 of DM particle have been produced. Thus, as long as $M_N \geq 100\,\mathrm{GeV}$ the result (A.22) serves as a good estimate.
Beside collision terms for $2 \leftrightarrow 2$ scattering processes, the collision term for the (inverse) decay $N \leftrightarrow \nu h$ is required. The procedure for performing the integration over the particle momenta follows the same lines as for the $2 \leftrightarrow 2$ scattering. Thus, we only give the result for the collision term resulting from the decay that appears in the Boltzmann

equation for the heavy neutrino N:

$$\mathcal{C}_N\left(p_N\right) = \frac{M_N}{\sqrt{p_N^2 + M_N^2}}\left[\frac{y_\nu^2 g_\nu g_h}{16\pi} M_N \exp\left(-\frac{\sqrt{p_N^2 + M_N^2}}{T}\right) - \Gamma_{N\to\nu h} f_N\left(p_N, T\right)\right]. \tag{A.23}$$

B. Neutrino Masses and Unitarity Violation in the extra dimensional Seesaw Mechanism

In Chapter 3 sums of the form

$$A^{F_1}A^{F_2}\sum_{k=-\infty}^{\infty}\frac{\cos\left(\frac{ka}{R}+\Phi^{F_1}\right)\cos\left(\frac{ka}{R}+\Phi^{F_2}\right)}{M_0+\frac{k}{R}-\lambda}\equiv S\left(F_1,F_2\right)=S\left(F_2,F_1\right). \tag{B.1}$$

have to be solved. In the following, we employ the methods described in [80]. The central point is to express the brane shift a such that $\frac{a}{\pi R}$ becomes a rational number, that is

$$a=\frac{r\pi R}{q}\quad r,q\in\mathbb{N}\quad\text{and}\quad q>r\,. \tag{B.2}$$

For the following calculation we choose $r=1$ but the calculation works in a similar way with $r\neq 1$. Using the periodicity of the Yukawa couplings of the KK modes to the SM neutrinos, the infinite sum over k is split into two sums: An infinite sum over n and another finite sum over l.
The old and new summation variables are related by $k=qn+l$. Since a step in n causes a step of q in k, the second sum over l had to be introduced. This sum has to fill the gaps between a given k and $k+q$. Hence, this sum has to run from $l=0$ to $l=q-1$. we find

$$\begin{aligned}
\frac{S\left(F_1,F_2\right)}{A^{F_1}A^{F_2}}&=\sum_{l=0}^{q-1}\sum_{n=-\infty}^{\infty}\frac{\cos\left(n\pi+\frac{l}{q}\pi+\Phi^{F_1}\right)\cos\left(n\pi+\frac{l}{q}\pi+\Phi^{F_2}\right)}{M_0+\frac{qn}{R}+\frac{l}{R}-\lambda}\\
\Rightarrow\frac{S\left(F_1,F_2\right)}{A^{F_1}A^{F_2}}&=\sum_{l=0}^{q-1}\sum_{n=-\infty}^{\infty}\frac{\cos\left(\frac{l}{q}\pi+\Phi^{F_1}\right)\cos\left(\frac{l}{q}\pi+\Phi^{F_2}\right)}{M_0+\frac{qn}{R}+\frac{l}{R}-\lambda}\\
\Rightarrow\frac{S\left(F_1,F_2\right)}{A^{F_1}A^{F_2}}&=\sum_{l=0}^{q-1}\cos\left(\frac{l}{q}\pi+\Phi^{F_1}\right)\cos\left(\frac{l}{q}\pi+\Phi^{F_2}\right)\sum_{n=-\infty}^{\infty}\frac{1}{M_0+\frac{qn}{R}+\frac{l}{R}-\lambda}.
\end{aligned}$$

In the calculation above $\frac{ka}{R}=\frac{qn+l}{R}a=n\pi+\frac{l}{q}\pi$ is used. Using the periodicity of the cosine, the dependence of the numerator on n is eliminated. Consequently, the numerator can be pulled out of the sum over n.
Then, we find a solution for the sum over n:

$$\sum_{n=-\infty}^{\infty}\frac{1}{B+\frac{qn}{R}}=\frac{1}{B}+\sum_{n=1}^{\infty}\left(\frac{1}{B+\frac{qn}{R}}+\frac{1}{B-\frac{qn}{R}}\right)=\frac{1}{B}+\sum_{n=1}^{\infty}\frac{2B}{B^2-\frac{q^2}{R^2}n^2}$$

where $B=M_0+\frac{l}{R}-\lambda$ holds.
Comparing the result with the series representation of $\cot\left(x\right)$ leads to the following

result:

$$\frac{1}{B}+\sum_{n=1}^{\infty}\frac{2B}{B^2-\frac{q^2}{R^2}n^2}=\frac{R}{q}\pi\cot\left(\frac{R}{q}\pi B\right).$$

Thus, it is possible to write the sum as:

$$\begin{aligned}\frac{S\left(F_1,F_2\right)}{A^{F_1}A^{F_2}}&=\sum_{l=0}^{q-1}\cos\left(\frac{l}{q}\pi+\Phi^{F_1}\right)\cos\left(\frac{l}{q}\pi+\Phi^{F_2}\right)\frac{R}{q}\pi\cot\left(\frac{\pi R\left[M_0-\lambda\right]}{q}+\frac{l}{q}\pi\right)\\&=\frac{R}{q}\pi\sum_{l=0}^{q-1}\cos\left(\frac{l}{q}\pi+\Phi^{F_1}\right)\cos\left(\frac{l}{q}\pi+\Phi^{F_2}\right)\frac{\cos\left(\frac{\Theta}{q}+\frac{l}{q}\pi\right)}{\sin\left(\frac{\Theta}{q}+\frac{l}{q}\pi\right)},\end{aligned}$$

where $\Theta=\pi R\left(M_0-\lambda\right)$. The finite sum over l remains:

$$\frac{R\pi}{q}\sum_{l=0}^{q-1}\left[\cos\left(2\frac{l}{q}\pi+\Phi^{F_1}+\Phi^{F_2}\right)+\cos\left(\Phi^{F_1}-\Phi^{F_2}\right)\right]\cos\left(\frac{\Theta}{q}+\frac{l}{q}\pi\right)\frac{\prod_{m\neq l}^{q-1}\sin\left(\frac{\Theta}{q}+\frac{m}{q}\pi\right)}{\prod_{k=0}^{q-1}\sin\left(\frac{\Theta}{q}+\frac{k}{q}\pi\right)}.$$

In this form, we can exploit the following relations used in [80]:

$$\begin{aligned}&\prod_{k=0}^{q-1}\sin\left(\frac{\Theta}{q}+\frac{k}{q}\pi\right)=2^{1-q}\sin\Theta\\&\sum_{l=0}^{q-1}\cos\left(\frac{\Theta}{q}+\frac{l}{q}\pi\right)\prod_{m\neq l}^{q-1}\sin\left(\frac{\Theta}{q}+\frac{m}{q}\pi\right)=2^{1-q}q\cos\Theta\\&\sum_{l=0}^{q-1}\cos\left(2\frac{l}{q}\pi+\Phi^{F_1}+\Phi^{F_2}\right)\cos\left(\frac{\Theta}{q}+\frac{l}{q}\pi\right)\prod_{m\neq l}^{q-1}\sin\left(\frac{\Theta}{q}+\frac{m}{q}\pi\right)=\\&2^{1-q}q\cos\left(\Phi^{F_1}+\Phi^{F_2}+\frac{q-2}{q}\Theta\right).\end{aligned}$$

Those relations lead to

$$\frac{S\left(F_1,F_2\right)}{A^{F_1}A^{F_2}}=\frac{\pi R}{2}\left[\frac{\cos\left(\Phi^{F_1}+\Phi^{F_2}+\frac{q-2}{q}\Theta\right)}{\sin\Theta}+\cos\left(\Phi^{F_1}-\Phi^{F_2}\right)\cot\Theta\right].$$

Eventually, $q=\frac{\pi R}{a}$ is resubstituted and we find:

$$\begin{aligned}\frac{S\left(F_1,F_2\right)}{\pi RA^{F_1}A^{F_2}}=&\left[\cot\left(\pi R\left[M_0-\lambda\right]\right)\cos\left(\Phi^{F_1}-a\left[M_0-\lambda\right]\right)\cos\left(\Phi^{F_2}-a\left[M_0-\lambda\right]\right)\right.\\&\left.-\frac{1}{2}\sin\left(\Phi^{F_1}+\Phi^{F_2}-2a\left[M_0-\lambda\right]\right)\right].\end{aligned}\tag{B.3}$$

The second sum, which is to solve, is:

$$A^{F_1}A^{F_2}\sum_{k=-\infty}^{\infty}\frac{\cos\left(\frac{ka}{R}+\Phi^{F_1}\right)\cos\left(\frac{ka}{R}+\Phi^{F_2}\right)}{\left(M_0+\frac{k}{R}-\lambda\right)^2}=S_2\left(F_1,F_2\right). \tag{B.4}$$

We find the solution by differentiating $S\left(F_1,F_2\right)$ with respect to Θ.

$$\begin{aligned}
&\frac{d}{d\Theta}S\left(F_1,F_2\right)=\frac{d}{d\Theta}A^{F_1}A^{F_2}\sum_{k=-\infty}^{\infty}\frac{\cos\left(\frac{ka}{R}+\Phi^{F_1}\right)\cos\left(\frac{ka}{R}+\Phi^{F_2}\right)}{\frac{k}{R}+\frac{\Theta}{\pi R}}\\
&=-\frac{A^{F_1}A^{F_2}}{\pi R}\sum_{k=-\infty}^{\infty}\frac{\cos\left(\frac{ka}{R}+\Phi^{F_1}\right)\cos\left(\frac{ka}{R}+\Phi^{F_2}\right)}{\left(\frac{k}{R}+\frac{\Theta}{\pi R}\right)^2}=-\frac{1}{\pi R}S_2\left(F_1,F_2\right)\\
\Rightarrow&S_2\left(F_1,F_2\right)=-\pi R\frac{d}{d\Theta}S\left(F_1,F_2\right).
\end{aligned}$$

The derivative with respect to Θ results in

$$\begin{aligned}
&\frac{S_2\left(F_1,F_2\right)}{\pi^2*R^2A^{F_1}A^{F_2}}=\frac{\cos\left(\Phi^{F_1}-a\left[M_0-\lambda\right]\right)\cos\left(\Phi^{F_2}-a\left[M_0-\lambda\right]\right)}{\sin\left(\pi R\left[M_0-\lambda\right]\right)^2}-\\
&\frac{a}{\pi R}\cot\left(\pi R\left[M_0-\lambda\right]\right)\left(\frac{\cos\left(\Phi^{F_1}-a\left[M_0-\lambda\right]\right)}{\sin\left(\Phi^{F_2}-a\left[M_0-\lambda\right]\right)}+\frac{\cos\left(\Phi^{F_2}-a\left[M_0-\lambda\right]\right)}{\sin\left(\Phi^{F_1}-a\left[M_0-\lambda\right]\right)}\right)\\
&\frac{a}{\pi R}\cos\left(\Phi^{F_1}+\Phi^{F_2}-2a\left[M_0-\lambda\right]\right).
\end{aligned} \tag{B.5}$$

C. Renormalization Group Equations in the Neutrino Portal to Dark Matter

Type-I seesaw Neutrino Portal to Dark Matter
We summarize the relevant one-loop β-functions of the type-I seesaw neutrino portal to DM, normalized as $\mathrm{d}g/\mathrm{d}\ln\mu = (4\pi)^{-2}\beta_g$ for any coupling g appearing in the Lagrangean. In the Yukawa sector we find

$$\begin{aligned}
\beta_{Y_e} &= Y_e\left[\frac{3}{2}\left(Y_e^\dagger Y_e - Y_\nu^\dagger Y_\nu\right) + T - \frac{15}{4}g_1^2 - \frac{9}{4}g_2^2\right], \\
\beta_{Y_\nu} &= Y_\nu\left[\frac{3}{2}\left(Y_\nu^\dagger Y_\nu - Y_e^\dagger Y_e\right) + T - \frac{3}{4}g_1^2 - \frac{9}{4}g_2^2\right] + \frac{1}{2}Y_\chi Y_\chi^\dagger Y_\nu\,, \\
\beta_{Y_\chi} &= \left[Y_\chi Y_\chi^\dagger + Y_\nu Y_\nu^\dagger + T_\chi\right]Y_\chi\,,
\end{aligned} \tag{C.1}$$

where we have defined $T \equiv \mathrm{Tr}[Y_e^\dagger Y_e + Y_\nu^\dagger Y_\nu + 3Y_u^\dagger Y_u + 3Y_d^\dagger Y_d]$ and $T_\chi \equiv \mathrm{Tr}[Y_\chi^\dagger Y_\chi]$. The RGEs of the fermion mass terms read

$$\begin{aligned}
\beta_{M_N} &= M_N(Y_\nu Y_\nu^\dagger)^* + (Y_\nu Y_\nu^\dagger)M_N + \frac{1}{2}\big(M_N(Y_\chi Y_\chi^\dagger)^* + (Y_\chi Y_\chi^\dagger)M_N\big)\,, \\
\beta_{M_\chi} &= \frac{1}{2}M_\chi Y_\chi^\dagger Y_\chi\,.
\end{aligned} \tag{C.2}$$

For the scalar sector RGEs it is useful to define $T_{\nu\chi} \equiv \mathrm{Tr}[Y_\nu^\dagger Y_\nu Y_\chi^\dagger Y_\chi]$, $T_4 \equiv \mathrm{Tr}[(Y_e^\dagger Y_e)^2 + (Y_\nu^\dagger Y_\nu)^2 + 3(Y_u^\dagger Y_u)^2 + 3(Y_d^\dagger Y_d)^2]$ and $T_{\chi 4} \equiv \mathrm{Tr}[Y_\chi^\dagger Y_\chi Y_\chi^\dagger Y_\chi]$. Using these, we obtain

$$\begin{aligned}
\beta_{\lambda_1} &= 12\lambda_1^2 + 2\lambda_3^2 + \frac{3}{4}\big(g_1^4 + 2g_1^2 g_2^2 + 3g_2^4\big) - 3\lambda_1(g_1^2 - 3g_2^2) + 4\lambda_1 T - 4T_4\,, \\
\beta_{\lambda_2} &= 10\lambda_2^2 + 4\lambda_3^2 + 12g_1^4 - 12g_1^2\lambda_2 + 4\lambda_2 T_\chi - 4T_{\chi 4}\,, \\
\beta_{\lambda_3} &= 4\lambda_3^2 + 2\lambda_3(3\lambda_1 + 2\lambda_2) - \frac{3}{2}\lambda_3(g_1^2 + 3g_2^2) + 2\lambda_3(T + T_\chi) - 4T_{\nu\chi}\,.
\end{aligned} \tag{C.3}$$

Finally, the scalar mass parameters obey

$$\begin{aligned}
\beta_{m_H^2} &= 6\lambda_1\, m_H^2 + 2\lambda_3\, m_\eta^2 - \frac{3}{2}m_H^2\,(g_1^2 + 3g_2^2) + 2m_H^2\, T - 4T_{\nu\nu}\,, \\
\beta_{m_\eta^2} &= 4\lambda_2\, m_\eta^2 + 4\lambda_3\, m_H^2 - 6m_\eta^2\, g_1^2 + 2m_\eta^2\, T_\chi - 4T_{\nu\chi} - 4T_{\chi\chi}\,,
\end{aligned} \tag{C.4}$$

where $T_{\nu\nu} \equiv \mathrm{Tr}[M_N^2 Y_\nu^\dagger Y_\nu]$ and $\beta_{m_\eta^2}$ is given in the limit of diagonal M_χ, which allows to define $T_{\chi\chi} \equiv \mathrm{Tr}[M_\chi^2 Y_\chi^\dagger Y_\chi]$.

Inverse seesaw Neutrino Portal to Dark Matter

We summarize the relevant one-loop β-functions of the inverse seesaw neutrino portal to DM, using the same notation and abbreviations as above. The parts of the Lagrangian involving new physics are given by [108]

$$\begin{aligned}\mathcal{L} &= \mathcal{L}_{\rm SM} + (\lambda)_\alpha \,\overline{N}_R \tilde{\phi}^\dagger L_\alpha + \big((Y_L)\,\overline{N}_L + (Y_R)\,\overline{N}_R\big)\,\eta\,\chi \\ &\quad - \frac{1}{2} M_N\,\overline{N}_R N_L - M_\chi\,\overline{\chi}_R\,\chi_L + \text{h.c.} - V\,,\end{aligned} \tag{C.5}$$

and the potential V is again given by Eq. (4.1.2). In contrast to the type-I seesaw N is describing a Dirac singlet fermion and, as in [108], only one generation of dark fermions χ and new fermionic singlet states N is considered.
In the Yukawa sector we find

$$\begin{aligned}\beta_{\lambda_e} &= \bigg[-\frac{3}{4}g_1^2 - \frac{9}{4}g_2^2 + \frac{1}{2}y_R^2 + \frac{5}{2}\left(\lambda_\mu^2 + \lambda_\tau^2 + T\right)\bigg]\lambda_e - \frac{3}{2}(Y_e^\dagger Y_e)_{\alpha 1}\lambda_\alpha\,, \\ \beta_{Y_L} &= \bigg[2Y_L^2 + Y_R^2\bigg] Y_L\,, \\ \beta_{Y_R} &= \bigg[2Y_R^2 + Y_L^2 + \sum_\alpha \lambda_\alpha^2\bigg] Y_R\,.\end{aligned} \tag{C.6}$$

For the scalar sector we obtain

$$\begin{aligned}\beta_{\lambda_1} &= 48\lambda_1^2 + 2\lambda_3^2 + \frac{3}{4}\big(g_1^4 + 2g_1^2 g_2^2 + 3g_2^4\big) - 3\lambda_1(g_1^2 - 3g_2^2) \\ &\quad + \lambda_1\bigg[-6\lambda_1 - 18g_1^2 + 8\sum_\alpha \lambda_\alpha^2 + 8T\bigg] - 4\sum_{\alpha\neq\beta}\lambda_\alpha^2\lambda_\beta^2 - 4T_4\,, \\ \beta_{\lambda_2} &= -4Y_L^4 + 8\lambda_2 Y_L^2 - 4Y_R^2 + 40\lambda_2^2 + 4\lambda_3^2 + 8Y_R^2\lambda_2\,, \\ \beta_{\lambda_3} &= \bigg[-4\sum_\alpha \lambda_\alpha^2 + 2\lambda_3\bigg] Y_R^2 + 4\lambda_3^2 \\ &\quad + \lambda_3\bigg[-\frac{3}{2}g_1^2 - \frac{9}{2}g_2^2 + 2Y_L^2 + 2\sum_\alpha \lambda_\alpha^2 + 2T + 12\lambda_1 + 8\lambda_2\bigg]\,.\end{aligned} \tag{C.7}$$

The new scalar mass parameter obeys

$$\beta_{m_\eta^2} = 2m_\eta^2\left(Y_L^2 + Y_R^2 + 8\lambda_2\right) - 4Y_R^2\left(M_N^2 + M_\chi^2\right) + 4m_h^2\lambda_3\,. \tag{C.8}$$

D. Additional Plots for the Consistency of the Neutrino Portal to Dark Matter

In this Appendix we provide scatter plots for the scenarios omitted in Section 4.3.2.
Scatter Plots in the μ_{DM}-y_χ plane

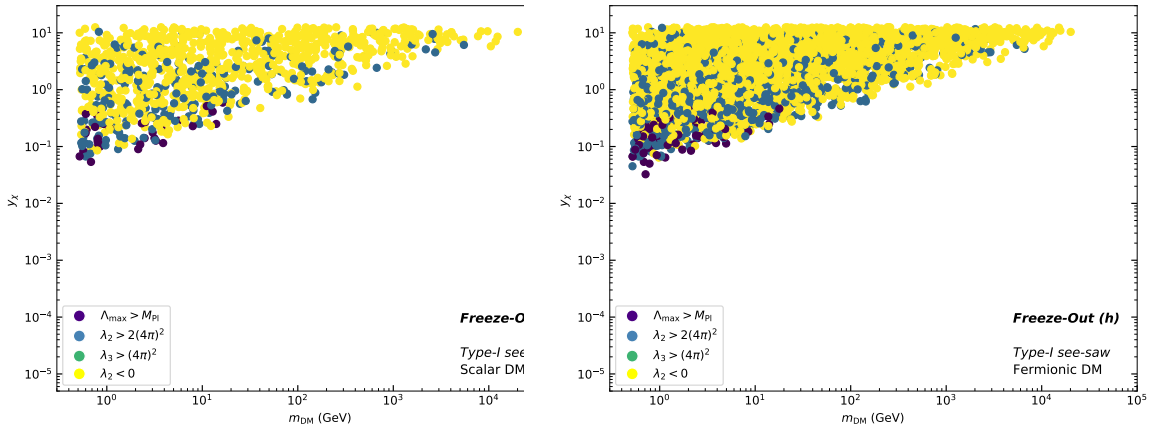

Figure D.1.: Phenomenologically viable data points of the NPDM colored according to their behavior at high energy scales. The data points are presented in the $\mu_{\rm DM} - y_\chi$ plane where $y_\chi = y_\chi(\mu_{\rm DM})$. The color code indicates if the data set leads to a model that is consistent up to the Planck scale (purple), an unstable vacuum (yellow) or results in a non-perturbative coupling (green and blue). The left (right) panel shows the results for data points involving scalar (fermionic) DM.

Scatter Plots in the y_χ-λ_2 Plane

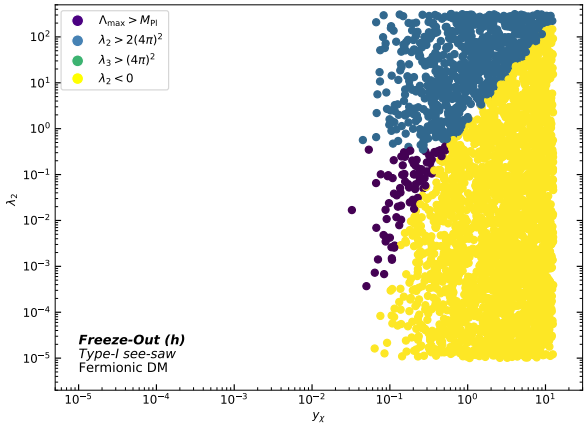

Figure D.2.: The data set for the case of fermionic DM with a vanishing λ_3 is displayed in the $y_\chi - \lambda_2$ plane. The values of both λ_2 and y_χ are given at the scale $\mu_{\rm DM}$.

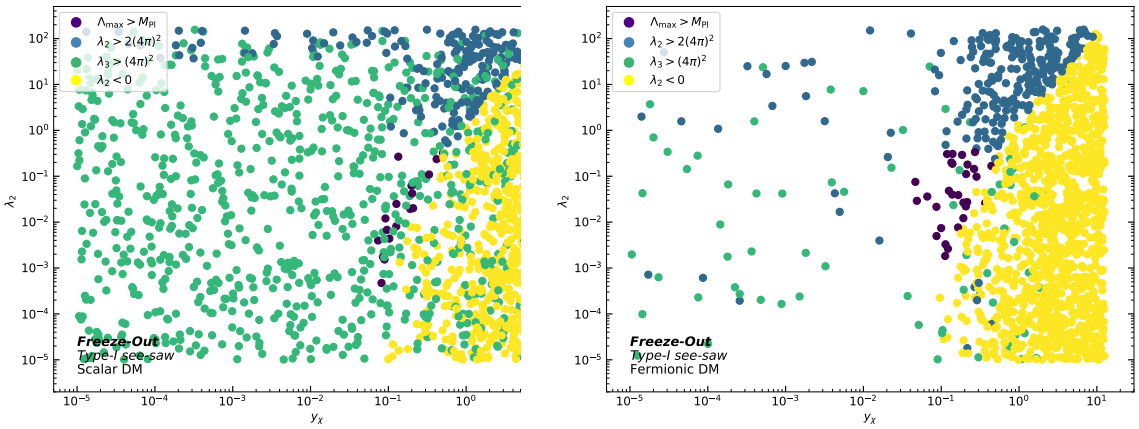

Figure D.3.: The data set for the case of scalar (fermionic) DM with $\lambda_3 \neq 0$ is displayed in the $y_\chi - \lambda_2$ plane. The values of both λ_2 and y_χ are given at the scale $\mu_{\rm DM}$.

Scatter Plots in the μ_χ-Λ_{max} Plane

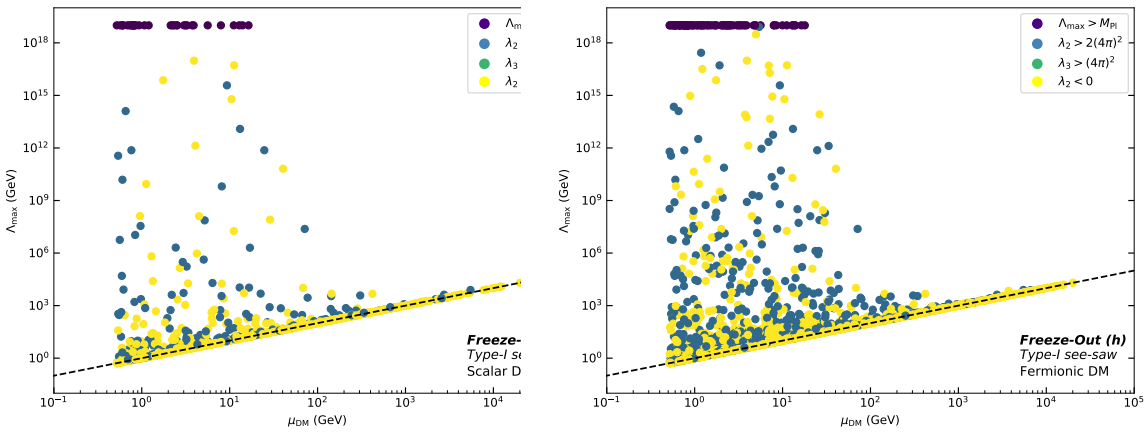

Figure D.4.: The data sets for scalar (left panel) and fermionic (right panel) DM with $\lambda_3 = 0$ are displayed in the $\mu_{\mathrm{DM}} - \Lambda_{\mathrm{max}}$ plane. The scale Λ_{max} describes the scale where the first inconsistency appears. The color code again denotes which specific inconsistency arises or if the model is safe up to the Planck scale. The dotted line indicates where $\Lambda_{\mathrm{max}} = \mu_{\mathrm{DM}}$, which is the starting point for the numerical solution of the RGE.

E. Relevant Wilson Coefficients

Here, we give the Wilson coefficients relevant to the for the model discussed in Chapter 6. The box diagrams given in Figure 6.1 contribute to the Wilson coefficients C_9 and C_{10} with $C_9 = -C_{10}$. Further, C_9 is given by [152]

$$C_9^{\text{box, a)}} = \frac{\sqrt{2}}{4G_F V_{tb} V_{ts}^*} \frac{\Gamma_s \Gamma_b^* |\Gamma_\mu|^2}{32\pi\alpha_{\text{em}} m_\psi^2} (\chi\eta F(x_Q, x_l) + 2\chi^M \eta^M G(x_Q, x_l)) \tag{E.1}$$

$$C_9^{\text{box, b)}} = -\frac{\sqrt{2}}{4G_F V_{tb} V_{ts}^*} \frac{\Gamma_s \Gamma_b^* |\Gamma_\mu|^2}{32\pi\alpha_{\text{em}} m_\phi^2} (\chi\eta - \chi^M \eta^M) F(y_Q, y_l) \tag{E.2}$$

with $x_{Q/L} = \frac{m^2_{\phi_{Q/L}}}{m_\psi^2}$ and $y_{Q/L} = \frac{m^2_{\psi_{Q/L}}}{m_\phi^2}$. F and G are the dimensionless loop-functions

$$F(x,y) = \frac{1}{(1-x)(1-y)} + \frac{x^2 \ln x}{(1-x)^2(1-y)} + \frac{y^2 \ln y}{(1-x)(1-y)^2} \tag{E.3}$$

$$G(x,y) = \frac{1}{(1-x)(1-y)} + \frac{x \ln x}{(1-x)^2(1-y)} + \frac{y \ln y}{(1-x)(1-y)^2} \,. \tag{E.4}$$

The $SU(2/3)$-factors η^M, χ^M can be extracted from table E.1 [152].

$SU(2)$	η	η^M	$\eta_{B\bar{B}}$	$\eta^M_{B\bar{B}}$
I	1	1	1	1
II	1	0	1	0
III	$\frac{5}{16}$	0	$\frac{5}{16}$	$\frac{1}{16}$
IV	$\frac{5}{16}$	$\frac{1}{16}$	$\frac{5}{16}$	$\frac{1}{16}$
V	$\frac{1}{4}$	0	$\frac{5}{16}$	0
VI	$\frac{1}{4}$	0	1	0
$SU(2)$	χ	χ^M	$\chi_{B\bar{B}}$	$\chi^M_{B\bar{B}}$
A	1	1	1	1
B	1	0	1	0

Table E.1.: $SU(2)$ and $SU(3)$ factors entering Wilson coefficients C_9^{box} and $C_{B\bar{B}}$. The factors relevant for the model in this thesis are highlighted in blue.

Further the model induces $B - \bar{B}$ mixing and the new physics contribution reads

$$C^{a)}_{B\bar{B}} = \frac{(\Gamma_s \Gamma_b^*)^2}{128^2 M_\psi^2} \left(\chi_{B\bar{B}} \eta_{B\bar{B}} F(x_Q, x_Q) + 2\chi^M_{B\bar{B}} \eta^M_{B\bar{B}} G(x_Q, x_Q)\right) , \tag{E.5}$$

$$C^{b)}_{B\bar{B}} = \frac{(\Gamma_s \Gamma_b^*)^2}{128^2 M_\phi^2} \left(\chi B\bar{B} \eta_{B\bar{B}} - \chi B\bar{B}^M \eta^M_{B\bar{B}}\right) F(y_Q, y_Q) \,. \tag{E.6}$$

F. Additional Plots for the Dark Matter Phenomenology in the one-loop Solutions to R_K

In Section 6.3, we gave a summary plot for the one-loop solution to the R_K anomaly in the light of DM. The plot assumed a democratic coupling structure in the quark sector for the second and third generation couplings to the new particle content, more precisely $\Gamma_s = \Gamma_b$. Additionally, Γ_s and Γ_b are chosen in a way such that they satisfy the limit induced from B-$\bar{B}$ mixing given in Eq. (6.1.9). This couplings structure generates the most stringent constraints from direct detection for the following reason:
The limits provided by XENON1T on the SI DM-nucleon cross section are rescaled with the relic density generated by a given data point according to Eq. (6.2.3). This directly implies less stringent constraints for a small relic density. In highly coannihilating scenarios, the effective annihilation cross section can be dominated by annihilations of the form $\psi_Q \bar{\psi}_Q \to q\bar{q}$ mediated by the couplings Γ_s and Γ_b and the corresponding Feynman diagram is shown in Figure fig:Appf. The final state quarks can be from the second and/or third generation. As their masses are negligible in the annihilation process, the annihilation cross section scales as

$$\langle \sigma v \rangle \sim \Gamma_b^4 + 2\Gamma_b^2 \Gamma_s^2 + \Gamma_s^4 \,. \tag{F.1}$$

Thus, as the product $\Gamma_s \Gamma_b$ remains constant, the annihilation cross section is minimized for $\Gamma_b = \Gamma_s$ and maximized for Γ_b or Γ_s at its perturbative limit of 4π. Thus the latter case leads to the smallest relic density and therefore weakest constraints from direct detection. A scan in the M_{Ψ_L}-Γ_μ plane with the same parameters that were used in Figure 6.5 but with $\Gamma_s = 4\pi$ shows that for the case of Dirac DM the model b)IIA cannot provide an explanation for the R_K anomaly in agreement with direct detection. The results of this scan are presented in Figure F.2.

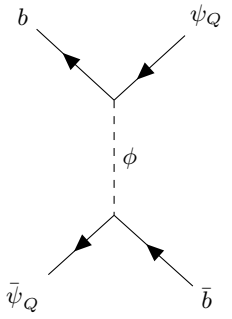

Figure F.1.: Feynman diagram for the process $\psi_Q \bar{\psi}_Q \to q\bar{q}$.

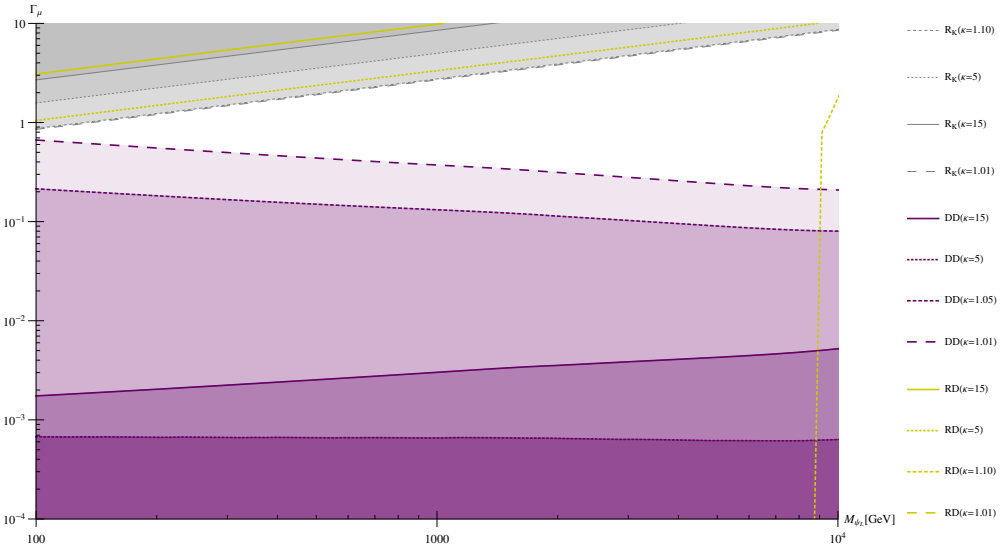

Figure F.2.: The regions that respect the current XENON1T limits (purple), allow for an explanation of R_K (gray) and reproduce the observed relic density (yellow) are presented in the $M_{\psi_L} - \Gamma_\mu$ plane for data sets with four different coannihilation parameters. Note that below a given yellow line, DM is overproduced thereby excluding the model. Above a yellow line DM is underproduced. The different boundary lines correspond to the different data sets, namely: $\kappa = 15$ (solid), $\kappa = 5$ (dotted), $\kappa = 1.1$ (finely dashed) and $\kappa = 1.01$ (roughly dashed). Only the case $\kappa = 15$ allows for an simultaneous explanation of R_K and the correct relic density. However, this scenario is excluded by direct detection experiments. As for the case of $\Gamma_s = \Gamma_b$, we do not find a region that explains the R_K anomaly and is not excluded by direct detection, as we do not observe an overlapping gray and purple area. Thus, in the form presented here, the model cannot serve as an explanation to R_K. Note that the figure does not show a yellow line for the case of $\kappa = 1.01$, as all data points underproduce DM in this case.

The same effect also applies to the case of Majorana DM where the limits on the SD DM-nucleon cross section are relaxed in case of a smaller relic density. The result of a parameter scan in the M_{Ψ_L}-Γ_μ plane with $\Gamma_s = 4\pi$ is presented in Figure F.3. We observe that the model might provide region of parameter space that explain the R_K anomaly and are in agreement with direct detection experiments. These regions extend up to roughly 850 GeV. Note however that this mass region might be constrained by collider mono-jet searches, which are subject to an ongoing study.

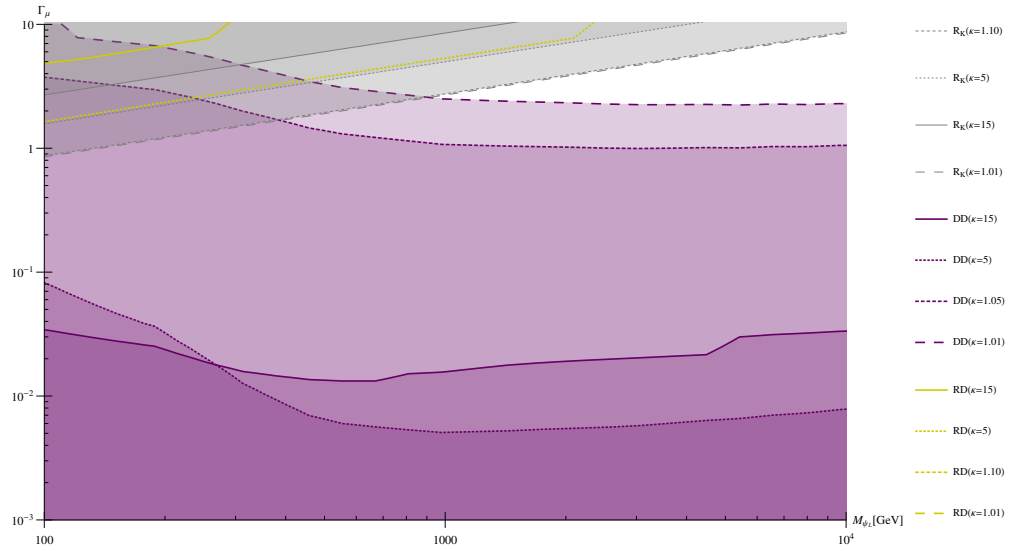

Figure F.3.: The regions that respect the current XENON1T limits (purple), allow for an explanation of R_K (gray) and reproduce the observed relic density (yellow) are presented in the $M_{\psi_L} - \Gamma_\mu$ plane for data sets with four different coannihilation parameters. Note that below a given yellow line, DM is overproduced thereby excluding the model. Above a yellow line DM is underproduced. The different boundary lines correspond to the different data sets, namely: $\kappa = 15$ (solid), $\kappa = 5$ (dotted), $\kappa = 1.1$ (finely dashed) and $\kappa = 1.01$ (roughly dashed). In this scenarios the areas allowing for an explanation of the R_K anomaly that are in agreement with direct detection experiments extend up to roughly 850 GeV. However, coannihilation remains mandatory.

Bibliography

[1] M. Becker and H. Päs, Eur. Phys. J. C **78**, 273 (2018), 1707.02882.

[2] M. Becker, Eur. Phys. J. C **79**, 611 (2019), 1806.08579.

[3] M. Becker and W.-C. Huang, (2019), 1911.06788.

[4] M. Becker and C. Hormigos-Feliu, To be published.

[5] M. Becker, D. Döring, S. Karmakar, and H. Päs, To be published.

[6] S. L. Glashow, Nucl. Phys. **22**, 579 (1961).

[7] S. Weinberg, Phys. Rev. Lett. **19**, 1264 (1967).

[8] ATLAS, G. Aad *et al.*, Phys. Lett. **B716**, 1 (2012), 1207.7214.

[9] CMS, S. Chatrchyan *et al.*, Phys. Lett. **B716**, 30 (2012), 1207.7235.

[10] Planck, N. Aghanim *et al.*, (2018), 1807.06209.

[11] B. Pontecorvo, Sov. Phys. JETP **6**, 429 (1957), [Zh. Eksp. Teor. Fiz.33,549(1957)].

[12] SNO Collaboration, Q. R. Ahmad *et al.*, Phys. Rev. Lett. **87**, 071301 (2001).

[13] Super-Kamiokande Collaboration, Y. Fukuda *et al.*, Phys. Rev. Lett. **81**, 1562 (1998).

[14] V. O. Egorov and I. P. Volobuev, Phys. Rev. **D97**, 093002 (2018), 1709.09915.

[15] KATRIN, M. Aker *et al.*, Phys. Rev. Lett. **123**, 221802 (2019), 1909.06048.

[16] G. Altarelli and F. Feruglio, Nuclear Physics B **741**, 215 (2006).

[17] G. Hiller, D. Loose, and K. Schönwald, JHEP **12**, 027 (2016), 1609.08895.

[18] MEG, A. M. Baldini *et al.*, Eur. Phys. J. **C76**, 434 (2016), 1605.05081.

[19] G. Hiller and F. Krüger, Phys. Rev. D **69**, 074020 (2004).

[20] LHCb Collaboration 1, R. Aaij *et al.*, Phys. Rev. Lett. **122**, 191801 (2019).

[21] M. Bordone, G. Isidori, and A. Pattori, Eur. Phys. J. C **76**, 440 (2016), 1605.07633.

[22] F. Zwicky, Helvetica Physica Acta **6**, 110 (1933).

[23] V. C. Rubin and W. K. Ford, Jr., Astrophys. J. **159**, 379 (1970).

[24] D. N. Schramm and M. S. Turner, Rev. Mod. Phys. **70**, 303 (1998), astro-ph/9706069.

[25] D. Clowe *et al.*, Astrophys. J. **648**, L109 (2006), astro-ph/0608407.

[26] B. Famaey and S. McGaugh, Living Rev. Rel. **15**, 10 (2012), 1112.3960.

[27] A. Abada, C. Biggio, F. Bonnet, M. B. Gavela, and T. Hambye, JHEP **12**, 061 (2007), 0707.4058.

[28] E. K. Akhmedov, Neutrino physics, in *Proceedings, Summer School in Particle Physics: Trieste, Italy, June 21-July 9, 1999*, pp. 103–164, 1999, hep-ph/0001264.

[29] A. Pilaftsis, Z. Phys. **C55**, 275 (1992), hep-ph/9901206.

[30] S. F. King, Rept. Prog. Phys. **67**, 107 (2004), hep-ph/0310204.

[31] S. King, Nucl. Phys. B **576**, 85 (2000), hep-ph/9912492.

[32] S. Weinberg, Phys. Rev. Lett. **43**, 1566 (1979).

[33] P. Minkowski, Phys. Lett. **B67**, 421 (1977).

[34] M. Magg and C. Wetterich, Phys. Lett. **94B**, 61 (1980).

[35] R. Foot, H. Lew, X. G. He, and G. C. Joshi, Z. Phys. **C44**, 441 (1989).

[36] R. Primulando, J. Julio, and P. Uttayarat, JHEP **08**, 024 (2019), 1903.02493.

[37] R. N. Mohapatra and J. W. F. Valle, Phys. Rev. D **34**, 1642 (1986).

[38] Physics Letters B **246**, 249 (1990).

[39] F. Deppisch and J. W. F. Valle, Phys. Rev. **D72**, 036001 (2005), hep-ph/0406040.

[40] A. Abada and M. Lucente, Nucl. Phys. **B885**, 651 (2014), 1401.1507.

[41] F. Bonnet, M. Hirsch, T. Ota, and W. Winter, JHEP **07**, 153 (2012), 1204.5862.

[42] D. Aristizabal Sierra, A. Degee, L. Dorame, and M. Hirsch, JHEP **03**, 040 (2015), 1411.7038.

[43] E. Ma, Phys. Rev. **D73**, 077301 (2006), hep-ph/0601225.

[44] S. Antusch and O. Fischer, JHEP **05**, 053 (2015), 1502.05915.

[45] S. Antusch, C. Biggio, E. Fernandez-Martinez, M. B. Gavela, and J. Lopez-Pavon, JHEP **10**, 084 (2006), hep-ph/0607020.

[46] S. Antusch and O. Fischer, JHEP **10**, 094 (2014), 1407.6607.

[47] S. Bilenky and B. Pontecorvo, Physics Reports **41**, 225 (1978).

[48] E. W. Kolb and M. S. Turner, Front. Phys. **69**, 1 (1990).

[49] X. Chu, T. Hambye, and M. H. G. Tytgat, JCAP **1205**, 034 (2012), 1112.0493.

[50] T. Hambye, M. H. G. Tytgat, J. Vandecasteele, and L. Vanderheyden, Phys. Rev. **D100**, 095018 (2019), 1908.09864.

[51] G. F. Giudice, A. Notari, M. Raidal, A. Riotto, and A. Strumia, Nucl. Phys. **B685**, 89 (2004), hep-ph/0310123.

[52] A. Merle, A. Schneider, and M. Totzauer, JCAP **1604**, 003 (2016), 1512.05369.

[53] J. König, A. Merle, and M. Totzauer, JCAP **11**, 038 (2016), 1609.01289.

[54] S. Profumo, L. Giani, and O. F. Piattella, Universe **5**, 213 (2019), 1910.05610.

[55] K. Griest and D. Seckel, Phys. Rev. **D43**, 3191 (1991).

[56] C. Niblaeus, PhD thesis.

[57] G. B langer *et al.*, JHEP **02**, 186 (2019), 1811.05478.

[58] T. Lin, PoS **333**, 009 (2019), 1904.07915.

[59] M. Schumann, J. Phys. G **46**, 103003 (2019), 1903.03026.

[60] XENON, E. Aprile *et al.*, Phys. Rev. Lett. **119**, 181301 (2017), 1705.06655.

[61] A. Berlin, D. Hooper, and S. D. McDermott, Phys. Rev. **D89**, 115022 (2014), 1404.0022.

[62] P. Junnarkar and A. Walker-Loud, Phys. Rev. D **87**, 114510 (2013), 1301.1114.

[63] C. Savage, G. Gelmini, P. Gondolo, and K. Freese, Journal of Cosmology and Astroparticle Physics **2009**, 010 (2009).

[64] R. Bernabei *et al.*, Nucl. Phys. Atom. Energy **19**, 307 (2018), 1805.10486.

[65] XENON, E. Aprile *et al.*, Phys. Rev. Lett. **121**, 111302 (2018), 1805.12562.

[66] S. Dodelson and L. M. Widrow, Phys. Rev. Lett. **72**, 17 (1994), hep-ph/9303287.

[67] N. Palanque-Delabrouille *et al.*, Astron. Astrophys. **559**, A85 (2013), 1306.5896.

[68] M. Garny and J. Heisig, Phys. Rev. D **98**, 095031 (2018), 1809.10135.

[69] J. Baur, N. Palanque-Delabrouille, C. Y che, C. Magneville, and M. Viel, JCAP **08**, 012 (2016), 1512.01981.

[70] M. Markevitch *et al.*, Astrophys. J. **606**, 819 (2004), astro-ph/0309303.

[71] S. W. Randall, M. Markevitch, D. Clowe, A. H. Gonzalez, and M. Bradač, The Astrophysical Journal **679**, 1173 (2008).

[72] A. H. Peter, M. Rocha, J. S. Bullock, and M. Kaplinghat, Mon. Not. Roy. Astron. Soc. **430**, 105 (2013), 1208.3026.

[73] D. Harvey, R. Massey, T. Kitching, A. Taylor, and E. Tittley, Science **347**, 1462 (2015), 1503.07675.

[74] F. Kahlhoefer, K. Schmidt-Hoberg, J. Kummer, and S. Sarkar, Mon. Not. Roy. Astron. Soc. **452**, L54 (2015), 1504.06576.

[75] T. R. Slatyer, Indirect Detection of Dark Matter, in *Theoretical Advanced Study Institute in Elementary Particle Physics: Anticipating the Next Discoveries in Particle Physics*, pp. 297–353, 2018, 1710.05137.

[76] Fermi-LAT, M. Ackermann *et al.*, Phys. Rev. Lett. **115**, 231301 (2015), 1503.02641.

[77] N. Sabti, J. Alvey, M. Escudero, M. Fairbairn, and D. Blas, JCAP **01**, 004 (2020), 1910.01649.

[78] C. Pitrou, A. Coc, J.-P. Uzan, and E. Vangioni, Phys. Rept. **754**, 1 (2018), 1801.08023.

[79] CMS, A. M. Sirunyan *et al.*, Phys. Lett. B **793**, 520 (2019), 1809.05937.

[80] G. Bhattacharyya, H. V. Klapdor-Kleingrothaus, H. Pas, and A. Pilaftsis, Phys. Rev. **D67**, 113001 (2003), hep-ph/0212169.

[81] K. R. Dienes, E. Dudas, and T. Gherghetta, Nucl.Phys. **B557**, 25 (1999), hep-ph/9811428.

[82] H. K. Dreiner, H. E. Haber, and S. P. Martin, Physics Reports **494**, 1 (2010).

[83] E. Accomando, I. Antoniadis, and K. Benakli, Nucl. Phys. **B579**, 3 (2000), hep-ph/9912287.

[84] A. Donini and S. Rigolin, Nucl. Phys. **B550**, 59 (1999), hep-ph/9901443.

[85] A. Pilaftsis, Phys. Rev. **D60**, 105023 (1999), hep-ph/9906265.

[86] ATLAS, G. Aad *et al.*, Eur. Phys. J. **C75**, 299 (2015), 1502.01518, [Erratum: Eur. Phys. J.C75,no.9,408(2015)].

[87] M. C. Gonzalez-Garcia, M. Maltoni, and T. Schwetz, (2015), 1512.06856.

[88] Particle Data Group, J. Beringer *et al.*, Phys. Rev. **D86**, 010001 (2012).

[89] G. Arcadi, A. Djouadi, and M. Raidal, Phys. Rept. **842**, 1 (2020), 1903.03616.

[90] M. Drewes and J. U. Kang, JHEP **05**, 051 (2016), 1510.05646.

[91] M. Drewes *et al.*, JCAP **01**, 025 (2017), 1602.04816.

[92] J. A. Casas and A. Ibarra, Nucl. Phys. **B618**, 171 (2001), hep-ph/0103065.

[93] M. Blennow, E. Fernandez-Martinez, and B. Zaldivar, JCAP **1401**, 003 (2014), 1309.7348.

[94] Particle Data Group, M. Tanabashi *et al.*, Phys. Rev. **D98**, 030001 (2018).

[95] N. Arkani-Hamed, S. Dimopoulos, G. R. Dvali, and J. March-Russell, Phys. Rev. **D65**, 024032 (2001), hep-ph/9811448.

[96] S. Tremaine and J. E. Gunn, Phys. Rev. Lett. **42**, 407 (1979), [,66(1979)].

[97] J. Baur *et al.*, JCAP **1712**, 013 (2017), 1706.03118.

[98] DES, E. Nadler *et al.*, (2020), 2008.00022.

[99] T. A. Chowdhury and S. Nasri, Phys. Rev. **D97**, 075042 (2018), 1801.07199.

[100] I. Esteban, M. C. Gonzalez-Garcia, A. Hernandez-Cabezudo, M. Maltoni, and T. Schwetz, JHEP **01**, 106 (2019), 1811.05487.

[101] T. Hambye, M. H. G. Tytgat, J. Vandecasteele, and L. Vanderheyden, Phys. Rev. **D98**, 075017 (2018), 1807.05022.

[102] B. Batell, T. Han, and B. Shams Es Haghi, Phys. Rev. **D97**, 095020 (2018), 1704.08708.

[103] P. Bandyopadhyay, E. J. Chun, and R. Mandal, (2020), 2005.13933.

[104] E. Molinaro, J. Phys. Conf. Ser. **447**, 012052 (2013), 1303.5856.

[105] M. Escudero, N. Rius, and V. Sanz, Eur. Phys. J. **C77**, 397 (2017), 1607.02373.

[106] A. M. Gago, P. Hernandez, J. Jones-Perez, M. Losada, and A. Moreno Briceno, Eur. Phys. J. **C75**, 470 (2015), 1505.05880.

[107] S. Alekhin *et al.*, Rept. Prog. Phys. **79**, 124201 (2016), 1504.04855.

[108] B. Batell, T. Han, D. McKeen, and B. Shams Es Haghi, Phys. Rev. **D97**, 075016 (2018), 1709.07001.

[109] S. Mandal, R. Srivastava, and J. W. Valle, Phys. Rev. D **101**, 115030 (2020), 1903.03631.

[110] A. Merle and M. Platscher, Phys. Rev. **D92**, 095002 (2015), 1502.03098.

[111] M. Lindner, M. Platscher, C. E. Yaguna, and A. Merle, Phys. Rev. **D94**, 115027 (2016), 1608.00577.

[112] R. Bouchand and A. Merle, JHEP **07**, 084 (2012), 1205.0008.

[113] A. Merle and M. Platscher, JHEP **11**, 148 (2015), 1507.06314.

[114] A. Merle, M. Platscher, N. Rojas, J. W. F. Valle, and A. Vicente, JHEP **07**, 013 (2016), 1603.05685.

[115] I. F. Ginzburg, K. A. Kanishev, M. Krawczyk, and D. Sokolowska, Phys. Rev. **D82**, 123533 (2010), 1009.4593.

[116] P. Arnold and S. Vokos, Phys. Rev. D **44**, 3620 (1991).

[117] M. Escudero, N. Rius, and V. Sanz, JHEP **02**, 045 (2017), 1606.01258.

[118] V. González-Macías, J. I. Illana, and J. Wudka, JHEP **05**, 171 (2016), 1601.05051.

[119] J. McDonald, Phys. Rev. D **50**, 3637 (1994), hep-ph/0702143.

[120] A. Sommerfeld, Annalen der Physik **403**, 257 (1931).

[121] A. D. Sakharov, Zh. Eksp. Teor. Fiz. **18**, 631 (1948), [Usp. Fiz. Nauk161,no.5,29(1991)].

[122] J. Ellis, F. Luo, and K. A. Olive, JHEP **09**, 127 (2015), 1503.07142.

[123] J. Ellis, J. L. Evans, F. Luo, and K. A. Olive, JHEP **02**, 071 (2016), 1510.03498.

[124] S. Kim and M. Laine, JHEP **07**, 143 (2016), 1602.08105.

[125] W.-Y. Keung, I. Low, and Y. Zhang, Phys. Rev. **D96**, 015008 (2017), 1703.02977.

[126] J. Harz and K. Petraki, Phys. Rev. **D97**, 075041 (2018), 1711.03552.

[127] J. Harz and K. Petraki, JHEP **04**, 130 (2019), 1901.10030.

[128] E. L. V.B. Berestetskii and L. Pitaevskii, *Quantum Electrodynamics* (USA: Addison-Wesley 842 p, 1982).

[129] M. Hamzavi, M. Movahedi, K.-E. Thylwe, and A. A. Rajabi, Chinese Physics Letters **29**, 080302 (2012).

[130] F. J. Rogers, H. C. Graboske, and D. J. Harwood, Phys. Rev. A **1**, 1577 (1970).

[131] K. Agashe, Y. Cui, L. Necib, and J. Thaler, JCAP **1410**, 062 (2014), 1405.7370.

[132] J. Berger, Y. Cui, and Y. Zhao, JCAP **1502**, 005 (2015), 1410.2246.

[133] J. Kopp, J. Liu, and X.-P. Wang, JHEP **04**, 105 (2015), 1503.02669.

[134] S. Nussinov, Phys. Lett. **165B**, 55 (1985).

[135] A. Falkowski, J. T. Ruderman, and T. Volansky, JHEP **05**, 106 (2011), 1101.4936.

[136] A. Falkowski, E. Kuflik, N. Levi, and T. Volansky, Phys. Rev. **D99**, 015022 (2019), 1712.07652.

[137] M. T. Frandsen and W.-C. Huang, (2019), 1912.02203.

[138] M. Yoshimura, Phys. Rev. Lett. **41**, 281 (1978), [Erratum: Phys. Rev. Lett.42,746(1979)].

[139] D. Toussaint, S. B. Treiman, F. Wilczek, and A. Zee, Phys. Rev. **D19**, 1036 (1979).

[140] S. Weinberg, Phys. Rev. Lett. **42**, 850 (1979).

[141] S. M. Barr, G. Segre, and H. A. Weldon, Phys. Rev. **D20**, 2494 (1979).

[142] C. Boehm, M. J. Dolan, and C. McCabe, JCAP **1212**, 027 (2012), 1207.0497.

[143] K. M. Nollett and G. Steigman, Phys. Rev. **D91**, 083505 (2015), 1411.6005.

[144] M. Hufnagel, K. Schmidt-Hoberg, and S. Wild, JCAP **1802**, 044 (2018), 1712.03972.

[145] G. Hiller and F. Kruger, Phys. Rev. **D69**, 074020 (2004), hep-ph/0310219.

[146] XENON, E. Aprile *et al.*, Phys. Rev. Lett. **122**, 141301 (2019), 1902.03234.

[147] S. Fajfer and N. Košnik, Phys. Lett. B **755**, 270 (2016), 1511.06024.

[148] C. Cornella, J. Fuentes-Martin, and G. Isidori, JHEP **07**, 168 (2019), 1903.11517.

[149] H. Päs and E. Schumacher, Phys. Rev. D **92**, 114025 (2015), 1510.08757.

[150] R. Gauld, F. Goertz, and U. Haisch, Phys. Rev. **D89**, 015005 (2014), 1308.1959.

[151] L. Bian, S.-M. Choi, Y.-J. Kang, and H. M. Lee, Phys. Rev. **D96**, 075038 (2017), 1707.04811.

[152] P. Arnan, L. Hofer, F. Mescia, and A. Crivellin, JHEP **04**, 043 (2017), 1608.07832.

[153] M. Alguer *et al.*, Eur. Phys. J. C **79**, 714 (2019), 1903.09578, [Addendum: Eur.Phys.J.C 80, 511 (2020)].

[154] G. C. Branco *et al.*, Phys. Rept. **516**, 1 (2012), 1106.0034.

[155] A. Alloul, N. D. Christensen, C. Degrande, C. Duhr, and B. Fuks, Comput. Phys. Commun. **185**, 2250 (2014), 1310.1921.

[156] N. D. Christensen *et al.*, Eur. Phys. J. **C71**, 1541 (2011), 0906.2474.

[157] T. Hahn, Comput. Phys. Commun. **140**, 418 (2001), hep-ph/0012260.

[158] T. Hahn and M. Perez-Victoria, Comput. Phys. Commun. **118**, 153 (1999), hep-ph/9807565.

[159] A. Belyaev, N. D. Christensen, and A. Pukhov, Comput. Phys. Commun. **184**, 1729 (2013), 1207.6082.

[160] G. Belanger, F. Boudjema, A. Pukhov, and A. Semenov, Comput. Phys. Commun. **185**, 960 (2014), 1305.0237.

[161] G. Belanger, F. Boudjema, A. Goudelis, A. Pukhov, and B. Zaldivar, Comput. Phys. Commun. **231**, 173 (2018), 1801.03509.

[162] IceCube, M. Aartsen *et al.*, Eur. Phys. J. C **77**, 146 (2017), 1612.05949, [Erratum: Eur.Phys.J.C 79, 214 (2019)].

[163] J. Aguilar-Saavedra, R. Benbrik, S. Heinemeyer, and M. P rez-Victoria, Phys. Rev. D **88**, 094010 (2013), 1306.0572.

[164] J. Heeck and D. Teresi, Phys. Rev. **D96**, 035018 (2017), 1706.09909.

[165] M. A. Luty, Phys. Rev. **D45**, 455 (1992).